Exploration of the gas phase chemistry in microwave activated plasmas used for diamond chemical vapour deposition

by

Jie Ma

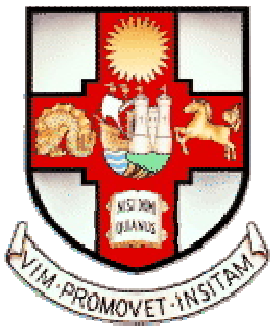

University of Bristol

A thesis submitted to the University of Bristol in accordance with the requirements of the degree of Doctor of Philosophy in the Department of Chemistry, Faculty of Science.

April 2008

Word count: 49,407

Abstract

The work presented in this thesis focuses on using laser spectroscopy and optical emission spectroscopy (OES) to diagnose microwave activated hydrocarbon/Ar/H_2 and hydrocarbon/Ar/H_2/B_2H_6 plasmas used in diamond chemical vapour deposition. Two laser spectroscopy methods, cavity ring-down spectroscopy (CRDS) and tuneable infrared laser absorption spectroscopy (TIRLAS), have been employed.

In the TIRLAS experiment, a novel quantum cascade laser (QCL) was used to measure the IR absorptions of two stable hydrocarbon species, CH_4 and C_2H_2, in different hydrocarbon/Ar/H_2 plasmas. The fast frequency chirp of the QCL also allows time resolved absorption measurements. Aspects of the gas phase chemistry of CH_4 and C_2H_2, and their interconversion, was thus explored.

CRDS is a highly sensitive and accurate, multi-pass absorption technique. In this thesis, it has been applied successfully to measure absolute column densities of $C_2(a^3\Pi_u)$ and $CH(X^2\Pi)$ radicals, and H(n=2) atoms, and their spatial profiles in CH_4/Ar/H_2 plasma, as functions of various discharge parameters (power, pressure, CH_4 flow rate, Ar flow rate). The gas temperature in the plasma region was also determined by measuring the C_2 rotational temperature, and found to have typical values around 3000 K.

OES has been used to study the behaviour of several species (Ar, H, CH, C_2, etc) emissions in CH_4/Ar/H_2 plasma, as functions of different discharge parameters. Actinometry was used to investigate the behaviour of H(n=1) atoms in the plasma. The spatial profiles of these emissions were also measured and compared with the column density profiles measured in CRDS experiments.

Finally, B/C/H chemistry was explored in B_2H_6/Ar/H_2/CH_4 plasma – using CRDS to measure column densities of BH radicals, and OES to measure emissions from BH and from B atoms – under different discharge conditions. The spatial profiles of BH column densities and emissions were also measured and compared.

Acknowledgement

I offer special thanks to my supervisor, Professor Mike Ashfold, for his invaluable guidance, suggestions, encouragement, inspiration and continued support throughout my PhD research. Next I would like to thank Dr. James Smith, Mr. Keith Rosser, Mr Gwyn Jones and Mr Charles Murray, for their innumerous technical help and advice. Special thanks also go to Dr. Chris Rennick, for teaching me how to use CRDS and for helping me with my first year research, and to Dr. Andy Cheesman for teaching me how to operate the microwave reactor. I also owe thanks to Dr. Ye Sun, Jon Henney, James Richley, Yang Li, Dr. Dane Comerford, Dr. Edward Crichton, Dr. Gareth Fuge, Dr. Dickon Young, and Manik Pradhan for their help and friendship. Also, I would like to thank Professor Andrew Orr-Ewing and Dr Yuri Mankelevich for their valuable advice and discussion. I also want to thank Professor Geoffrey Duxbury and Dr. Stephen Wright for the help with the QCL experiments.

I would like to thank the Overseas Research Scholarship (ORS) and University of Bristol for financial support. Thanks to Element Six for loaning us the microwave reactor and for sponsoring my attendance at the De Beers Diamond Conference.

Many thanks to my flatmates in Hodgkin House: KC, Jianru, Yugang, Lizzy, Chunliang, Uncle Yin, Cheng Fan, Qi Yin, Sila, Kanchaya, Bo, Michael, Nitrat, Quanguo and Naichun etc for their wonderful friendships and endless fun. Particular thanks to my dear girl friend, Miss Thitima Rujiralai for her encouragement and strong support!

Thanks also go to my previous supervisor in Tsinghua University in China, Professor Yi-kang Pu, for his non-stop encouragement and valuable advice.

I also want to give special thanks to my parents and brother, my best friend, Xulei and all his family, for their unfaltering love and continued support. Without this, I could not finish my PhD study.

The last special thanks go to Dr Paul May for the wonderful Postdoctoral job offer.

Authors Declaration

I declare that the work in this dissertation was carried out in accordance with the Regulations of the University of Bristol. The work is original except where indicated by special reference in the text and no part of the dissertation has been submitted for any other degree. Any views expressed in the dissertation are those of the author and in no way represent those of the University of Bristol. The dissertation has not been presented to any other University for examination either in the United Kingdom or overseas.

SIGNED:…… DATE: …….....

Contents

List of Figures

List of Tables

Chapter 1 Introduction

1.1. Plasma

Plasma, named the fourth state of matter, is a collection of charged particles (electrons, positive and negative ions), neutrals (atoms, molecules and radicals) and fields that exhibit collective effects. It is the commonest matter form, occupying almost 99% of the visible universe. Plasmas in nature can be found in stars, nebula, aurora, etc and always are of great interest to astronomers. Today, humans can also produce varieties of plasmas to fulfill a range of purposes of their own. For example, the H_2 plasma is used in fusion as a possible solution to the energy problem. [1] Some Ar/Hg plasmas are also used for illumination. However, one of the most important applications of plasma is for material processing. Especially in today's semiconductor industries, the processing involving plasmas, such as etching, ashing, cleaning and nitriding, plays an essential role. [2]

The versatility of plasma provides many advantages in material processing. Firstly, in a plasma, there are lots of charged particles, which can be controlled by applying an external electric or magnetic field. Secondly, a non-equilibrium plasma can have quite different temperatures for electrons and heavy particles, e.g, electrons can be very hot and energetic (good for producing active species) while the gas temperature can still remain low (very important for processing materials like photoresist, biomaterials, etc which can not survive under high temperature). Thirdly, the plasma can produce many kinds of active species and energetic particles with high densities. Also, plasma induced processes can be much more efficient than corresponding processes brought about by thermal methods. Thus the plasma is good at providing a very reactive environment and inducing many chemical reactions.

On the other hand, the flexibility advantage of the plasma has to be offset by its

complexity. In most cases, many processes are combined and linked together. The inhomogenity of species concentration and temperature further enhances such complexities. Sometimes, plasma instability will also make accurate prediction of the plasma behaviour impossible.

A good understanding of the plasma behaviour needs knowledge from both discharge physics and gas-phase chemistry. To gain such knowledge, people resort to the plasma diagnostics (i.e. experiments) and theoretical simulation. Plasma diagnostics involves using various (such as optical or electrical) techniques to study the plasma properties and behaviour, The reason to call it “diagnostics”, not “measurement” is that, to understand the plasma behaviour requires not only the measurement of plasma parameters but also reasonable assumptions and logical deductions based on the pre-existent physical and chemical knowledge. This is somewhat similar to what the doctor does for a patient in order to establish his/her illness, which is called diagnosis in the clinic.

1.2. Diamond structure and properties

Diamond is a wonderful material. Not only is it famous to the public as gemstones, but also it is attractive to scientists and engineers for its unique, excellent properties.
Diamond is simply an allotrope of carbon. Other major members in this family include graphite, Buckminster Fullerene (bucky balls), carbon nanotube (CNT), see **Figure 1. 1**. Due to the different structures, diamond exhibits many excellent properties that are quite different from the other allotropes.

The structure of diamond is shown in **Figure 1. 1 (a)**. It can be regarded as a 3D network of carbon atoms tetrahedrally bonded by sp^3 hybridized bonds. Since each carbon atom in the diamond lattice is firmly “supported” by four neighbouring atoms, this structure makes diamond the hardest material known to man. Thus, it is ideal to be used as the blade of cutting and/or polishing machines. [3]

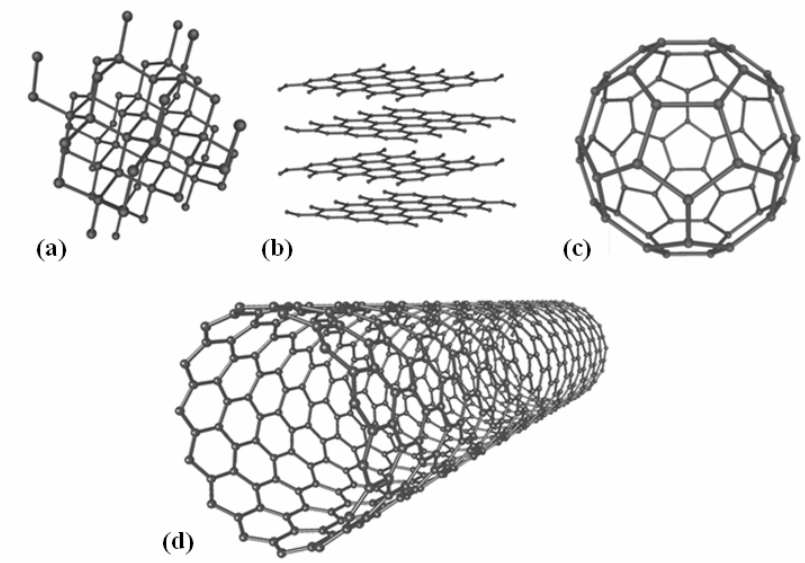

Figure 1. 1 Structures of several allotropes of carbon: (a) diamond; (b) graphite; (c) C_{60}; (d) single wall carbon nanotube (SWCNT)

Diamond also has the highest thermal conductivity and the lowest thermal expansion coefficient, thus can be used as a heat sink for integrated chips (ICs) and laser diodes. [4]

In addition, diamond has a very big band gap, around 5.45 eV at room temperature. Due to the high symmetry, it has very few absorption bands. Therefore, it is an excellent material for optical windows, allowing the light transmission from the deep UV to the far IR. [5]

The resistivity of diamond is very high as well, normally > 10^{15} Ωcm^{-1}. So it is actually regarded as an insulator. However, after doped with suitable elements, it can become semiconductor with very high carrier mobility. Diamond can be grown directly on silicon, which is good for integration with the present semiconductor processing arts. All these attributes make diamond promising as a next generation semiconductor material. Some electronic device prototypes based on diamond have already been demonstrated. [6-8]

Due to its chemical inertness, diamond is suitable to be used in many tough

environments. For example, diamond is more resistant against X-rays, γ-rays, UV and nuclear particles than other materials commonly used as solid-state detectors. It is much more robust than silicon under neutron bombardment. [9]

Also, never forget, diamond is biologically compatible. boron-doped diamond is thus a very promising candidate for bioelectronics as it shows good electronic and chemical properties. [10, 11] Besides that, some surfaces of diamond exhibit very low or even 'negative' electron affinity, which is suitable for making field emitters. Such research is being carried out in many labs. [12, 13] Some of the main properties of diamond and their related applications are summarized in **Table 1.1.**

Table 1. 1 Diamond properties and its applications [5]

Properties	Value	Applications
extreme hardness	10000 kg/mm^2	cutting and grinding machine
highest thermal conductivity	2000 Wm^{-1}K^{-1}	thermal conductor for diode laser
Electron mobility	2,200 cm^2/V· s	fast electronics
Hole mobility	1,600 cm^2/V· s	fast electronics
Band gap	5.45 eV	optical window
Resistivity	$10^{13} - 10^{16}$Ohm · cm	insulator
Sound speed	18,000 m/s	SAW filter
Work function	small and negative on [111] surface	field emission devices

1.3. Chemical vapour deposition of diamond

Chemical Vapour Deposition (CVD) is a process which includes both gas phase reactions and gas-solid surface reactions. The former usually leads to the production of a number of active species. The species can then react with or through the solid surface and finally result in the deposition of the material.

There are varieties of diamond CVD techniques, [5, 14] classified by means of how the energy is coupled into the system (called gas activation), which will be briefly

introduced in the following sections.

1.3.1 Hot filament

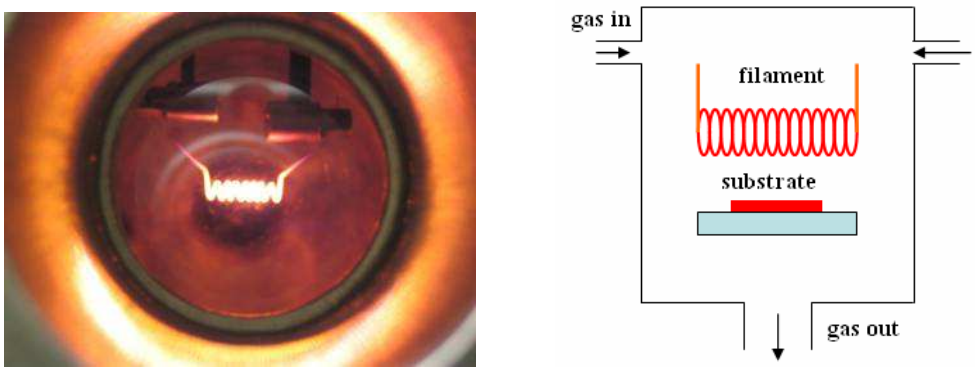

Figure 1. 2 Picture and schematic of hot filament CVD reactor

Hot filament CVD (HFCVD) (as shown in **Figure 1. 2**) uses a metal coil, resistively heated to around 2000~2500 K to activate the gas phase reactions. The feedstock normally is methane/hydrogen mixture. HFCVD provides a cheap and simple way to make diamond. The filament works as a power source and catalyst at the same time to help dissociate the H_2. The resulting H atoms then initiate most gas phase reactions with the hydrocarbon and finally lead to diamond deposition on the Si or Mo substrate, which is heated separately by an electric heater to 1000~1200 K. Therefore, the properties of the filament are very important for HFCVD. The commonly used filament material is a kind of chemically-inert metal, e.g. tungsten or tantalum. However, under the high temperature, it will inevitably react with carbon-containing species and gradually degrade, and finally become more brittle and resistive. This then will influence both the power coupling efficiency and the catalysis activity. Also, due to the presence of the filament in the reactor, the input gas for HFCVD cannot contain oxidizing or corrosive gases. Even so, the contamination from the filament material is still difficult to avoid. Thus, usually, HFCVD-grown diamond has low quality and is suitable for mechanical, but not for electronic applications. Besides those drawbacks, the diamond growth rate by HFCVD is also low.

1.3.2 Arcjet plasma

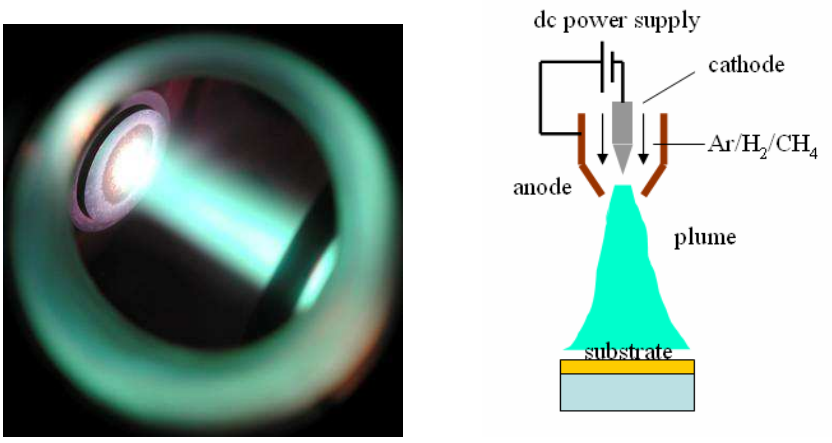

Figure 1. 3 Picture and schematic of a DC arcjet reactor

The DC arcjet is another commercial way to produce diamond. In the DC-arc jet, an anode and a cathode are connected by a DC power supply. Between the two electrodes a discharge region is formed. When gases such as an $Ar/H_2/CH_4$ mixture flow through this region, ionization occurs and a jet of plasma is generated and accelerated by a pressure drop towards the substrate, where the diamond film is deposited. The advantage of this technique is its high growth rate, which is usually unobtainable by other methods. The maximum can be 1mm/hr. [15] However, this method cannot grow diamond over large areas and, again, metal contamination (from the cathode) tends to impair the diamond purity and quality.

1.3.3 Microwave plasma

Microwave (MW) plasma are now the most popular way to produce high quality diamond film. The two most common types of MWCVD reactor are shown in **Figure 1. 4**. In a microwave reactor, the CH_4 and H_2 mixture is introduced. The microwave power is coupled into the chamber through a dielectric window (such as a quartz window). Firstly, electrons will pick up energy from the electromagnetic field. Then, through their collisions, the energy is transferred to the heavy species, making them dissociated, excited or ionized. The “active” species so produced then react on the substrate surface and form the diamond film.

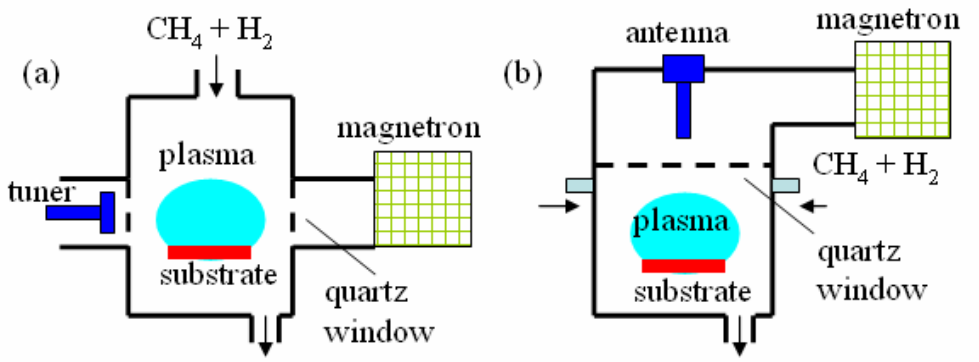

Figure 1. 4 Schematic of Microwave reactor: (a) NIRIM type; [16] (b) ASTEX type [17]

The advantage of this method is that there is no electrode or filament in the reactor. this provides a clean environment for diamond growth. Also, the diamond growth rate is relatively fast due to high input power and the immersion of the substrate into the plasma. The main drawback is that such systems are usually expensive.

1.4. Diamond growth mechanism

The chemistry behind diamond CVD is very complicated. It can be divided into gas-phase chemistry and surface chemistry.

1.4.1 Gas phase chemistry

It is believed that hydrogen atoms usually play a crucial role in initiating the relevant gas phase reactions. [18, 19] For example, when a H_2 and CH_4 mixture is introduced into the reactor, H_2 is dissociated at the surface of the filament or by collisions. This results in an H-abundant environment. Under high atomic hydrogen concentration and high T_{gas} conditions, CH_4 reacts with H through a series of abstraction reactions, producing many radicals like CH_3, CH_2, CH and C. These can also react with one another through "self-scavenging" reactions, producing C2 species, like C_2H_6. Then, following similar H abstraction reactions, species like C_2H_5, C_2H_4, etc are also formed. Among them, C_2H_2 is the thermodynamically favoured hydrocarbon species at high T_{gas}. Some of the species will act as precursors for diamond growth in the following gas-solid surface interactions

1.4.2 Surface Chemistry

The H atoms also play an important role in surface reactions: they can continuously create and re-terminate (thereby preventing the reconstruction to non-diamond forms) the reactive surface sites necessary for the propagation of the diamond lattice sites. H atoms can also selectively etch any graphitic sp^2 carbon through so-called β-scission processes, [20] see **Figure 1. 5**.

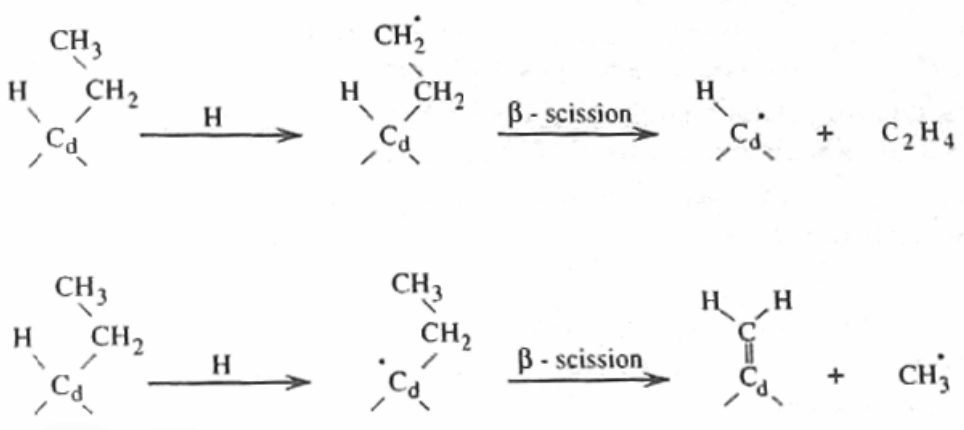

Figure 1. 5 Two β-scission processes to attack a surface-bonded ethyl group [20]

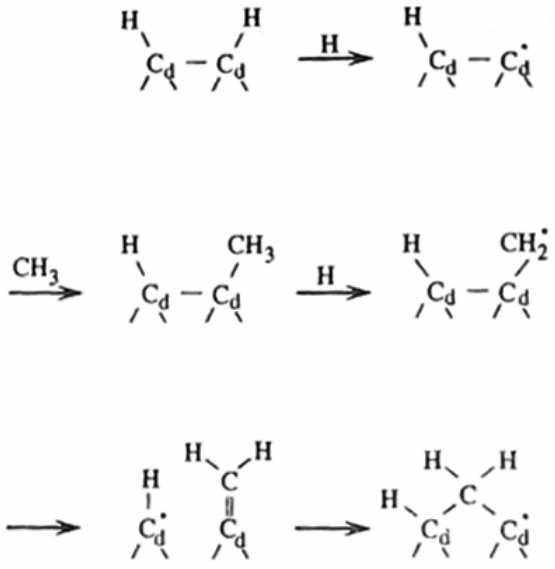

Figure 1. 6 The GDSB mechanism for methyl insertion. [21]

The currently accepted diamond growth mechanism can be classified into two

groups: C1 and C2 mechanisms. For C1 mechanisms, the usually assumed growth species is CH_3 due to its abundance in the gas phase. In 1992, Garrison et al [21] suggested a so-called GDSB mechanism, (shown in **Figure 1. 6**) for methyl addition to the (100) surface.

For C2 mechanism, Skokov, Weimer and Frenklach [22] in 1994 suggested a mechanism as shown in **Figure 1. 7** for the addition of acetylene to the (100)-(2×1):1H surface.

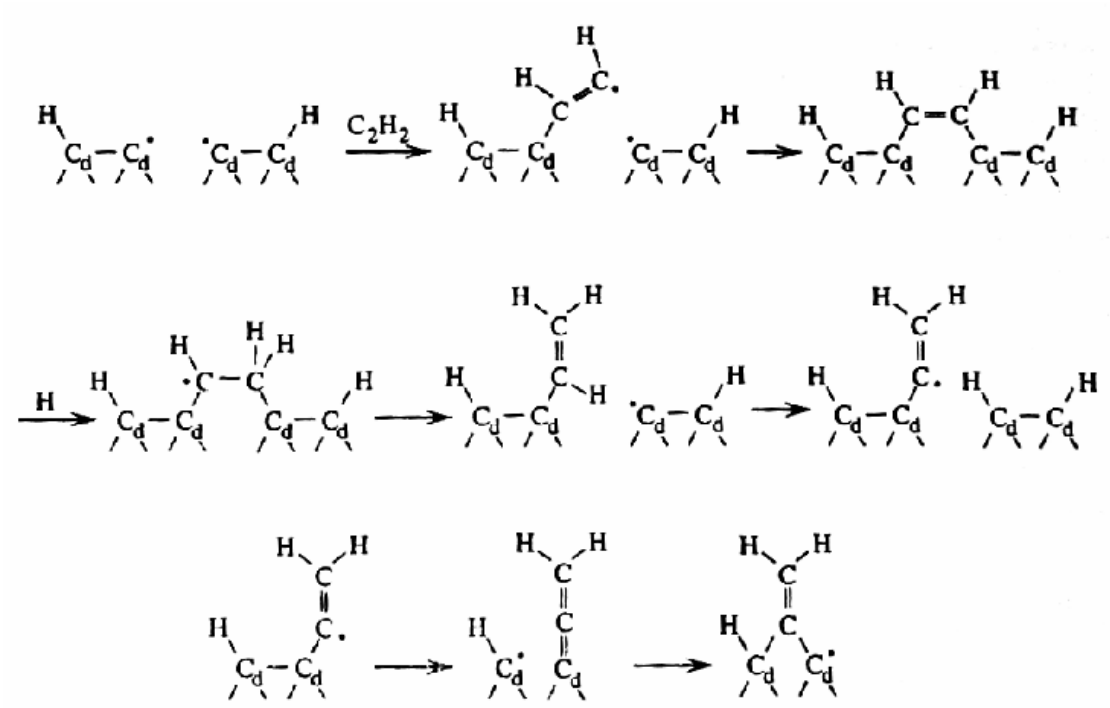

Figure 1. 7 Mechanism of Skokov, Weimer and Frenklach for addition of acetylene. [22]

1.5. Diamond doping [23]

As mentioned before, diamond is a wide band gap material with many excellent properties. If diamond can be used as a semiconductor to make electronic and optic devices, these combined properties will make it very advantageous in many fields, such as high temperature, high power and high speed electronic devices. However, the large band gap and high resistivity of pure diamond (without defects) make it more of an insulator than a semiconductor. To solve this issue, some donor or

acceptor atoms have to be introduced as dopants during diamond growth. For example, when diamond is doped by boron, the band gap at room temperature (RT) can be 370meV.

There are several methods for producing doped diamond: high pressure high temperature (HPHT) method, CVD and ion implantation. These techniques have been used successfully to synthesize the p-type doped diamond. However, synthesis of high quality n-type diamond is still only possible within a few labs [24] and hasn't been well solved. Different elements like N, P and As have been tried. However, these dopant atoms readily form some complexes in diamonds, leading to much higher doped energy band-gap than expected. [23] This limits further application of diamond in semiconductor devices.

1.6. Diagnostics

Using CVD techniques, diamond films can now be synthesized with very good quality, but challenges remain in this field. For example, single crystalline diamond synthesis is still quite challenging. Also, n-type doped diamond with good quality is still quite difficult to achieve. These two are essential for future use of diamond in electronic devices. In addition, from a commercial view point, it is of interest to ask if diamond can be grown faster, more efficiently, and with higher quality. The solutions of all these issues are strongly dependent on how deeply we can understand the diamond CVD processes. Thus, the diagnostics (of both gas phase and surface chemistry) shall play important role in helping us open such a "black box".

The early experiments show that the diamond growth rate and film quality (uniformity, morphology, texture, etc) are closely related to the state of the gas phase (ingredients, temperature, gas flow rate, etc). Thus, before understanding diamond growth, it is essential firstly to understand the gas phase chemistry prevailing in the reactor.

Since the focus of this thesis is the use of a microwave plasma for diamond CVD, a brief overview of the early diagnostics work in this field will be given below.

1.6.1 Neutral species

Optical emission spectroscopy (OES) may be the most popular diagnostic tool used to provide a qualitative insight into the species present in the plasma. As early as 1989, Inspektor et al [25] used OES to monitor C_2, H_α and H_β emissions as a function of hydrocarbon percentage in a bell-jar microwave reactor at conditions of 1 kW input power and 50 Torr total pressure. They found the C_2 Swan band head (516.5 nm) emission shows a linear dependence on hydrocarbon mole fraction, whereas the emissions from H_α (656.2 nm) and H_β (486.1 nm) decreased in a polynomial fashion as the hydrocarbon percentage in the system increases.

Goyette et al [26] also measured C_2 Swan band emissions in an $Ar/H_2/CH_4$ plasma used in the deposition of nanocrystalline diamond. They compared the measured C_2 emission with the absolute C_2 concentration obtained by white-light absorption spectroscopy. They found that the absolute C_2 emission intensity correlated linearly with the C_2 density whilst varying several plasma parameters and across two decades of species concentration. Although optical emission intensities are generally not a quantitative diagnostic for gas phase species concentrations, their results confirmed the reliability of the (0,0) Swan band for determining relative C_2 density with high sensitivity. However, the conditions in their experiment was a hydrogen-deficient mixture (97% Ar:2% H_2:1% CH_4) used for deposition of nanocyrstalline diamond, which is quite different from the “normal” condition of growing diamond film (<5% CH_4, ~95% H_2, i.e. the hydrogen concentration is much higher).

A special OES method, called actinometry, has also been frequently used by many people to determine the relative concentration of ground state H atoms and the hydrogen molecule dissociation fractions. [27-29] However, these experiments only demonstrated the validity of this method at pressures below 20 Torr. The reliability

in the higher pressure conditions still needs to be further investigated. A good discussion about the validity of this method in the diamond CVD conditions has been given by Gicquel et al. [30]

Accurate determination of species concentration requires use of some advanced techniques such as laser spectroscopy. For example, by using tuneable diode absorption spectroscopy (TDLAS), Lombardi et al [31] measured the CH_3 ground state in two different types of microwave plasmas (planar and bell jar). The chosen absorption lines are Q(2,2) in planar reactor and Q(12,12) in the bell-jar reactor. Both belong to the υ_2 fundamental band of CH_3. The measured CH_3 concentrations were compared with those obtained using UV absorption spectroscopy and found to be in qualitative agreement. Besides CH_3, these works also used TDLAS to measure various stable hydrocarbon species like CH_4, C_2H_2 and C_2H_6 as functions of the so-called microwave power density (MWPD) and the CH_4 percentage. [32]

In our group, Cheesman et al [33] used a quantum cascade laser (QCL) to measure the absorption of CH_4 and C_2H_2 as functions of different discharge parameters (carbon flow rate, pressure etc) in both $CH_4/Ar/H_2$ and $C_2H_2/Ar/H_2$ plasmas. The temporal behaviour of these species was also studied.

Though very sensitive and accurate, laser spectroscopy methods are sometimes limited by the lack of suitable laser sources in the necessary wavelength range for the interested species. Mass spectrometry instead, can be a good choice to solve this problem. McMaster et al reported using a molecular beam mass spectrometer (MBMS) to measure absolute species concentrations near the substrate in a microwave reactor at 20 Torr pressure [34]. In their work, the effects of hydrocarbon source (CH_4 and C_2H_2), hydrocarbon concentration, and substrate temperature on the gas-phase species concentration distributions near the substrate were studied. However, their results show that over the range of inlet carbon mole fractions considered, the composition near the substrate was independent of the specific

source gas, indicating the very similar chemistry behind these two plasmas. The detailed reasons for this phenomenon will be one topic considered in this thesis, see Chapter 4. The composition was also found to be insensitive to substrate temperature. Although the film growth rate was temperature dependent, this result shows that the gaseous species distributions are governed by the local equilibrium of the gas phase chemistry. In both CH_4/H_2 and C_2H_2/H_2 plasmas, when the mole fraction of carbon in the feed was less than 1%, CH_4 was the dominant species near the substrate, whereas C_2H_2 was dominant at input carbon mole fractions greater than 1%. Atomic hydrogen was found to be relatively insensitive to the inlet carbon mole fraction.

A new mass spectrometry technique named Li^+-ion attachment mass spectrometry has also been used to detect both radicals and stable species, and even the ions in the gas phase. [35] However, these results remain further verification by others.

Besides diagnoses of the gas phase chemistry, some works also relate the measured plasma characters to the diamond growth rate and film properties. For example, Han et al [36] used OES to study the effect of argon and oxygen additions to the microwave plasma. They found that small addition of Ar into a CH_4/H_2 plasma increases the diamond growth rate. The extra Ar addition corresponds to maximize growth rate depending on the CH_4 mole fraction. Also, the surface morphology of the diamond films changes from (100) square feature to cauliflower type. The spectral linewidth of the diamond Raman feature increases and the graphite and diamond peak ratio, I_G/I_D, becomes higher. On the other hand, by using OES, they found that the measured C_2, CH and H Balmer series emissions all increased with Ar mole fraction. However, the increase in hydrocarbon radical emissions is larger than that of atomic hydrogen, and the relative content of C_2 radicals to CH radicals rapidly increases with increasing argon concentration. Thus they attribute the enhancement of the growth rate to the increased hydrocarbon radical densities and the decline of the film quality to the increase of C_2/CH ratio.

When oxygen is added into a CH_4/H_2 plasma, the growth rate is also observed to pass through a maximum as the oxygen inlet mole fraction increases. This increase is reportedly due to surface activation by OH or O. Such active radical sites are presumably produced by H atom abstraction, and the decrease in growth rate observed when higher levels of oxygen are added to the feed gas comes from the enhanced oxidation rate of solid carbon at the growing diamond surface and the depletion of gas phase hydrocarbons in the plasma due to CO formation. The quality of diamond film is found to increase as the oxygen concentration increases, regardless of the presence of Ar in the feed gas. OES shows that the intensities of CH, C_2 and H decrease but those of OH and CO increase with increasing oxygen concentration. However, C_2 radical emission is seen to decrease far more than that from that of CH radicals. Thus, the improved film quality appears to correlate with the decrease of the C_2/CH ratio. [36]

1.6.2 Temperatures

The microwave plasma used for diamond CVD is non-equilibrium, which means that the electron temperature and the gas (heavy species) temperature are quite different. However, all the reactions are driven by electrons or thermal chemistry. The reaction rates are strongly dependent on these temperatures. Thus, accurately measuring them is essential.

Both OES and laser spectroscopy can be used successfully to obtain the gas temperature. For example, one can measure the rotational temperature of the H_2 Fulcher (0-0) Q branch or measure the translational temperature of excited H atoms from the Doppler linewidth of H_α emission. Besides that, one can also measure the rotational temperature of C_2 [37] or CH radicals.

Using two-photon-allowed transition laser induced fluorescence (TALIF) method and OES (measure H_α Doppler broadening), Gicquel et al [38] measured temperatures of H atoms in their ground and excited H(n=3) states, respectively. They also

measured rotational temperatures of molecular hydrogen in its ground electronic state with the method of coherent anti-Stokes Raman spectroscopy (CARS). The gas temperatures measured by these three methods agree with one another within the respective uncertainties. The determined temperatures over their typical conditions (power densities from 4.5 to 37 W/cm^3) span the range 1500-3200 K.

Lang et al [39]also measured the gas temperature in the microwave plasma by different methods, i.e. the rotational temperature of H_2 Fulcher (0-0) Q branch, the Doppler broadened linewidth of the H_2 Fulcher (0-0) Q(1) line at 601.83 nm and the translation temperature of H atoms determined from H_α emission Doppler broadening. In their experiments, one of the process parameters – pressure (50 to 100 mbar), microwave power (400 to 880 W) and ratio of methane to hydrogen in the feed (0 to 3.2%) -- was varied while the others were kept constant (standard values: 80 mbar; 720 W for the pressure variation, 800 W for the methane variation; 1.2% methane and 4% argon). The temperatures determined by the different methods show similar trends, but the values of these temperatures are quite different. Reasons for this difference include: (1) rotational temperature of H_2 from OES is prone to underestimate the real gas temperature due to the very high rotational relaxation collision number of H_2, (i.e. the average collision number for making an excited H_2 quenched, the value is around 200 [40] -280 [41]); (2) the Hydrogen Balmer lines possibly suffer some extra Stark effect introduced by the strong average field strength in the microwave (2.45 GHz) CVD reactor. Thus it is easy to overestimate the real gas temperature. They conclude that the Doppler temperature of H_2 provides the most reliable estimate of the real gas temperature, which under their standard conditions is around 2000 K.

Unfortunately, there appears to be no literature describing measurement of the electron temperature in moderate pressure microwave plasmas used for diamond CVD. However, several papers [38, 42-44]suggest that the intensity ratio between different hydrogen Balmer lines could be an indicator of the electron temperature.

1.6.3 Electron density and electric fields

The electron density in a microwave reactor used for diamond CVD has been measured by Grotjohn et al using a millimeter-wave open resonator technique. [45] Details of this technique can be found in their paper. The measured electron density under their typical conditions is ~ $10^{11}cm^{-3}$. Also, it is worth mentioning that the electron density in H_2/CH_4 plasma is always higher than in a pure H_2 plasma at the same pressure.

The microwave electric field in a diamond CVD reactor has been measured by Hassouni et al. [46] In their experiments, a small coaxial probe was inserted through the outer metal cavity wall so as to sample the microwave electric field as a function of both the z and φ directions along the outer wall of the reactor. The measured electric field was found to change from 1000 to 4000 V/cm at different positions and was consistent with their simulation results.

1.7. About this thesis

Though many diagnostic studies have been reported, there are still several good reasons for us to carry out the work described in this thesis:

(1) Due to the complexity of the microwave plasma used in diamond CVD (many species, many reactions, inhomogeneity, non-equilibrium between T_e and T_{gas}, etc), a full understanding of such a plasma has still not been achieved. Some proposed mechanisms, for example, the interconversion between C1 and C2 species still need further evidence from experiments.

(2) The microwave plasma diagnosed in most of the earlier studies normally work at relatively low pressure (below 100 Torr) and low power (below 1 kW) conditions. However, the standard conditions of microwave plasma used here are 150 Torr and 1.5 kW, which therefore corresponds to much higher power density conditions. The plasma under this condition has quite different features. For example, high power density will lead to higher gas temperature, much higher H

atom concentrations and generation of more reactive hydrocarbon radicals, which should be better for growing high quality diamond.

(3) Though several diagnoses of CH_4/H_2 plasmas have been reported, only very few [47-49] can be found that attempt to investigate the chemistry behind the $B_2H_6/CH_4/H_2$ plasmas, which are becoming increasingly important for growing p-type doped diamond. Such doped diamond has already been demonstrated to have big potential in biological and electronic applications.

This thesis has been organized as follows: In Chapter 2, a brief introduction of gas phase models established by a French group [46, 50-54] and by the Bristol-Moscow group will be presented. Some important features of the microwave plasma used in diamond CVD will be given. Then in Chapter 3, due to the fact that the major diagnostic techniques used here are OES and laser spectroscopy, a quick introduction of the important concepts and methods in spectroscopy will be given. In Chapter 4 experiments on using a QCL to investigate the gas phase chemistry behind C1-C2 interconversion will be reported. Chapter 5 will discuss experimental results obtained using spatially resolved CRDS to detect selected "hot" species like C_2, CH and H(n=2). Experimental results about the unknown absorption discovered by CRDS are also summarized. OES studies (including use of the actinometry method) have been used to investigate the behaviour of several species as a function of different discharge parameters and positions within the reactor. Results of these studies are presented in Chapter 6. Chapter 7 reports preliminary experimental results using OES and CRDS to explore boron chemistry in $B_2H_6/CH_4/H_2$/Ar plasma. Finally, in Chapter 8, a short overview and perspective are provided.

1.8. References

[1] J. P. Freidberg, *Plasma Physics and Fusion Energy*, (Cambridge University Press, 2007).

[2] M. A. Lieberman and A. J. Lichtenberg, *Principles of Plasma Discharges and Materials Processing*, (John Wiley & Sons, Inc., 2005).

[3] B. Mills, *J. Material Processing Tech.*, **56** (1996) 16.

[4] B. Fiegl, M. Hible, W. Kiffe, *et al.*, *Hybrid Circuits*, **35** (1994) 15.

[5] P. W. May, *Philosophical Transactions of The Royal Society London A.*, **358** (2000) 473.

[6] K. Hayashi, Y. Yokota, T. Tachibana, *et al.*, *New Diamond and Frontier Carbon Technology*, **11** (2001) 101.

[7] M. Geis, N. Efremow and D. Rathman., *J Vac Sci Technol A*, **6** (1988) 1953.

[8] H. Shiomi, Y. Nishibayashi and N. Fujimore., *Jpn J Appl Phys*, **28** (1989) L2153.

[9] D. R. Kania, M. I. Landstrass, M. A. Plano, *et al.*, *Diamond Relat. Mater.*, **2** (1993) 1012.

[10] C. E. Nebel, D. Shin, B. Rezek, *et al.*, *J. Royal Soc. Interface*, **4** (2007) 439.

[11] C. E. Nebel, B. Rezek, D. Shin, *et al.*, *J. Phys. D: Appl. Phys*, **40** (2007) 6443.

[12] S. Katsumata, Y. Oobuchi and T. Asano, *Diamond Relat. Mater.*, **3** (1994) 1296.

[13] N. Kumar, H. Schmidt and C. Xie, *Sol. State Tech.*, **38** (1995) 71.

[14] C.-P. Klages, *Appl. Phys. A*, **56** (1993) 513.

[15] N. Ohtake and M. Yoshikawa, *J. Electrochem. Soc.*, **137** (1990) 717.

[16] M. Kamo, Y. Sato, S. Matsumoto, *et al.*, *Cryst. Growth. .* **62** (1983) 642.

[17] P. K. Bachmann, W. Drawl, D. Knight, *et al.*, *Mater. Res. Soc. Symp. Proc.*, **EA-15** (1988.) 99.

[18] M. A. Prelas, G. Popovici and L.K.Bigelow, *Handbook of Industrial Diamonds and Diamond Films*, (Marcel Dekker, New York, 1998).

[19] M. N. R. Ashfold, P. W. May, J. R. Petherbridge, *et al.*, *Phys. Chem. Chem.*

Phys., **3** (2001) 3471.

[20] J. E. Butler and R. L. Woodin, *Philos. Trans. R. Soc. London*, **342** (1993) 209.

[21] B. J. Garrison, E. J. Dawnkaski, D. Srivastava, *et al.*, *Science*, **255** (1992) 835.

[22] S. Skokov, B. Weimer and M. Frrenklach, *J.Phys.Chem*, **98** (1994) 8.

[23] R. Kalish, *Carbon*, **37** (1999) 781.

[24] M. Nesladek, *Semicond. Sci. Technol.*, **20** (2005) R19.

[25] A. Inspektor, Y. Liou, T. McKenna, *et al.*, *Surf. Coat. Technol.*, **39-40** (1989) 211.

[26] A. N. Goyette, J. E. Lawler, L. W. Anderson, *et al.*, *Plasma Sources Sci. Technol.*, **7** (1998) 149.

[27] A. Rousseau, A. Granier, G. Gousset, *et al.*, *J. Phys. D: Appl. Phys*, **27** (1994) 1412.

[28] A. Gicquel, K. Hassouni, S. Farhat, *et al.*, *Diamond Relat. Mater.*, **3** (1994) 581.

[29] Z.-C. Geng, Y. Xu, X.-F. Yang, *et al.*, *Plasma Sources Sci. Technol.*, **14** (2005) 76.

[30] A. Gicquel, M. Chenevier, K. Hassouni, *et al.*, *J. Appl. Phys.*, **83** (1998) 7504.

[31] G. Lombardi, G. D. Stancu, F. Hempel, *et al.*, *Plasma Sources Sci. and Technol.*, **13** (2004) 27.

[32] G. Lombardi, K. Hassouni, G. D. Stancu, *et al.*, *Plasma Sources Sci. Technol.*, **14** (2005) 440.

[33] A. Cheesman, J. A. Smith, M. N. R. Ashfold, *et al.*, *J. Phys. Chem. A*, **110** (2006) 2821.

[34] M. C. McMaster, W. L. Hsu, M. E. Coltrin, *et al.*, *Diamond Relat. Mater.*, **4** (1995) 1000.

[35] T. Fujii and M. Kareev, *J. Appl. Phys.*, **89** (2001) 2543.

[36] Y.-S. Han, Y.-K. Kim and J.-Y. Lee, *Thin Solid Films*, **310** (1997) 39.

[37] G. Lombardi, F. Benedic, F. Mohasseb, *et al.*, *Plasma Sources Sci. Technol.*, **13** (2004) 375.

[38] A. Gicquel, M. Chenevier, Y. Breton, *et al.*, *J. Phys. III France*, **6** (1996)

1167.

[39] T. Lang, J. Stiegler, Y. v. Kaenel, *et al.*, *Diamond Relat. Mater.*, **5** (1996) 1171.

[40] G. Dixon-Lewis, *Combustion Chemistry,*, (1984) 21.

[41] R. J. Kee, G. Dixon-Lewis, J. Warnatz, *et al.*, *Sandia Report,*, **86-8246** (1989) UC.

[42] Y. Shigesatov, R. E. Boekenhauer and B. W. Sheldon, *Appl. Phys. Lett.*, **63** (1993) 314.

[43] W. Zhu, A. Inspektor, A. R. Badzian, *et al.*, *J. Appl. Phys.*, **68** (1990) 1489.

[44] M. D. Whitfield, R. B. Jackman, D. Rodway, *et al.*, *J. Appl. Phys.*, **80** (1996) 3710.

[45] T. A. Grotjohn, J. Asmussen, J. Sivagnaname, *et al.*, *Diamond Relat. Mater.*, **9** (2000) 322.

[46] K. Hassouni, T. A. Grotjohn and A. Gicquel, *J. Appl. Phys.*, **86** (1999) 134.

[47] M. Osiac, B. P. Lavrov and J. Ropcke, *J. Quant. Spec. Radiat. Transfer*, **74** (2002) 471.

[48] M. Rayar, P. Veis, C. Foissac, *et al.*, *J. Phys. D: Appl. Phys*, **39** (2006) 2151.

[49] D. W. Comerford, A. Cheesman, T. P. F. Carpenter, *et al.*, *J. Phys. Chem. A*, **110** (2006) 2868.

[50] K. Hassouni, S. Farhat, C. D. Scott, *et al.*, *Journal de Physique III (Applied Physics, Materials Science, Fluids, Plasma and Instrumentation)*, **6** (1996) 1229.

[51] K. Hassouni, O. Leroy, S. Farhat, *et al.*, *Plasma Chemistry and Plasma Processing*, **18** (1998) 325.

[52] K. Hassouni, A. Gicquel, M. Capitelli, *et al.*, *Plasma Sources Sci. and Technol.*, **8** (1999) 494.

[53] K. Hassouni, G. Lombardi, X. Duten, *et al.*, *Plasma Sources Sci. Technol.*, **15** (2006) 117.

[54] G. Lombardi, K. Hassouni, G.-D. Stancu, *et al.*, *J. Appl. Phys.*, **98** (2005) 053303.

Chapter 2 Models of the moderate pressure microwave plasmas used in diamond CVD

2.1. General

In a microwave activated plasma, the microwave is coupled to the vacuum chamber, forming some electromagnetic modes which are determined by the geometry of the reactor. Electrons then pick up energy from the electromagnetic field and are heated by the so-called Ohmic heating mechanism. [1] Stochastic heating will not be important due to the low sheath voltage at typical operating pressures. Simultaneously, the electrons transfer their energy to heavy species through collisions, making the gas hot and also generating a lot of energetic species e.g excited states. The collisions between heavy species induce lots of thermal chemistry, which also results in the generation of many active species. Such species react on the surface of the substrate, heating it and also leading to film deposition on it.

It is not easy to model a moderate pressure microwave plasma used in diamond CVD. Besides the mathematical difficulties associated with solving strongly-coupled, nonlinear equations, other problems are also present, namely

1. Many species and reactions need to be considered.
2. Unlike the cold low-pressure plasma (where the gas temperature is so low that most chemistry is driven by electrons) and the thermal atmospheric plasma (where thermal equilibrium is reached between electrons and heavy species and thus all the chemistry can be characterized by one temperature), both electron driven chemistry and thermal chemistry occur within the plasma. These chemistries are governed by quite different temperatures. Thus the moderate pressure plasma exhibits strong thermal non-equilibrium and intermediate behaviour.
3. There is strong spatial inhomogeneity present. The electron and gas temperatures have different spatial distributions. The chemistry occurring in the different

regions of the reactor can thus be quite different due to these different temperatures.

4. Accurate cross sections are not available for many of the important reactions.

Much pioneering work combining diagnostics with modelling has been carried out by Gicquel and colleagues at LIMHP, Universtiy Paris-Nord [2-7] and also by our group [8] in cooperation with Mankelevich at Moscow State University in order to clarify the major mechanisms in such MW plasmas used for diamond CVD. The former have reported a self-consistent model both in pure H_2 and H_2/CH_4 plasmas. Though their calculations are based on a cylindrically symmetric bell-jar reactor and different operating pressures, powers and gas flow rates from those used in Bristol, their results are still quite insightful and instructive. Moreover, their higher power density condition, i.e. $MWPD_{av}$ is equal to 30 W/cm^3, is quite similar to the power density in our plasmas at standard condition. Therefore, many of their results are described here. We also note that the model presented by the Gicquel group considers a pure H_2 plasma and a CH_4/H_2 plasma (without Ar), but, as shown in our experiments, the addition of a small amount of Ar has only a limited effect on the plasma, see Chapters 5 - 7.

2.2. Results from the French model

2.2.1. Pure H_2 plasma

2.2.1.1. Microwave power coupling

The microwave field in a moderate pressure H_2 plasma has been calculated by Hassouni et al based on a self-consistent two-dimension model. [5] The calculated spatial distribution (vs *r* and *z*) of several discharge parameters at 25hPa (~ 19 Torr) and 600 W input power is shown in **Figure 2. 1**. Since this condition corresponds to a much lower $MWPD_{av}$ (~8.0 W/cm^3) condition than in our reactor where $MWPD_{av}$ is around 30 W/cm^3, the calculated values for all quoted parameters in this figure are

expected to be lower than those in our reactor. However, this figure is still useful as it illustrates some general features of a microwave reactor for diamond CVD. From **Figure 2. 1 (a)** and **(b)**, it can be seen that both the absorbed power density and the electron temperature have peak values close to the substrate. Such a distribution is due to the strong electric field in this region as a result of the sharp edge of the substrate. However, because of the long mean free path, the electron temperature profile shows a good spatial homogeneity.

The T_{gas} distribution is also smooth but peaks further from the substrate, reflecting the role of conduction and diffusion in transporting energy from the point of maximum power deposition. The electron density distribution, however, emphasizes the importance of transport (ambipolar diffusion [1]) in establishing the electron density balance.

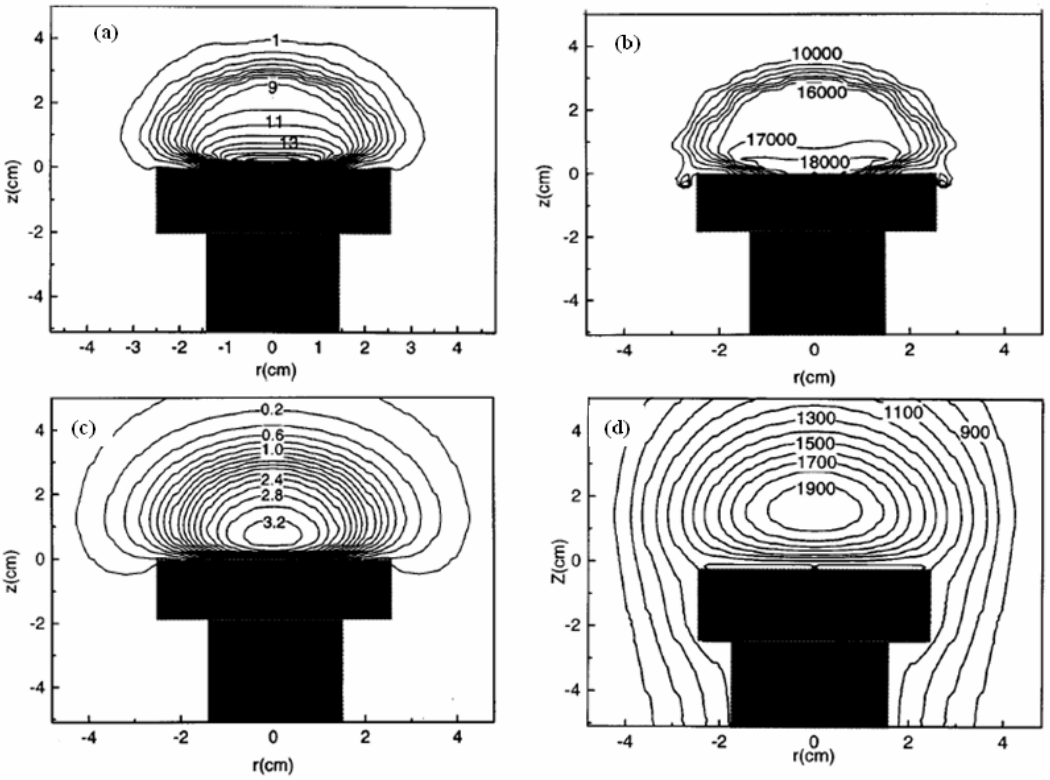

Figure 2. 1 Spatial distribution (~vs *r* and *z*) of H_2 plasma at 25 hPa (~19 Torr) and 600 W. (a) Absorbed microwave power density ~W/cm^3; (b) Electron temperature ~K; (c) Electron density ($\times 10^{11}$ cm^{-3}) (d).Gas temperature ~K. (after Ref. [5])

A further quasi-homogenous plasma (0 D) model has been proposed by Hassouni et

al [3] in order to describe the chemical kinetics and energy transfer in a moderate pressure MW H_2 plasma. In this model, the $MWPD_{av}$ is taken as a key parameter determining the plasma characteristics. The calculated dissipated power density as a function of $MWPD_{av}$ is shown in **Figure 2. 2 (a)**. It is noted that vibrational excitation (e-V) processes like

$$e^- + H_2(\upsilon) \rightarrow e^- + H_2(w) \quad \text{with } (|w-\upsilon| < 6) \tag{R2. 1}$$

and

$$e^- + H_2(\upsilon) \rightarrow e^- + H_2(^1Y, \upsilon') \tag{R2. 2}$$

account for most of the power dissipation. Especially in the high power density conditions ($MWPD_{av}$~30 W/cm^3), such e-V processes consume more than 90% of the input power. The gas temperature and H_2 vibrational temperature show similar behaviour. Both increase with $MWPD_{av}$ increasing as shown in **Figure 2. 2 (b)** and both show reduced sensitivity to $MWPD_{av}$ at high power densities.

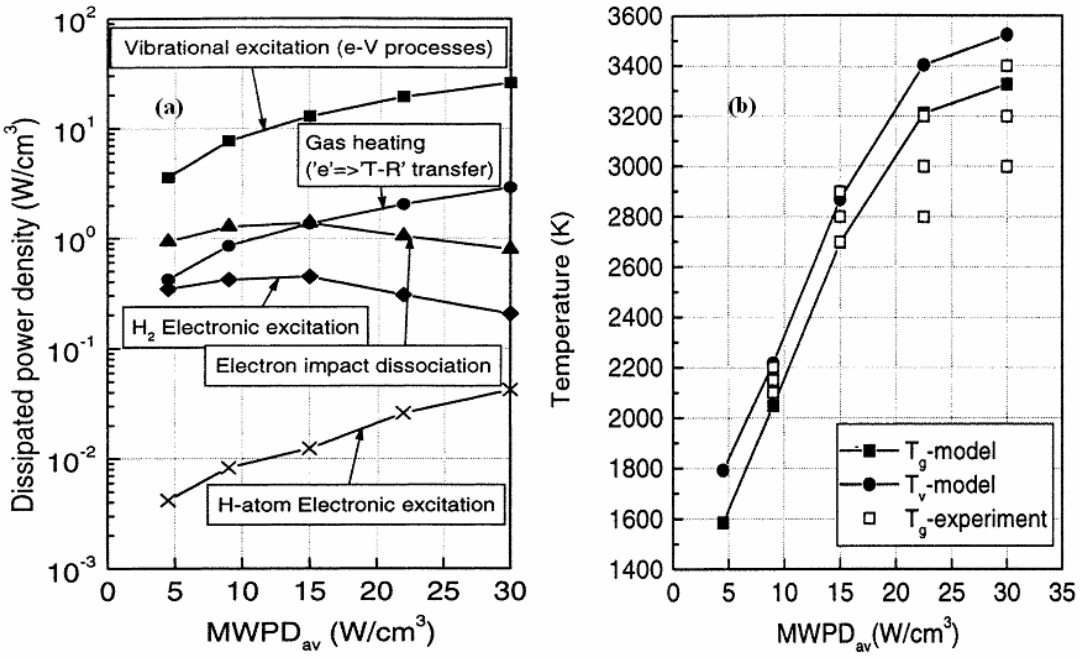

Figure 2. 2 (a) Main electron energy dissipation channels in the investigated H_2 plasmas and (b) variation with $MWPD_{av}$ of the calculated gas temperature, the H_2-vibration temperature and the gas temperature measured using Doppler broadening of H_α (labelled the T_g-experiment). (After Ref. [3])

2.2.1.2. Ionization

The main ionization processes in pure H_2 plasma are shown in **Figure 2. 3**. The dominant ion (more than 99%) at the investigated power densities here is H_3^+, not H_2^+. In fact, the H_2^+ density is very low and also decreases as $MWPD_{av}$ increases because of the fast reaction rate of **R2.3**. According to this model, most H_3^+ is produced from reaction **R2. 4**. The contribution from reaction **R2. 3** become less and less important as $MWPD_{av}$ increases

$$H_2 + H_2^+ \rightarrow H_3^+ + H \qquad \text{(R2. 3)}$$

$$H(n = 2-6) + H_2 \rightarrow H_3^+ + e^- . \qquad \text{(R2. 4)}$$

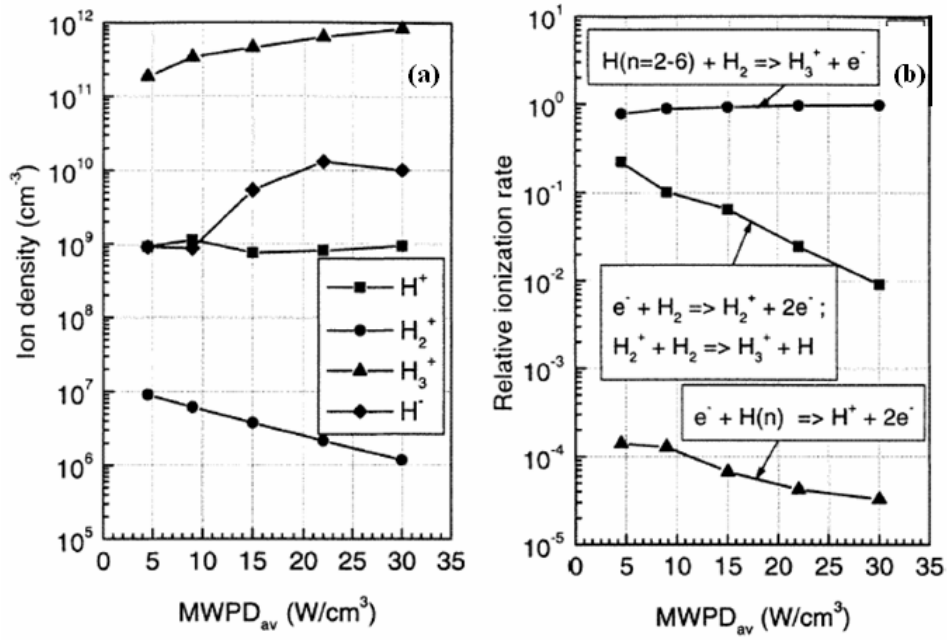

Figure 2. 3 Variations of the different charged species densities (left) and relative rates of the different ionization channels (right) with $MWPD_{av}$. (After Ref. [3])

2.2.1.3. Electrons

The electron energy distribution function (EEDF) shown in **Figure 2. 4 (a)** was calculated by solving the electron Boltzmann equation making a two-term approximation. [9] These EEDFs in H_2 plasma are clearly non-Maxwellian. Thus two electron temperatures, i.e. $T_{e\text{-}l}$ and $T_{e\text{-}h}$, can be defined to characterize the distribution of low and high energy electrons separately. **Figure 2. 4 (b)** shows that both of these

electron temperatures decrease as $MWPD_{av}$ increases, while the electron density exhibits a nearly linear increase with $MWPD_{av}$.

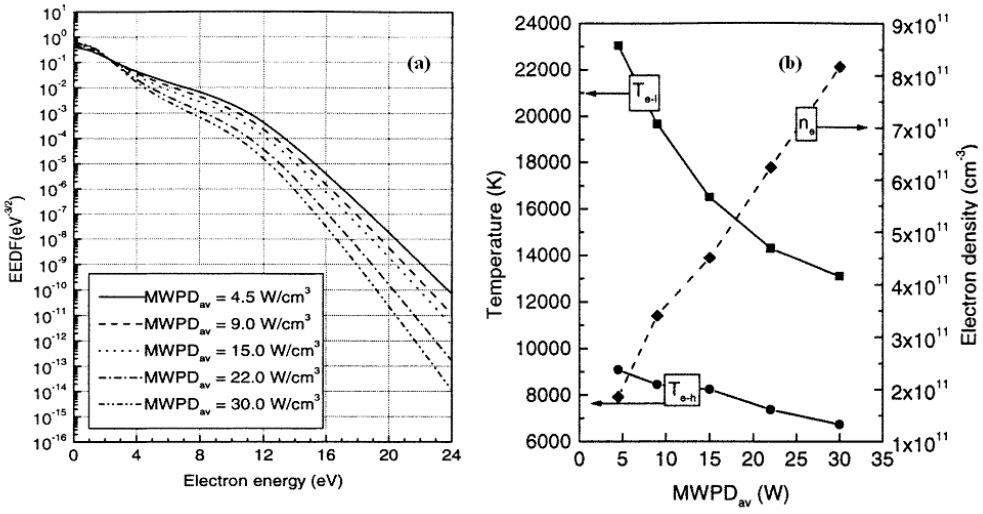

Figure 2. 4 (a) Calculated EEDFs for different discharge conditions and (b) variations of the temperatures of the low-energy electrons (T_{e-l}), high-energy electrons temperature (T_{e-h}) and the electron density (n_e) with $MWPD_{av}$. (After Ref. [3])

2.2.1.4. H atom production

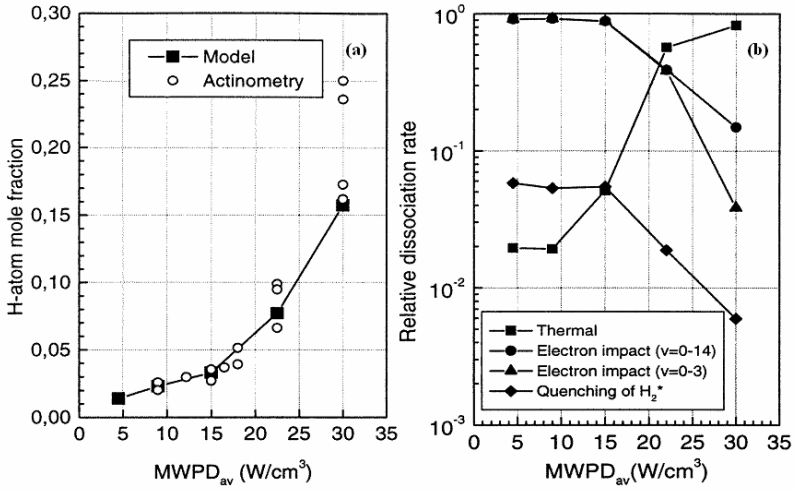

Figure 2. 5 (a) Variation of the calculated and measured (by actinometry) H-atom mole fraction with $MWPD_{av}$ and (b) relative rates of the main dissociation channels in the plasma. (After Ref. [3])

The hydrogen atom mole fraction in **Figure 2. 5 (a)** shows a fast increase as $MWPD_{av}$ increases. **Figure 2. 5 (b)** shows that, at low power density conditions, H_2

dissociation is mainly through electron impact processes, i.e.

$$e^- + H_2(\upsilon = 0-3) \rightarrow e^- + 2H \qquad \text{(R2. 5)}$$

At higher power densities, the electron temperature will drop which finally renders **R2.5** less efficient. On the other hand, the energy transferred from the electrons to the H_2 vibration mode can enhance both H_2 vibrational and rotational temperatures. Thus when the power density is high, raising T_v and T_r high enough, thermal dissociation from H_2(υ=14), for example

$$H_2(\upsilon = 14) + H_2 \rightarrow 2H + H_2 \qquad \text{(R2. 6)}$$

will become predominant. Such an evolution in the dominant H_2-dissociation mechanism conversion is clearly shown in **Figure 2. 5 (b)**.

2.2.1.5. The excited states

The excited states discussed here refer to the electronically excited states of hydrogen molecules H_2* and atoms H*. The H_2* is mainly generated through electron impact excitation reactions and consumed by collisional quenching. As in **Figure 2. 6** shows, increasing $MWPD_{av}$ leads to a decrease in the densities of most of the excited states. This is because the electron temperature exhibits a decreasing trend as $MWPD_{av}$ increases.

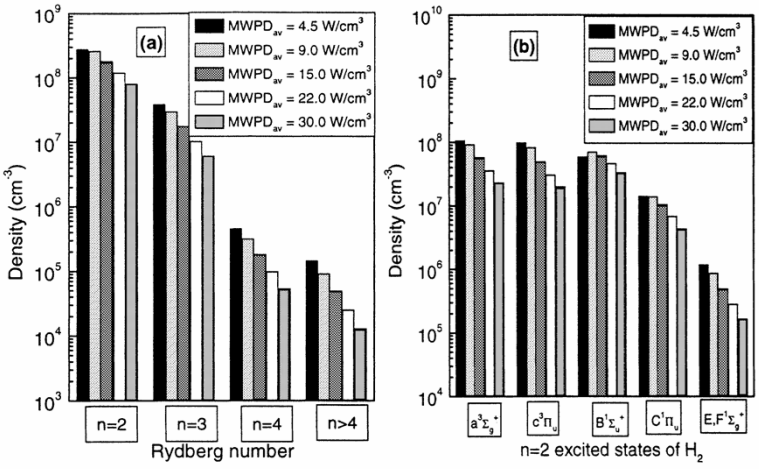

Figure 2. 6 (a) Variations of the densities for the states of H corresponding to a given Rydberg number *n* and (b) the low-lying *n* =2 excited state densities of H_2 as a function of $MWPD_{av}$. (After Ref. [3])

Figure 2. 7 shows that excited hydrogen atoms, like H(n=2) and H(n=3), are predominantly produced through the electron impact excitation of H (n=1). As $MWPD_{av}$ increases, the contribution from other processes like electron impact dissociative excitation or deexcitation from the higher *n* levels becomes even less important.

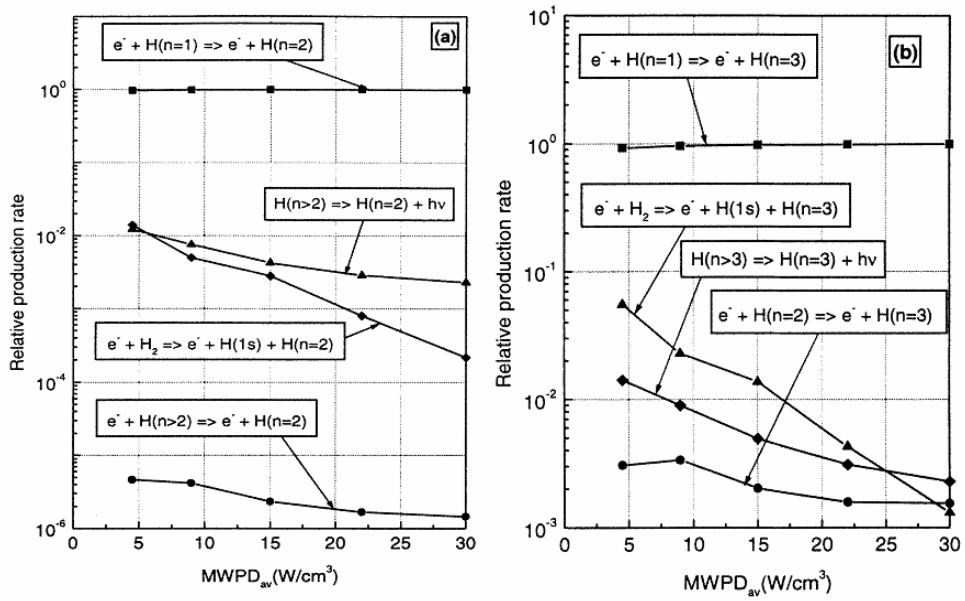

Figure 2. 7 (a) Relative rates of the different H(n=2) production channels and (b) Relative rates of the different H(n=3) production channels. (After Ref. [3])

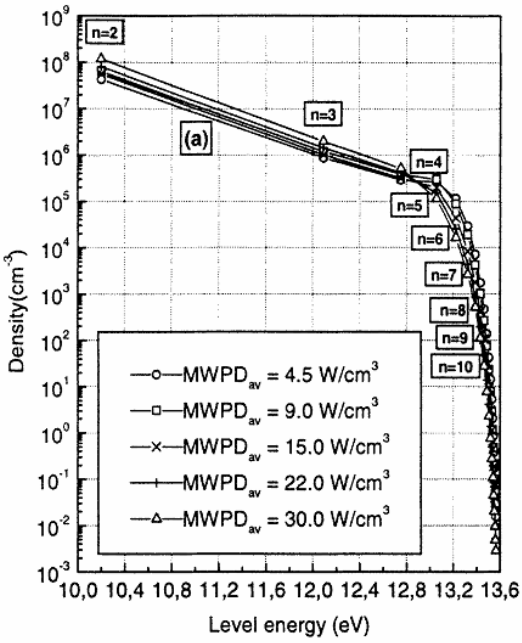

Figure 2. 8 Calculated population distributions of the H-atom excited states under different $MWPD_{av}$. (After Ref. [3])

Figure 2. 8 shows the excited H atom population under different power density conditions. It is worth noticing that only population in the excited states with n=2-4 roughly obeys a Boltzmann distribution. Excited hydrogen atoms with n>4 suffer more serious quenching and thus deplete much more quickly. Based on these calculations, it is concluded that only H_α and H_β emissions are suitable for electron temperature estimation by the line-ratio technique. In contrast to H_2*, the density of excited H atoms with n=2-4 is predicted to increase with increasing $MWPD_{av}$ in spite of the drop of T_e. The reason is that the dissociation degree of H_2 increases a lot as $MWPD_{av}$ becomes higher.

2.2.2. CH_4/H_2 plasma [7]

2.2.2.1. C1 species

When CH_4 is added to a pure hydrogen plasma, due to the H-abstraction reactions

$$CH_y + H \Leftrightarrow CH_{y-1} + H_2, \qquad \text{(R2. 7)}$$

lots of the C1 (i.e. containing only one carbon atom) radicals can be produced. The formed axial and radial profiles of C1 species are shown in **Figure 2. 9** and **Figure 2. 10**. It can be seen that, in the cool region outside the plasma ball, CH_4 is the most abundant C1 species while in the hot region, CH_3 has the highest mole fraction among all C1 species. Due to its abundance in the plasma, CH_3 has been assumed, in many papers, to be the main growth species especially for diamond deposition under low temperature and low power conditions (e.g. HF-CVD). [10-13]

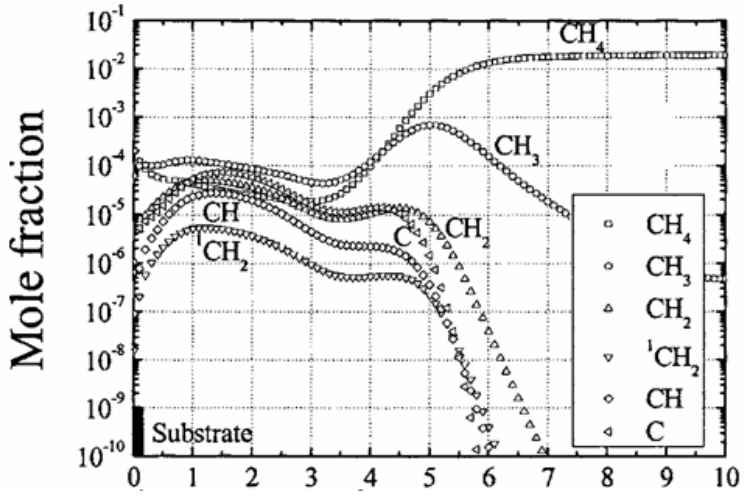

Figure 2. 9 Calculated axial profiles of C1 species at 30 Wcm^{-3} in a mixture of H_2 and CH_4 (95:5). The *x* axis is the axial position in cm. (After Ref. [7])

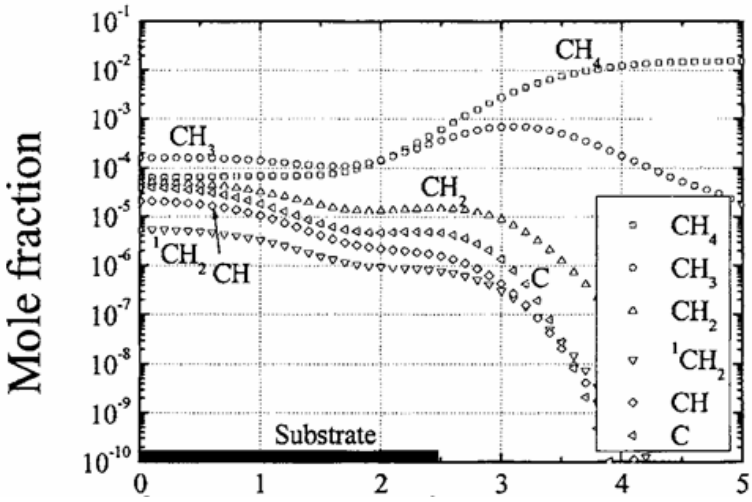

Figure 2. 10 Calculated radial profiles of C1 species at 30 Wcm^{-3} in a mixture of H_2 and CH_4 (95:5). The *x* axis is the radial position in cm. (After Ref. [7])

2.2.2.2. C2 species

Figure 2. 11 and **Figure 2. 12** show the calculated axial and radial distributions of C2 species. Acetylene is found to be the most abundant hydrocarbon species in the plasma. C2 species can be generated through self-reactions of C1 radicals stabilized by a third body, then followed by a series of H-abstraction reactions

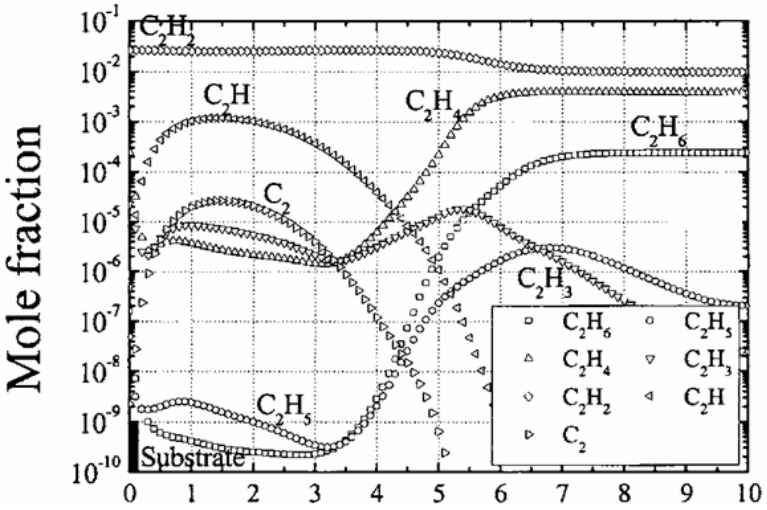

Figure 2. 11 Calculated axial profiles of C_2 species at 30 Wcm^{-3} in a mixture of H_2 and CH_4 (95:5). The *x* axis is the axial position in cm. (After Ref. [7])

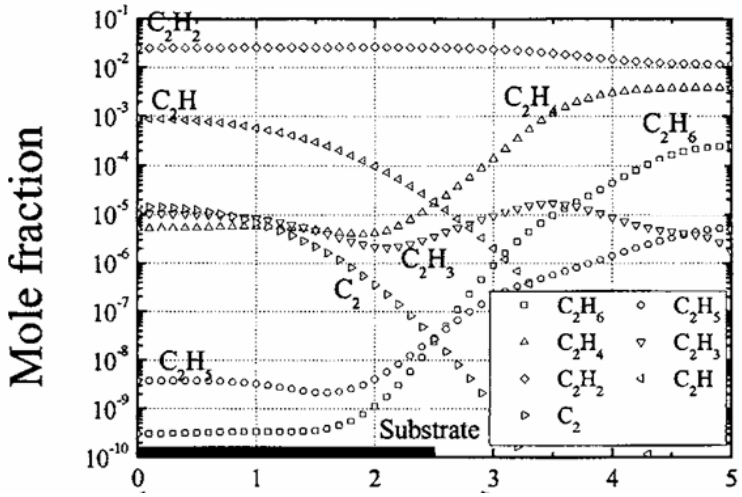

Figure 2. 12 Calculated radial profiles of C_2 species at 30 Wcm^{-3} in a mixture of H_2 and CH_4 (95:5). The *x* axis is the radial position in cm. (After Ref. [7])

2.2.2.3. Ionization,

Profiles of hydrocarbon ion densities along both the axial and radial directions are shown in **Figure 2. 13** and **Figure 2. 14**. The major ions in CH_4/H_2 plasma are $C_2H_2^+$ and $C_2H_3^+$ due to electron impact ionization of C_2H_2 and by $C_2H_2 - H_3^+$ conversion. However, outside the discharge region, the dominant ion is H^+ due to its slow radiative recombination rate while all other ions ($C_2H_2^+$, $C_2H_3^+$ and H_3^+) suffer the fast dissociative recombination and are rapidly consumed.

Another result that needs to be highlighted is the high efficiency of the $H_3^+ - C_xH_y$ ion conversion, which ensures that even adding a small mount of CH_4 will totally change the dominant ions in the plasma. Lombardi et al calculated that 1% methane addition could lead to a two orders of magnitude drop in the H_3^+ densities. [7]

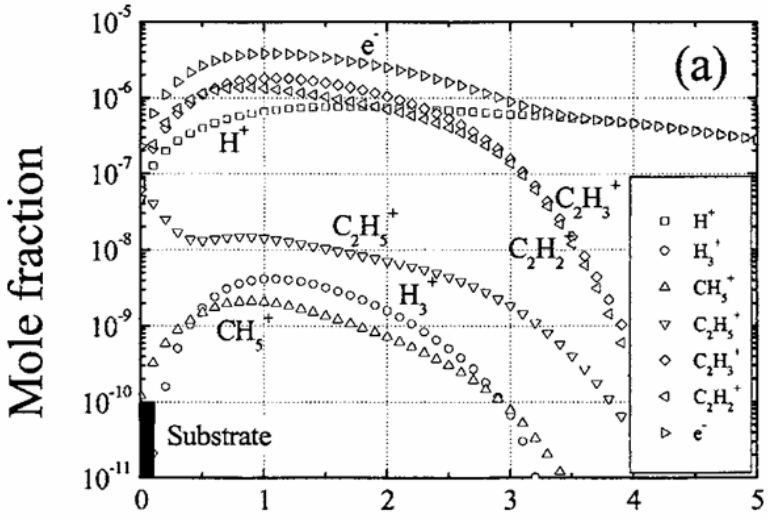

Figure 2. 13 Calculated axial profiles of hydrocarbon ions at 30 Wcm^{-3} in a mixture of H_2 and CH_4 (95:5). The *x* axis is the axial position in cm. (After Ref. [7])

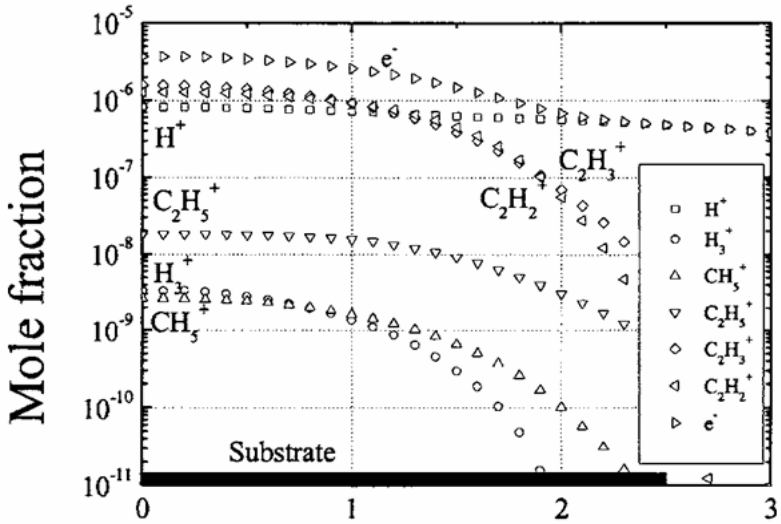

Figure 2. 14 Calculated radial profiles of hydrocarbon ions at 30 Wcm^{-3} in a mixture of H_2 and CH_4 (95:5). The *x* axis is the radial position in cm. (After Ref. [7])

2.3. Brief introduction of Bristol-Moscow model

In contrast to the French (1D) model discussed above, in order to trace the plasma behaviour more accurately, a 2D model for $CH_4/Ar/H_2$ plasma is established here which involves 35 species and 300 reactions (listed in Appendix A). The model comprises three blocks addressing (i) activation of the reactive mixture (i.e. electromagnetic fields and plasma parameters, power absorption and gas heating), (ii) gas-phase processes (heat and mass transfer and plasma-chemical kinetics), and (iii) gas-surface processes at the substrate. Some typical values of plasma parameters obtained from this model are: E/N~$23\cdot10^{-17}$ V·cm^2 (23 Td), T_e ~ 1.2 eV for the standard conditions (i.e 4.4%CH_4/7%Ar/88.6%H_2 mixture at 150 Torr, 1.5kW input power), gas temperature T_{gas}=3000 K and absorbed power density Q_J =30 W/cm^3.

The absorbed power density Q_J (W/cm^3) as a function of *E/N*, gas temperature T_{gas} and electron density was approximated as follows:

$$Q_J = jE = e \cdot n_e \cdot \mu_e \cdot N \cdot (\frac{E}{N}) \cdot E = e \cdot (\mu_e \cdot N) \cdot (E/N)^2 \cdot n_e \cdot (\frac{P}{k \cdot T}) \approx C(P_W, (E/N)^2) \cdot \frac{n_e}{T} \quad \text{(Eq.2. 1)}$$

Here, *e*, *j* and μ_e are the electron charge, current density and mobility, respectively. The value of coefficient *C* was varied during calculations to provide an absorption of total input power P_W in given plasma volume (typically 1000-1500 W per 50 cm^3 of plasma volume).

Some preliminary results are shown here. **Figure 2. 15** displays the 2D distribution of CH_4 and C_2H_2. One can see CH_4 peaks in the cooler region while C_2H_2 is most abundant around the plasma ball.

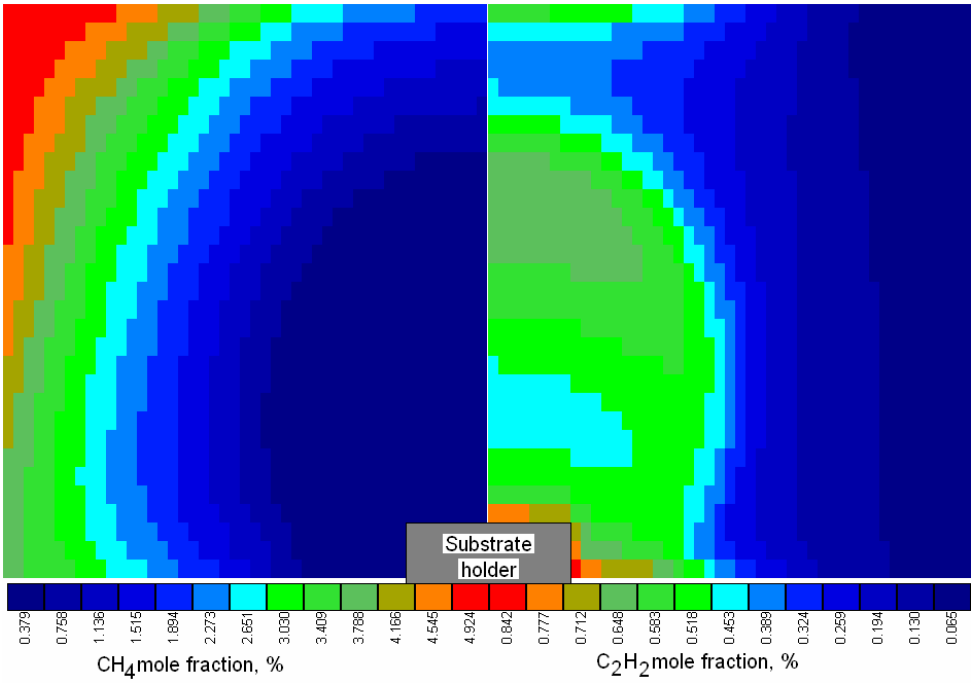

Figure 2. 15 CH_4 (left) and C_2H_2 (right) mole fractions for base MW reactor conditions: 150 Torr, 4.4%CH_4/7%Ar/H_2, input power 1.5 kW.

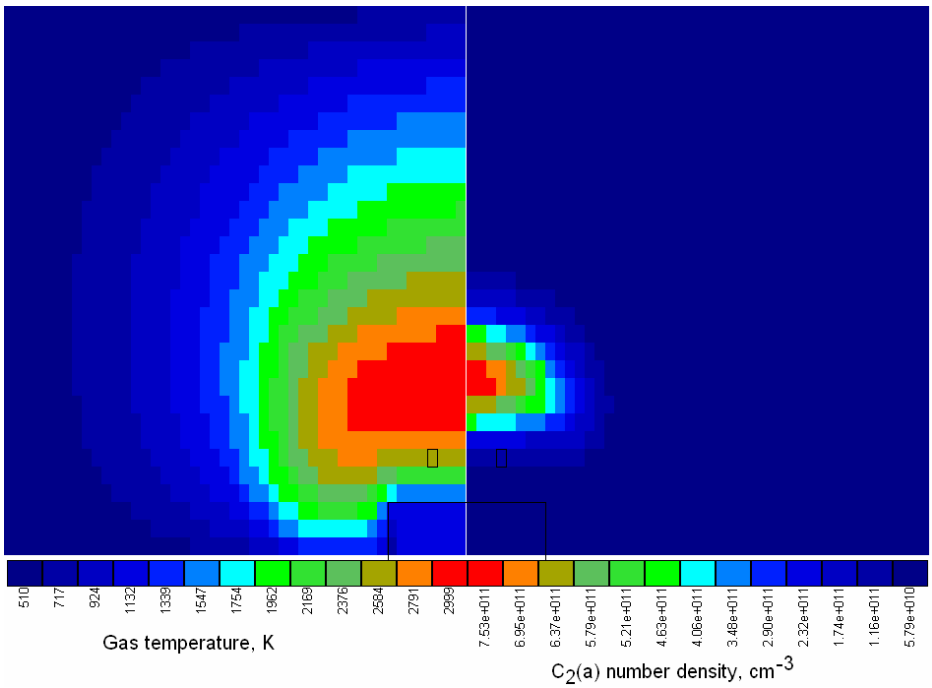

Figure 2. 16 Gas temperature and C_2(a) number density distributions for base mw reactor conditions: 150 Torr, 4.4%CH_4/7%Ar/H_2, input power 1.5 kW.

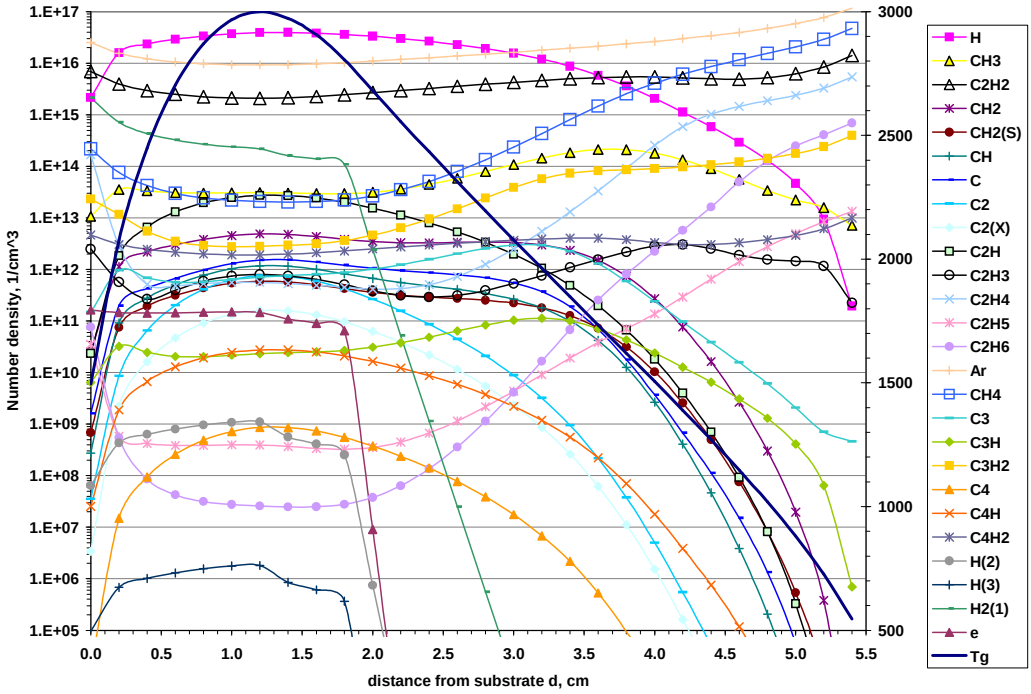

Figure 2. 17 Axial distribution of species number densities and gas temperature at r=0 for standard MW reactor conditions: 150 Torr, 4.4%CH_4/7%Ar/H_2, input power 1.5 kW. The T_{gas} scale (in K) is shown on the right hand vertical axis.

The calculated axial density profiles of 26 important species, together with the axial distribution of the gas temperature are shown in **Figure 2. 17**. It is noted that the electron density decreases much faster than most of other species as d increases. The behaviour of H(n=2) and H(n=3), however, follows that of the electrons quite well, consistent with previous discussions regarding the dominance of electron impact excitation in the formation of these species.

2.4. References

[1] M. A. Lieberman and A. J. Lichtenberg, *Principles of Plasma Discharges and Materials Processing*, (John Wiley & Sons, Inc., 2005).

[2] K. Hassouni, S. Farhat, C. D. Scott, *et al.*, *Journal de Physique III (Applied Physics, Materials Science, Fluids, Plasma and Instrumentation)*, **6** (1996) 1229.

[3] K. Hassouni, A. Gicquel, M. Capitelli, *et al.*, *Plasma Sources Sci. and Technol.*, **8** (1999) 494.

[4] K. Hassouni, O. Leroy, S. Farhat, *et al.*, *Plasma Chemistry and Plasma Processing*, **18** (1998) 325.

[5] K. Hassouni, T. A. Grotjohn and A. Gicquel, *J. Appl. Phys.*, **86** (1999) 134.

[6] K. Hassouni, G. Lombardi, X. Duten, *et al.*, *Plasma Sources Sci. Technol.*, **15** (2006) 117.

[7] G. Lombardi, K. Hassouni, G.-D. Stancu, *et al.*, *J. Appl. Phys.*, **98** (2005) 053303.

[8] A. Cheesman, J. A. Smith, M. N. R. Ashfold, *et al.*, *J. Phys. Chem. A*, **110** (2006) 2821.

[9] W. L. Morgan and B. M. Penetrante, *Comp. Phys. Commun.*, **58** (1990) 127.

[10] M. Tsuda, M. Nakajima and S. Oikawa, *J. Am. Chem. Soc.*, **108** (1986) 5780.

[11] S. J. Harris, A. M. Weiner and T. A. Perry, *J. Appl. Phys.*, **53** (1988) 1605.

[12] F. G. Celii, P. E. Pehrsson, H. T. Wang, *et al.*, *Appl. Phys. Lett.*, **52** (1988) 2043.

[13] D. G. Goodwin, *Appl. Phys. Lett.*, **59** (1991) 277.

Chapter 3 Important concepts and experimental methods

3.1. Atomic and molecular spectra

The details of an atomic or molecular spectrum include: (1) line position (i.e. the wavelength of the spectral lines); (2) line intensity; (3) line shape and line width. In a plasma environment, there are many factors that could contribute to the measured spectra. Carefully analysis of these spectral details (line position, line intensity and line width etc) can provide lots of information about the underlying physics and chemistry. Therefore, it is first necessary to understand the origins of these spectral parameters.

3.1.1. Quantum mechanics and the Schrödinger equation

The atom and molecule are one of the most important concepts in modern science. In most cases, different atoms and molecules are characterized by different spectral features. Though some spectral lines have been observed for many years, the real understanding and interpretation of spectroscopy had to wait until the early 20th century and the birth of quantum mechanics. It is exactly the motivation of understanding the Hydrogen Balmer lines that made Bohr finally give up the classic radiation theory and replace it with the new quantum assumptions, which finally led to the revolution of quantum mechanics. Thus, it is no exaggeration to say that the history of atomic and molecular spectroscopy is actually the history of the establishment and development of quantum mechanics.

Quantum mechanics seems an inherently “beautiful language” to describe atoms and molecules. One of the most important “sentences” in this language is the Schrödinger equation, i.e.

$$\left(-\frac{\hbar^2}{2m}\nabla^2 + V\right)\psi = E\psi \qquad \text{(Eq.3. 1)}$$

After giving the suitable potential function V and the correct boundary conditions, in principle, all the energy levels and wave functions ψ of any atom or molecule systems can be calculated. In practice, it is very hard to do this because solving the Schrödinger equation of an atom with many electrons, or of a molecule including many atoms, the electron-electron interaction has to be considered, and this finally leads to a "giant" strongly coupled set of nonlinear equations. In order to treat such systems, some *ab initio* methods like Hartree-Fock method, [1] or methods based on density functional theory (DFT) [2] have to be used. Developments in the latter method were recognized by the award of the Nobel Prize to Kohn and Pople in 1998.

3.1.2. Atomic spectra

3.1.2.1. Quantum numbers

It is found that only four quantum numbers are required for describing the wave functions of all atoms. [3] The principal quantum number n, which can take integral values from 1 to infinity, governs the energy and size of the orbitals. The orbital quantum number l, which can only take the integral values from 0 to n-1 governs the shape of the orbitals and also the electronic angular momentum. The magnetic quantum number m_l, which takes the values from 0 to $\pm l$, governs the direction of an orbital and the electrons' behaviour in a magnetic field. Finally, the spin quantum number, s, which only has a value 1/2, governs the axial spin angular momentum of the electron. When given a principal quantum number n, the total orbital number is given by

$$\sum_{l=0}^{n-1}\sum_{m_l=-l}^{l}=\sum_{l=0}^{n-1}(2l+1)=n^2. \qquad \text{(Eq.3. 2)}$$

Each electron can have two spin orientations and each orbital can accommodate a pair of electrons; this number of orbitals can thus hold $2n^2$ electrons.

These orbitals of atoms are labelled as s, p, d etc according to l=0, 1, 2 etc. For different n quantum numbers, the orbital will be called: *ns*, *np*, *nd* …

3.1.2.2. Angular momentum for single-electron atoms

When one electron is moving in its orbital around the nucleus, it will possess an orbital angular momentum which can be written as

$$|\mathbf{l}| = \sqrt{l(l+1)} \quad \text{(Eq.3. 3)}$$

Note $\mathbf{l}$ is a vector, which means its direction is as important as its magnitude. The component of $\mathbf{l}$ in the *z* direction can be written as

$$l_z = m_l \hbar \quad \text{(Eq.3. 4)}$$

Here, m_l can only take values *l*, *l*-1,…,0, …,-(*l*-1), -*l*.

On the other hand, the electron also has a spin angular momentum, i.e.

$$|\mathbf{s}| = \sqrt{s(s+1)} \quad \text{(Eq.3. 5)}$$

Finally, the total angular momentum is

$$|\mathbf{j}| = |\mathbf{l} + \mathbf{s}| = \sqrt{j(j+1)} \quad \text{(Eq.3. 6)}$$

and its component in the *z* direction is

$$j_z = m_j \hbar \quad \text{(Eq.3. 7)}$$

Here,

$$j = |l - s| \ldots |l + s|, \quad \text{(Eq.3. 8)}$$

i.e.

$$j = |l - 1/2| \ldots |l + 1/2|. \quad \text{(Eq.3. 9)}$$

And

$$m_j = -m_l \pm 1/2 \quad \text{(Eq.3. 10)}$$

3.1.2.3. Angular momentum for many-electron atoms

When the atom has many electrons, the total angular momentum shall include the contribution from all of them. There are two different ways to sum the orbital and

spin momentum of several electrons (i.e., two kinds of angular momentum coupling).

One is called *L-S* coupling (i.e. Russell-Saunders coupling), which means we first sum the orbital contribution and spin contributions separately to obtain the total orbital and spin angular momenta, then add them to give the final total angular momentum. Symbolically, *L-S* coupling can be expressed as

$$\sum_i \mathbf{l}_i = \mathbf{L}, \ \sum_i \mathbf{s}_i = \mathbf{S}, \ \mathbf{L}+\mathbf{S} = \mathbf{J}. \quad \text{(Eq.3. 11)}$$

This method is more suitable for small and medium-sized atoms, wherein spin-orbital coupling is relatively weak.

The other is called *j-j* coupling, which means we first sum the orbital and spin momenta of each electron separately, then sum the individual totals so obtained to give the total angular momentum of the atom. Such a procedure can be expressed as

$$\mathbf{l}_i + \mathbf{s}_i = \mathbf{j}_i, \ \sum_i \mathbf{j}_i = \mathbf{J}. \quad \text{(Eq.3. 12)}$$

This method is more appropriate for heavy atoms.

In Russell-Saunders coupling, when considering the summation of two electrons' orbital contributions or spin contributions, they follow the rule as below:

For orbital angular momentum

$$|\mathbf{L}| = \sqrt{L(L+1)}, \quad L = l_1 + l_2, l_1 + l_2 - 1, \ldots, \ |l_1 - l_2|. \quad \text{(Eq.3. 13)}$$

and for spin angular momentum.

$$|\mathbf{S}| = \sqrt{S(S+1)}, \ S = s_1 + s_2, s_1 + s_2 - 1, \ldots, \ |s_1 - s_2|. \quad \text{(Eq.3. 14)}$$

So the total angular momentum follows the rule

$$|\mathbf{J}| = \sqrt{J(J+1)}, J = L+S, L+S-1, \ldots, \ |L-S|. \quad \text{(Eq.3. 15)}$$

In *j-j* coupling, the summation of two electron's total angular momenta obeys the rule

$$|\mathbf{J}| = \sqrt{J(J+1)}, \ J = j_1 + j_2, j_1 + j_2 - 1, \ldots, \ |j_1 - j_2|. \quad \text{(Eq.3. 16)}$$

3.1.2.4. Term symbols

In order to describe the states of atoms, a term symbol system is adopted.

Specifically, the term symbol for an atomic state (here only consider the cases of weak spin-orbital coupling) can be written as

Term symbol = $^{2S+1}L_J$.

For L=0, 1, 2, 3 …, the corresponding symbols are *S*, *P*, *D*, *F* ….

Here, 2S+1 is called the spin multiplicity of the state. When S=0, J has only one value L, such states are called singlet. When S=1, J can have three values, L+1, L, L-1 and states with S=1 are thus called triplets. Similarly, depending on different 2S+1 values, the atoms can have quartet, quintet, etc.

3.1.2.5. Selection rules

Not all transitions between the upper and lower energy levels are allowed in quantum mechanics. Such restriction arises as a result of the selection rules. For the single-electron atomic state, transitions are allowed only if they fulfill the following conditions:

$$\Delta l = \pm 1,\ \Delta j = 0, \pm 1. \qquad \text{(Eq.3. 17)}$$

For many-electron atoms, allowed transitions must satisfy the selection rules

$$\Delta S = 0, \Delta L = 0, \pm 1 \ \ (\text{but } \Delta l = \pm 1),\ \Delta J = 0, \pm 1, \ \ (\text{but } J = 0 \nleftrightarrow J' = 0). \qquad \text{(Eq.3. 18)}$$

3.1.2.6. Hydrogen atom spectrum

The hydrogen atom is the simplest atom with just one electron and there is thus no need to consider the repulsion between electrons. The wave functions and energy levels of H atom can be accurately calculated through solving the Schrödinger equation (**Eq 3.1**). The calculated energy is

$$E_n = -\frac{me^4}{8h^2\varepsilon_0^2 n^2} \text{ Joules} \qquad \text{(Eq.3. 19)}$$

or written as

$$\varepsilon_n = -\frac{me^4}{8h^3 c\varepsilon_0^2 n^2} = -\frac{R}{n^2}. \qquad \text{(Eq.3. 20)}$$

in units of cm^{-1}. ε_0 is the vacuum permittivity and R is known as Rydberg constant in

memory of this Swedish physicist who first devised the formula to predict the H atom spectrum.

Figure 3. 1 shows the calculated hydrogen atom energy levels. Some famous transitions, like H_α and H_β are also marked.

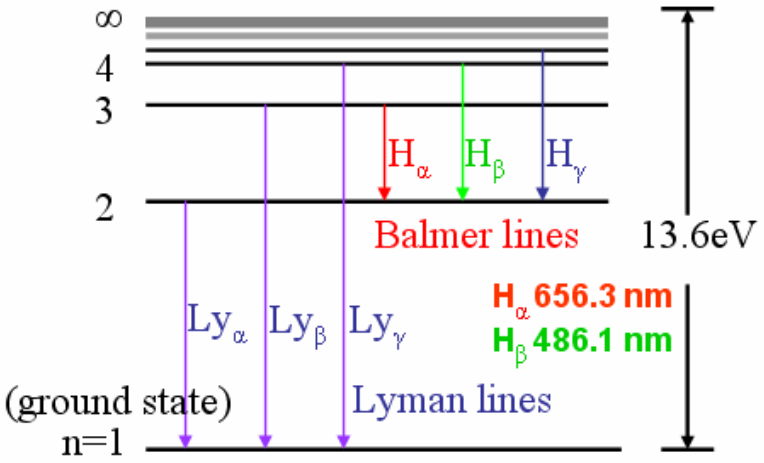

Figure 3. 1 Hydrogen atom energy levels and Lyman and Balmer emissions

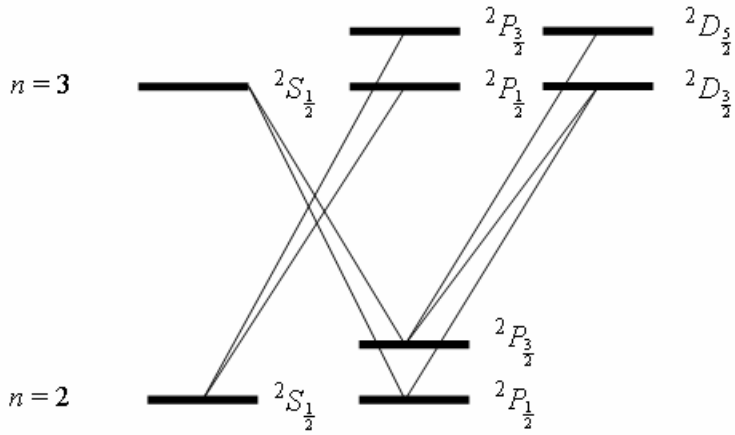

Figure 3. 2 Fine structure of the Hydrogen Balmer alpha absorption

Due to the coupling of the orbital and spin angular momentum, some of hydrogen levels will split into several close levels which give rise to the fine structure in the hydrogen atom spectrum. For example, for hydrogen Balmer-α absorption, the two involves the energy levels, n=2 and n=3, which split into 3 and 5 fine structure levels, respectively. However, due to the selection rules, only seven transitions are allowed

here as shown in **Figure 3. 2**. These are

$^2S_{1/2} \rightarrow {}^2P_{1/2} \quad (\Delta l = +1, \Delta j = 0)$

$^2S_{1/2} \rightarrow {}^2P_{3/2} \quad (\Delta l = +1, \Delta j = +1)$

$^2P_{1/2} \rightarrow {}^2S_{1/2} \quad (\Delta l = -1, \Delta j = 0)$

$^2P_{1/2} \rightarrow {}^2D_{3/2} \quad (\Delta l = +1, \Delta j = +1)$

$^2P_{3/2} \rightarrow {}^2S_{1/2} \quad (\Delta l = -1, \Delta j = -1)$

$^2P_{3/2} \rightarrow {}^2D_{3/2} \quad (\Delta l = +1, \Delta j = 0)$

$^2P_{3/2} \rightarrow {}^2D_{5/2} \quad (\Delta l = +1, \Delta j = +1)$

3.1.3. Molecular spectra

The molecule includes more than one atom. Thus it can rotate around a given axis. The relative positions of the atoms in the molecule can also change, which means the molecule can also vibrate. Therefore, the spectra of molecules are more complicated. Molecular spectra can be easily distinguished from spectra of atoms by the breadth of their band features introduced by the effects of rotation and vibration of molecules.

3.1.3.1. The rotation of molecules

For simplicity, here, we consider diatomic molecules. By using the Schrödinger equation, the rotational energy levels of a rigid diatomic molecule are given by

$$E_J = \frac{h^2}{8\pi^2 I} J(J+1) \quad \text{Joules,} \qquad \text{(Eq.3. 21)}$$

where J=0,1,2,… is called the rotational quantum number

In most cases, **Eq. 3.21** is rewritten in the following form

$$F(J) = \frac{E_J}{hc} = BJ(J+1) \quad \text{cm}^{-1}. \qquad \text{(Eq.3. 22)}$$

where $F(J)$ is called the spectral term value, and B is called the rotational constant and given by

$$B = \frac{h}{8\pi^2 Ic} \ \text{cm}^{-1}. \qquad \text{(Eq.3. 23)}$$

The selection rules for a pure rotational transition require

$$\Delta J = \pm 1 \ \text{ and } \ \Delta M_J = 0, \pm 1. \qquad \text{(Eq.3. 24)}$$

Thus, the allowed transition wave number is

$$\tilde{\nu} = F(J+1) - F(J) = 2B(J+1). \qquad \text{(Eq.3. 25)}$$

Since *B* normally is very small, the frequency of pure rotational spectra falls into the microwave range.

The spacing between two neighbouring lines is equal to 2*B*. So, to a first approximation, all these rotational lines are evenly seperated in wave number.

However, the conclusion above is only valid for rigid molecules. When centrifugal distortion is considered, the allowed transition wave number will be modified

$$\tilde{\nu} = F(J+1) - F(J) = 2B(J+1) - 4DJ^2(J+1)^2, \qquad \text{(Eq.3. 26)}$$

where *D* is centrifugal distortion constant. In the harmonic approximation, *D* is related to the vibration wave number ω by

$$D = \frac{4B^3}{\omega^2}. \qquad \text{(Eq.3. 27)}$$

Due to centrifugal distortion, the lines in a pure rotation spectrum will no longer have an even spacing.

3.1.3.2. The vibration of molecules

When the vibrating molecule is treated as a simple harmonic oscillator, by solving the Schrödinger equation, the discrete vibrational energies can be obtained,

$$E_\upsilon = (\upsilon + 1/2)h\omega_0 \ \text{ Joules, } (\upsilon = 0, 1, 2 \ldots). \qquad \text{(Eq.3. 28)}$$

Here υ is called the vibrational quantum number and ω_0 is the classical oscillation frequency

$$\omega_0 = \frac{1}{2\pi}\sqrt{\frac{k}{\mu}} \text{ Hz,} \qquad \text{(Eq.3. 29)}$$

where μ is the reduced mass of the system. In wavenumber units, **Eq.3.29** is written as

$$\tilde{\omega}_0 = \frac{1}{2\pi c}\sqrt{\frac{k}{\mu}} \text{ , cm}^{-1}. \qquad \text{(Eq.3. 30)}$$

The vibrational term values $G(\upsilon)$ are given by

$$G(\upsilon) = \frac{E_\upsilon}{hc} = (\upsilon + 1/2)\tilde{\omega}_0 \qquad \text{(Eq.3. 31)}$$

The selection rules require

$$\Delta\upsilon = \pm 1 . \qquad \text{(Eq.3. 32)}$$

The allowed transition wave number is given by

$$\tilde{\nu} = G(\upsilon+1) - G(\upsilon) = \tilde{\omega}_0 . \qquad \text{(Eq.3. 33)}$$

When anharmonic effects are considered, the vibrational term values become more complicated,

$$G(\upsilon) = \tilde{\omega}_e(\upsilon + 1/2) - \tilde{\omega}_e x_e(\upsilon + 1/2)^2 , \qquad \text{(Eq.3. 34)}$$

where $\tilde{\omega}_e$ is an oscillation frequency in cm^{-1} and x_e is the anharmonicity constant. The relationship between $\tilde{\omega}_e$ and $\tilde{\omega}_0$ is given by

$$\tilde{\omega}_0 = \tilde{\omega}_e\left[1 - x_e(\upsilon + 1/2)\right]. \qquad \text{(Eq.3. 35)}$$

The selection rules also change to

$$\Delta\upsilon = \pm 1, \pm 2, \pm 3, \ldots \qquad \text{(Eq.3. 36)}$$

but $\Delta\upsilon = \pm 1$ transitions generally dominate the infrared spectrum of a molecule.

The molecules can rotate and vibrate at the same time. Within Born-Oppenheimer approximation, the coupling between rotation and vibration can be neglected and the total energy of the rotation and vibration can be given by

$$E_{J,\upsilon} = E_{rot} + E_{vib} \qquad \text{(Eq.3. 37)}$$

Thus, for a diatomic molecule, the total term values S can be given

$$S(\upsilon, J) = F(J) + G(\upsilon) \\ = B_\upsilon J(J+1) - D_\upsilon J^2(J+1)^2 + \tilde{\omega}_e(\upsilon + 1/2) - \tilde{\omega}_e x_e(\upsilon + 1/2)^2 \quad \text{(Eq.3. 38)}$$

The selection rule is given by

$$\Delta\upsilon = \pm 1, \pm 2, \pm 3\ldots, \Delta J = \pm 1 \quad \text{(Eq.3. 39)}$$

The line series with ΔJ=1 and ΔJ= -1 are referred to as P and R branches by following the labelling customs in spectroscopy, i.e.

Lines arising from ΔJ=	-2	-1	0	+1	+2	
Called:	O	P	Q	R	S	branch

Due to the selection rules, few diatomic rovibrational spectra exhibit a Q branch.

The case for a polyatomic molecule is more complicated. There, the selection rules allow transitions with ΔJ=0, thus their rovibrational spectra often show a Q branch.

3.1.3.3. The electronic states of molecules [4]

For simplification, here, we use diatomic molecules as an example in our discussion. Unlike atoms, diatomic molecules have cylindrical symmetry, which means that the orbital angular momentum **L** is no longer a conservative variable. Thus, the orbital angular momentum number L is no longer a good quantum number. However, the axial component of **L** along the internuclear axis is still conservative, thus a good quantum number Λ still can be defined.

The total axial orbital momentum $\mathbf{\Lambda}$ is given by

$$\mathbf{\Lambda} = \sum \boldsymbol{\lambda}_i \quad \text{(Eq.3. 40)}$$

Here, $\boldsymbol{\lambda}_i$ is the axial orbital momentum of the *i*th electron and its corresponding quantum number is m_{l_i} (m_{l_i} can be positive and negative). Then Λ can be given by

$$\Lambda = \left|\sum m_{l_i}\right| \quad \text{(Eq.3. 41)}$$

According to the value of Λ (0, 1, 2, 3…), the electronic states of linear molecules are denoted by Σ, Π, Δ, Φ… of which Π, Δ, Φ…are doubly degenerate.

Only for Σ states, depending on whether the molecular orbital is symmetric or

anti-symmetric with respect to reflection across any plane containing the internuclear axis, the states are denoted by Σ^+ or Σ^-.

In addition, if the diatomic molecule has two identical nuclei (H_2, C_2 …), subscripts g and u must be added to distinguish electronic functions that are “gerade” or “ungerade" upon inversion through the center of the molecule.

The spin $\mathbf{s}_i$ of each electron has to be added to give the total spin,

$$\mathbf{S} = \sum \mathbf{s}_i \,. \qquad \text{(Eq.3. 42)}$$

The corresponding quantum number S determines the multiplicity (2S+1), as in atoms.

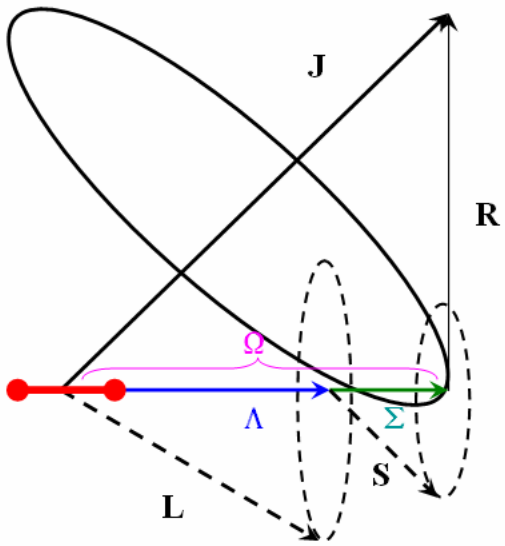

Figure 3. 3 Vector diagram of the several angular momenta in a diatomic molecule.

The total angular momentum is given by

$$\mathbf{J} = \mathbf{\Omega} + \mathbf{R} \qquad \text{(Eq.3. 43)}$$

$\mathbf{\Omega}$ is the component of $\mathbf{J}$ on internuclear axis and is given by

$$\mathbf{\Omega} = \mathbf{\Lambda} + \mathbf{\Sigma} \qquad \text{(Eq.3. 44)}$$

as shown in **Figure 3. 3**.

The electric dipole selection rules for a diatomic molecule are given by

$$\Delta\Lambda = 0, \pm 1 \qquad \text{(Eq.3. 45)}$$

$$\Delta S = 0 \qquad \text{(Eq.3. 46)}$$

$$\Delta\Omega = 0, \pm 1$$

$$\Sigma^+ \leftrightarrow \Sigma^+, \quad \Sigma^- \leftrightarrow \Sigma^-, \quad \Sigma^+ \not\leftrightarrow \Sigma^- \qquad \text{(Eq.3. 47)}$$

$$g \leftrightarrow u\,,\quad g \not\leftrightarrow g\,,\quad g \not\leftrightarrow u \qquad \text{(Eq.3. 48)}$$

The electronic states of a diatomic molecule can be written as

Term symbol = ${}^{2S+1}\Lambda^{+\,or\,-}_{g\,or\,u}$

The ground states normally are marked by *X* before its term symbol. The higher excited states with the same spin multiplicity as the ground state are labelled by *A, B, C* etc. The higher excited states of a different spin multiplicity are marked by *a, b, c* etc.

3.1.4. Line intensity

The line intensity is determined by the product of the population (in the upper level for emission or in the lower level for absorption) and transition probability. Under equilibrium conditions, the population in different energy levels obeys the Boltzmann distribution. Therefore, the population of upper level N_j and lower level N_i satisfies the following equation

$$\frac{N_j}{N_i} = \frac{g_j}{g_i}\exp\left(-\frac{\Delta E}{kT}\right) \qquad \text{(Eq.3. 49)}$$

Here g_i and g_j are the degeneracy of the lower and upper levels. If *i* or *j* refer to specific rotational levels *J*'' and *J*',

$$\frac{g_j}{g_i} = \frac{2J'+1}{2J''+1}. \qquad \text{(Eq.3. 50)}$$

If *i* and *j* refer to two vibrational levels υ'' and υ', then

$$\frac{g_j}{g_i} = 1 \qquad \text{(Eq.3. 51)}$$

If *i* and *j* refer to two electronic states, then

$$g_{i(j)} = \begin{cases} (2S+1) & if\ \Lambda = 0 \\ 2(2S+1) & if\ \Lambda \neq 0 \end{cases} \qquad \text{(Eq.3. 52)}$$

The transition probability is closely related to the wave functions of the upper and lower level, as detailed in the following subsections.

3.1.4.1. Einstein coefficients

When a two-state system as shown in **Figure 3. 4** is subjected to radiation with wavenumber $\tilde{\nu}$, three processes will occur. They are spontaneous emission, absorption and stimulated emission.

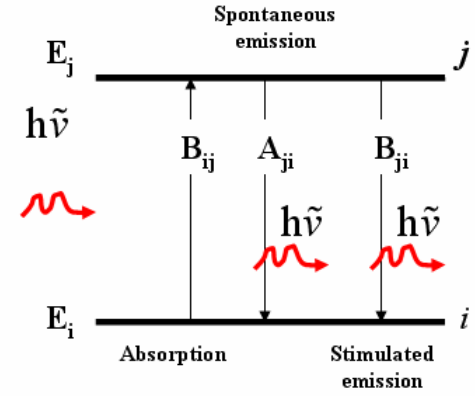

Figure 3. 4 Absorption and emission processes between states *i* and *j*.

Such processes can be characterized by three Einstein coefficients as shown in **Figure 3. 4**.

The relationship among them is given by

$$A_{ji} = 8\pi h\tilde{\nu}^3 B_{ji} \qquad \text{(Eq.3. 53)}$$

$$B_{ij} = \frac{g_j}{g_i} B_{ji} \qquad \text{(Eq.3. 54)}$$

The Einstein coefficients can also be related to the wave functions of the upper and lower states through the transition dipole moment $\mathbf{R}^{\mathbf{ji}}$,

$$\mathbf{R}^{\mathbf{ji}} = \langle i \,|\, \boldsymbol{\mu} \,|\, j \rangle = \int \psi_j^* \boldsymbol{\mu} \psi_i \, \mathrm{d}\tau \qquad \text{(Eq.3. 55)}$$

where $\boldsymbol{\mu}$ is the dipole moment operator and is given by

$$\boldsymbol{\mu} = \sum_i q_i \mathbf{r}_i \,. \qquad \text{(Eq.3. 56)}$$

Thus the Einstein coefficients can be written as

$$A_{ji} = \frac{64\pi^4 \tilde{\nu}^3}{(4\pi\varepsilon_0)3h} \left|\mathbf{R}^{\mathbf{ji}}\right|^2, \qquad \text{(Eq.3. 57)}$$

$$B_{ji} = \frac{8\pi^3}{(4\pi\varepsilon_0)3h^2}\left|\mathbf{R}^{\mathbf{ji}}\right|^2. \qquad \text{(Eq.3. 58)}$$

3.1.4.2. Relationship between absorption coefficient α and B_{ij}

Consider radiation of intensity I_0 passing through an absorption cell of length l, cross-section S. The concentration of the absorbing materials in the cell is n and the absorption cross section $\sigma(v)$ is a function of the frequency of the incident light. According to the Beer-Lambert Law,

$$I = I_0 e^{-\alpha l} \qquad \text{(Eq.3. 59)}$$

or

$$\ln\frac{I}{I_0} = -\alpha l\,. \qquad \text{(Eq.3. 60)}$$

Here, α is the absorption coefficient in a unit distance and given by

$$\alpha = \int_v n\sigma(v)\,\mathrm{d}v\,. \qquad \text{(Eq.3. 61)}$$

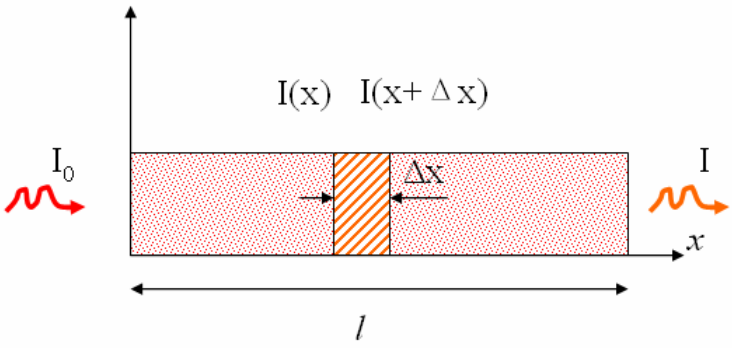

Figure 3. 5 Absorption in a cell of length l and cross-section S

On the other hand, we can also calculate I from I_0 by using calculus methods. The whole absorption cell can be divided into many small cells with the constant length Δx, as shown in **Figure 3. 5**. Thus,

$$I(x+\Delta x) - I(x) = -\rho(x)\cdot B_{ij}\cdot N_i\Delta V\cdot h\nu + \rho(x)\cdot B_{ji}\cdot N_j\Delta V\cdot h\nu \qquad \text{(Eq.3. 62)}$$

(absorption) (stimulated emission)

Here, $\rho(x)$ is the radiation density and is given by

$$\rho(x) = \frac{I(x)}{Sc}, \qquad \text{(Eq.3. 63)}$$

N_i and N_j are the populations in the lower and upper energy levels, respectively. ΔV is the volume of each small cell and can be written as

$$\Delta V = S \cdot \Delta x. \qquad \text{(Eq.3. 64)}$$

Substituting **Eq. 3.63** and **3.64** into **Eq. 3.62** gives

$$I(x+\Delta x) - I(x) = -\frac{I(x)}{\cancel{S}\cancel{c}} \cdot B_{ij} \cdot N_i \cancel{S} \cancel{\Delta x} \cdot h\nu + \frac{I(x)}{\cancel{S}\cancel{c}} \cdot B_{ji} \cdot N_j \cancel{S} \cancel{\Delta x} \cdot h\nu. \qquad \text{Eq.3. 65)}$$

Thus

$$\frac{I(x+\Delta x) - I(x)}{\Delta x} = -\frac{I(x) h\nu}{c}(B_{ij} \cdot N_i - B_{ji} \cdot N_j). \qquad \text{(Eq.3. 66)}$$

If $\Delta x \to 0$, then **Eq. 3.66** will change into

$$\frac{\mathrm{d}I}{\mathrm{d}x} = -\frac{I(x) h\nu}{c}(B_{ij} \cdot N_i - B_{ji} \cdot N_j). \qquad \text{(Eq.3. 67)}$$

Dividing both sides by $I(x)$ and then integrating x from 0 to l, we get

$$\ln\frac{I}{I_0} = -\frac{h\nu l}{c}\left(B_{ij}N_i - B_{ji}N_j\right). \qquad \text{(Eq.3. 68)}$$

Use the relationship in **Eq. 3.54** we get

$$\ln\frac{I}{I_0} = -\frac{h\nu}{c} B_{ij} N_i l\left(1 - \frac{g_i N_j}{g_j N_i}\right). \qquad \text{(Eq.3. 69)}$$

Comparing **Eq. 3.60** and **Eq. 3.69** we have

$$\alpha = \int_{\nu} n\sigma(\nu)\,\mathrm{d}\nu = \frac{h\nu}{c} B_{ij} N_i\left(1 - \frac{g_i N_j}{g_j N_i}\right). \qquad \text{(Eq.3. 70)}$$

if $N_j << N_i$, then

$$\alpha = \int_{\nu} n\sigma(\nu)\,\mathrm{d}\nu = \frac{h\nu}{c} B_{ij} N_i. \qquad \text{(Eq.3. 71)}$$

As we shall see, **Eq. 3.71** is very useful in converting measured absorptions into the species concentrations.

3.1.4.3. Symmetry and selection rules

As seen from **Eq. 3.55**, besides the wave functions, which can make the integration

$\int \psi_j^* \boldsymbol{\mu} \psi_i \, d\tau$ zero, the transition probability will also be zero if transition dipole moment operator is zero. Thus, a symmetric molecule without a permanent dipole moment, e.g. C_2H_2, CO_2, won't show a pure rotational spectrum. On the other hand, for a vibrating molecule, the dipole moment can be written as

$$\boldsymbol{\mu} = \boldsymbol{\mu}_e + \left(\frac{d\boldsymbol{\mu}}{dx}\right)_e x + \frac{1}{2!}\left(\frac{d^2\boldsymbol{\mu}}{dx^2}\right)_e x^2 + \ldots \quad \text{(Eq.3. 72)}$$

The transition moment now becomes

$$\mathbf{R}_\upsilon = \boldsymbol{\mu}_e \int \psi_{\upsilon'}^* \psi_{\upsilon''} dx + \left(\frac{d\boldsymbol{\mu}}{dx}\right)_e \int \psi_{\upsilon'}^* x \psi_{\upsilon''} dx + \ldots . \quad \text{(Eq.3. 73)}$$

The first integration is zero because $\psi_{\upsilon'}$ and $\psi_{\upsilon''}$ are orthogonal to each other. The second integration is non-zero if

$$\Delta\upsilon = \pm 1 . \quad \text{(Eq.3. 74)}$$

Thus, the vibration spectra can occur when the molecule changes its dipole moment in its vibration motion.

3.1.4.4. Nuclear spin effect

The nuclear spin can also introduce a modulation of the line intensity. When nuclear spin is included, the total wave function can be given by

$$\psi = \psi_e \psi_\upsilon \psi_r \psi_{ns} , \quad \text{(Eq.3. 75)}$$

where, ψ_e, ψ_υ, ψ_r and ψ_{ns} are the electronic, vibrational, rotational and nuclear spin wave functions, respectively.

For a diatomic or linear polyatomic molecule possessing a center of symmetry, if the nuclei have the nuclear spin quantum number $I=n+1/2$, it is said to be a Fermi particle and will obey Fermi-Dirac statistics. For such a molecule, exchange of any two identical nuclei which are equidistant from the symmetric center will result in a change of sign of ψ. In contrast, if $I=n$, it is called a Boson and will obey Bose-Einstein statistics. Exchange of two equivalent nuclei in such molecules will not change ψ.

Exchange of two equivalent nuclei will not change ψ_e or ψ_υ. ψ_r will change sign only if J is an odd number. Thus, for a fermion molecule, ψ_{ns} must be symmetric when J is an odd number and must be antisymmetric when J is an even number in order to satisfy the overall Pauli requirement that the total wavefunction shall be antisymmetric. The case for a boson molecule is exactly opposite.

In general, a homonuclear diatomic molecule has $(2I+1)(I+1)$ symmetric nuclear spin wave functions and $(2I+1)I$ antisymmetric nuclear spin wave functions. The population ratio of odd and even J levels will thus exhibit an extra modulation (for fermions the ratio is $(I+1)/I$ and for bosons it is $I/(I+1)$) due to nuclear spin effect.

One good example is acetylene ($^1H-^{12}C\equiv^{12}C-^1H$). Since I=0 for ^{12}C, its case is similar to that of H_2. Because each H nucleus has spin I=1/2, the population of odd and even J levels of C_2H_2 thus have statistical weights of 3 and 1 due to the nuclear spin effect. This reveals itself in the measured, for example, rovibrational spectrum, as a "strong-weak-strong-weak…" pattern.

3.1.4.5. Franck-Condon principle

In the vibrational-electronic spectra, there is another effect that will influence the relative intensities of different vibrational lines. The mechanism behind this phenomenon is called the Franck-Condon principle. It reflects a fact that "an electronic transition takes place so rapidly that a vibrating molecule does not change its internuclear distance during the transition". [3]

The Franck-Condon principle can be illustrated in **Figure 3. 6**. In **Figure 3. 6 (a)** the upper and lower electronic states have the same equilibrium internuclear distance. If we assume the molecule is initially in the ground state υ''=0, then, according to the Franck-Condon principle, the transition shall occur "vertically" because the internuclear distance does not change in this "short time". So the most probable transition is from υ''=0 to υ'=0 (i.e. (0,0) transition) and (1,0), (2,0) … transitions

will become less and less possible. Therefore, the line intensity distribution appears as shown in the diagram in the bottom of **Figure 3. 6 (a)**. However, if the equilibrium internuclear distance of the upper level is slightly bigger than that of the lower level, as shown in **Figure 3. 6 (b)**, the Franck-Condon principle tells us that the vertical transition from υ''=0 to υ'=2 (i.e. (2,0) transition) is now the most probable. The line intensity distribution in such a case will look like the diagram at the bottom of **Figure 3. 6 (b)**.

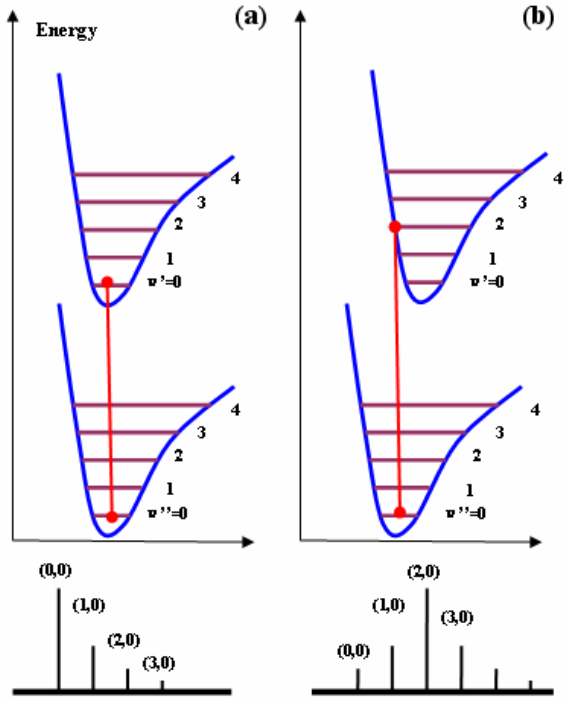

Figure 3. 6 Illustration of the Franck-Condon principle for (a) $r'_e \approx r''_e$ and (b) $r'_e > r''_e$

In fact, we can also treat the Franck-Condon principle in the "language" of quantum mechanics. As discussed before, the intensity of a vibronic transition is proportional to the square of the transition moment $\mathbf{R}_{ev}$, which is given by

$$\mathbf{R}_{ev} = \int \psi'^{*}_{ev}\, \boldsymbol{\mu} \psi''_{ev}\, \mathrm{d}\tau_{ev} . \qquad \text{(Eq.3. 76)}$$

Under the Born-Oppenheimer approximation,

$$\psi_{ev} = \psi_e \psi_\upsilon . \qquad \text{(Eq.3. 77)}$$

Thus,

$$\mathbf{R}_{ev} = \iint \psi'^{*}_{e} \psi'^{*}_{\upsilon}\, \boldsymbol{\mu} \psi''_{e} \psi''_{\upsilon}\, \mathrm{d}\tau_e \mathrm{d}r = \int \psi'^{*}_{\upsilon} \mathbf{R}_e \psi''_{\upsilon}\, \mathrm{d}r . \qquad \text{(Eq.3. 78)}$$

where r is the internuclear distance and $\mathbf{R}_e$ is the electronic transition moment given by

$$\mathbf{R}_e = \int \psi'^*_e \boldsymbol{\mu} \psi''_e \, \mathrm{d}\tau_e . \qquad \text{(Eq.3. 79)}$$

In the Born-Oppenheimer approximation, the nuclei can be treated as stationary compared with the fast movement of electrons. Therefore, $\mathbf{R}_e$ can be removed from the integral in **Eq.3. 76**

$$\mathbf{R}_{ev} = \mathbf{R}_e \int \psi'^*_v \psi''_v \, \mathrm{d}r . \qquad \text{(Eq.3. 80)}$$

The quantity of $\int \psi'^*_v \psi''_v \, \mathrm{d}r$ is called the vibrational overlap integral. Its square is known as the Franck-Condon factor.

3.1.5. Line shape and Line width

In practice, any observed spectral line always has a finite line width. There are several effects that will contribute to this broadening.

3.1.5.1. Natural line broadening

Each excited state has a certain life time τ, which is given by

$$\tau = \frac{1}{A_{ji}}, \qquad \text{(Eq.3. 81)}$$

where A_{ji} is Einstein coefficient and is given by **Eq. 3.58**.

The Heisenberg uncertainty principle tells us

$$\tau \Delta E \geq \hbar . \qquad \text{(Eq.3. 82)}$$

Thus, combining Eq. 3.82 and 3.83 , we have

$$\Delta \nu \geq \frac{32\pi^3 \nu^3}{(4\pi\varepsilon_0)3hc^3} \left| \mathbf{R}^{\mathbf{ji}} \right|^2 . \qquad \text{(Eq.3. 83)}$$

Such broadening is called natural broadening. It has a Lorentzian line shape. The typical value for an excited electronic state is ~30MHz, which usually is much smaller than the broadening from other effects.

3.1.5.2. Doppler broadening

An atom or molecule should only emit or absorb photons with one certain frequency if the natural line broadening is ignored. However, when an atom or molecule is travelling with a velocity $\upsilon_{a,}$ due to the Doppler effect, the observed photon frequency ν_a in such a system is related to the frequency ν_0 in a stationary atom or molecule by

$$\nu_a = \nu_0 \left(1 \pm \frac{\upsilon_a}{c}\right)^{-1}. \qquad \text{(Eq.3. 84)}$$

However, under thermal equilibrium conditions, the thermal velocity of atoms or molecules obeys a Maxwellian distribution and has a spread of values. This spread of velocities will lead to a Gaussian shaped broadening named Doppler broadening. The linewidth due to Doppler broadening is given by

$$\Delta\nu = \frac{\nu_0}{c}\left(\frac{2kT\ln 2}{m}\right)^{1/2}. \qquad \text{(Eq.3. 85)}$$

It is worth mentioning that Doppler broadening is an important method for determining the temperature of atoms or molecules, especially for H atoms. However, due to the relationship

$$\Delta\nu \propto m^{-1/2}, \qquad \text{(Eq.3. 86)}$$

Doppler broadening is not so important for the heavy atoms or molecules unless the temperature is extremely high.

3.1.5.3. Stark broadening

An external electric field can also introduce extra broadening to an atomic or molecular line width through the Stark effect. The linear Stark effect causes only line broadening while the quadratic effect can also lead to a line shift. The line shape due to Stark broadening is Lorentzian. Stark broadening is important in plasma spectroscopy because of the strong interactions between the electric field and charge particles in the plasma environment. The electron or ion densities and the gas temperature can be determined through careful measurement of Stark broadening

line shapes. A good example of this involves using H_β Stark broadening to determine the electron densities in various plasmas. [5]

3.1.5.4. Pressure broadening

Under high pressure conditions, collisions between atoms and molecules become very frequent. As a result, quenching processes will seriously reduce the life time of the excited states. From the Heisenberg uncertainty principle, we know this will cause an increase in the atomic and molecular linewidth. This broadening, called Pressure broadening, is given by

$$\Delta\nu = (2\pi\tau_{col})^{-1} \qquad \text{(Eq.3. 87)}$$

where τ_{col} is the mean time between collisions. Like natural line broadening, the pressure broadening also has a Lorentzian shape.

3.2. Laser

3.2.1 General principle

The word “laser” comes from the abbreviation of light amplification by stimulated emission of radiation. Generally, a laser comprises three parts: pumping source, gain medium and optical resonator. There are two necessary conditions to realize a laser: population inversion and gain coefficient G >1. The former ensures a net output from stimulated emission. The latter means that the resonator must be a cavity with a high quality factor Q (i.e. low loss).

3.2.1.1. Population inversion [6]

Figure 3. 7 shows a typical four-level laser system. As shown in this figure, due to the fast decay rates of levels 2 and 4, very little population accumulates in them, thus

$$N_2 \approx 0\,,\quad N_4 \approx 0\,. \qquad \text{(Eq.3. 88)}$$

The total population

$$N_0 = \sum N_i \approx N_1 + N_3\,. \qquad \text{(Eq.3. 89)}$$

For simplicity, we assume the degeneracy of level 3 and 2 are equal. The total contribution for level 1 through level 4 to level 3 can be combined into an effective pumping rate W_p. Therefore, for level 3, we have

$$\frac{dN_3}{dt} = N_1 W_p - N_3 A_{32} - N_3 W_{32} + N_2 W_{23}$$

$$= N_1 W_p - N_3 A_{32} - \rho c B_{32}(N_3 - N_2)\,. \qquad \text{(Eq.3. 90)}$$

Using **Eq.3.88** and **Eq. 3.89**, and define

$$\Delta N = N_3 - N_2\,. \qquad \text{(Eq.3. 91)}$$

Eq.3.90 can be rewritten as

$$\frac{\mathrm{d}N_3}{\mathrm{d}t} \approx N_0 W_p - (W_p + A_{32} + \rho c B_{32})\Delta N \qquad \text{(Eq.3. 92)}$$

Making steady state approximation, $\mathrm{d}N_3/\mathrm{d}t = 0$, we have

$$\Delta N = N_0 \frac{W_p}{W_p + A_{32} + \rho c B_{32}} > 0\,. \qquad \text{(Eq.3. 93)}$$

Therefore, population inversion can be realized for such a four-level system as shown in **Figure 3. 7**.

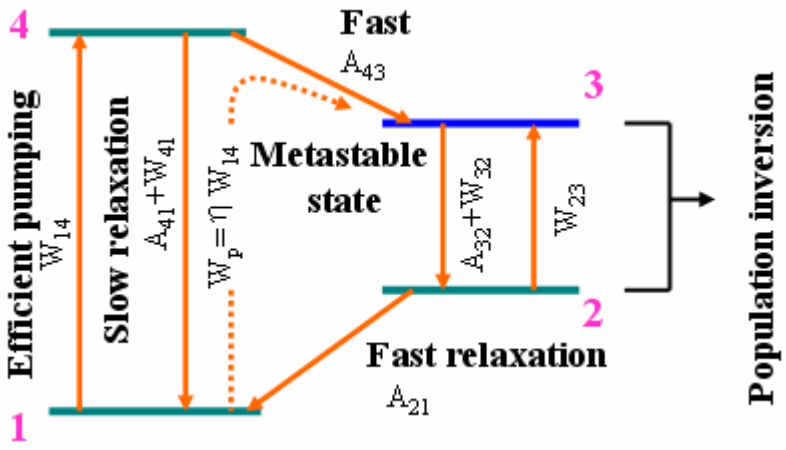

Figure 3. 7 Diagram of a four-level laser system

3.2.1.2. Resonator [6]

For a resonator as shown in **Figure 3. 8**, if we ignore all the other losses except the transmission loss through the mirrors, the loop gain or gain factor of the resonator can be written as:

$$G_L = \frac{I_6}{I_1} = G_a^2 R_1 R_2 . \qquad \text{(Eq.3. 94)}$$

Here, G_a is the gain factor for the gain medium.

$$G_a = \exp(\alpha d) \qquad \text{(Eq.3. 95)}$$

where d is the length of the gain medium, and R_1 and R_2 are the reflectivities of the mirrors.

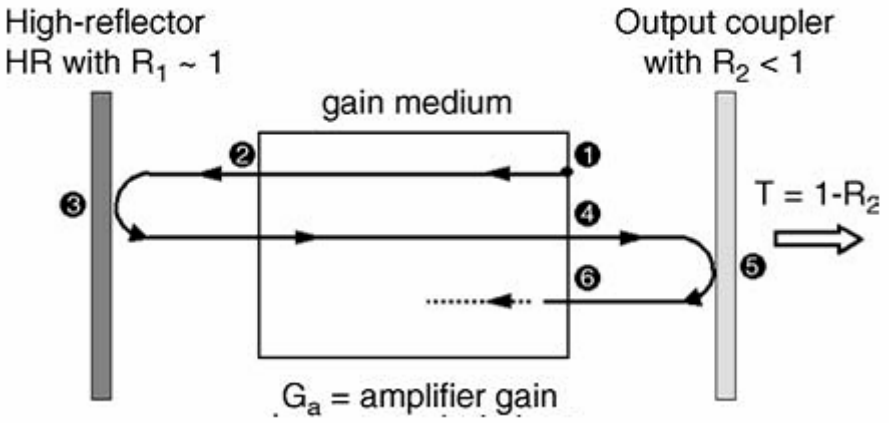

Figure 3. 8 Loop gain of a resonator

To get amplification of the stimulated emission, the gain factor of the resonator shall be greater than 1, i.e.

$$e^{2\alpha d} R_1 R_2 > 1 . \qquad \text{(Eq.3. 96)}$$

So it requires

$$\alpha > \frac{1}{2d} \ln \frac{1}{R_1 R_2} . \qquad \text{(Eq.3. 97)}$$

For $G_L = 1$, it corresponds to the case of steady laser output.

To fulfil the condition in **Eq. 3.97** requires that R_1 and R_2 are close to 1 so that $\ln(1/R_1 R_2)$ can be quite small. In another words, this means that the quality factor of the cavity

$$Q = \frac{2\pi}{\ln(R_1 R_2)} \qquad \text{(Eq.3. 98)}$$

must be high. Such a conclusion is consistent with the previously mentioned high Q requirement for a laser.

The G_L is actually a function of the laser frequency. Due to the existence of multiple cavity modes, the out put laser in frequency space is as shown in **Figure 3. 9**.

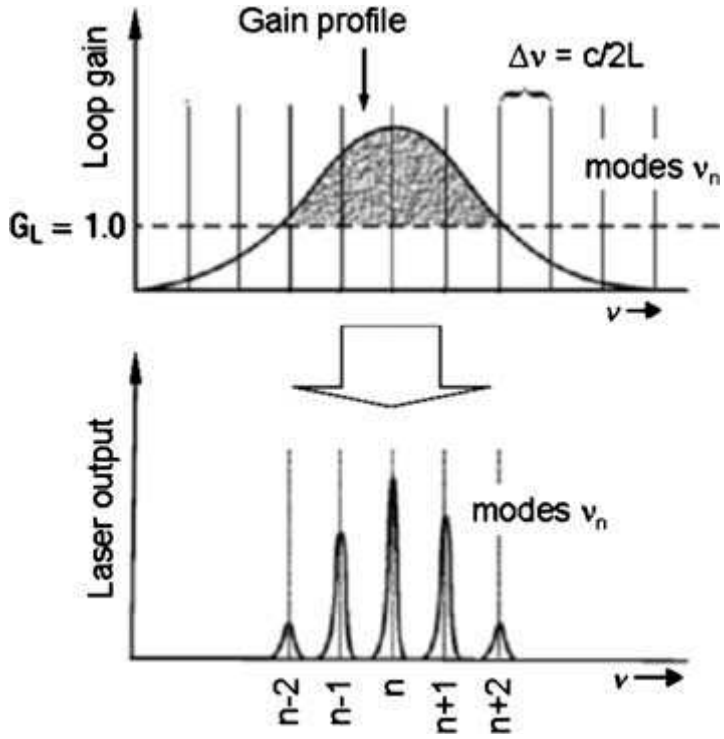

Figure 3. 9 Relationship between gain profile and laser modes.

3.2.1.3. *Q*-switching [6]

A laser working in the pulsed mode will normally give a laser pulse in the regime 0.1- 100 μs. However, sometimes even shorter laser pulses are required so that the power concentration (the intensity) can be higher. One technique often used to achieve this is called *Q*-switching.

Using an electro-optical (EO) *Q*-switch device as an example, the principle of *Q*-switching can be described as follows, see **Figure 3. 10**. An EO *Q*-switch device usually includes a linear polarization filter (passive element) and an EO polarization rotator (active element) such as Pockels cell or Kerr cell. When the high voltage (HV) is applied to the Pockels cell, the polarization plane of the light that passes through it will be shifted by 45 degrees. Before the light returns to the polarizer, because it has passed through the Pockels cell twice, its polarization plane has been rotated by 90

degrees. Then the polarizer will not transmit the light and the resonator cavity is under a high loss condition (low Q). At that moment, though the population inversion has built up in the gain medium, because G_L in the resonator is <1, there is no laser output. The energy is just stored in the gain medium. Then, if the HV on the Pockels cell is suddenly switched off (typically the switching time is less than 1ns), the polarization plane of the light will revert to its unshifted state and the polarizer will then allow the light to pass through. Thus the resonator is under a low loss condition (high Q) with G_L>1. All the lasing conditions are satisfied. The laser pulse builds up very quickly, and concomitantly the stored energy and amplifier gain are severely depleted before the next pumping pulse replenishes them. The laser will soon cease after reaching its maximum. Finally a giant laser pulse output (of typical duration 5-50 ns) is produced.

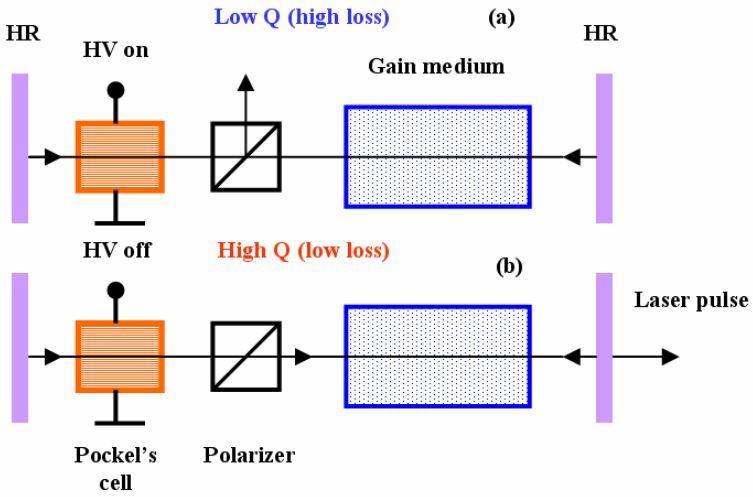

Figure 3. 10 An EO Q-switch laser system (a) Pockels cell is on, the quality factor of cavity is low; (b) Pockels cell is off, the quality factor of cavity is high.

3.2.1.4. Mode locking [6]

One challenging field today involves use of lasers to explore reaction dynamics. Fast reactions normally happen in less than one picosecond (10^{-12} s). Thus an ultrashort laser pulse (~100 fs) is needed. Such short laser pulses can be achieved using a technique called mode locking. With the help of this laser technique, a new research field called femto-chemistry was born. One of the initiators in this field, Ahmed H.

Zewail was awarded the chemistry Nobel Prize in 1999.

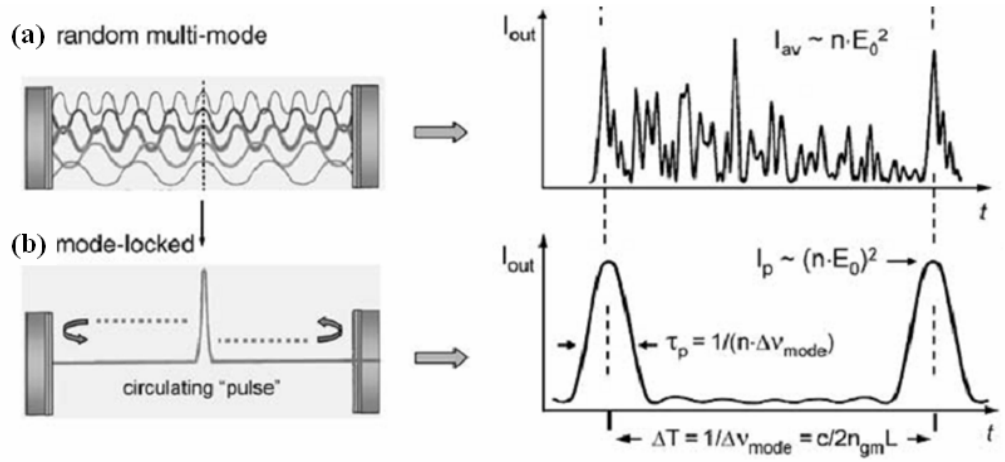

Figure 3. 11 Temporal characteristics of laser output intensity: (a) for a random multi-mode CW laser; (b) for a mode-locked ultra-short pulse laser. [6]

The principle of mode locking is illustrated in **Figure 3. 11**, following the discussion given in section 3.6 of the book written by Teller et al. [6] Consider a laser resonator that oscillates in a large number of longitudinal modes. Normally, these modes have no common phase correlation and the summation of these waves will appear in the laser output in a form similar to that shown on the right in **Figure 3. 11 (a)**. The maximum instantaneous output intensity is given by

$$I_{out\max} \propto nE_0^2, \qquad \text{(Eq.3. 99)}$$

where n is the number of the modes, and E_0 is the electric field amplitude of each of these modes (here they are assumed to be the same).

Now, if the phase of two consecutive modes only differs by a constant value, i.e. their phases are locked, then the interference between these modes will occur to give a series of sharp peaks with a time interval $2L/c$ as shown in **Figure 3. 11 (b)**. The maximum of laser pulse output is given by

$$I_{out\max} \propto (nE_0)^2 \qquad \text{(Eq.3. 100)}$$

In practice, mode locking is realized by modulating the resonator loss with a frequency equal to $c/2L$. The method of changing the resonator loss is similar to that used in Q switching. A picosecond or femtosecond laser pulse can be generated by this method.

3.2.2 YAG laser [6]

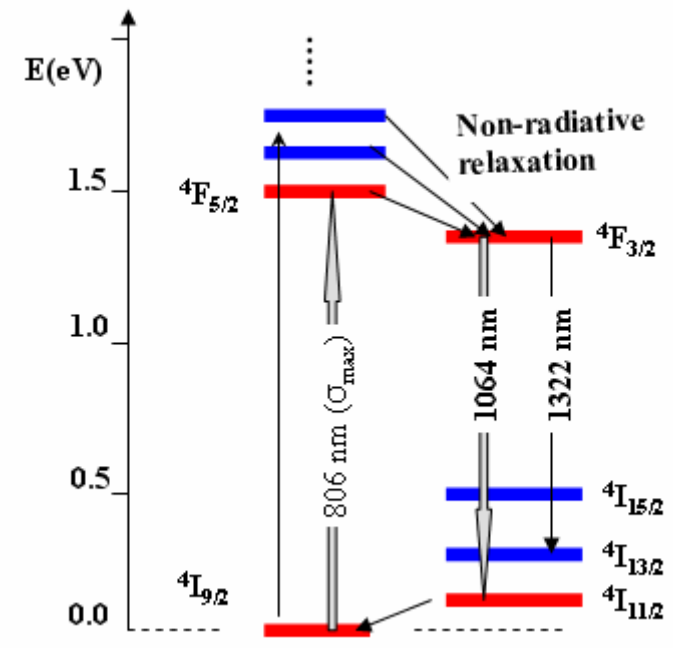

Figure 3. 12 Energy level diagram of an Nd:`YAG laser system

One of the most widely used solid state laser is the Nd:YAG laser. The name comes from the materials used in this laser, which means neodymium atoms (Nd) being implanted in an yttrium aluminium garnet crystal host ($Y_3Al_5O_{12}$). These implants, in the form of triply ionized neodymium Nd^{3+} ions, form the actual active laser medium.

The principle of Nd-YAG laser is shown in **Figure 3. 12**. It is actually a four-level system (see the energy levels marked by red color). The $^4F_{5/2}$ energy levels of Nd^{3+} are populated using a Xe flash lamp (for pulsed laser operation) or a tungsten arc lamp (for CW operation) to pump the ground-state ions ($^4I_{9/2}$) with light of wavelength 800–820 nm. The $^4F_{5/2}$ energy levels and further higher levels thus serve as level 4 in this system. The Nd^{3+} ions relax by exchanging phonons with the host crystals from the pumped energy levels to the upper laser level, $^4F_{3/2}$, which serves as level 3. Level $^4F_{3/2}$ exhibits a long lifetime t ~ 230 µs, then radiates to the sub-states of the lower lying energy levels 2, including those of the levels $^4I_{13/2}$ and $^4I_{11/2}$. The main laser transition is the one between the levels $^4F_{3/2}$ and $^4I_{11/2}$, which gives the

laser output at the wavelength of 1064 nm. The ions return to their ground state from the lower laser level 2 through non-irradiative relaxation.

The Nd:YAG laser radiation at 1064 nm can easily be converted by frequency multiplication techniques (e.g. using nonlinear crystals) to give second-harmonic generation (SHG), third-harmonic generation (THG) and fourth-harmonic generation (FHG) waves, corresponding to the wavelength at 532 nm, 355 nm and 266 nm. The first two are normally used in pumping the dye lasers to cover the visible spectral range. However, due to the conversion efficiency, the output power will drop dramatically.

3.2.3 Dye laser [6, 7]

Getting a laser that can be tuned continuously over a large wave length range has long been a dream of people who study spectroscopy. The development of the dye laser, to some degree, fulfilled this fantasy. Recently, however, some new tuneable laser sources like Ti:sapphire laser, semiconductor diode laser and optical parametric oscillation (OPO) have appeared as rivals, but, the outstanding performance of dye laser means that it is still one of the most important tuneable lasers.

Just as its name suggests, dye lasers use organic dyes (usually in solutions) as its active medium. Compared with other laser materials, the dyes in solutions have very dense and broadened structures (energy bands) rather than a single energy level. Thus a dye can be used for a much wider range of wavelengths, which makes it very suitable for tuneable lasers.

The principle of dye lasers is illustrated in **Figure 3. 13**. As shown in this figure, a dye laser can be considered as a four-level system. The lowest vibrational state in the S_0 singlet band serves as level 1. The electrons in this state can be pumped into any of the electronically excited singlet states S_1, S_2, …, which are summarily designated as level 4. After excitation, due to collisions with solvent molecules, the excited dye

molecules quickly relax to the lowest vibrational level in the S_1 state which serves as the upper laser level 3. Then the population inversion is achieved between the lowest level in S_1 and the higher rovibronic levels in S_0 which are also summarily designated as level 2. The system finally returns to the ground vibrational level of S_0 (level 1) through collision-induced relaxation which is similar to that in S_1.

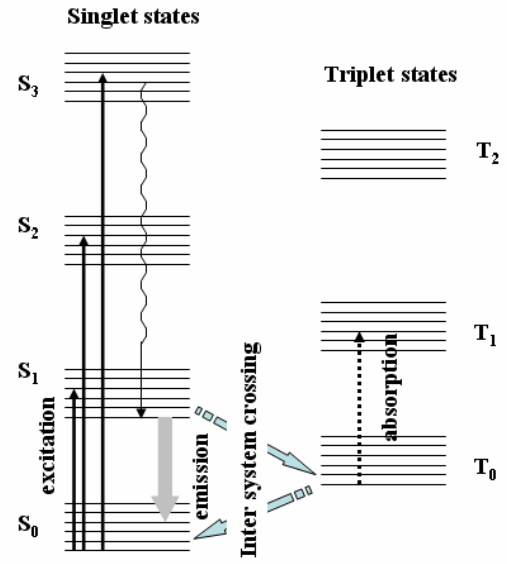

Figure 3. 13 Energy level diagram of a dye laser

By using different dyes, a dye laser can easily cover the range from ultraviolet to near infrared, see **Figure 3. 14**

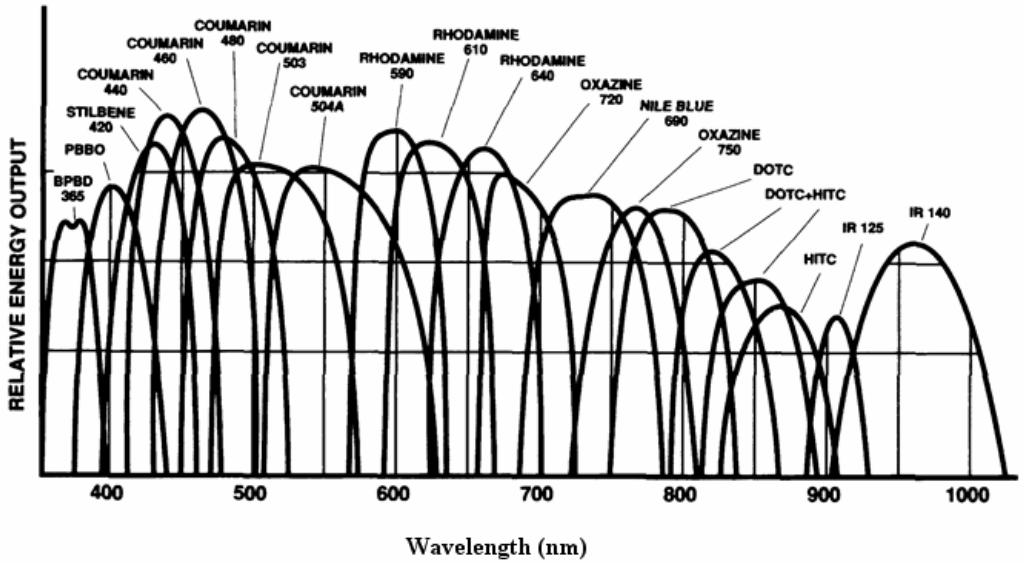

Figure 3. 14 Spectral gain profiles of different dyes illustrated in terms of the output power of pulsed lasers [7]. The *x* axis represents the wavelength in the unit of nm.

3.2.4 Diode laser [6, 7]

Though the first laser diode was demonstrated as early as in 1962 by Robert N. Hall and his team at the General Electric research center, [8] it is only in the last few years that the diode laser has developed remarkably and become one of the most important devices in photonics. The diode laser has many advantages, such as compactness, fast scanning speed, very narrow linewidth and relatively low cost.

The principle of the diode laser is quite different from that of the conventional lasers, which is shown in **Figure 3. 15**. It doesn't make use of the transition between energy levels of individual atoms or molecules. In contrast, radiation that results from the recombination of electrons and holes in the junction region (called "depletion layer") are used here to produce the laser. Thus, whereas the conventional laser is pumped by another light source, the diode laser is driven by an external electron current source. When a forward bias is applied, both electrons in the conduction band in the n-region and holes in the valence band in the p-region are driven towards the depletion layer and recombine there. As a result, photons with energy equal to, or a bit higher than, the band gap energy E_g are released. Thus, the central wavelength of a diode laser is mainly determined by the band gap energy, E_g.

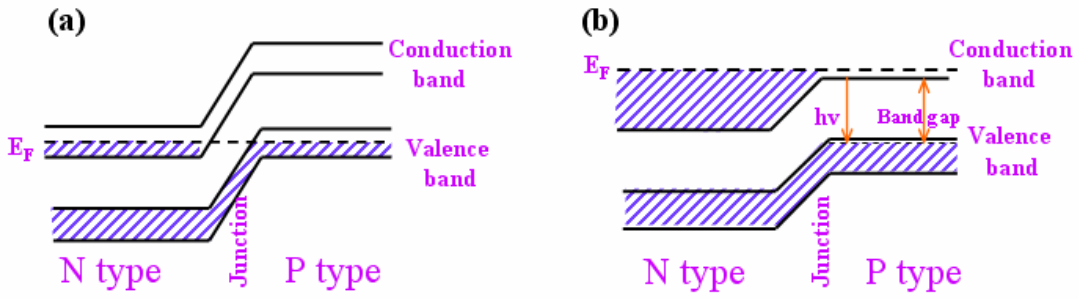

Figure 3. 15 Principle of a semiconductor diode laser: (a) no forward bias; (b) with forward bias.

An internal resonator formed by the two flat surfaces of the crystal of the diode laser is used to select a specific wavelength. Such a resonator is called a Fabry-Perot resonator. The length of the resonator cavity is influenced by the temperature, which

can be controlled by the current that flows through the diode. Therefore, by applying a linearly-increasing current, a diode laser can normally be scanned 3-5 nm corresponding to the secure operating temperatures of 5–45 ºC. Using an external resonator technique, the overall tuning range of the diode laser can be expanded to 20~60 nm.

3.2.5 Quantum cascade laser

As a novel semiconductor laser source, the quantum cascade laser (QCL) was first invented and demonstrated in Bell laboratories in 1994. [9] Though not necessary in principle, today most of the commercialized QCLs are designed to work in the mid-infrared region. Such a wavelength range is known as the “fingerprint” region of many molecules and radicals. Because of its novel principle, interesting features and more important roles in the study of molecules and radicals, a relatively more detailed introduction is presented here.

The QCL is based on a very different principle from those bipolar (homojunction or heterojunction) semiconductor laser diodes discussed in **Subsection 3.2.4**, where the radiation comes from the recombination of electrons and holes in the depletion layer. The QCL uses only electrons and thus is called a unipolar laser. Also, unlike conventional semiconductor lasers, in QCL, the optical transitions occur between electronic sub-bands (i.e. quantum well energy levels, see **Figure 3. 16**) rather than between the conduction and valence bands. The QCL thus essentially is a laser of multiple quantum wells and its wavelength is principally independent of the fixed material properties. To illustrate these principles clearly, several important concepts related to a QCL are firstly explained.

3.2.5.1. Quantum well [10]

A quantum well is a potential well that confines electron movement in one dimension while leaving the other two dimensions free. If the well thickness is small enough to be comparable with the electron’s de Broglie wavelength, a quantum

confinement effect will occur, which leads to a series of discrete energy levels called "energy subbands".

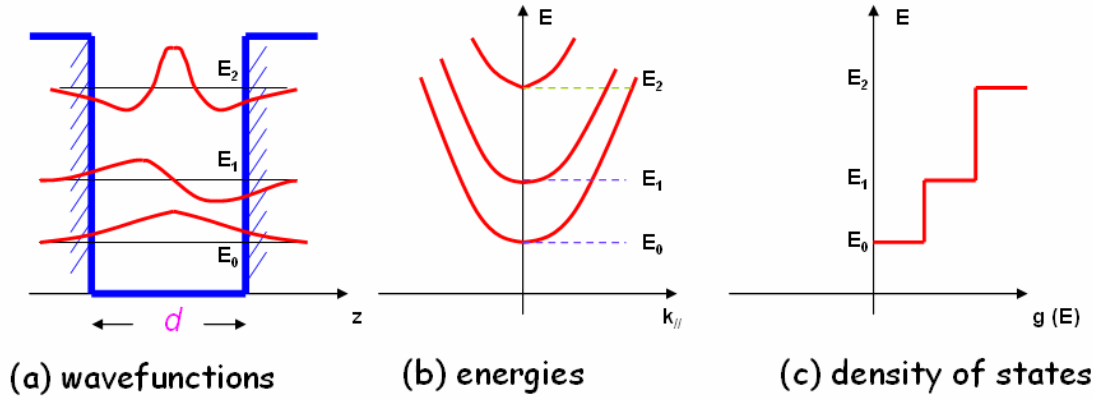

Figure 3. 16 Characteristics of quantum wells: (a) wavefunctions; (b) energies; (c) density of states. [10]

When an electron is confined in a quantum well, its energy can be expressed as

$$E = E_n + \frac{\hbar^2}{2m^*}(k_x^2 + k_y^2) = E_n + \frac{\hbar^2}{2m^*}k_{//}^2. \qquad \text{(Eq.3. 101)}$$

For an infinite square quantum well, the discrete energy

$$E_n = \frac{\hbar^2 \pi^2 n^2}{2m^* d^2} \qquad n = 1, 2, \cdots \qquad \text{(Eq.3. 102)}$$

where d is the width of the quantum well, m^* is the effective mass of electrons. Since there is no confinement along x and y direction, k_x and k_y, (or $k_{//}$ given in **Eq.3.102**) can take any values. Thus **Eq 3.101** represents a series of parabolic curves with their minima at different E_ns. The wave function, energy and density of states of electrons in a finite square quantum well are shown in **Figure 3. 16 (a), (b)** and **(c)**. As can be seen, the density of states, $g(E)$ shows a "hopping" increase with energy, i.e.

$$g_n(E) = \sum_{i=1}^{n} \frac{m^*}{\pi\hbar^2}\Theta(E - E_i), \qquad \text{(Eq.3. 103)}$$

where Θ is a unit step function.

3.2.5.2. Superlattice and molecular beam epitaxy [10]

The quantum well discussed above actually is only a physical concept. To turn it into real life, a structure called a superlattice is manufactured using a technique named

molecular beam epitaxy (MBE). A superlattice is a material with periodically alternating layers of several substances. For example, a superlattice formed by AlAs and GaAs is shown in the left of **Figure 3. 17**. Such a structure is often used in making QCLs. Due to the different band gap of these two semiconductor materials, the alternating structures lead to the formation of multiple quantum wells, as shown in the right hand diagram of **Figure 3. 17**. The superlattice possesses periodicity both on the scale of each layer's crystal lattice and on the scale of the alternating layers (or multiple quantum wells). The latter can introduce extra minibands and minigaps.

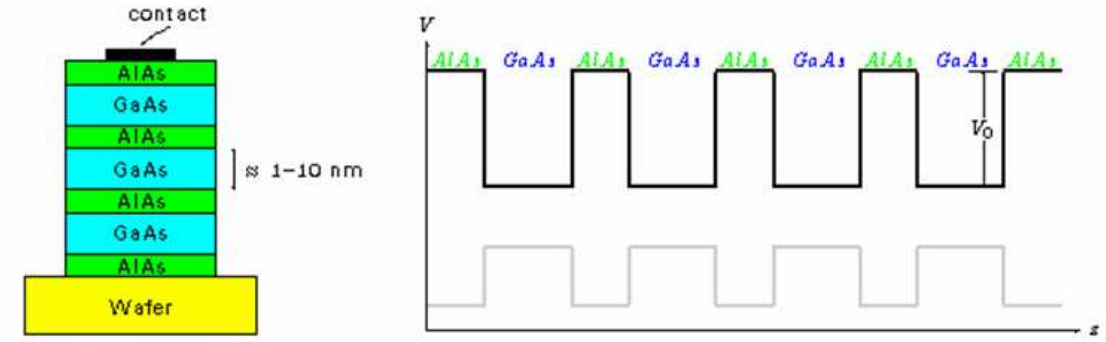

Figure 3. 17 Structure and energy band diagram of a AlAs:GaAs superlattice

MBE, the method used to make superlattices, is a technique based on ultra-high-vacuum (UHV, 10^{-8} Pa) technology. This method can produce high quality epitaxial structures with mono-atomic layer control. The typical configuration of a MBE apparatus is shown in the left hand panel of **Figure 3. 18**. The different atom sources (Al, Ga, As…) are mounted around the deposition chamber. Shutters between these sources and the deposition chamber are controlled by a computer so that the “on” and “off” time for different atom sources are accurately determined. During operation, Reflection High Energy Electron Diffraction (RHEED) is often used for monitoring the growth of the crystal layers. The principle of RHEED can be found in many textbooks. A typical RHEED signal during MBE process is shown in the right of **Figure 3. 18**.

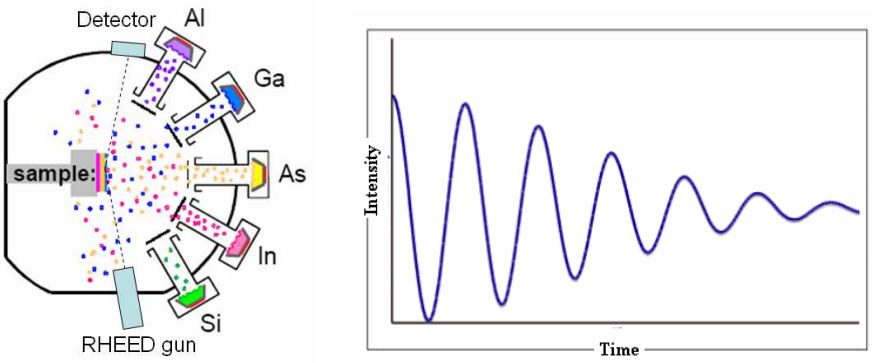

Figure 3. 18 Schematic of a common MBE reactor (left) and a typical RHEED signal (right)

3.2.5.3. Principles of a QCL [9]

A QCL consists of a multiple-layer sandwich structure of differently doped semiconductor materials. Essentially, it is an assembly of many three-level quantum well laser units. The detailed structure of one unit is shown in the left hand panel of **Figure 3. 19**. It is composed of many quantum well structures.

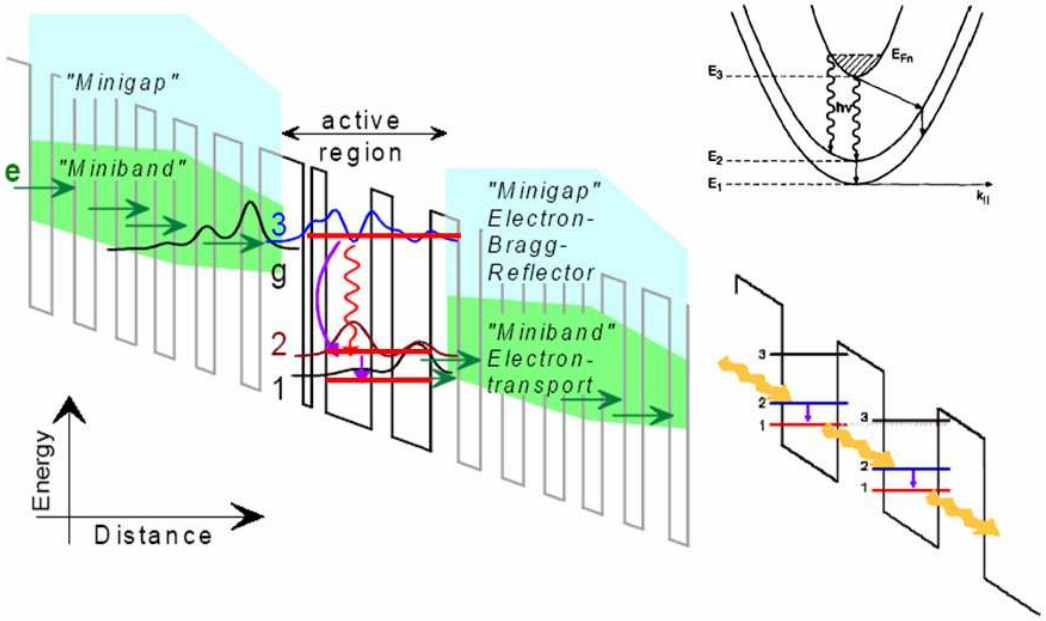

Figure 3. 19 Schematic of illustrating the principle of a quantum cascade laser (QCL) based on a multiple quantum-well structure. Top right: Schematic representation of the dispersion of the n=1,2,3 states parallel to the layers. The bottom of these subbands correspond to energy levels n=1,2 and 3 indicated in the left and the bottom right diagram. Bottom right: schematic of reduced conduction band energy diagram. [9]

When an external electric voltage is applied, electrons are driven by the electric field and inject from the left injector region into the active region through the minibands. Such minibands are the result of the periodicity of the multiple quantum wells in the injector region and are intentionally designed to be as high as the energy level 3, see **Figure 3. 19**. Thus the electrons can quickly tunnel into the level 3.

The active region design is based on an "anticrossed diagonal" scheme, where the wavefunction of the excited state of the laser transition (i.e. level 3) has a reduced overlap with the lower state (level 2). [11] The spatial separation between the wavefunctions is tailored so that it weakens the electron-optical phonon scattering processes, preventing a strong reduction of the dipole radiation. The radiation from level 3 to level 2 corresponds to the laser transition.

The energy separation between level 1 and 2 is deliberately designed to be approximately equal to that of a longitudinal optical (LO) phonon (e.g. 36 meV for GaAs). Thus the population in level 2 can be efficiently evacuated through the electron-phonon interactions. As a result, the population inversion between level 2 and 3 is realized. The electrons quenched by the phonons from level 2 to level 1 can tunnel into the next active region through the following minibands. Such cascade processes can then be repeated 20-100 times, generating a photon in each step as shown in the right bottom of **Figure 3. 19**.

The cascade effect makes it easy to achieve high power output from a QCL even when operated under CW mode. The output power of a QCL operating continuously atr room-temperature is normally a few milliwatts, sufficient for standard spectroscopic applications. By using thermoelectric (TE) cooling, the output power can be increased to hundreds of milliwatts. In contrast, to achieve such output power with a leadsalt diode laser requires use of the cryogenic cooling. In pulsed operation, one can even achieve peak powers at the level of watts from a QCL at room temperature.

3.3. Spectroscopy

3.3.1. Optical emission spectroscopy, Absorption spectroscopy and Laser spectroscopy

Spectroscopy is the study of the interaction between radiation and matter. It is very important in providing both the qualitative and quantitative analysis of materials. Most spectroscopic methods can be divided into two classes: Optical emission spectroscopy (OES), which measures the radiation from target materials, and absorption spectroscopy (AS), which measures the loss when light is passed through a substance.

OES is a passive method, sensitive to the upper (excited) states involved in a transition. In non-equilibrium plasma, the gas temperature is not so high, and excitation processes are dominated by electron impact. OES thus is much more sensitive to electron characteristics (n_e and T_e). Though difficult to give a quantitative result, OES in some special cases, like actinometry, can also give qualitative information about species concentration. Interpretation of the OES results is usually more difficult and depends strongly on the specific objects studied. But this method is easy to implement experimentally. From the measured intensity, the OES can provide indirect information about species concentration. Besides this indirect information about species concentration, line ratios can sometimes be used to estimate the electron temperature. [12-14] In addition, the measured Doppler linewidth of emission lines can be used to determine the gas temperature. Stark broadened linewidths can also be used to estimate the electron density.

Absorption spectroscopy is an active method, sensitive to the lower level in the transition of interest. It is a good way to measure the concentration of some “dark species” like ground states or metastable states, quantitatively. In non equilibrium plasma, the ground states of the active species are dominated by thermal reactions,

AS is thus a sensitive method to investigate thermal chemistry. The explanation of AS results is generally easier and more direct than in the case of OES. But the experimental setup for AS is more complicated.

Laser spectroscopy is a special spectroscopic method that involves using a laser as the light source. The unique features of lasers, such as monochromaticity, narrow line width, high directionality, polarized, etc make laser spectroscopy advantageous in terms of in resolution and sensitivity.

3.3.2. Actinometry

Actinometry is an OES based method that allows estimation of the relative concentration of species in their ground states. This method was first introduced by Coburn et al in 1980's. [15] They measured the relative concentration of F atoms by using one Ar line (750.4 nm) and one F line (703.7 nm). The principle of actinometry is very simple, but the conditions required for its validity are very strict. Gicquel et al [ ] have given a very detailed discussion about this method and its validity as a means of diagnosing plasmas. Here, following their discussion, we make a brief introduction.

The actinometry method involves consideration of the excitation processes of two species: the species to be determined, X, and the actinometer. If these excitation processes meet the following requirements: [16]

(1) the trace amount of actinometer does not perturb the plasma;
(2) both species are excited to their radiative excited states mainly by a direct electron impact process;
(3) the excitation cross sections for these two species have the same shape and a similar threshold,

then the emission intensity ratio of these two species, I_X / I_{Act} can be linked to their concentration ratio by a very simple relationship

$$[X]/[Actinometer] = k\ I_X / I_{Act}\ . \qquad \text{(Eq.3. 104)}$$

Furthermore, if the quenching processes as well as all other processes for the loss of these excited states are negligible, the coefficient *k* can be a constant. Thus, the concentration of species X has a linear dependence on that of the actinometer.

3.3.3. Tuneable diode laser absorption spectroscopy

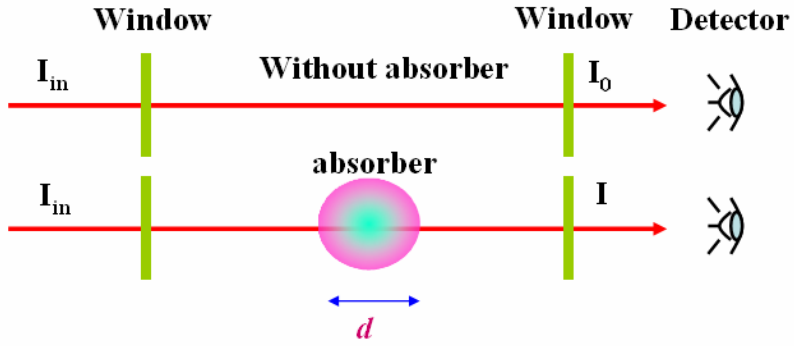

Figure 3. 20 General configuration of tuneable diode laser spectroscopy (TDLAS)

The general principle of tuneable diode laser absorption spectroscopy is shown in **Figure 3. 20**. According to the Beer-Lambert law,

$$I = I_0 \exp(-n\sigma d), \qquad \text{(Eq.3. 105)}$$

where I_0 is the detected transmission light intensity without absorber, I is the transmission intensity with absorber present. d is the effective absorption length of the absorber, σ is the absorption cross section.

Thus, the column density of the absorber is given by

$$D = nd = \frac{1}{\sigma}\ln\frac{I_0}{I}. \qquad \text{(Eq.3. 106)}$$

3.3.4. Cavity ring-down spectroscopy

3.3.4.1. History

Cavity ring-down spectroscopy (CRDS) is a highly sensitive multi-path laser absorption technique. It was first developed in the mid 1980s for the purpose of measuring the ultra high reflectivity of the mirrors. Then, in 1988, O'Keefe and Deacon [17] first demonstrated the application of CRDS as a spectroscopic technique,

by measuring the very weak $b^1\Sigma_g^+ \leftarrow X^3\Sigma_g^-$ transition of oxygen molecules with CRDS. After that, due to its impressive sensitivity and flexibility for measuring species under various environments, such as atmosphere, flames, plasma reactors, solutions, solids and solid surfaces, CRDS has developed quickly into a wide and fruitful field. [18-28]

The early CRDS studies involved using a pulsed tuneable laser source, e.g a dye laser pumped by a YAG laser working in pulsed mode; thus it is called pulsed-CRDS. The advantage of pulsed-CRDS is that the mode matching in this method is much simplified due to the broad Fourier-limited line widths of the laser pulse (normally in the range of several hundreds MHz to several GHz) in comparison with the free spectral range (FSR) of the longitudinal mode of the cavity formed by two highly reflective mirrors (about 150 MHz for a typical cavity of length 1m). However, like a double-side sword, the broad line width of the laser pulse also limits the resolution of pulsed-CRDS. In addition, the laser system used in pulsed-CRDS is normally bulky and expensive, and can not be scanned with a fast speed. CW-CRDS, based on using a single mode tuneable diode laser (SMTDL), can overcome all of the drawbacks of pulsed-CRDS. The CW- SMTDLs normally have a linewidth of several hundreds kHz to several MHz, which is much narrower than the FSR of the cavity longitude mode (but still much wider than the line width of each longitudinal mode of the high finesse cavity, e.g., for a 1m cavity bounded by mirrors with reflectivity R=0.999, the linewidth of a longitudinal mode is ~50kHz). Thus mode matching has to be considered carefully. The first demonstration of applying CW-CRDS to the measurement of molecular absorption spectra was reported by Engeln et al. [19] However, a CW ring dye laser was used in that work. The first cw-CRDS demonstration using a SMTDL was given by Romanini et al in 1997. [24] Details regarding the configuration of CW-CRDS can be found in these papers. Another trend in the development of CRDS is the extension of the usable wavelength range from visible, ultraviolet, near infrared to the mid infrared today with the help of

QCLs. [29]

Traditional CRDS is generally limited to relatively narrow wavelength scans. There are limits imposed by the available laser sources, CRDS mirrors and detectors. New inventions in broad band CRDS technology aim to solve this problem. Some interesting works in this field include: Prism CRDS [30] and broadband CRDS based on optical frequency comb. [31]

Besides those mentioned above, several variations of CRDS are also being developed in different groups. These include polarization dependent CRDS (PDCRDS), [19] phase shift CRDS (PS-CRDS). [32]

All of the above merely serve to confirm one truth: Today, CRDS is becoming an even more and more active and exciting research field!

3.3.4.2.Principles of CRDS

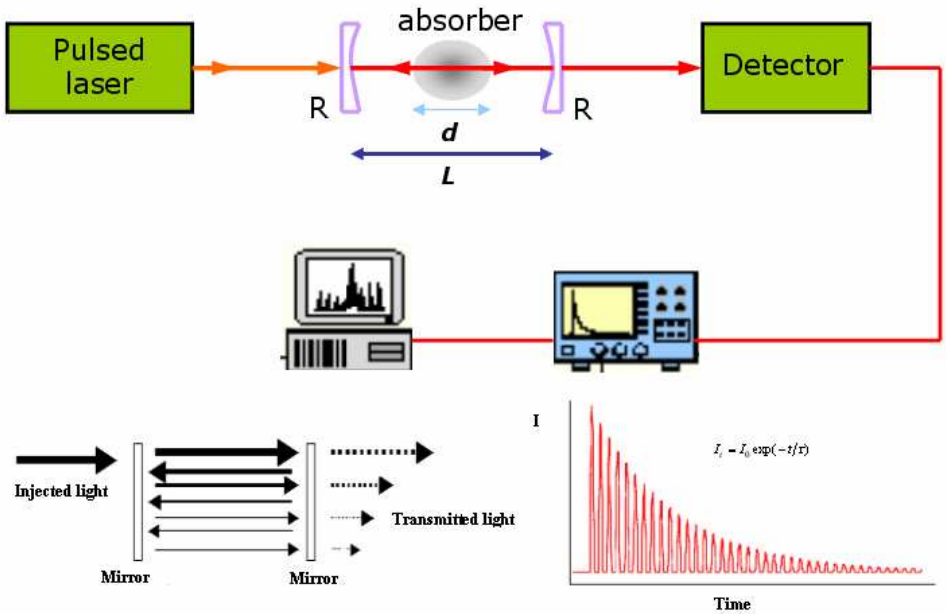

Figure 3. 21 General configuration of CRDS and its principle

The principle of CRDS is very simple and can be illustrated through a typical pulsed-CRDS configuration as shown in **Figure 3. 21**: Using two highly reflective

mirrors, the injected laser beam can be trapped and will travel back and forth between these mirrors for thousands of times, making the absorption path length much longer than the single path. The transmission intensity as a function of time *t* is given by

$$I_T = I_0 \exp(-t/\tau) . \quad . \qquad \text{(Eq.3. 107)}$$

Here τ is the ring down time and in an empty cavity can be given by

$$\tau_0 = \frac{L}{c|\ln R|} \approx \frac{L}{c(1-R)} ; \quad \text{for } R\approx 1 \qquad \text{(Eq.3. 108)}$$

In a cavity with absorbing species, τ is modified such that

$$\tau \approx \frac{L}{c(1-R+\alpha d)} \quad \text{for } R\approx 1 \qquad \text{(Eq.3. 109)}$$

Here, *c* is speed of light, R is the reflectivity of the mirrors, *L* is the distance between the two mirrors, *d* is the effective path length of the absorbing species and α is the absorption coefficient, which can be written as

$$\alpha = n\sigma , \qquad \text{(Eq.3. 110)}$$

where *n* is the number density of absorbing species, and σ is its absorption cross section. The difference Δk of the decay rates for the cases of (i) empty cavity and (ii) absorbing medium present is given by

$$\Delta k = \frac{1}{\tau} - \frac{1}{\tau_0} = \frac{c(1-R+\alpha d)}{L} - \frac{c(1-R)}{L} = \frac{c\alpha d}{L} = \frac{nc\sigma d}{L} , \qquad \text{(Eq.3. 111)}$$

which is proportional to the density of absorbing species. Experimentally, the transmission intensity is measured as the function of time *t* and the decay rates were then calculated for both cases (without and with absorbing species). Finally, the absolute concentration *n* and the absolute column densities *D* of the absorbing species can be deduced using **Eq. 3.112** and **Eq. 3.113**.

$$n = \frac{L \cdot \Delta k}{c\sigma d} , \qquad \text{(Eq.3. 112)}$$

$$D = \frac{L \cdot \Delta k}{c\sigma}, \qquad \text{(Eq.3. 113)}$$

3.3.4.3. Cavity stability [33]

(1) *Gaussian beam*

A Gaussian beam travelling in free space can be characterized by a set of beam parameters, see **Figure 3. 22**.

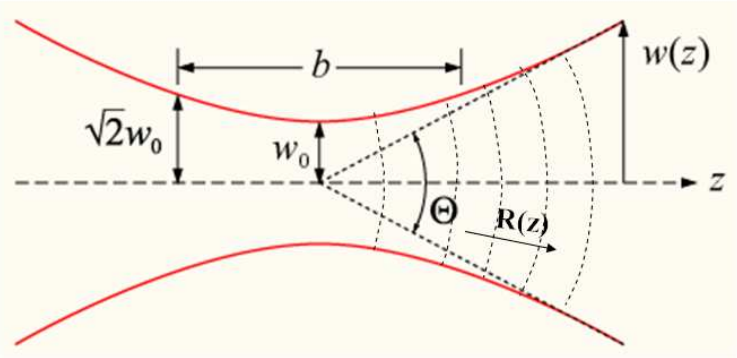

Figure 3. 22 A Gaussian beam in free space

The spot size (the radius of the beam) $w(z)$ is defined as the value at which the field amplitude drop to $1/e$. The minimum value w_0 along the beam axis is known as the *beam waist*. We define the origin of z axis at the beam waist. Assuming the beam has a spot size w_0 and a wave front radius of curvature R_0 at z=0, then the spot size at different z positions is given by

$$w(z) = w_0\sqrt{1+\left(\frac{z}{z_0}\right)^2}. \qquad \text{(Eq.3. 114)}$$

where

$$z_0 = \frac{\pi w_0^2}{\lambda} \qquad \text{(Eq.3. 115)}$$

is called the Rayleigh range and λ is the wavelength. The beam width at Rayleigh range is

$$w(\pm z_0) = \sqrt{2}w_0 \qquad \text{(Eq.3. 116)}$$

The distance between two z_0 points is known as the confocal parameter or the depth of focus of the beam.

$$b = 2z_0 = \frac{2\pi w_0^2}{\lambda} \qquad \text{(Eq.3. 117)}$$

The wave front radius of curvature R(z) can be written in terms of the Rayleigh range:

$$R(z) = z + \frac{z_0^2}{z} \qquad \text{(Eq.3. 118)}$$

The beam divergence is defined by the angle between the asymptotic line of $w(z)$ when $z>>z_0$ and the central axis of the beam.

$$\theta \approx \frac{\lambda}{\pi w_0} \qquad \text{(Eq.3. 119)}$$

and

$$\Theta = 2\theta . \qquad \text{(Eq.3. 120)}$$

(2) *Cavity stability*

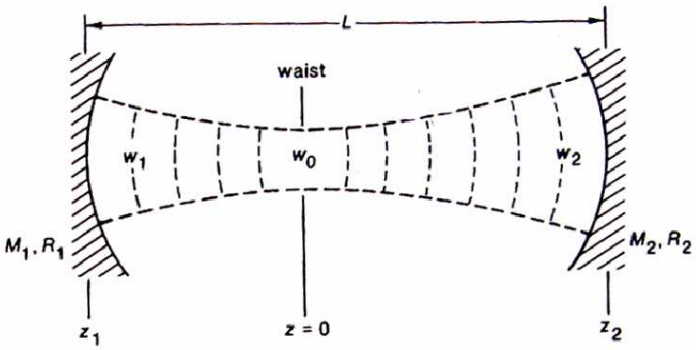

Figure 3. 23 A Gaussian beam in a cavity

Now consider a Gaussian beam propagating within an optical cavity formed by two highly reflective concave mirrors M_1 and M_2 which are separated by a distance L. The radii of curvature of these two mirrors are R_1 and R_2. Thus the focal lengths of these two mirrors are $R_1/2$ and $R_2/2$. Assume the waist of the Gaussian beam is at z=0, and that the two mirrors are at z_1 (which is negative in **Figure 3. 23)** and z_2. We have

$$z_2 - z_1 = L \qquad \text{(Eq.3. 121)}$$

For a Gaussian beam TEM_{00} mode in the cavity, the wave front radius of curvature at

z_1 and z_2 is equal to the two mirrors curvatures R_1 and R_2, respectively. Thus we have

$$R(z_1) = z_1 + \frac{z_0^2}{z_1} = -R_1 \qquad \text{(Eq.3. 122)}$$

$$R(z_2) = z_2 + \frac{z_0^2}{z_2} = R_2 . \qquad \text{(Eq.3. 123)}$$

Two parameters g_1 and g_2 (called the resonator g parameters) are defined as follows

$$g_1 = 1 - \frac{L}{R_1}, \qquad \text{(Eq.3. 124)}$$

$$g_2 = 1 - \frac{L}{R_2} . \qquad \text{(Eq.3. 125)}$$

Combining **Eqs 3.122** to **3.126**, the Rayleigh range of a trapped Gaussian beam can be solved to yield

$$z_0^2 = \frac{g_1 g_2 (1 - g_1 g_2)}{(g_1 + g_2 - 2 g_1 g_2)^2} L^2 \qquad \text{(Eq.3. 126)}$$

and the positions of two mirrors relative to the position of beam waist

$$z_1 = \frac{g_2 (1 - g_1)}{g_1 + g_2 - 2 g_1 g_2} L , \qquad \text{(Eq.3. 127)}$$

$$z_2 = \frac{g_1 (1 - g_2)}{g_1 + g_2 - 2 g_1 g_2} L . \qquad \text{(Eq.3. 128)}$$

From **Eq.3.116** and **3.126**, the spot size at the waist position is given by

$$w_0^2 = \frac{L\lambda}{\pi} \sqrt{\frac{g_1 g_2 (1 - g_1 g_2)}{(g_1 + g_2 - 2 g_1 g_2)^2}} . \qquad \text{(Eq.3. 129)}$$

Then, using **Eq 3.114**, the spot size at the ends of the cavity can be determined as

$$w_1^2 = \frac{L\lambda}{\pi} \sqrt{\frac{g_2}{g_1 (1 - g_1 g_2)}} , \qquad \text{(Eq.3. 130)}$$

$$w_2^2 = \frac{L\lambda}{\pi} \sqrt{\frac{g_1}{g_2 (1 - g_1 g_2)}} , \qquad \text{(Eq.3. 131)}$$

which yields real and finite solutions for w_1 and w_2 provided

$$0 \le g_1 g_2 \le 1 .$$

In another words, only when the above inequality is fulfilled, the cavity is stable. Such cavity stability conditions are shown as the shaded region in **Figure 3. 24**. Several important cavity configurations are also marked in this figure.

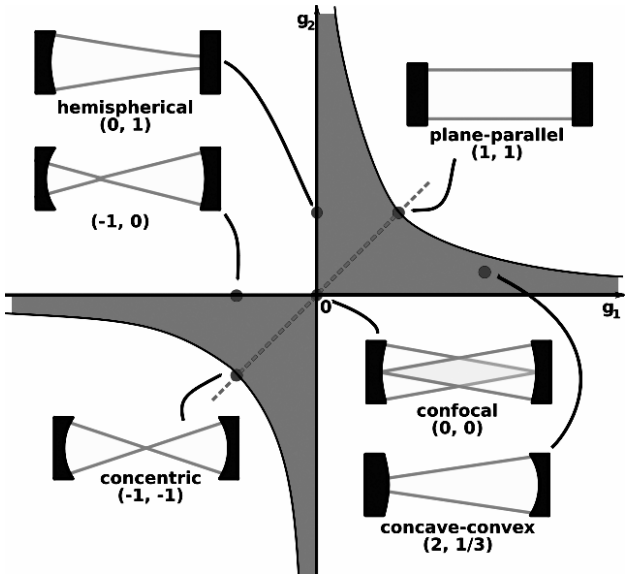

Figure 3. 24 A cavity stability diagram. The shadow region represents the stable cavity.

3.3.4.4.Mode and mode matching

The frequencies of the stable cavity modes can be found by applying standing wave condition that the total round trip phase shift must be an integer multiple of 2π, i.e.

$$\frac{2\pi\nu L}{c} - (n+m+1)\cos^{-1}\sqrt{g_1 g_2} = q\pi \text{ , } q, m, n=0, 1, 2\ldots \qquad \text{(Eq.3. 132)}$$

Such determined resonance frequencies are as follows

$$\nu = \nu_{qnm} = \left[q + (n+m+1)\frac{\cos^{-1}\sqrt{g_1 g_2}}{\pi} \right] \times \frac{c}{2L} . \qquad \text{(Eq.3. 133)}$$

The *q* parameter represents the longitudinal mode numbers, and *n*, *m* represent the transverse mode numbers. The frequency spacing between two adjacent longitude modes

$$\Delta\nu = \frac{c}{2L} \qquad \text{(Eq.3. 134)}$$

is known as the free spectral range (FSR). For a cavity of length 1m, the FSR is around 150 MHz (0.005 cm^{-1}). The laser pulse linewidth is normally several GHz (0.05-0.1 cm^{-1}). So without any special attention, the laser pulse can be easily

coupled into the cavity.

For the transverse mode, if the cavity is perfectly aligned, only the lowest order transverse mode, TEM_{00} is excited. This mode is cylindrical symmetric about the axis. However, if there is a small misalignment with the mirrors, other higher order transverse modes can also be excited in the cavity. These higher modes have different cavity losses from TEM_{00}, due to the different light path and different diffraction losses. This will distort the ring down decay curve. The different transverse modes can also mix with each other (mode beating), leading to a modulation of the output intensity. All these effects conspire to limit the sensitivity of CRDS.

Several methods for optimizing mode matching in pulsed-CRDS have been reported, such as using a CCD camera to monitor the different spatial mode patterns, (see **Figure 3. 25)**, or using a fast detector to monitor the transverse mode beating. [22, 34, 35] Another simpler and more interesting method has been proposed by Lee et al, [36] where they inserted a pinhole aperture behind the exit CRDS mirror and then monitor an audio frequency oscillation in the fitted residual. Such modulation originates from the non-degenerate transverse mode beating, see **Figure 3. 26**, and its frequency is sensitive to cavity alignment.

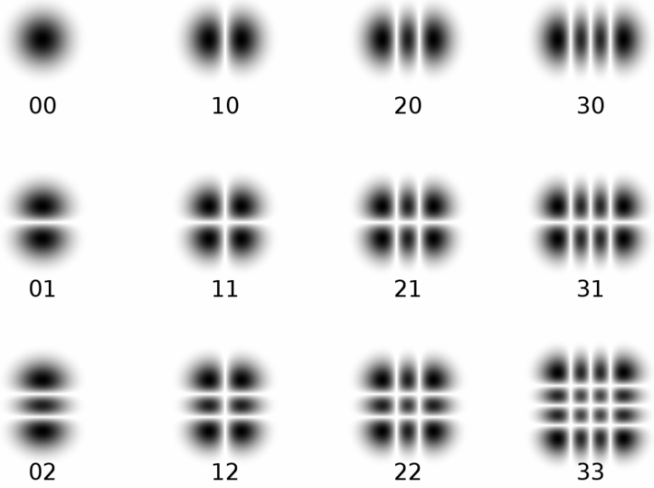

Figure 3. 25 Intensity patterns of several low order TEM_{mn} modes

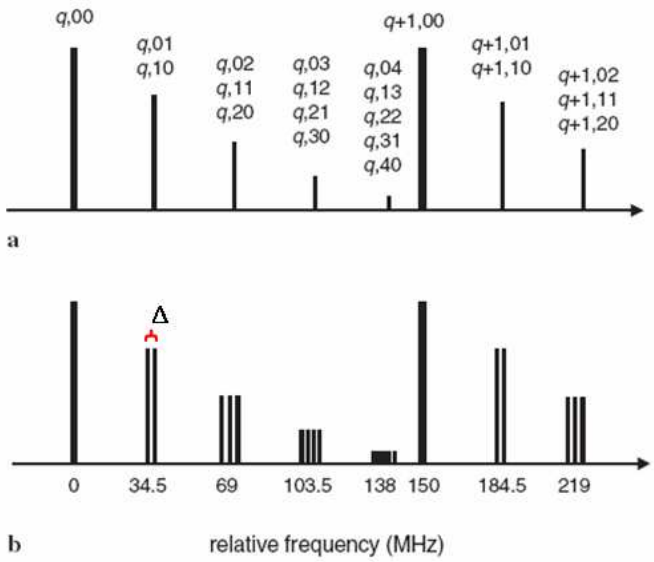

Figure 3. 26 The spectral structure of the cavity eigenmodes as given for a stable, symmetric two-mirror cavity with l = 1m and y = 4m: (a) when the transverse modes are degenerate; (b) when the transverse modes are non-degenerate. The cavity eigenmodes are denoted by an index set (q, m, n) with q representing the node number of the longitudinal mode and (m+n) the total node number of the transverse mode. The spacing Δ corresponds to the modulation frequency, which is strongly dependent on the cavity alignment.

3.3.4.5. Sensitivity

The sensitivity of CRDS is given by

$$\alpha d_{eff} = (1-R)\left(\frac{\Delta\tau}{\tau}\right) \qquad \text{(Eq.3. 135)}$$

α is the absorption coefficient, d_{eff} is the effective absorption path length, R is the reflectivity of the mirrors, t is the ring-down time, and Δτ is the fluctuation of the ring-down time. In our experiments, the mirrors reflectivity is >0.9997. Δτ/τ is around 0.02~0.06, depending on the different mirrors and the wavelengths at which spectra are measured. Thus the detectable absorption limit is

$$\left(\alpha d_{eff}\right)_{\min} \sim 3\times10^{-6} - 1.8\times10^{-5} \qquad \text{(Eq.3. 136)}$$

Since

$$\alpha d_{eff} = n\sigma d_{eff} = D\sigma \qquad \text{(Eq.3. 137)}$$

(n, D are species number density and column density respectively), the detectable

limit for the species number densities or column densities is not only determined by detectable absorption limit but also influenced by the absorption cross section. For example, the $C_2(\upsilon=0, J)$ column densities measured in our plasma are around 10^9 cm^{-2}, while the estimated H(n=2) column density is around 10^8 cm^{-2}. However, due to the large absorption cross section, the H(n=2) absorption line measured by CRDS is still quite strong.

3.4. References

[1] A. Szabo and N. S. Ostlund, *Modern Quantum Chemistry: Introduction to Advanced Electronic Structure Theory*, (Dover Publications, 1996).

[2] W. Koch and M. C. Holthausen, *A Chemist's Guide to Density Functional Theory*, (Wiley - VCH, 2001).

[3] C. N. Banwell and E. M. McCash, *Fundamentals of Molecular Spectroscopy*, (McGraw-Hill International (UK) Limited, 1994).

[4] G. Herzberg, *The Spectra and Structures of Simple Free Radicals*, (Cornell University Press, 1971).

[5] C. J. Rennick, R. Engeln, J. A. Smith, *et al.*, *J. Appl. Phys.*, **97** (2005) 113306.

[6] H. H. Telle, A. G. Urena and R. J. Donovan, *Laser Chemistry - Spectroscopy, Dynamics and Applications*, (John Wiley & Sons, Ltd, 2007).

[7] W. Demtröder, *Laser Spectroscopy - Basic Concepts and Instrumentation*, (Springer, 2003).

[8] R. N. Hall, G. E. Fenner, J. D. Kingsley, *et al.*, *Phys. Rev. Lett.*, **9** (1962) 366 .

[9] J. Faist, F. Capasso, D. L. Sivco, *et al.*, *Science*, **264** (1994) 553.

[10] K. Barnham and D. Vvedensky, *Low-Dimensional Semiconductor Structures*, (Cambridge University Press, 2001).

[11] C. Gmachl, F. Capasso, D. L. Sivco, *et al.*, *Rep. Prog. Phys.*, **64** (2001) 1533.

[12] I. H. Hutchinson, *Principles of Plasma Diagnostics*, (Cambridge University Press, 1987).

[13] M. V. Malyshev and V. M. Donnelly, *J. Vac. Sci. Technol. A*, **15** (1997) 550.

[14] Z. D. Kang and Y. K. Pu, *Chin. Phys. Lett.*, **19** (2002) 1139.

[15] J. W. Coburn and M. Chen, *J. Appl. Phys.*, **51** (1980) 3134.

[16] A. Gicquel, M. Chenevier, K. Hassouni, *et al.*, *J. Appl. Phys.*, **83** (1998) 7504.

[17] A. O'Keefe and D. A. G. Deacon, *Rev. Sci. Instrum.*, **59** (1988) 2544.

[18] M. D. Wheeler, S. M. Newman, A. J. Orr-Ewing, *et al.*, *J. Chem. Soc., Faraday Trans.*,, **94** (1998) 337.

[19] R. Engeln, G. Berden, E. van den Berg, *et al.*, *J. Chem. Phys.*, **107** (1997)

4458.

[20] R. Engeln, G. Berden, R. Peeters, *et al.*, *Rev. Sci. Instrum.*, **69** (1998) 3763.

[21] I. Labazan and S. Milosevic, *Chem. Phys. Lett.*, **352** (2002) 226.

[22] J. Martin, B. A. Paldus, P. Zalicki, *et al.*, *Chem. Phys. Lett.*, **258** (1996) 63.

[23] D. Romanini, A. A. Kachanov, N. Sadeghi, *et al.*, *Chem. Phys. Lett.*, **264** (1997) 316.

[24] D. Romanini, A. A. Kachanov and F. Stoeckel, *Chem. Phys. Lett.*, **270** (1997) 538.

[25] J. J. Scherer, D. Voelkel, D. J. Rakestraw, *et al.*, *Chem. Phys. Lett.*, **245** (1995) 273.

[26] C. Wang, S. P. Koirala, S. T. Scherrer, *et al.*, *Rev. Sci. Instrum.*, **75** (2004) 1305.

[27] P. Zalicki and R. N. Zare, *J. Chem. Phys.*, **102** (1995) 2708.

[28] G. Berden, R. Peeters and G. Meijer, *Int. Reviews in Physical Chemistry*, **19** (2000) 565.

[29] J. Manne, O. Sukhorukov, W. Jäger, *et al.*, *Appl. Opt.*, **45** (2006) 9230.

[30] J. Dudek, K. Lehmann, P. Rabinowitz, *et al.*, *Semiconductor instrumentation*, (2002) 32.

[31] M. J. Thorpe, K. D. Moll, R. J. Jones, *et al.*, *Science*, **311** (2006) 1595.

[32] R. Engeln, G. von. Helden, G. Berden, *et al.*, *Chem.Phys.Lett*, **262** (1996) 105.

[33] A. E. Siegman, *Lasers*, (University Science Books, 1986).

[34] D. B. Atkinson and J. W. Hudgens, *J. Phys. Chem. A*, **101** (1997) 3901.

[35] J. T. Hodges, J. P. Looney and R. D. von. Zee, *J. Chem. Phys.*, **105** (1996) 10278.

[36] D.-H. Lee, Y. Yoon, B. Kim, *et al.*, *Appl. Phys. B*, **74** (2002) 435.

Chapter 4 QCL study of the gas phase chemistry in Ar/H_2/hydrocarbon plasmas in a microwave reactor used for diamond CVD

4.1. Introduction

Ar/H_2/hydrocarbon gas mixtures are the most commonly used feed stock in diamond chemical vapour deposition. The complex chemical processes occurring during CVD provide a lot of interesting questions, challenging both our theoretical knowledge and the experiment techniques. One such question is how the C_1H_x species ($x \leq 4$, e.g. CH_4, CH_3 etc) and C_2 species (like C_2H_2, C_2 etc) interconvert between one another. For example, how do CH_4 and C_2H_2 (the most stable C_1 and C_2 species) interconvert? After more than 15 years of study, the important role of H atoms in initiating reactions and producing radicals is now widely accepted. [1-3] In the traditional reaction scheme known today, for example, starting from CH_4, a series of H-abstraction reactions lead to generation of radicals like CH_3, CH_2, CH, and C atoms as shown in **Figure 4. 1** (following the arrows on the left hand side). Self-reaction between the resulting CH_{x-1} radicals can result in the production of C_2H_y ($y \leq 6$) species. The resulting C_2H_y species also react with H atoms, yielding more species like C_2H_5, C_2H_4, C_2H_2 and C_2 etc (see **Figure 4. 1**). This scheme paves the way for efficient conversion of CH_4 to C_2H_2. However, the analogous gas-phase processes for creating C_1H_x species from acetylene are less well established. Nevertheless, both CH_4 and C_2H_2 have been observed (e.g. by mass spectrometry [4]) in diamond growing plasmas, irrespective of whether methane or acetylene is used as the carbon source gas. Thus, a mechanism must exist that converts acetylene to methane efficiently!

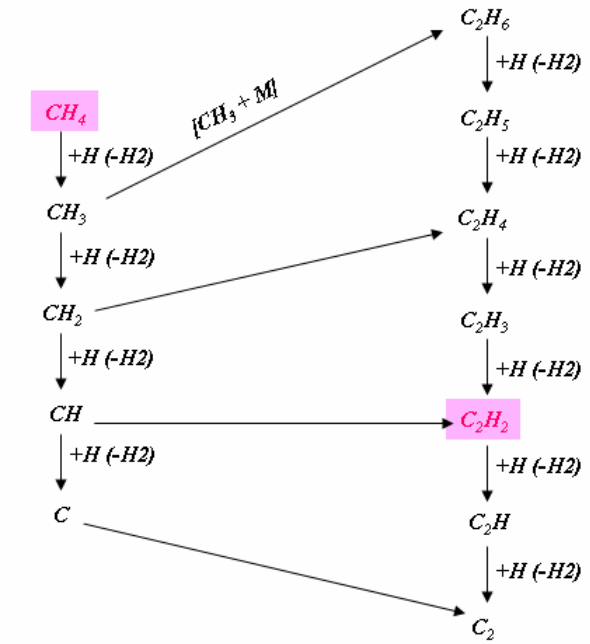

Figure 4. 1. Traditional reaction scheme for converting C_1H_x to C_2H_y species in diamond CVD: high T_{gas} and high [H].

One possible path suggested to solve the above puzzle involves heterogeneous chemistry, on the reactor walls or the growing diamond surface. [1] The acetylene is assumed to pyrolyze on such surfaces, and the resulting radicals form graphitic carbon films on the walls or the diamond surface. These films are then etched by hydrogen atoms, yielding gas phase species like CH_3. [5]

Another possible solution, proposed by Ashfold et al in 2001, [2] invokes a sequence of H-atom addition steps to C_2H_2, followed by C_2H_y to C_1H_x dissociation (follow the blue arrows in **Figure 4. 2**). Such reactions are unlikely at high gas temperatures, but become favourable when the temperature is low and the hydrogen concentration is high. [2]

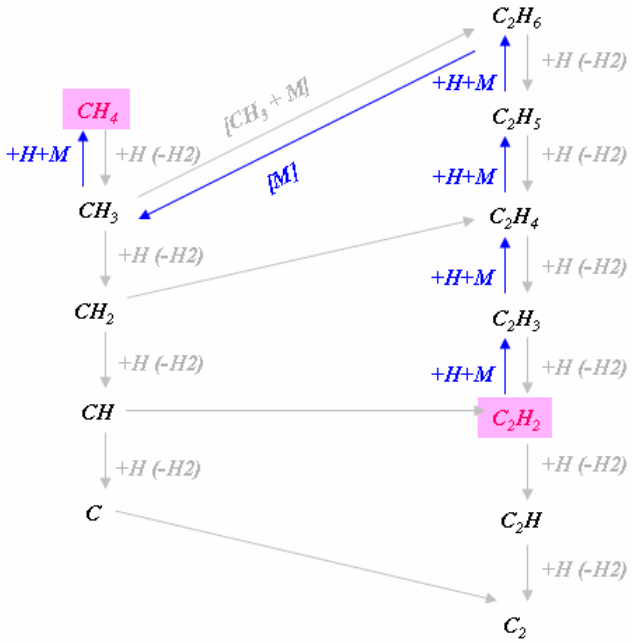

Figure 4. 2. Proposed reaction scheme for converting C_2H_y to C_1H_x species in diamond CVD [2]: high [H] but lower T_{gas}.

If the inter-conversion between C_1 and C_2 species is sufficiently fast, one would expect not only that the equilibrium gas mixture but also the eventual plasma should be relatively insensitive to the choice of hydrocarbon feedstock gas. This assumption has been tested further in the following experiments by choosing different hydrocarbon feedstock gases and by profiling several different species in the different plasmas.

4.2. Experimental setup

The microwave reactor used here is purpose-designed. It is built by Element Six Ltd. **Figure 4. 3** gives one schematic of the experimental setup. The microwave power is delivered along the rectangular waveguide. At the end of the waveguide it is converted into the TM_{01} mode and coupled into the cylindrical chamber. The chamber is divided into two parts by a centrally mounted quartz window. The bottom one is vacuum-sealed, and the plasma is formed in this chamber. When growing diamond, the pre-mixed $CH_4/Ar/H_2$ source gas mixture is fed through two opposed

inlets located at the top of the lower chamber. The microwave radiation partially ionizes and dissociates the gas mixture, 'active' species are produced, some of which react on the substrate (~3 cm in diameter) and lead finally to diamond film deposition on the substrate.

The measurements described here involve using a quantum cascade laser (QCL) to study behaviour of the "cold" (i.e. stable at low temperature) species CH_4 and C_2H_2. We have previously reported preliminary experiments of this type, [6] but now describe a more extensive, detailed and spatially resolved study.

In the QCL experiment, a pulsed QC laser (developed by Cascade Technologies Ltd) operating within the range 1274~1279 cm^{-1} is used to measure rovibrational transitions of CH_4 and C_2H_2 molecules. These transitions correspond to excitation of bending vibrational modes of these molecules. The QCL is cooled at -12°C to define the center wavenumber. The frequency is chirped by use of a long current pulse (2 μs) and the complete wavelength resolved spectrum is then obtained in one pulse. The QCL is said to be working in an intra-pulse mode. [7] The time interval of two pulses is 0.1 ms. The final spectrum is the average of 5000 wavelength scans. Thus the interval of two consecutively obtained spectra is 0.5 s. The fast chirp of the QCL allows time-resolved absorption measurements. The wavelength of the laser during scanning is calibrated by sending the beam through a Ge Etalon (free spectral range = 0.0481 cm^{-1}). To align the IR quantum cascade laser beam, a visible diode laser (6) is used as a guide. The laser beam then passes through two diamond windows (2) that bound the chamber. After that it is focused by a parabolic mirror (15) onto a fast Mercury Cadmium Telluride (MCT) detector (3) (cooled by liquid nitrogen) and finally is detected. All these optical components are mounted on a translatable bench which allows the whole system to be moved up and down by ~3 cm. This design allows us to measure the CH_4 and C_2H_2 column absorptions as a function of height above the substrate. In the following experiments, we first compare $CH_4/Ar/H_2$ and $C_2H_2/Ar/H_2$ plasmas.

For future reference, we define the discharge conditions of 150 torr total pressure, 1.5 kW input power, 40 sccm Ar, 25 sccm CH_4 (or 25 sccm carbon flow rate) and 500 sccm H_2 as the 'standard' condition, which corresponds to the best diamond growth condition in this reactor. When investigating effects of Ar and/or hydrocarbon flow rates, and variation away from the 'standard' conditions is compensated by a corresponding adjustment in the H_2 flow rate so that the total flow is always 565 sccm.

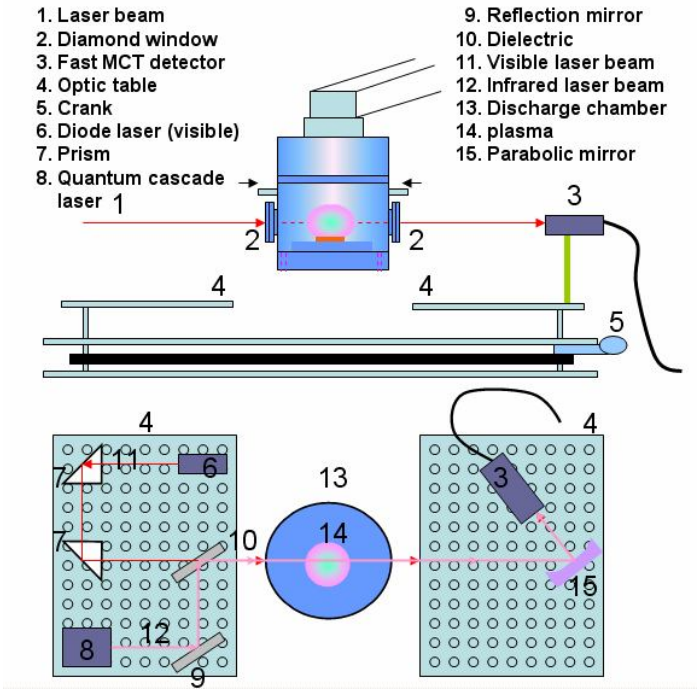

Figure 4. 3. Schematic of the QCL experimental setup

4.3. Results and discussion

4.3.1 MFC reading calibration

Our first aim is to compare $CH_4/Ar/H_2$ and $C_2H_2/Ar/H_2$ plasmas under the same carbon flow rate conditions. To do this, two prerequisites are needed: One is to check the purity of the CH_4 and C_2H_2 source gases, the other is to ensure that the mass flow

controllers (MFCs) provide accurately metered flow rates for CH_4 and C_2H_2.

The purities of the CH_4 and C_2H_2 gases used in this work are quoted (by the supplier) as 99.5% and 98.5%, respectively. In order to ascertain that the C_2H_2 in a CH_4/Ar/H_2 plasma or the CH_4 in a C_2H_2/Ar/H_2 plasma is not from impurities in the respective feedstock hydrocarbons, some CH_4 or C_2H_2 gas was introduced into the chamber without igniting the plasma, and the absorption spectra of CH_4 and C_2H_2 were measured by scanning the QC laser. The recorded spectra are shown in **Figure 4. 4(a)** and **(b)**. The corresponding transitions for those spectral lines are listed in details in **Table 4. 1** and **Table 4. 2**. Only CH_4 absorptions are observed when using CH_4 as the source gas, and only C_2H_2 absorptions when using C_2H_2. However, when the plasma is on, both CH_4 and C_2H_2 absorption lines can be observed (see **Figure 4. 4 (c)** and **(d)**), no matter which input hydrocarbon gas is used. This result clearly implies the existence of an efficient route for interconversion between CH_4 and C_2H_2! Note here, the C_2H_2* in **Figure 4. 4 (c)** and **(d)** is vibrationally excited C_2H_2 (e.g $C_2H_2(\nu_5=1)$). In the future, for convenience, we refer to it as "hot" acetylene and call the ground state acetylene, marked as C_2H_2 for convenience in **Figure 4. 4 (c)** and **(d),** "cold" acetylene. The red color C_2H_2* line in **Figure 4. 4 (c)** and **(d)** in fact is blended by two "hot" CH_4 lines (i.e. CH_4 $15F_{2\ 4}$ - $15F_{1\ 1}$ and $15F_{1\ 5}$ - $15F_{2\ 1}$).

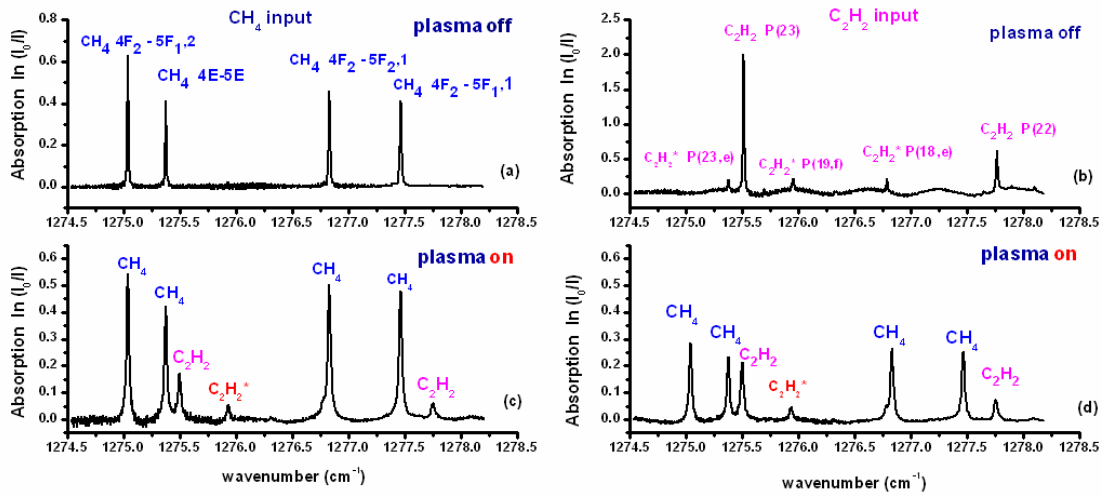

Figure 4. 4 Measured absorption spectra: (a) CH_4 input, without ignition of the plasma; (b) C_2H_2 input, without ignition of the plasma; (c) CH_4 input, with plasma on; (d) C_2H_2 input, with plasma on.

Table 4. 1 The wavenumber and transitions for the observed CH_4 absorption lines

Wavenumber (cm^{-1})	**Vibrational transition**	**Rotational transition**
1277.47335	4_0^1	$4F_2$-$5F_1$, 1
1276.84431	4_0^1	$4F_1$-$5F_2$, 1
1275.38678	4_0^1	4E-5E
1275.04168	4_0^1	$4F_2$-$5F_1$, 2
1275.94566	4_0^1	$15F_{2\ 4}$ - $15F_{1\ 1}$
1275.94776	4_0^1	$15F_{1\ 5}$ - $15F_{2\ 1}$

Table 4. 2 The wavenumber and transitions for the observed C_2H_2 absorption lines

Wavenumber (cm^{-1})	**Vibrational transition**	**Rotational transition**
1277.76105	$4_0^1 5_0^1(\Sigma_u^+ — \Sigma_g^+)$	P(22)
1276.79005	$4_1^2 5_0^1(\Pi_g — \Pi_u)$	P(18,*e*)
1275.95852	$4_0^1 5_1^2(\Pi_u — \Pi_g)$	P(19,*f*)
1275.51215	$4_0^1 5_0^1(\Sigma_u^+ — \Sigma_g^+)$	P(23)
1275.37459	$4_1^2 5_0^1(\Pi_u — \Pi_g)$	P(23,*e*)

Under plasma-free conditions, the number densities of CH_4 or C_2H_2 can be calculated from the measured line-integrated absorbances of individual lines in spectra such as those shown in **Figure 4. 4 (a)** and **Figure 4. 4 (b)**; these are shown as y in **Figure 4. 5** and **Figure 4. 6**. To convert the measured line-integrated absorbances (LIAs) of CH_4 and C_2H_2 to their number densities, we assume the gas is evenly distributed inside the chamber. The column length of line of sight l for the absorption measurements is 19.0±0.3 cm, the line strength data of CH_4 and C_2H_2 can be found from the HITRAN database. Then, by the following equation,

$$N_{CH_4/C_2H_2} = \frac{I_{ij}}{S_{ij} l}, \qquad \text{(Eq.4. 1)}$$

the number densities of CH_4 and C_2H_2 can be obtained. Note, here, I_{ij} is the measured line-integrated absorbance due to the transition of $i \rightarrow j$, S_{ij} is the corresponding line

strength found from HITRAN with T=297 K (room temperature).

On the other hand, knowing the pressure and assuming T_{gas} = 297 K, the CH_4 (and C_2H_2) number densities can also be calculated from the ideal gas law.

$$N = \frac{p}{kT} \qquad \text{(Eq.4. 2)}$$

Such obtained number densities of CH_4 and C_2H_2 are shown in **Figure 4. 5** and **Figure 4. 6** as x. The relationship between the densities calculated by these two methods should be $y=x$ in the ideal case. In our measurements, the data follow a straight line well with gradient close to 1. This result reveals the reading from the MFC has an error less than 1% for the gas CH_4, while for C_2H_2, the inaccuracy is within 5%. The relative larger error in C_2H_2 calibration is possibly because the C_2H_2 gas purity is not as high as CH_4.

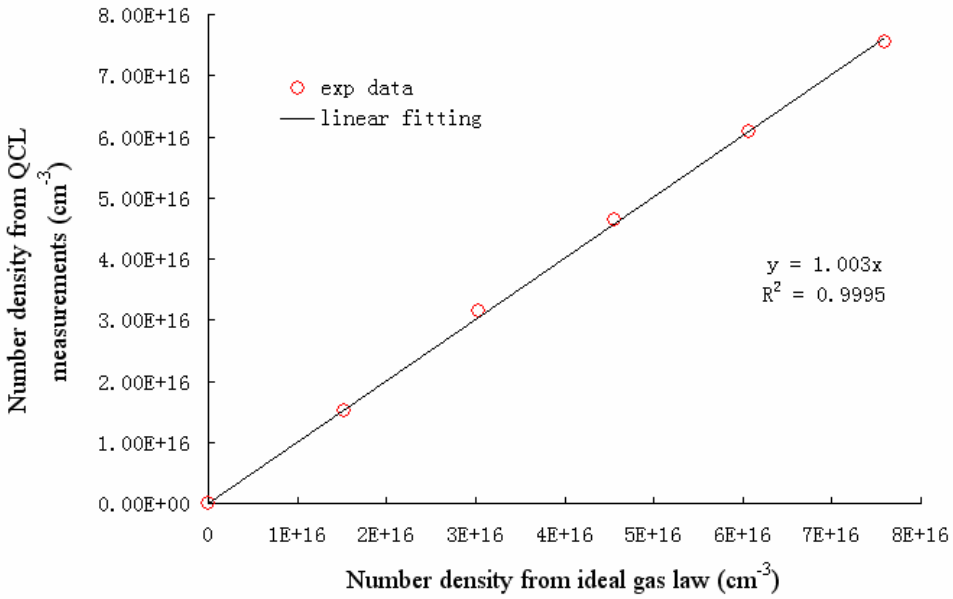

Figure 4. 5 Calibration of the MFC reading by CH_4

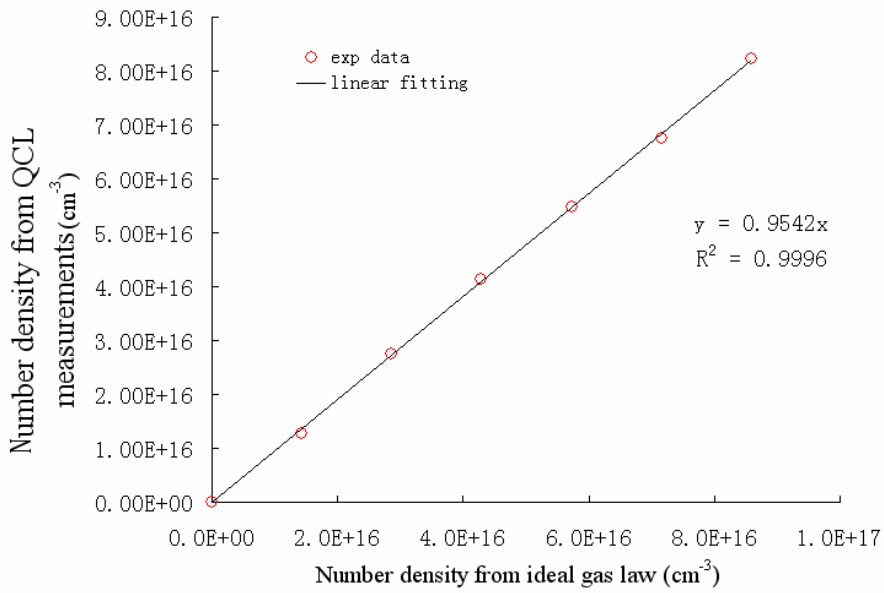

Figure 4. 6 Calibration of the MFC reading by C_2H_2

4.3.2 Vertical profiles

The wavenumber range scanned allows monitoring of the population in selected rotational levels within the ground vibrational state of CH_4 and C_2H_2. The detailed energy level diagram for C_2H_2 is shown in **Figure 4. 7.** The measured variations in CH_4 and C_2H_2 (i.e. C_2H_2 (v=0)) LIAs for both $CH_4/Ar/H_2$ and $C_2H_2/Ar/H_2$ plasmas with increasing distance *d* from the substrate surface are shown in **Figure 4. 8 (a)** and **(b)**. These profiles appear rather flat compared with those for the C_2 and CH radicals, and the excited H(n=2) atoms – see later (**Figure 5. 22** in Chapter 5) – where over a similar, or shorter, range of distances the column densities can change by an order of magnitude. This indicates that most of the measured absorption due to CH_4 and C_2H_2 is from molecules in the cold region, not in the plasma. This conclusion is quite reasonable because (i) the absorbers are "cold" stable species and the cold region spans a larger column length than the plasma, (ii) the total number density is inversely related to temperature and (iii) the line strength for the probed transitions decreases rapidly with increasing temperature (see **Figure 4. 9**). Another point to note from these figures is that relatively more CH_4 is observed when using a $CH_4/Ar/H_2$ gas mixture, while more C_2H_2 is measured in the case of the

$C_2H_2/Ar/H_2$ plasma. This can be explained as an excessive feedstock effect (the feedstock gases are not fully processed).

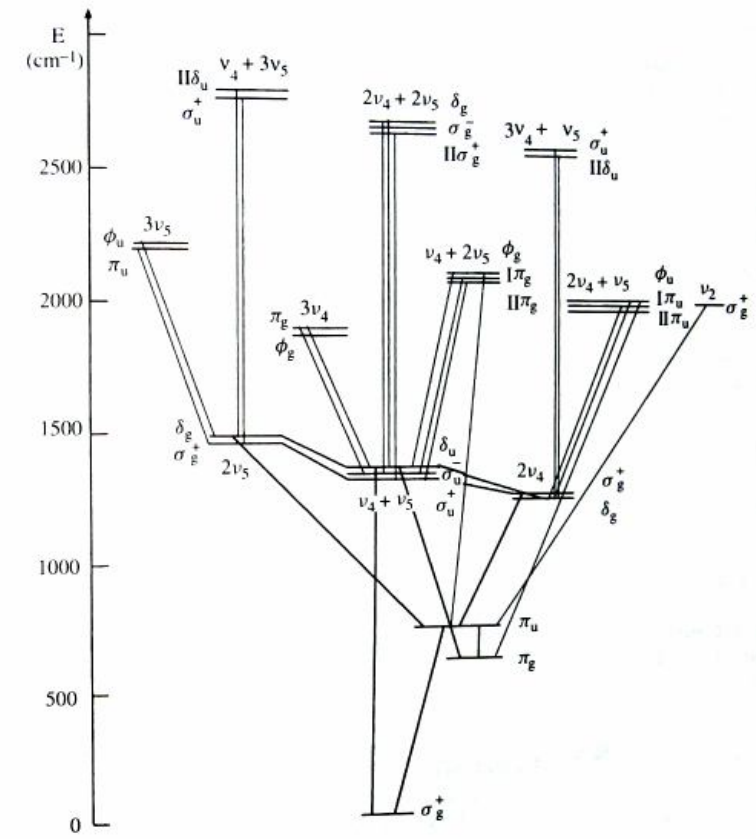

Figure 4. 7 Energy diagram showing low vibrational energy levels of C_2H_2 and the corresponding transitions [8]

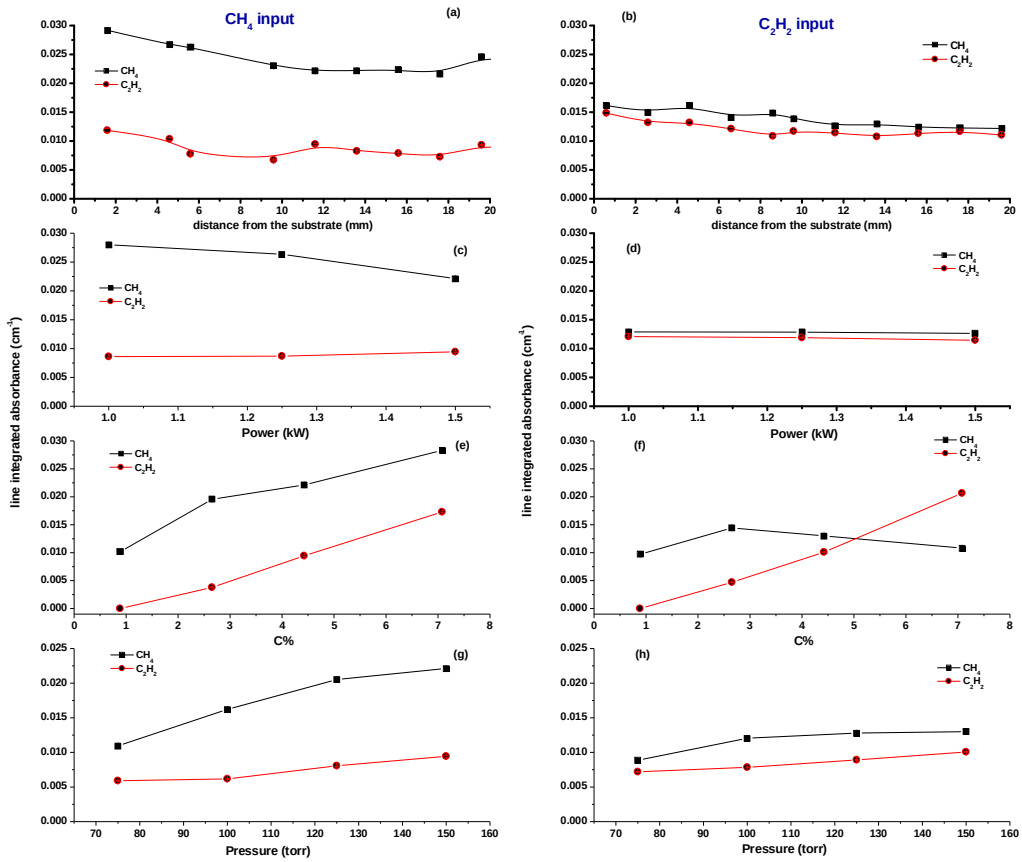

Figure 4. 8. Comparisons between $CH_4/Ar/H_2$ and $C_2H_2/Ar/H_2$ plasmas: (a) vertical (*d*) profiles in $CH_4/Ar/H_2$ plasma; (b)) vertical (*d*) profiles in $C_2H_2/Ar/H_2$ plasma; (c) effect of varying power in $CH_4/Ar/H_2$ plasma; (d) effect of varying power in $C_2H_2/Ar/H_2$ plasma; (e) effect of varying carbon flow rate in $CH_4/Ar/H_2$ plasma; (f) effect of varying carbon flow rate in $C_2H_2/Ar/H_2$ plasma; (g) effect of varying pressure in $CH_4/Ar/H_2$ plasma; (h) effect of varying pressure in $C_2H_2/Ar/H_2$ plasma. (a) and (b) are measured under standard conditions. For (c)-(h), all of the discharge parameters are as for the "standard" conditions except for the variable shown on the x-axis.

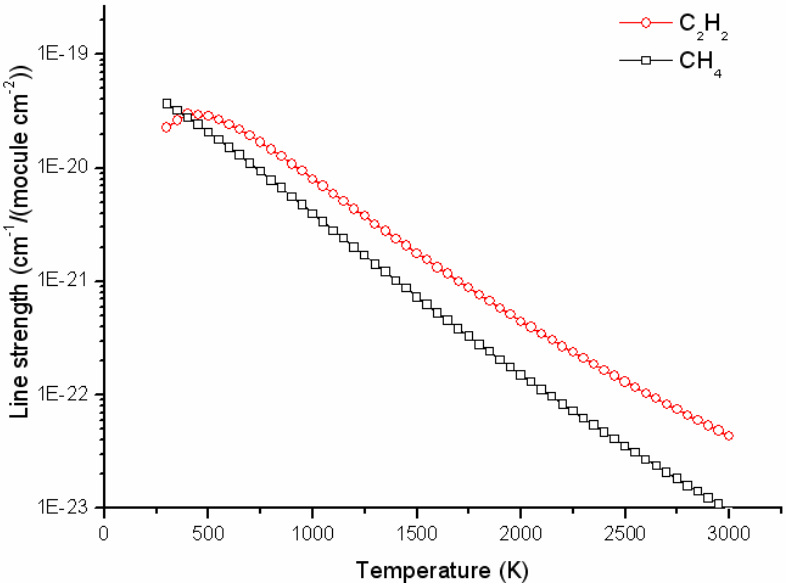

Figure 4. 9. Temperature dependent line strengths of rovibrational transitions used to monitor CH_4 and C_2H_2.

4.3.3 Power effect

In the case of the $CH_4/Ar/H_2$ plasma, increasing the supplied microwave power, *P*, results in a modest drop in CH_4 LIA and a small increase in C_2H_2 signal, see **Figure 4.8 (c)**. In a $C_2H_2/Ar/H_2$ plasma, in contrast, neither the CH_4 nor the C_2H_2 LIA shows any significant change upon increasing *P*, see **Figure 4.8 (d)**.

4.3.4 Carbon flow rate effect

From **Figure 4.8 (e)** and **(f)**, it can be seen that in both $CH_4/Ar/H_2$ and $C_2H_2/Ar/H_2$ plasmas, the C_2H_2 LIA shows very similar trends with increasing carbon flow rate, whereas the CH_4 LIA shows a different behaviour. Notice that the CH_4 in the $C_2H_2/Ar/H_2$ plasma must come totally from reaction while, in the $CH_4/Ar/H_2$ plasma, some of the measured CH_4 signal is likely to be from unprocessed feedstock gas (especially when the carbon flow rate is high) if the conversion of CH_4 to C_2H_2 is not 100% efficient. This likely explains the different behaviours observed at higher CH_4 flow rates.

We can estimate the 'excess' CH_4 by subtracting the CH_4 LIA measured using the

C_2H_2/Ar/H_2 plasma from that measured in the CH_4/Ar/H_2 plasma (under the same carbon flow rate conditions). The 'excess' CH_4 so obtained shows a linear dependence on CH_4 flow rate (see **Figure 4. 10**), and is essentially zero at low CH_4 flow rates (≤5 sccm). This suggests that at low carbon flow rates, the inter-conversion between CH_4 and C_2H_2 is so efficient that almost all of the CH_4 and C_2H_2 measured at small *d* come from reactions. This efficient inter-conversion also ensures that plasmas operating with CH_4/Ar/H_2 and C_2H_2/Ar/H_2 feedstock (and the same carbon flow rate) are essentially equivalent; even the values of CH_4, and C_2H_2 absorbance measured for the two input gas mixtures are very similar under low carbon flow rate conditions.

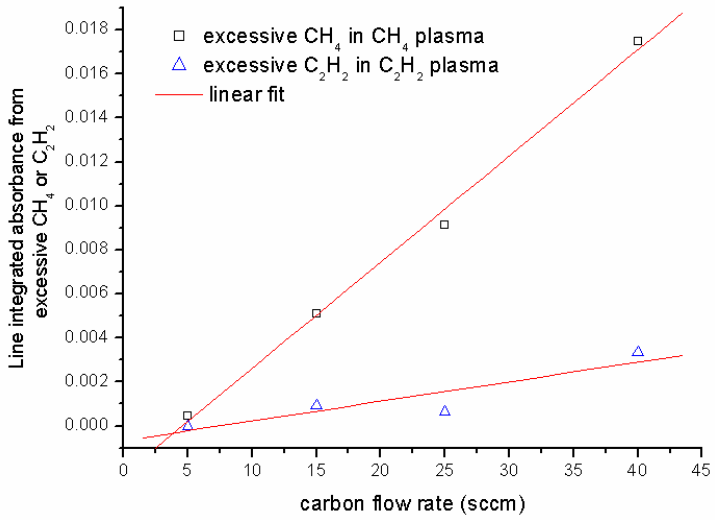

Figure 4. 10. Deduced 'excess' CH_4 in CH_4/Ar/H_2 plasma and 'excess' C_2H_2 in C_2H_2/Ar/H_2 plasma plotted as a function of carbon flow rate

In an analogous manner, we can estimate the 'excess' C_2H_2 LIA as a function of carbon flow rate when using a C_2H_2/Ar/H_2 plasma, by subtracting the measured C_2H_2 LIA from a CH_4/Ar/H_2 plasma from that found for the corresponding C_2H_2/Ar/H_2 (same %C, see **Figure 4. 10**). The 'excess' C_2H_2 derived in this way is much smaller than the 'excess' CH_4 found when using a CH_4/Ar/H_2 plasma. This may suggest that in our reactor $C_2H_2 \rightarrow CH_4$ conversion is more efficient than the conversion of $CH_4 \rightarrow C_2H_2$. The reaction schemes shown in **Figure 4. 1** and **Figure 4. 2** suggest a possible explanation for such behaviour. According to these

schemes, $C_2H_2 \rightarrow CH_4$ conversion is favoured in cool regions with sufficiently high [H], whereas $CH_4 \rightarrow C_2H_2$ is favoured by conditions of both high T_{gas} and high [H]. The 'cold' volume in our reactor is much larger than the volume of the plasma ball. So, simply on relative volume grounds, conversion from C_2H_2 to CH_4 might be expected to be the more efficient process.

4.3.5 Pressure effect

Figure 4.8 (g) and **(h)** show that the CH_4 and C_2H_2 (v=0) LIA in both $CH_4/Ar/H_2$ and $C_2H_2/Ar/H_2$ plasmas all increase upon increasing the total pressure, *p*. As shown in the analysis of OES experiments (see Chapter 6), such behaviour is characteristic of thermo-dominated chemistry. However, though the C_2H_2 LIA shows quite similar values and trends for both process gas mixtures, the CH_4 LIA behaves differently. As discussed above, this is because (when viewed along the whole column) $C_2H_2 \rightarrow CH_4$ conversion is more efficient than the reverse $CH_4 \rightarrow C_2H_2$ conversion.

4.3.6 Low carbon flow rate

The absorption spectra of $CH_4/Ar/H_2$ and $C_2H_2/Ar/H_2$ plasmas using carbon flow rates of 5 sccm are shown in **Figure 4. 11** and **Figure 4. 12**, respectively. As mentioned before, the inter-conversion between CH_4 and C_2H_2 is so efficient at these low carbon partial pressures that these two spectra are very similar. In both these figures, the C_2H_2(v=0) absorption is too weak to be recognized. But the absorptions due to the blended line, i.e. C_2H_2 (v_5=1) and CH_4 (v=0, J=15) are clearly shown. Careful examination of another absorption line which is due to C_2H_2(v_4=1) (not shown in these spectra) suggests that the population of to C_2H_2(v_4=1) appears to track the behaviour of the C_2H_2(v=0) level. This indicates that, under low carbon flow rate conditions, the main contribution to the blended absorption observed here is from hot CH_4 (v=0, J=15).

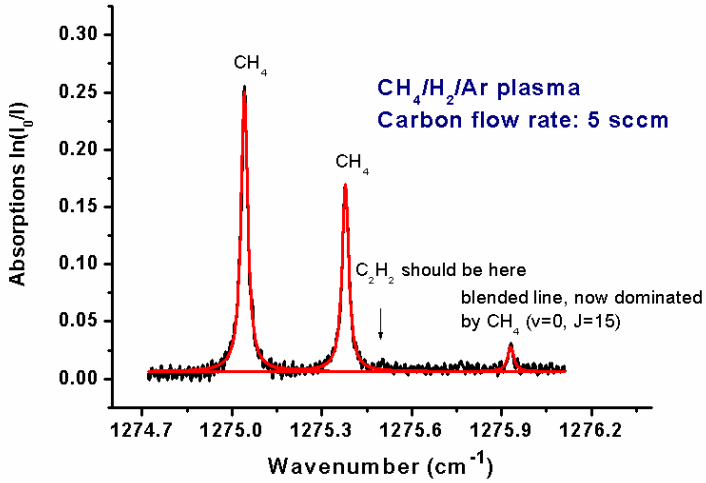

Figure 4. 11. Absorption spectrum in $CH_4/Ar/H_2$ plasma with 5 sccm carbon flow rate (i.e. 5 sccm CH_4)

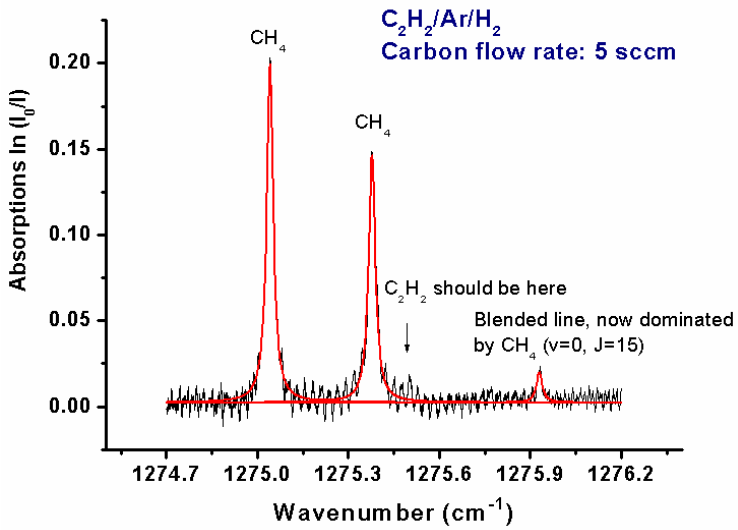

Figure 4. 12. Absorption spectrum in $C_2H_2/Ar/H_2$ plasma with 5 sccm carbon flow rate (i.e. 2.5 sccm C_2H_2)

4.3.7 Temporal behaviour

The temporal resolution of the QCL opens another window through which we can gain dynamical information about the plasma. The variations in CH_4, C_2H_2(v=0) and the blended C_2H_2 (v_5=1) and CH_4 (v=0, J=15) absorptions with time after introduction of CH_4 (or C_2H_2) into a pre-existing Ar/H_2 plasma are shown in **Figure 4. 13** (for CH_4 addition) and **Figure 4. 15** (for C_2H_2 addition). The time-dependent growth of the LIA of each of these species, and of C_2H_2 (v_4=1) line, as a function of

time is shown in **Figure 4. 14** (for CH_4 addition) and **Figure 4. 16** (for C_2H_2 addition). Several interesting phenomena are observed.

In **Figure 4. 13**, we notice that the CH_4 absorption lines appear first. (For the blended line, at this moment, the absorption is almost purely due to CH_4 (v=0, J=15)). Then, as time progresses, the C_2H_2 absorption line grows in and increases quickly. This behaviour is more clearly shown in **Figure 4. 14**. It can be seen that CH_4 appears first and reaches its steady state column absorption value faster and earlier than C_2H_2. The blended C_2H_2 (v_5=1) and CH_4 (v=0, J=15) absorptions shows an intermediate temporal behaviour in comparison with CH_4 and C_2H_2 (v=0), which implies that the early absorption is mainly due to CH_4 (v=0, J=15). But with time going on, the C_2H_2 (v_5=1) makes a more significant contribution to this absorption line. The C_2H_2 (v_4=1) absorption (not shown in the spectrum in **Figure 4. 13** and **Figure 4. 15**) exhibits a time dependence similar to that of ground state C_2H_2, showing itself not "contaminated" by any other CH_4 lines (see **Figure 4. 14** and **Figure 4. 16**). Consider the first few seconds after starting the CH_4 flow by switching the appropriate MFC (at t = 0). The gas is fed from the top of the reactor and has to flow/diffuse down to the region of the plasma ball and the viewing column. The carbon partial pressure in the viewing region will thus gradually rise from zero (at t = 0) and, at early times, will be low – i.e. similar to the situation prevailing at low carbon flow rates (recall **Figure 4. 11** and **Figure 4. 12**). In the present, time-dependent, studies, any carbon source gas introduced into the pre-existing Ar/H_2 plasma first encounters a region of high [H] and moderate T_{gas}, and the equilibria will shift towards CH_4 (**Figure 4. 2**). Hence the early time observation of CH_4. The monitored gas must have reached the viewing column – and thus the region of high T_{gas} associated with the plasma ball. In this region, the $CH_4 \leftrightarrow C_2H_2$ equilibria will shift back towards C_2H_2. Given the relatively slow turn over time of gas in the reactor (volume ~600 cm^3, gas flow rate ~565 sccm), these C_2H_2 products will diffuse away from the 'hot' region, and reach local thermal equilibrium with the surrounding gas and be detected by the laser beam. Hence the slower build up of the C_2H_2(v=0) absorption. That the time dependence of the

absorption due to $C_2H_2(v_4=1)$ molecules mimics that of $C_2H_2(v=0)$ molecules serves to suggest a local thermal equilibrium (LTE) is valid here.

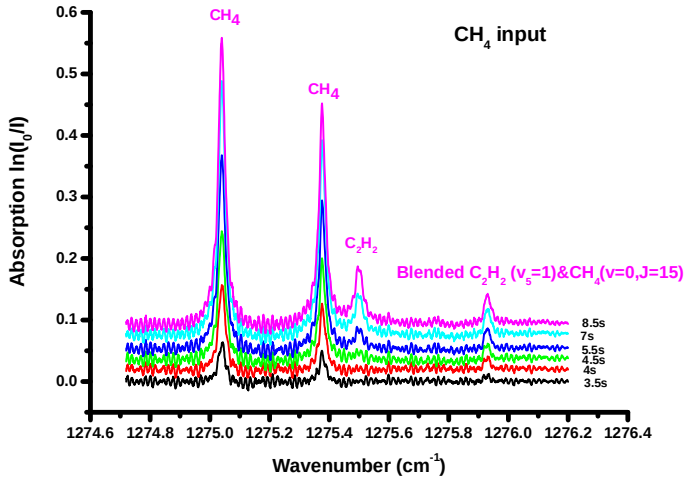

Figure 4. 13. CH_4, C_2H_2 (v=0) and blended C_2H_2 (v_5=1) & CH_4 (v=0, J=15) absorption spectra measured at different times *t* after CH_4 is introduced at the standard conditions of flow rate, pressure and power.

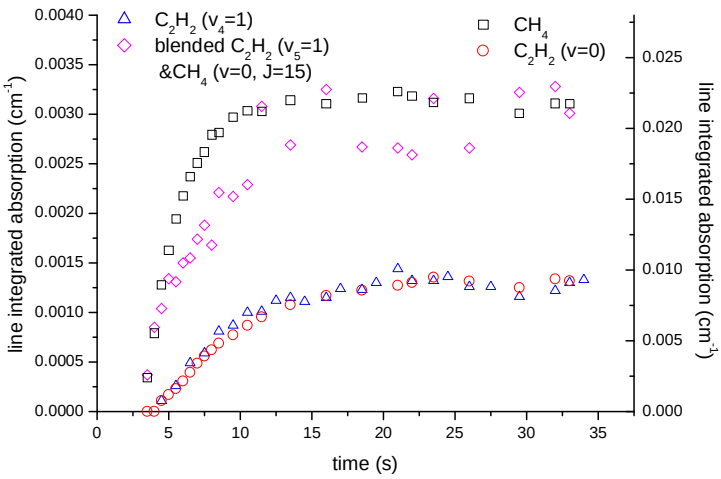

Figure 4. 14. Build up of CH_4, C_2H_2 (v=0), C_2H_2 (v_4=1) and blended C_2H_2 (v_5=1) & CH_4 (v=0, J=15) LIAs when CH_4 is added to a pre-existing Ar/H_2 plasma as a function of time (standard conditions are attained at long time).

The same phenomenon is observed when C_2H_2 is used as the input hydrocarbon gas, reflecting the efficiency of the $C_2H_2 \rightarrow CH_4$ conversion when the first C_2H_2 enters

the high [H], moderate T_{gas} conditions prevailing at the top of the reactor. These observations provide further evidence for the complete conversion of C_2H_2 to CH_4 at early *t*.

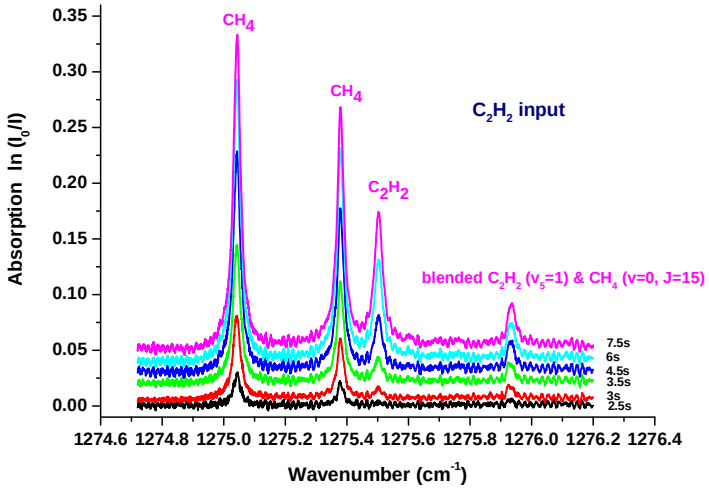

Figure 4. 15. CH_4, C_2H_2 (v=0) and blended C_2H_2 (v_5=1) & CH_4 (v=0, J=15) absorption spectra measured at different times *t* after C_2H_2 is introduced at the standard conditions of flow rate, pressure and power

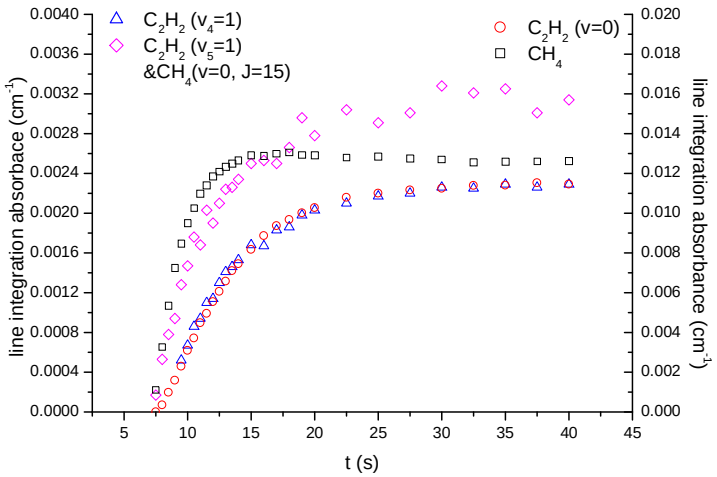

Figure 4. 16. Build up of CH_4, C_2H_2 (v=0), C_2H_2 (v_4=1) and blended C_2H_2 (v_5=1) & CH_4 (v=0, J=15) LIAs when C_2H_2 is added to a pre-existing Ar/H_2 plasma as a function of time (standard conditions are attained at long time).

4.3.8 Behaviour of other hydrocarbon feedstocks

Very similar trends in relative absorbance of CH_4, C_2H_2 and CH_4(v=0, J=15) are observed when using low carbon fractions of hydrocarbon source gases other than CH_4 and C_2H_2 – as illustrated for the cases of propane, C_3H_8 (**Figure 4. 17**), butane, C_4H_{10} (**Figure 4. 18**), ethane, C_2H_4 (**Figure 4. 19**) and propyne (methyl acetylene), C_3H_4 (**Figure 4. 20**). Only CH_4 absorption can be seen at low carbon flow rates. Similarly, time resolved absorption studies show that the CH_4 features always appear first and reach their asymptotic levels at earlier *t* than does the C_2H_2 absorption (see **Figure 4. 21** and **Figure 4. 22**). These observations imply that the chemistry occurring in these plasmas is essentially the same as for $CH_4/Ar/H_2$ and $C_2H_2/Ar/H_2$ plasmas; in all cases, at low carbon mole fractions and/or at early *t* the input feedstock hydrocarbon must be converted quantitatively to CH_4 and the chemistry then evolves as discussed above when CH_4 was used as the source hydrocarbon. The studies with propyne reinforce this view. Prior to igniting the plasma, strong absorptions from the $2\nu_9$ band [9] of C_3H_4 can be observed (**Figure 4. 23**) but, once the plasma is on, these absorptions totally disappear and only CH_4 and C_2H_2 absorption lines are seen. Such observations serve to confirm the view that, at low carbon flow rates (e.g. 5 sccm), the high [H] and moderate T_{gas} conditions prevailing in the reactor suffice to convert *all* of the input hydrocarbon, (initially) to CH_4.

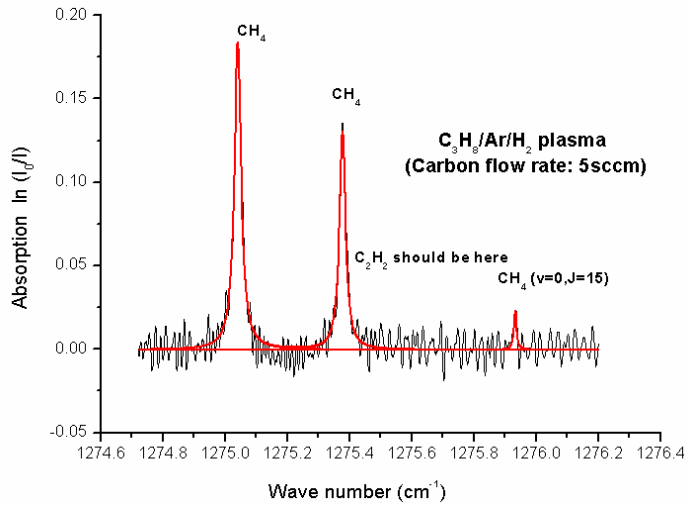

Figure 4. 17 Absorption spectrum in $C_3H_8/Ar/H_2$ plasma, using a carbon flow rate of 5 sccm

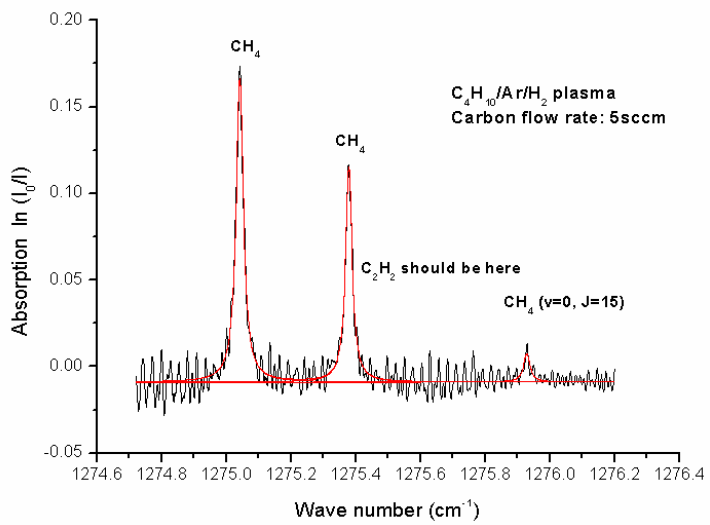

Figure 4. 18. Absorption spectrum in $C_4H_{10}/Ar/H_2$ plasma, using a carbon flow rate of 5 sccm

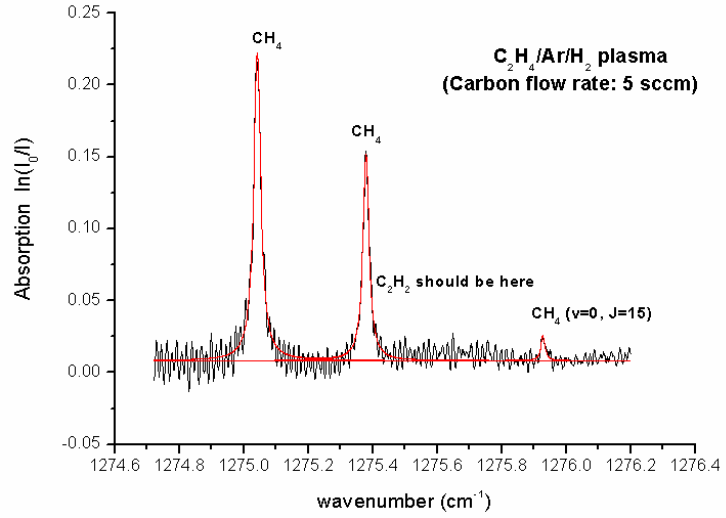

Figure 4. 19. Absorption spectrum in $C_2H_4/Ar/H_2$ plasma, using a carbon flow rate of 5 sccm

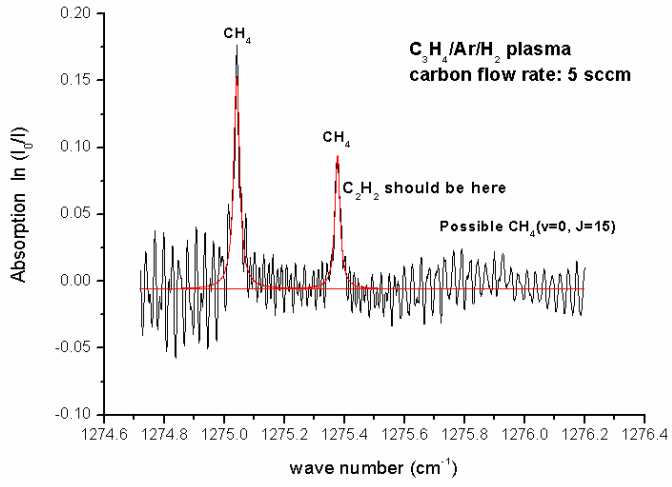

Figure 4. 20. Absorption spectrum in $C_3H_4/Ar/H_2$ plasma, using a carbon flow rate of 5 sccm

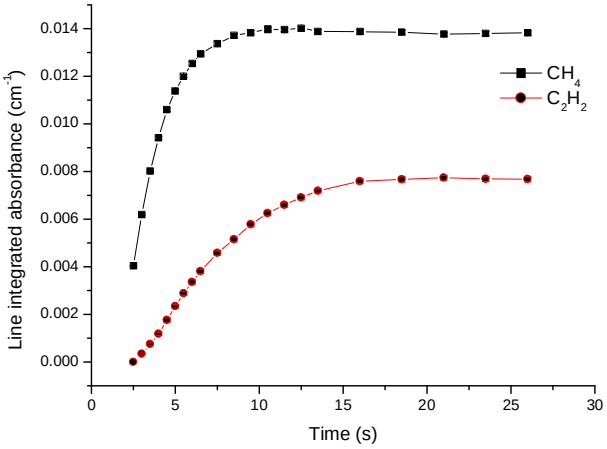

Figure 4. 21. CH_4 and C_2H_2 LIAs in $C_2H_4/Ar/H_2$ plasma as a function of time

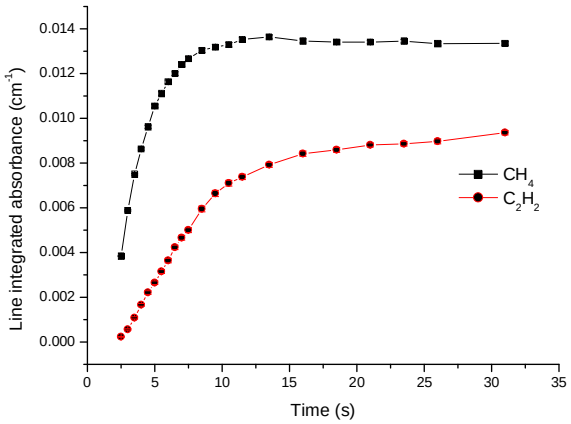

Figure 4. 22. CH_4 and C_2H_2 LIAs in $C_3H_4/Ar/H_2$ plasma as a function of time

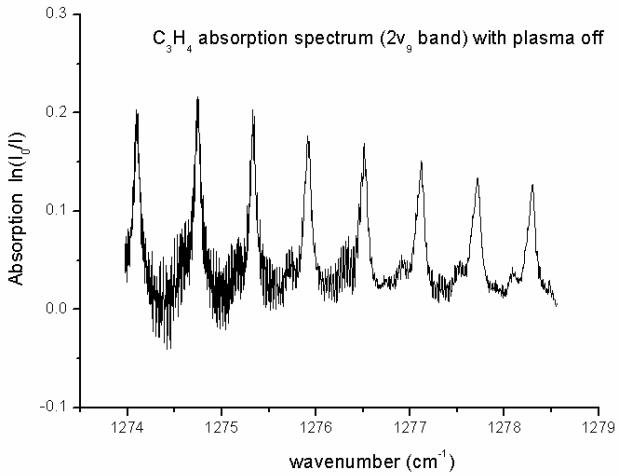

Figure 4. 23. C_3H_4 absorption spectrum measured in a $C_3H_4/Ar/H_2$ gas mixture without ignition of the plasma

The measured CH_4 and C_2H_2 absorptions when using $C_3H_8/Ar/H_2$, $C_4H_{10}/Ar/H_2$, $C_2H_4/Ar/H_2$ and $C_3H_4/Ar/H_2$ plasmas, together with those observed when using $CH_4/Ar/H_2$ and $C_2H_2/Ar/H_2$ plasmas, are plotted on a common scale as a function of carbon flow rate in **Figure 4. 24**. Evidently, these species behave very similarly in all cases, apart from the excessive C_2H_2 absorption in $C_2H_2/Ar/H_2$ plasma under high carbon flow rates. CH_4 shows a similar 'excess' when using a $CH_4/Ar/H_2$ plasma and high carbon flow rates. As discussed before, this is attributable to the fact that under high carbon flow rates some of the input C_2H_2 (CH_4) avoids processing.

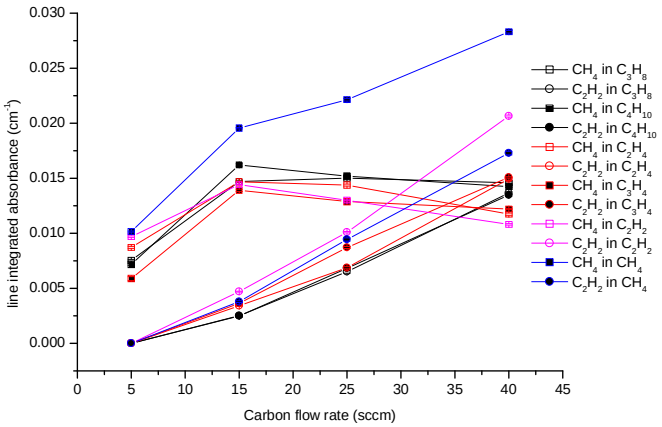

Figure 4. 24 CH_4, and C_2H_2 LIAs as a function of carbon flow rate for different hydrocarbon source gases.

4.4. Summary

By using the QCL, the column absorptions of CH_4 and C_2H_2 are measured under different discharge conditions in both $CH_4/Ar/H_2$ and $C_2H_2/Ar/H_2$ plasmas. The measured results show that an efficient inter-conversion between CH_4 and C_2H_2 must be present in these plasmas. The observed phenomena can be explained well by combining the effects of two reaction schemes prevailing in different regions of the chamber at the same time. Specifically, when the Ar/H_2 plasma is ignited, lots of H atoms are produced. They are not only abundant in the hot region (i.e. the plasma glow region) but also have relatively high concentrations in the cooler region. Therefore, when a small amount of hydrocarbon gas is fed into the chamber, firstly,

in the cool region, due to the low temperature but high [H], the H addition reactions will convert the input hydrocarbon into CH_4, (the most stable C1 species). Then, the processed hydrocarbon species diffuse into the hot region and are converted into C_2H_2 (the most stable C2 species) by H abstraction reactions because of the high temperature and high [H] there.

When the C/H ratio is small, in the cool region, due to the high [H] and low temperature, the C_2H_2 product can not survive and will be rapidly converted into CH_4. That is why C_2H_2 absorption is not observed at the earlier times after hydrocarbon gas introduction, or when the carbon flow rate is low.

When the carbon flow rate is high, or if more and more hydrocarbon gas is fed into the chamber at later time, many of the H atoms in the cool region will be consumed, so the C_2H_2 product now can survive in the cool region and be detected by the laser beam.

Based on the picture discussed above, no matter what hydrocarbon gas is introduced into the chamber, the favoured stable hydrocarbon in and around the plasma ball is mainly C_2H_2. Thus one should expect the plasma chemistry to be largely insensitive to the choice of hydrocarbon feedstock. To verify this, some hot (energetic) species like C_2, CH and H(n=2) which are only concentrated in the plasma ball shall be measured and compared in both $CH_4/Ar/H_2$ and $C_2H_2/Ar/H_2$ plasmas. Results of such experiments will be reported in Chapter 5. It will be shown that under the same carbon flow rate and the same discharge conditions, the C_2, CH and H(n=2) profiles of column densities measured in $CH_4/Ar/H_2$ and $C_2H_2/Ar/H_2$ plasmas are essentially the same. Such results provide strong support to the reaction schemes proposed here.

4.5. References

[1] M. A. Prelas, G. Popovici and L.K.Bigelow, *Handbook of Industrial Diamonds and Diamond Films*, (Marcel Dekker, New York, 1998).

[2] M. N. R. Ashfold, P. W. May, J. R. Petherbridge, *et al.*, *Phys. Chem. Chem. Phys.*, **3** (2001) 3471.

[3] P. W. May, *Philosophical Transactions of The Royal Society London A.*, **358** (2000) 473.

[4] M. C. McMaster, W. L. Hsu, M. E. Coltrin, *et al.*, *Diamond Relat. Mater.*, **4** (1995) 1000.

[5] R. R. Rye, *Surf. Sci.*, **69** (1977) 653.

[6] A. Cheesman, J. A. Smith, M. N. R. Ashfold, *et al.*, *J. Phys. Chem. A*, **110** (2006) 2821.

[7] N. L. G. Duxbury, M.T. McCulloch and S. Wright, *Chem. Soc. Rev.*, **34** (2005) 1.

[8] M. Herman, T. R. Huet, Y. Kabbadj, *et al.*, *Mol. Phys.*, **72** (1991) 75.

[9] N. F. Henfrey and B. A. Thrush, *J. Mol. Spec.*, **121** (1987) 139.

Chapter 5 Cavity ring-down spectroscopy investigations of the plasma chemistry

5.1. Introduction

As mentioned in Chapter 1, lots of radicals and excited states of atoms and molecules are produced in the plasma used in microwave plasma enhanced diamond CVD. These "active" species are highly reactive and energetic, and are thus likely to have an important influence both on the gas phase chemistry and the subsequent diamond film growth. Here, we focus on H(n=2) atoms, and C_2 and CH radicals, both because they can be probed easily with contemporary dye lasers, and because of their ubiquity in diamond CVD plasmas.

It is well known that the H atom plays several important roles in diamond CVD. For example, it initiates most of the CVD gas phase chemistry, aiding the production of active gas phase species (such as CH_3, CH and C, etc) that may be responsible for diamond growth. It also can continuously create and re-terminate (thereby preventing the reconstruction to non-diamond forms) the reactive surface sites, which are necessary for the propagation of the growing diamond surface. Finally, the H atom also can preferentially etch graphitic carbon from the growing surface, thereby improving the film quality. Theoretical models point to several ways of producing hydrogen atoms. For example, the impact of high energy electrons with H_2 can cause H_2 dissociation, producing two H atoms. Another way, termed thermal dissociation, in fact involves a series of vibrational pumping collisions with electrons followed by a final collision with heavy species to induce dissociation. Ground state H_2 molecules can also dissociate as a result of collisions with energetic heavy species (e.g. excited metastables and ions). One such example involves collision between H_2 and Ar^+, see **R.5.1**.

Excited (e.g. $n \geq 2$) hydrogen atoms can also be produced through several different

pathways. When relatively little Ar is present in the plasma, electron impact excitation is usually the main production channel of excited H atoms. However, at higher Ar mole fractions, the reactions

$$Ar^+ + H_2 \rightarrow ArH^+ + H \quad \text{(R5. 1)}$$

$$ArH^+ + e \rightarrow Ar + H(n \geq 2) \quad \text{(R5. 2)}$$

will play a major role. [1, 2]

Many papers have suggested that CH_x and C_2H_x have different impact on the characteristics of synthetic diamond. [3, 4] C_2H_x easily forms sp^2 bonds, and thus tends to produce some non-diamond components, while CH_x prefers forming sp^3 bonds and therefore contributes to diamond growth. [4, 5] On some occasions, C has been suggested as the main precursor for diamond growth. [6] Due to the equilibrium $CH + H \Leftrightarrow C + H_2$, the CH number densities are proportional to the local densities of C atoms and thus CH densities may be a good indicator of the C densities. More generally, the C_2/CH emission intensity ratio has been chosen as an "indicative parameter" for best growth conditions. When the ratio decreases, high quality diamond is formed. [4, 7] Routes to producing C_2 and CH radicals, starting from CH_4 and/or C_2H_2 molecules and a succession of H-shifting reactions were shown in **Figure 4.1** and **2** in Chapter 4.

5.2. Experimental

The experimental set-up used for these measurements is shown in **Figure 5. 1**. The Ar/H_2/hydrocarbon (which is usually CH_4) plasma is generated by 2.45GHz microwave excitation. Pulsed cavity ring down spectroscopy (CRDS) is used to determine the absolute column densities of C_2 (a, v=0) and CH (X, v=0) radicals, and H(n=2) atoms. The dye laser is pumped by a Nd:YAG laser. The laser pulse is several nano seconds in duration and the repetition rate is 10 Hz. The dyes used in

measuring these three species are Coumarin 302, Exalite 428 and DCM. In pumping the first two dyes, the YAG laser output is set at 355 nm. In pumping DCM, the 532 nm output is used. The three pairs of CRDS mirrors used in measuring these three species are all from LayerTec GmbH. The reflectivity is normally higher than 0.999. The movable bench allows profiling of the column densities of these species over a vertical range of ~3 cm. Absorption due to C_2 (a, v=0) radicals is probed via the $C_2(d^3\Pi_g \leftarrow a^3\Pi_u)$ transition. CH (X, v=0) radical absorption is measured via the $CH(A^2\Delta \leftarrow X^2\Pi)$ transition while, for H(n=2) atoms, the Balmer α (n=3←n=2) absorption is used. Typical CRD spectra obtained for each species are shown in **Figures 5.2-5**. In the following experiments, the probing laser beam was first fixed at the position *d* ~9.8 mm above the substrate surface to study the behaviour of these three species as a function of plasma discharge parameters (e.g. the input power, the Ar flow rate, the CH_4 flow rate and the total pressure). Subsequently, the *z*-dependence (see **Figure 5. 1**) of these species' profiles was also measured under different discharge conditions.

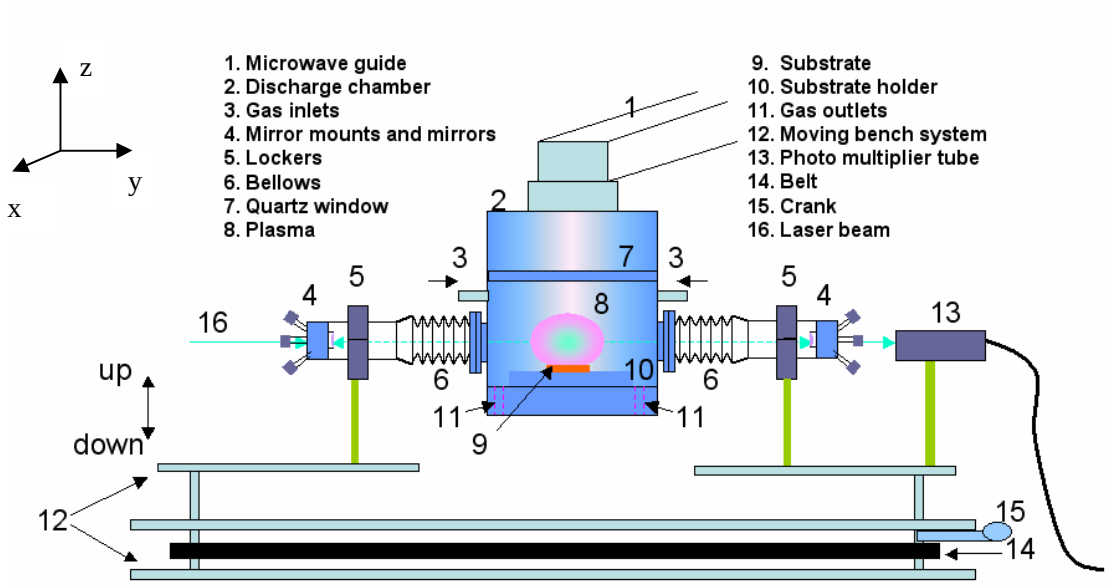

Figure 5. 1. Schematic of the experimental set-up for spatially resolved CRDS measurements

5.3. Results and discussions

5.3.1. Typical absorption spectra of C_2, CH and H(n=2)

A typical spectrum of the C_2 ($d^3\Pi_g \leftarrow a^3\Pi_u$) transition is shown in **Figure 5. 2**. The first three lines correspond to transitions between low *J* levels in the R branch. The last two lines (in fact three lines because the last one is a doublet) correspond to transitions between two high *J* levels in the P branch. The intensity ratio between the low *J* lines and high *J* lines is sensitive to the rotational temperature of C_2 ($a^3\Pi_u$) (see **Figure 5. 3**). Since collisions between the heavy species are very frequent at the high pressures (*p* = 75 to 175 torr) used in these experiments, rotational-translational (R-T) energy transfer processes are sufficiently efficient that these degrees of freedom are expected to be in local thermodynamic equilibrium throughout most of the reactor. Thus it is reasonable to equate the rotational temperature with the gas temperature. As shown in **Figure 5. 3**, the gas temperature estimated by this method is around 3000 K under our typical discharge conditions in the experiments. Such values are then be used in converting the measured spectral lines into the species column densities.

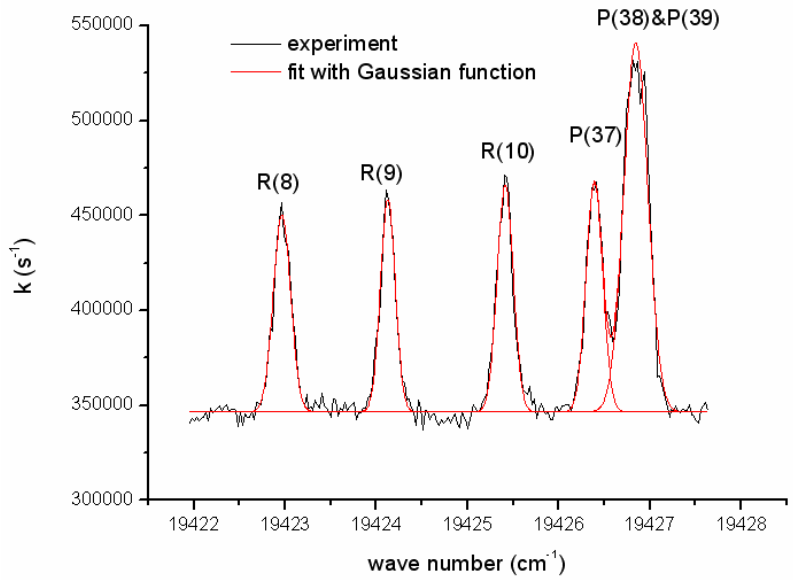

Figure 5. 2. Typical absorption spectrum of C_2 (a, v=0) radicals obtained by CRDS

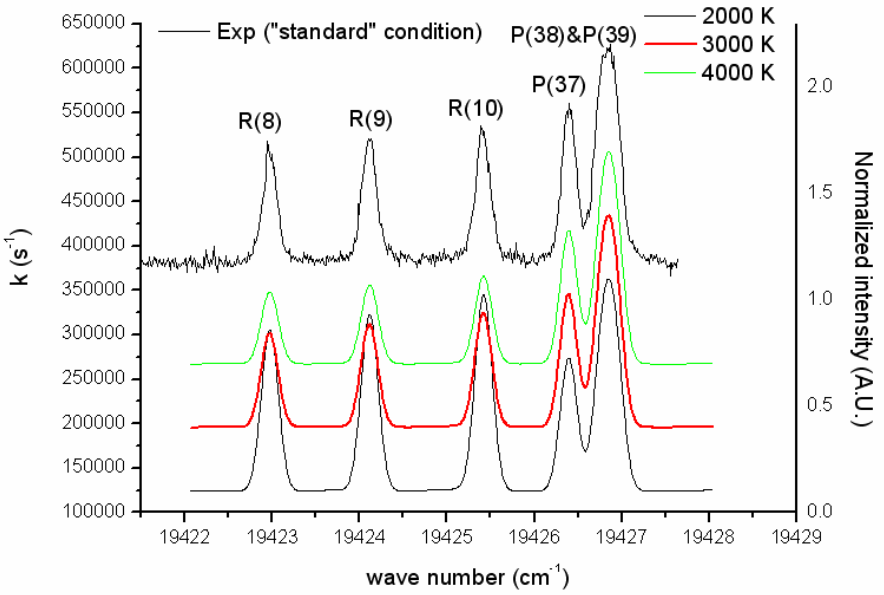

Figure 5. 3. Rotational temperature determination from a typical C_2 (d-a, 0,0) absorption spectrum under standard conditions. Measured spectrum (top): P = 1.5 kW, p = 150 Torr, total flow rate = 565 sccm comprising CH_4: 25 sccm; Ar: 40 sccm; H_2: 500 sccm, probing at d = 9.8 mm above the substrate. Simulated spectrum by Pgopher [8] (bottom): T_{rot} = 2000 (black), 3000 (red, fit best) and 4000 (green) K, Gaussian linewidth: 0.23 cm^{-1}(FWHM). Notice that the intensity ratios of high *J* and low *J* lines are very sensitive to the gas temperature.

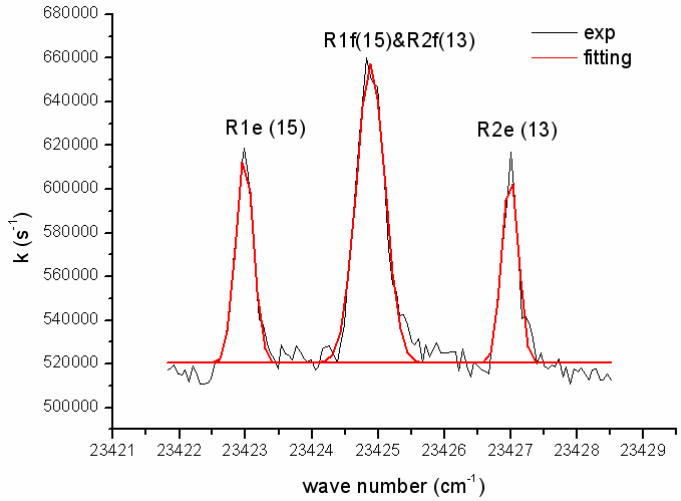

Figure 5. 4. Typical absorption spectrum of CH (X ,v=0) radicals obtained by CRDS

However, in **Figure 5. 4**, all the measured lines of CH are associated with transitions between low *J* levels. Therefore, their ratio is not as sensitive as the measured C_2

lines when used to estimate the temperature. The line in the middle looks wider because actually it is a doublet.

The measured H_α absorption can be fitted very well with a Gaussian function, see **Figure 5.5**. The line width, which is mainly due to Doppler broadening, can also provide information about the gas temperature.

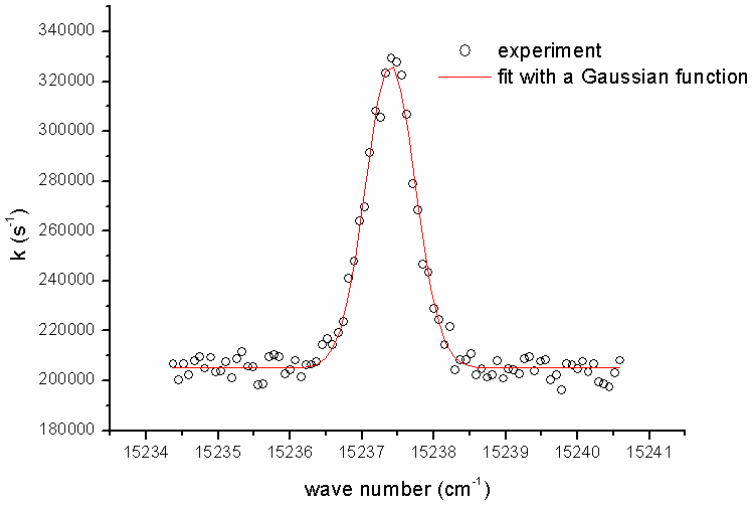

Figure 5.5. Typical absorption spectrum of H (n=2) atoms obtained by CRDS

5.3.2. Column density calculation

The column density of species can be worked out from the measured spectral lines. For example, in order to calculate C_2 (a, v=0) column density, first, the integral over laser wavenumber of the absorption coefficient, α, can be written as

$$\int \alpha \, d\bar{\nu} = \frac{\lambda^2}{8\pi c} \cdot \frac{g_{upper}}{g_{lower}} \left[C_2(a, \upsilon = 0) \right] A_{00} p \qquad \text{(Eq.5. 1)}$$

Here, α is the absorption coefficient, $\bar{\nu}$ is the wavenumber. λ is the wavelength of the measured spectral line. g_{upper} and g_{lower} are the electronic degeneracies of the upper (i.e. *d* state for C_2) and lower (i.e. *a* state for C_2) levels, respectively. A_{00} is the Einstein A-coefficient for the (0,0) band of the C_2(d-a) transition and *p* is the fraction of the oscillator strength associated with the measured rotational line in the total (0,0) band. *p* is temperature dependent and can be calculated through Pgopher simulations. [8] For convenience, we will refer to it as the Pgopher coefficient here.

The values of these parameters used in the calculation of C_2 column densities are listed in **Table 5. 1**.

Table 5. 1 Parameter values of C_2 and CH for their column density calculation

Parameters	C_2	CH
transitions	$d^3\Pi_g \leftarrow a^3\Pi_u$	$A^2\Delta \leftarrow X^2\Pi$
g_{upper}	6	4
g_{lower}	6	4
A_{00}	$7.21\times10^6 s^{-1}$	$1.85\times10^6 s^{-1}$

On the other hand, in CRDS, the absorption coefficient is related to the ring-down time via equation

$$\alpha = \frac{L\Delta k}{c l_{eff}} \qquad \text{(Eq.5. 2)}$$

where c is light speed, L is the distance between two mirrors and is ~ 85 cm in our experiment, Δk is the difference of the ring down rate with and without absorber and l_{eff} is effective length of the absorber.

Therefore,

$$D_{C_2(a,\upsilon=0)} = \left[C_2(a,\upsilon=0)\right]\cdot l_{eff} = \frac{8\pi L}{\lambda^2 A_{00} p}\frac{g_{lower}}{g_{upper}}\int \Delta k \mathrm{d}\bar{\nu} = \frac{8\pi L}{\lambda^2 A_{00} p}\frac{g_{lower}}{g_{upper}} A_{spec} \qquad \text{(Eq.5. 3)}$$

Here,

$$A_{spec} = \int \Delta k \mathrm{d}\bar{\nu} \qquad \text{(Eq.5. 4)}$$

is actually the area covered by the spectral line in the spectrum measured by CRDS.

Similarly, for CH(X, v=0), we have

$$D_{CH(X,\upsilon=0)} = \left[CH(X,\upsilon=0)\right]\cdot l_{eff} = \frac{8\pi L}{\lambda^2 A_{00} p}\frac{g_{lower}}{g_{upper}}\int \Delta k \mathrm{d}\bar{\nu} = \frac{8\pi L}{\lambda^2 A_{00} p}\frac{g_{lower}}{g_{upper}} A_{spec} \text{.(Eq.5. 5)}$$

The values of those parameters for CH are also shown in **Table 5. 1**.

For converting the measured H_α absorption into the column density of H(n=2), the following analysis is followed:

Firstly, we know that

$$\int \alpha \, \mathrm{d}\nu = \frac{1}{c}\frac{L}{l_{eff}} \int \Delta k \, \mathrm{d}\nu \,. \qquad \text{(Eq.5. 6)}$$

Secondly, there are 7 allowed transitions contributing to the Balmer-α absorption (see **Figure 3.2**), each having its own center frequency and absorption cross-section. Therefore,

$$\int \alpha \, \mathrm{d}\nu = \sum_{j,k} N_j \sigma_{jk} \qquad \text{(Eq.5. 7)}$$

Here, j and k refer to the lower (n=2, $^2S_{1/2}$, $^2P_{1/2}$ and $^2P_{3/2}$) and upper levels (n=3, $^2S_{1/2}$, $^2P_{1/2}$ and $^2P_{3/2}$, $^2D_{3/2}$ and $^2D_{5/2}$) associated with these allowed transitions. N_j is the population in the lower level j. Since these lower energy levels (n=2, $^2S_{1/2}$, $^2P_{1/2}$ and $^2P_{3/2}$) are quite close to one another, the population in these n=2 levels is assumed to be proportional to their degeneracy g_j, i.e.

$$N_j = N_{H(n=2)} \frac{g_j}{\sum_j g_j} == N_{H(n=2)} \frac{g_j}{g_{total-lower}} \qquad \text{(Eq.5. 8)}$$

where $g_{total-lower}$ is the sum of the degeneracy of the lower levels (n=2, $^2S_{1/2}$, $^2P_{1/2}$ and $^2P_{3/2}$) and is equal to 8, $N_{H(n=2)}$ is the total population in the n=2 levels.

Using **Eqs. 3.72**, **3.54** and **3.55, Eq. 5.7** can be rewritten as

$$\begin{aligned} \int \alpha \, \mathrm{d}\nu &= \sum_{j,k} N_j \sigma_{jk} = \sum_{j,k} N_j \frac{h\nu_{jk}}{c} B_{jk} \\ &= \sum_{j,k} N_{H(n=2)} \frac{g_j}{g_{total-lower}} \cdot \frac{h\nu_{jk}}{c} \cdot \frac{g_k}{g_j} \cdot \frac{\lambda_{jk}^3}{8\pi h} A_{kj} \,. \\ &= \frac{N_{H(n=2)}}{64\pi} \sum_{j,k} A_{kj} \lambda_{jk}^2 g_k \end{aligned} \qquad \text{(Eq.5. 9)}$$

Comparing **Eq.5.6** and **Eq.5.9**, finally the column density of H(n=2) can be given by

$$\begin{aligned} D_{H(n=2)} = N_{H(n=2)} \cdot l_{eff} &= \frac{64\pi L}{c \sum_{j,k} A_{kj} \lambda_{jk}^2 g_k} \int \Delta k \mathrm{d}\nu \\ &= \frac{64\pi L}{\sum_{j,k} A_{kj} \lambda_{jk}^2 g_k} \int \Delta k \mathrm{d}\bar{\nu} = \frac{64\pi L}{\sum_{j,k} A_{kj} \lambda_{jk}^2 g_k} A_{spec} \end{aligned} \qquad \text{(Eq.5. 10)}$$

5.3.3. CH_4 flow rate effect

Figure 5.6 gives the trends of C_2 (a, v=0), CH (X, v=0) and H (n=2) column densities measured at *d* ~9.8 mm (nearly the center of the plasma illuminating region) as a function of CH_4 flow rate. The three species show quite different behaviors. Whereas the C_2 (a, v=0) column densities exhibit a near-linear dependence on CH_4 flow rate, the CH (X, v=0) density appears to saturate at high CH_4 flows. This suggests that the chemistry underpinning their production is somehow different, though both are dominated by thermal chemistry. The ratio of the CH to C_2 column densities is plotted as function of CH_4 flow rate in **Figure 5.7**; the ratio decreases with increasing CH_4. Some authors [3, 4] have suggested that CH_x radicals favour formation of sp^3 bonds, whereas gas-surface reactions involving C_2H_x radicals favour sp^2 bond formation. That being the case, increasing the C_2 to CH ratio in the plasma would be expected to result in the formation of a greater proportion of non-diamond structure.

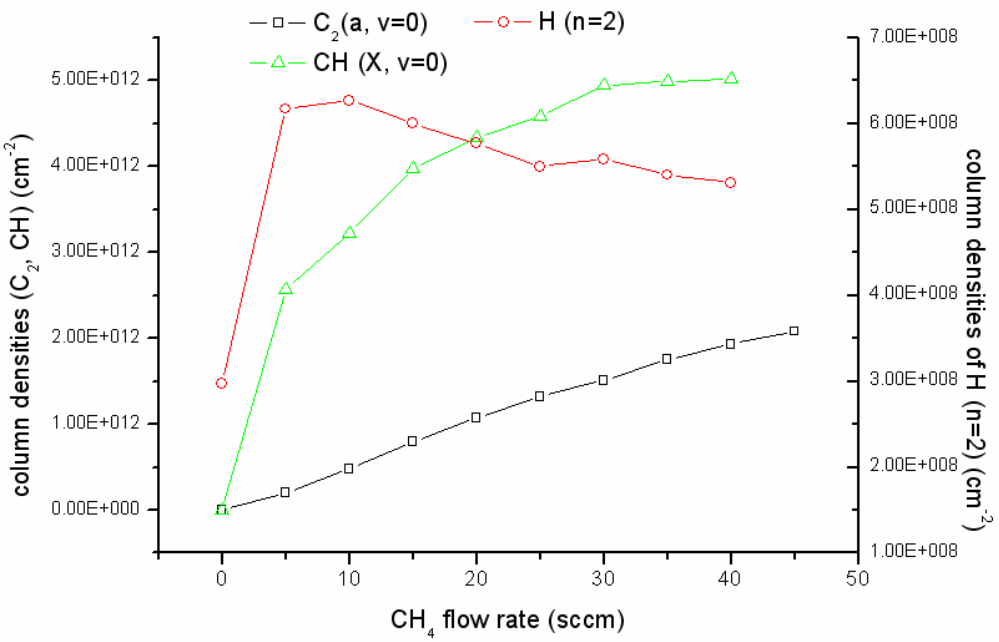

Figure 5.6. C_2 (a, v=0), CH (X, v=0) and H (n=2) column densities vs CH_4 flow rate, probed at d ~9.8 mm above the substrate.

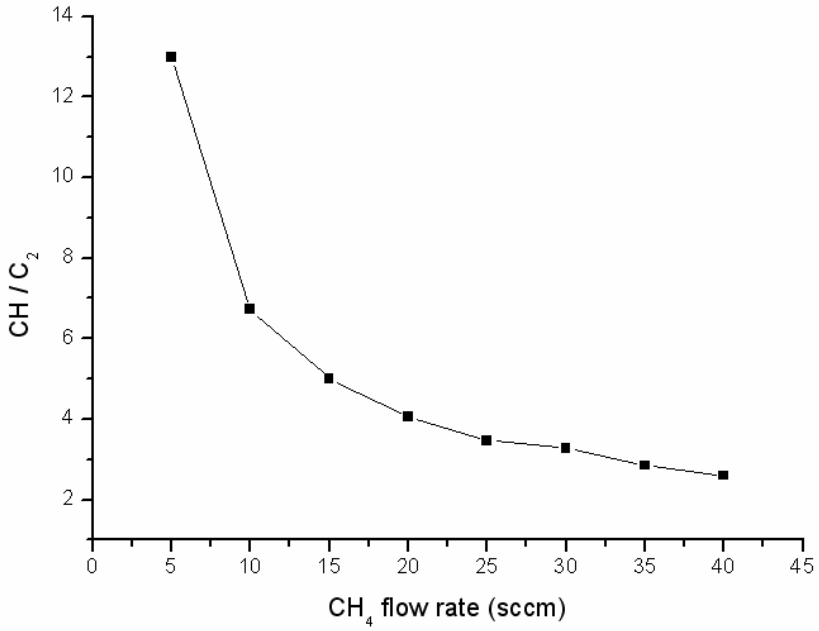

Figure 5.7. CH/C_2 column density ratio from **Figure 5.6**, plotted as a function of CH_4 flow rate

Figure 4.1 in Chapter 4 provides a possible explanation for the different behaviors of CH and C_2 species as functions of CH_4 flow rate. The reaction scheme suggests that C_2 derives from C_2H_2, via H abstraction reactions, whereas CH is more related to CH_4. Differences in the behavior of CH and C_2 may thus be a reflection of the different trends in CH_4 and C_2H_2 in the "hot" region as the CH_4 flow rate increases. However, as shown in Chapter 4, in the hot region, most CH_4 is converted into C_2H_2, thus C_2H_2 has a roughly linear dependence on the CH_4 flow rate, which can not explain the different behaviour of C_2 and CH shown in **Figure 5.6**. In order to find a suitable explanation, a more detailed analysis is presented. The analysis follows that given by Goodwin and Butler [9].

In C1 chemistry, the CH_y are governed by the equilibrium between the following reactions:

(1) The hydrogen shift reactions

$$CH_y + H \Leftrightarrow CH_{y-1} + H_2 \quad (y\text{=}1\text{-}4) \qquad \text{(R5. 3)}$$

These reactions are fast in both the forward and reverse directions;

(2) The pressure dependent recombination reactions

$$CH_{y-1} + H + M \rightarrow CH_y + M \qquad \text{(R5. 4)}$$

These reactions can be neglected in the hot regions (but not in the cooler periphery). Therefore, in the plasma ("hot" region), we have

$$\frac{[CH_{y-1}][H_2]}{[CH_y][H]} = K_y(T) \quad (y\text{=1-4}) \qquad \text{(Eq.5. 11)}$$

Here, $K_y(T)$ is the equilibrium constant of the *y*th hydrogen shift reaction.

Applying this equation for different *y*s, one obtains

$$\frac{[CH_y]}{[CH_4]} = \left(\frac{[H]}{[H_2]}\right)^{4-y} \prod_{j=y+1}^{4} K_j(T) \qquad \text{(Eq.5. 12)}$$

For CH, we have

$$\frac{[CH]}{[CH_4]} = \left(\frac{[H]}{[H_2]}\right)^{3} \prod_{j=2}^{4} K_j(T) \qquad \text{(Eq.5. 13)}$$

which shows that the concentration of CH must be very sensitive to the atomic hydrogen concentration.

As shown in many works, CH_4 addition normally will lead to the reduction of H atoms, Also, here, notice in **Figure 5.6**, the measured excited states H(n=2) also decrease as CH_4 increases. So we use this conclusion and assume

$$[H] \propto [CH_4]^{-\gamma}, \ \gamma>0 \qquad \text{(Eq.5. 14)}$$

Then, using this relationship in **Eq.5.13** we have,

$$[CH] \propto [CH_4]^{1-3\gamma} \qquad \text{(Eq.5. 15)}$$

If $0<\gamma<1/3$, i.e. if $0<1-3\gamma<1$, the CH concentration will exhibit a behaviour as shown in **Figure 5.6**.

In C2 chemistry, we can obtain a similar formula, i.e.

$$\frac{[C_2H_y]}{[C_2H_2]} = \left(\frac{[H]}{[H_2]}\right)^{2-y} \prod_{j=y+1}^{2} K_j(T) \qquad \text{(Eq.5. 16)}$$

For C_2 species,

$$\frac{[C_2]}{[C_2H_2]} = \left(\frac{[H]}{[H_2]}\right)^{2} \prod_{j=1}^{2} K_j(T) \qquad \text{(Eq.5. 17)}$$

Then, assuming $[H] \propto [CH_4]^{-\gamma}$ as in **Eq.5.14** and considering the relationship between C_2H_2 and CH_4 flow rate shown in **Figure 4.8(e)**, i.e. $[C_2H_2] \propto [CH_4]^{\alpha}$, α is very close to 1, thus we have

$$[C_2] \propto [CH_4]^{1+\alpha-2\gamma} \qquad \text{(Eq.5. 18)}$$

Assuming $0<\gamma<1/3$, then $4/3<1+\alpha-2\gamma<2$, so $1-3\gamma<1+\alpha-2\gamma$. Thus C_2 shows a faster increase than CH as the CH_4 flow rate increases. The essential reason for this difference is that CH is more sensitive to the atomic hydrogen concentration.

The H (n=2) absorption shows a strikingly different trend from C_2 and CH with increasing CH_4; addition of <1% mole fraction of CH_4 to the plasma leads to a 3× enhancement of the H(n=2) column density. Gicquel et al [10] have reported a similar phenomenon when measuring the optical emission spectrum of Ar. These authors attributed the observation to an enhancement of the electron density when CH_4 is introduced to the plasma. A similar trend could arise as a result of a change in electron temperature, but these authors argued against such an explanation because they observed little change in the H_α, H_β and H_γ intensity ratios. However, this explanation still feels incomplete. How could such a small amount of CH_4 lead to a big change of electron density? Inspecting the electron impact ionization cross sections of CH_4 and H_2 (shown in **Figure 5.8**) we see that the maximum cross-section for CH_4 is only ~4× larger than that for H_2 and the ionization threshold energy of CH_4 (14.25 eV) is only 1.2 eV lower than that of H_2 (15.43 eV) [22]. If the key electron forming processes within the plasma were simply electron impact

ionization of H_2 and CH_4, it is very hard to understand how the addition of 1% CH_4 could cause a 2-fold increase in electron density (which means 1 mole CH_4 corresponds to 100 mole H_2 in its contribution to ionization)! Also, it may be not very legitimate to assume that CH_4 addition has no effect on the electron temperature simply on the basis of H Balmer line intensity ratios. In the OES studies reported later, we observe no obvious change in the H_α to H_β line ratio upon reducing the total pressure from 175 to 75 Torr, yet the very obvious increase in the intensities of the Ar lines suggests a definite increase in electron temperature.

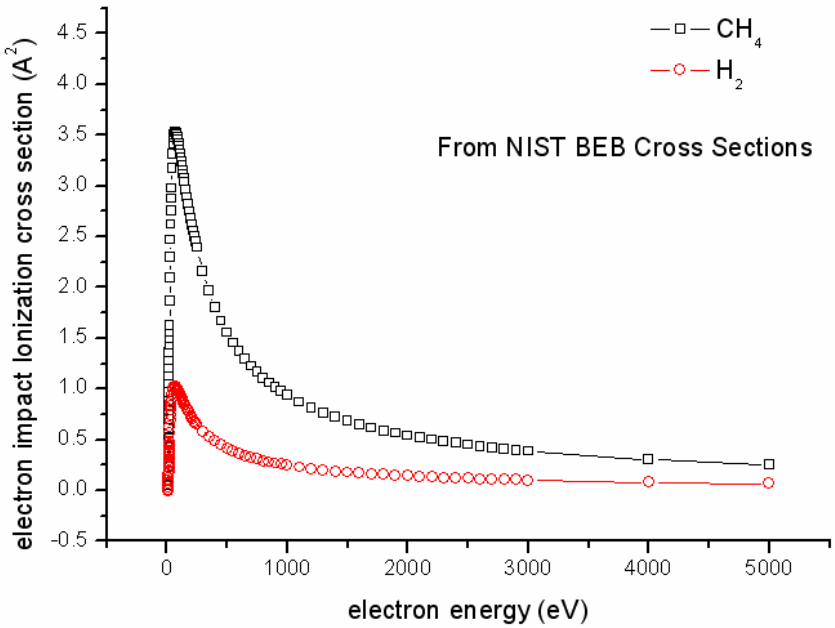

Figure 5.8. Electron impact ionization cross sections for CH_4 and H_2 from NIST [11]

On the other hand, several papers [12, 13] have pointed out that it is likely that the most abundant hydrocarbon species in the plasma are C_2H_2 not CH_4, such a conclusion is also consistent with our discussion in Chapter 4. In the paper by Lombardi et al, [12] the predicted mole fraction of C_2H_2 and C_2H is much (hundreds and tens times) bigger than CH_4. Even CH_3 and CH radicals in the plasma region are predicted to have comparable mole fractions to CH_4. These species have generally larger electron impact ionization cross sections and, more importantly, their ionization threshold energies are much lower than CH_4 (see **Figure 5.9**). Since C_2H_2 is most abundant in

the plasma, for simplicity, we only consider the contribution from this species. The ionization energy for C_2H_2 is 11.4 eV, which is quite low compared with that of CH_4 (14.25 eV) and H_2 (15.43 eV). This leads to an essential change of the ionization processes. The dominant ionization process is now not H_2 ionization, but the ionization of C_2H_2. The low ionization threshold of C_2H_2 will undoubtedly benefit the ionization, producing more electrons and H(n=2) atoms.

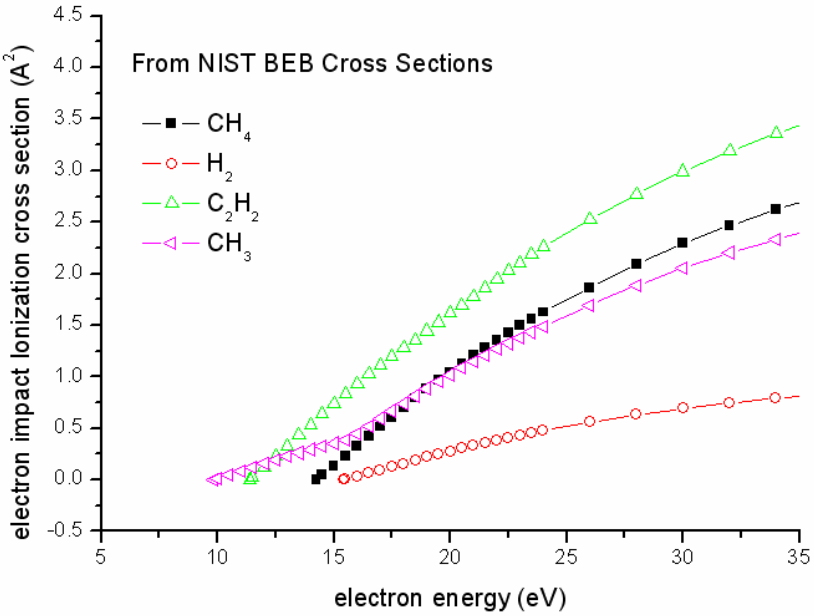

Figure 5.9. Electron impact ionization cross sections for CH_4 , H_2, C_2H_2 and CH_3 from NIST [11]

However, as shown in **Figure 5.6**, further addition of CH_4 does not lead to the continuous increase of H(n=2) column densities. On the contrary, the column density of H(n=2) atoms show a decrease. Such behavior can be attributed to the electron cooling effect through reaction **R5.5**.

$$e^-(hot) + C_xH_y \rightarrow C_xH_y^+ + 2e^-(cold) \qquad \text{(R5. 5)}$$

The electron temperature will drop. In addition, in order to fulfill the energy balance in **Eq. 2.1**, when n_e increases, the reduced electric field (E/N) has to become smaller, which can also decrease T_e. The electron impact excitation process is exponentially dependent on T_e and only linearly dependent on n_e. Thus, though n_e still increases

with CH_4 introduction, the column density of H(n=2) will decrease.

Another possible effect of CH_4 addition is a reduction of the plasma volume. The sudden change of dominant ions from H_3^+ to $C_2H_2^+$ may influence the electron dynamics as well. The $C_2H_2^+$ is much heavier than H_3^+, thus the electrons would be "confined" more "tightly" in the plasma due to the ambipolar diffusion. [14] This effect will be further examined in Chapter 6.

5.3.4. Ar flow rate effect

Figure 5.10 shows that changing the Ar flow rate from 0-50 sccm results in a very modest increase of the measured column densities of each of the monitored species. However, in the paper given by Han et al, [4] it was shown that addition of large amounts of Ar does lead to a substantial increase in C_2 and CH emissions. The authors also showed that when Ar flow rate was higher than 4%, the C_2 enhancement is much larger than CH, which leads to the drop of the CH/C_2 ratio and finally will inhibit the diamond growth.

According to the reactions suggested in the paper of Han et al, [4] the Ar can play several roles in the plasma which may account for these moderate increase of H(n=2), C_2 and CH observed.

(1) for H(n=2) increase

There are several reactions involving Ar which can help atomic hydrogen production. These include neutralization processes, which are considered to be the dominant process of excited hydrogen atoms generation when Ar flow rate is high,

$$Ar^+ + H_2 \rightarrow ArH^+ + H \qquad \text{(R5. 6)}$$

$$ArH^+ + e \rightarrow Ar + H(n \geq 2) \qquad \text{(R5. 7)}$$

and Penning excitation processes.

$$Ar^* + H \rightarrow Ar + H(n \geq 2) \qquad \text{(R5. 8)}$$

(2) for C_2 and CH increase

Ar can contribute to reactions that produce hydrogen atoms (like reactions **R5. 6** and **R5. 7**) and more H will encourage production of more hydrocarbon radicals. Thus, as claimed by Han et al, [4] "Ar ions and Ar excited states in the plasma can accelerate the dissociation of hydrogen molecules and methane". However, as shown in **Figure 5.10**, such an effect of Ar is very limited here due to the small amount of Ar introduced in our experiment.

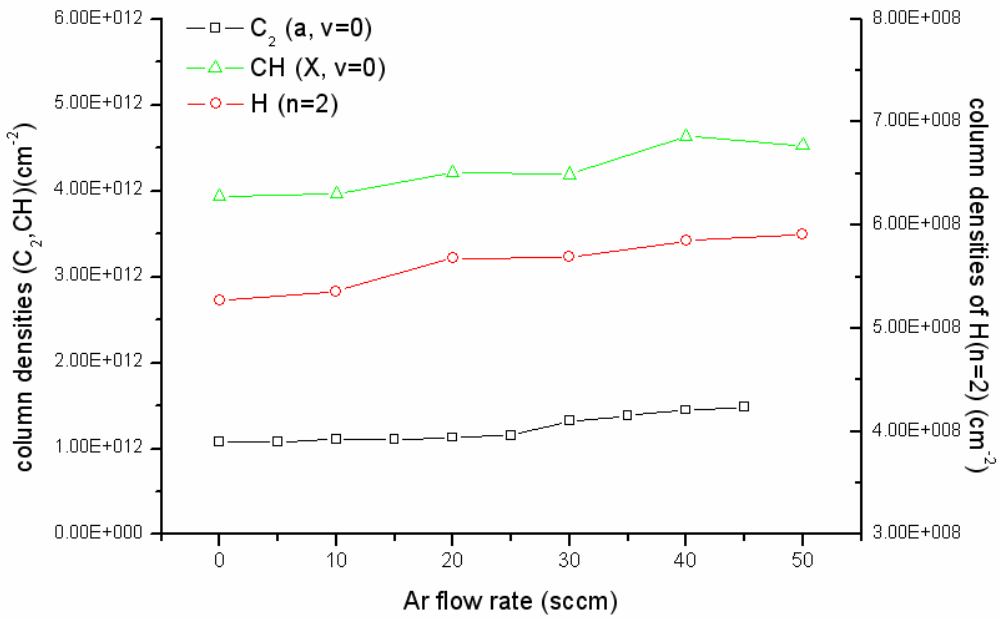

Figure 5.10. C_2 (a, v=0), CH (X, v=0) and H (n=2) column densities versus Ar flow rate, probed at *d* ~9.8 mm above the substrate.

5.3.5. Power effect

The column density of all three species increases with increasing power, *P*, as shown in **Figure 5.11**, though the H(n=2) and CH (X, v=0) column densities appear to increase somewhat faster than that for C_2 (a, v=0). Many factors can contribute to this H(n=2) enhancement. Increasing power means increasing the $MWPD_{av}$ if the plasma volume remains relatively constant. Thus, both the electron density and the electron temperature will increase. This will lead to more H(n=2) generation. The

increased $MWPD_{av}$ will also produce more H(n=1), which will also benefit H(n=2) generation. The increase of C_2 and CH are also likely to be the result of the more H-enriched environment.

We note that the measured CH column density exceeds that for C_2(a) at all *P*, in contrast to the DC arc jet reactor where we consistently found $[C_2] > [CH]$. [15] As discussed above, the high $[CH]/[C_2]$ ratio is likely to be beneficial for growing good quality diamond.

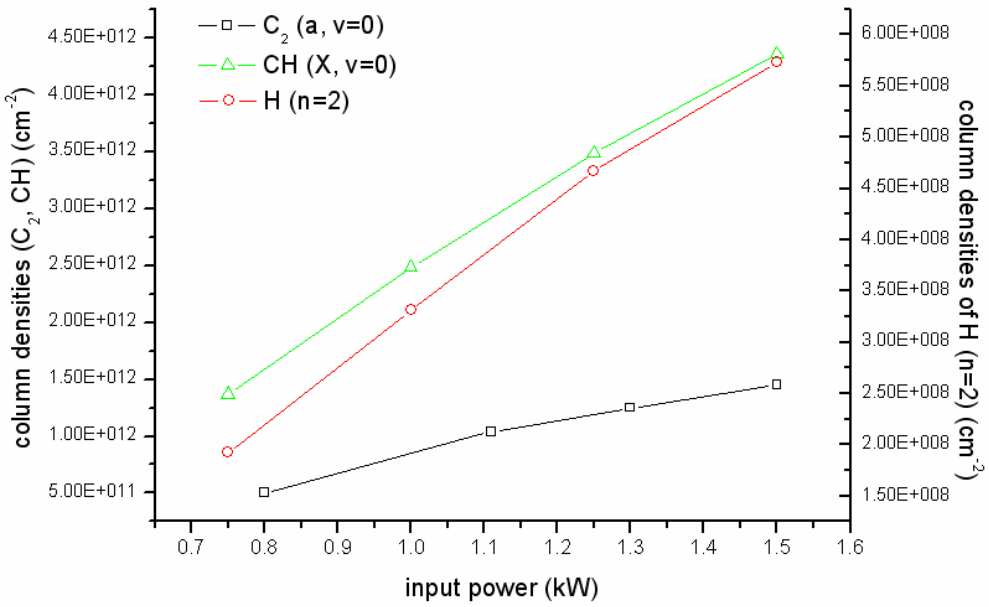

Figure 5.11. C_2 (a, v=0), CH (X, v=0) and H (n=2) column densities versus input power, *P*, probed at *d* ~9.8 mm above the substrate.

5.3.6. Pressure effect

Figure 5.12 shows the measured variation in C_2 (a, v=0), CH (X, v=0) and H(n=2) column densities with pressure, *p*. C_2 and CH show similar behaviors, but H(n=2) shows a different dependence. The difference comes from the fact that H(n=2) is a highly energetic species with energy 10.2 eV above its ground state, in contrast to C_2 and CH which are either ground state or just 0.09eV above the ground state. Therefore, the H (n=2) generation is strongly influenced by the electrons (i.e. dominated by electron impact excitation of H(n=1)) while C_2 and CH are produced

from thermal reactions.

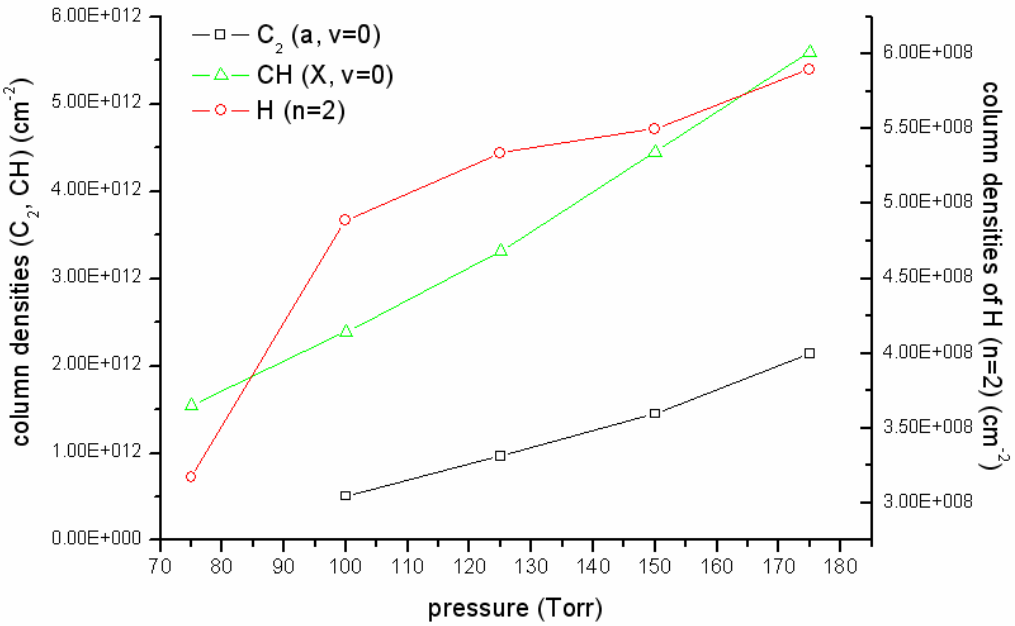

Figure 5.12. C_2 (a, v=0), CH (X, v=0) and H (n=2) column densities versus pressure, *p*, probed at *d* ~9.8 mm above the substrate.

The densities of species whose production is dominated by thermal chemistry should thus be expected to increase with increasing pressure. In general, increasing *p* leads to an increase in the electron density, n_e, but a drop in the electron temperature, T_e. The production rates of species formed via collisions with electrons tend to increase near-exponentially with T_e. Thus, in contrast to thermal processes, the densities of species formed by electron chemistry tend to decrease with increasing pressure. Consistent with such expectations, the densities of species like C_2 and CH that are traditionally viewed as being formed by (predominantly) thermal reactions are seen to increase with increasing *p* (**Figure 5.12**) The main production channel for H(n=2) atoms involves electron impact excitation of H(n=1). Contrary to the foregoing discussion, **Figure 5.12** shows that the measured column density of H(n=2) atoms actually increases, not decreases, with increasing *p*. This apparent inconsistency can be understood by recognizing that the H(n=1) production rate scales with *p* (as will be shown in Chapter 6).

5.3.7 Profiles

Figure 5. 13-15, **16-18** and **19-21** show the measured *d* dependences of the C_2 (a, v=0), CH (X, v=0) and H(n=2) column densities as a function of, respectively, input power, *P*, CH_4 flow rate, and total pressure, *p*. Key observations are summarized below:

1. In the cases of C_2 and CH, changing the power, CH_4 flow rate or pressure leads to a change in the absolute values of the column densities, but rather little change in their *d* dependent profiles. Only in the case of changing pressure do we discern some change (broadening in the lower pressure conditions) in profile; the column densities measured at *d* ~10 mm (near the peak of the profile) appear to vary more than those at small and large *d*. Such observations would be consistent with some expansion of the plasma ball (and increase in its homogeneity) when the pressure is reduced.

2. The measured H(n=2) column densities show similar *P* and *p* dependences to those of C_2 and CH but, as **Figure 5. 20** shows, the H(n=2) profile recorded in the absence of CH_4 is very different from those recorded with any CH_4 flow rate in the range 5-40 sccm. This data serves to re-emphasize the behavior shown in **Figure 5.6**. In addition, the H(n=2) also shows a wider profile at 125 Torr than at 150 Torr.

3. Plotting C_2, CH and H(n=2) profiles measured under the same discharge conditions on a common figure (as in **Figure 5. 22**), we see that that the maxima of the C_2 and CH distributions lie at essentially the same *d* (~10 mm above the substrate), whereas the maximum of the H(n=2) profile is closer to the substrate (*d* ~7 mm). This difference reflects the different chemistry behind the production of these three species. The main production mechanisms for C_2 and CH involve thermal chemistry; the peak in their column densities is related to the *d* dependent shape (width) of the plasma ball. As discussed previously, the principal source of H(n=2) atoms is electron impact excitation of ground state H atoms; the H(n=2) profile will thus be determined by a convolution of the spatial distributions of H(n=1) atoms and of the electrons. [The electron temperature distribution in the plasma (not near the

substrate) is not expected to show a large gradient since electrons have a much longer mean free path than the heavy species].

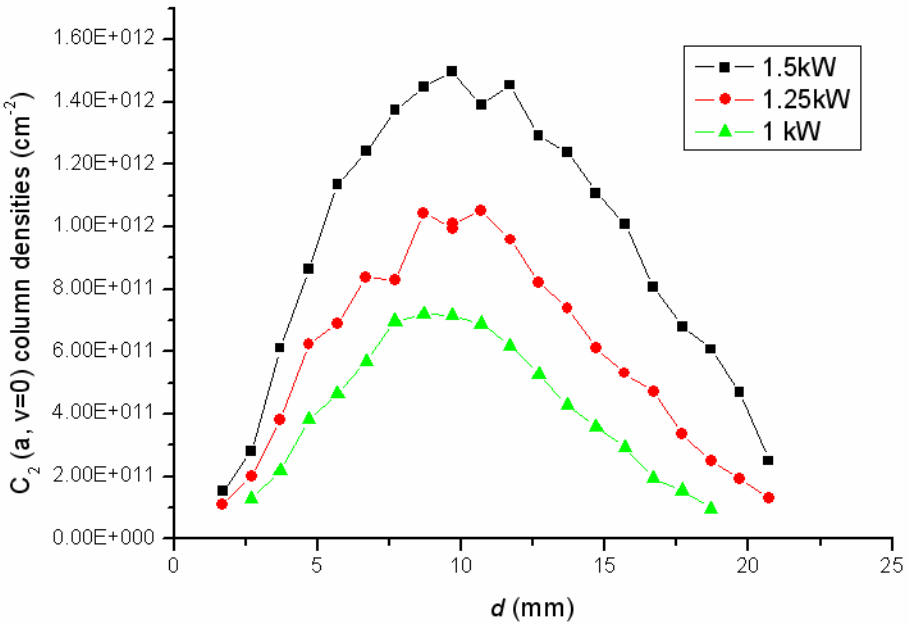

Figure 5. 13. *d* dependent profiles of C_2 (a, v=0) radical column densities measured at three different input powers

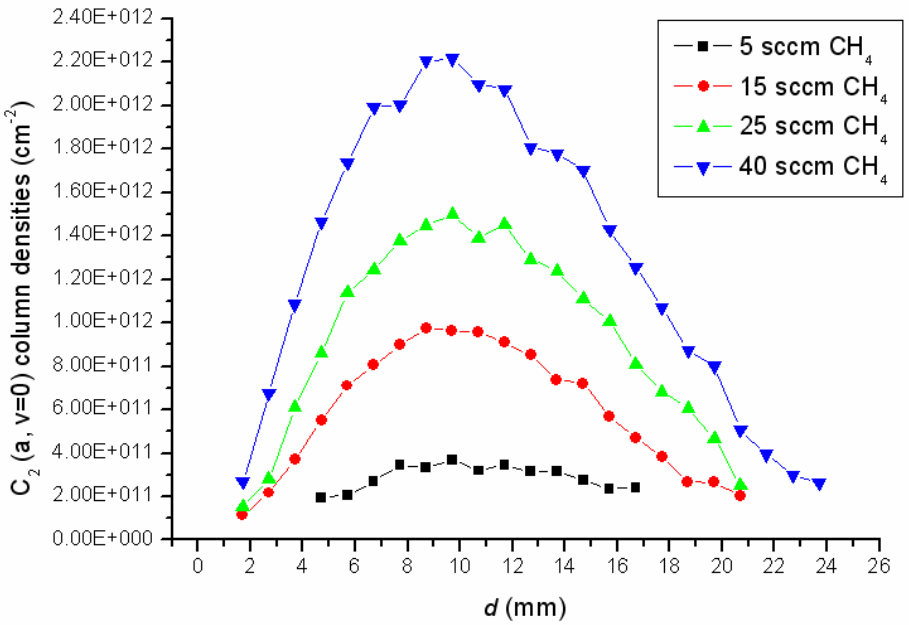

Figure 5. 14 *d* dependent profiles of C_2 (a, v=0) radical column densities measured at different CH_4 flow rates

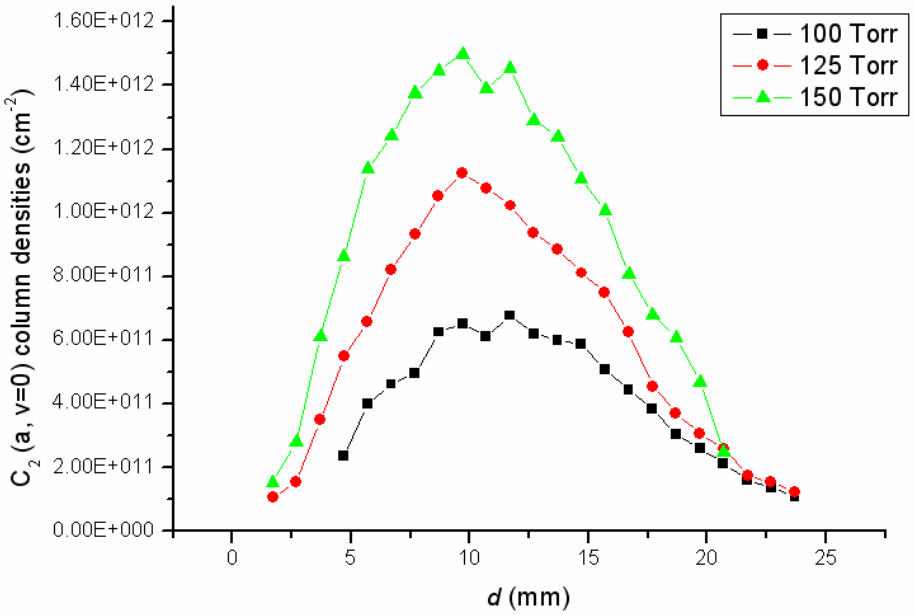

Figure 5. 15. *d* dependent profiles of C_2 (a, v=0) radical column densities measured at *p* = 100, 125 and 150 Torr.

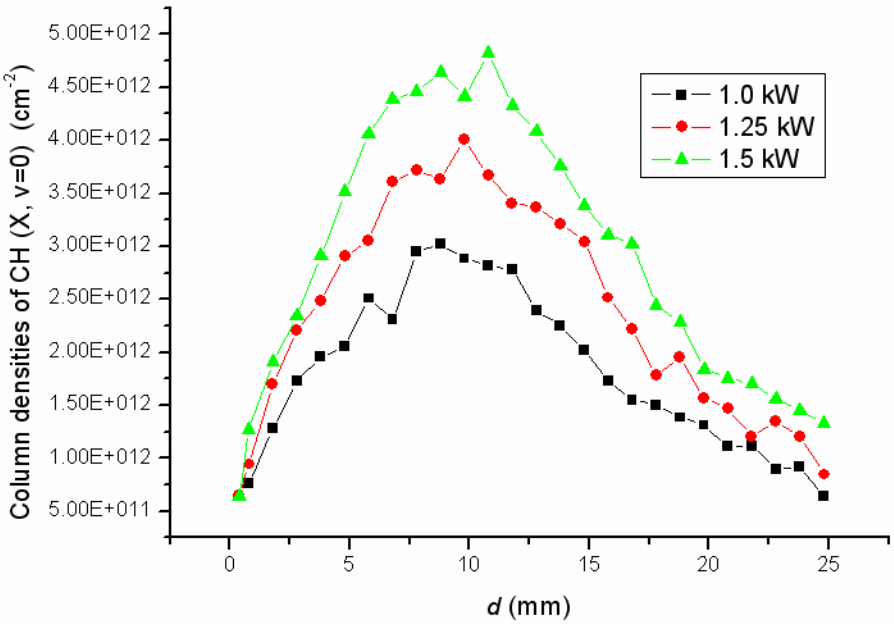

Figure 5. 16. *d* dependent profiles of CH (X, v=0) radical column densities measured at three different input powers

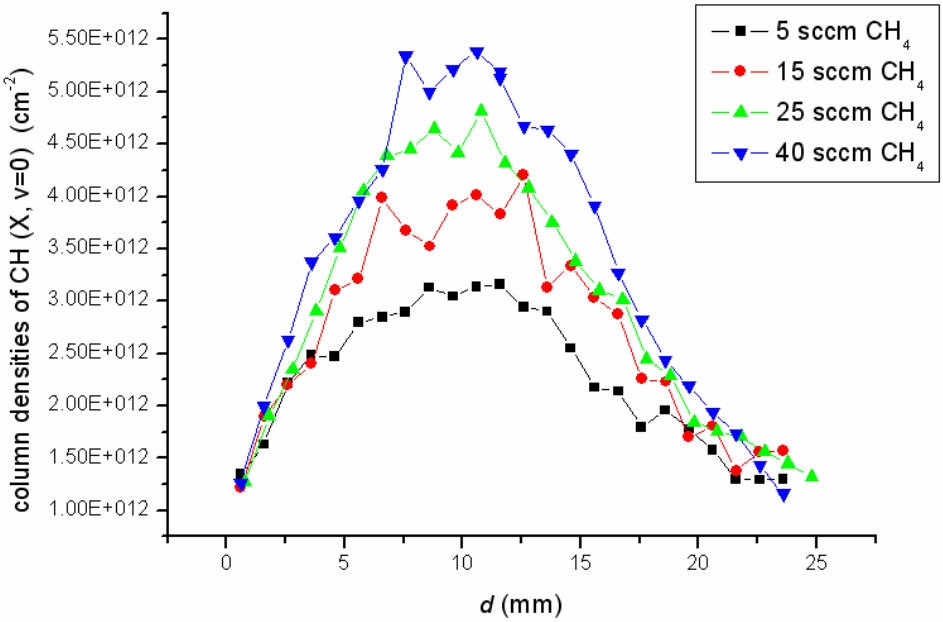

Figure 5. 17. *d* dependent profiles of CH (X, v=0) radical column densities measured at different CH_4 flow rates

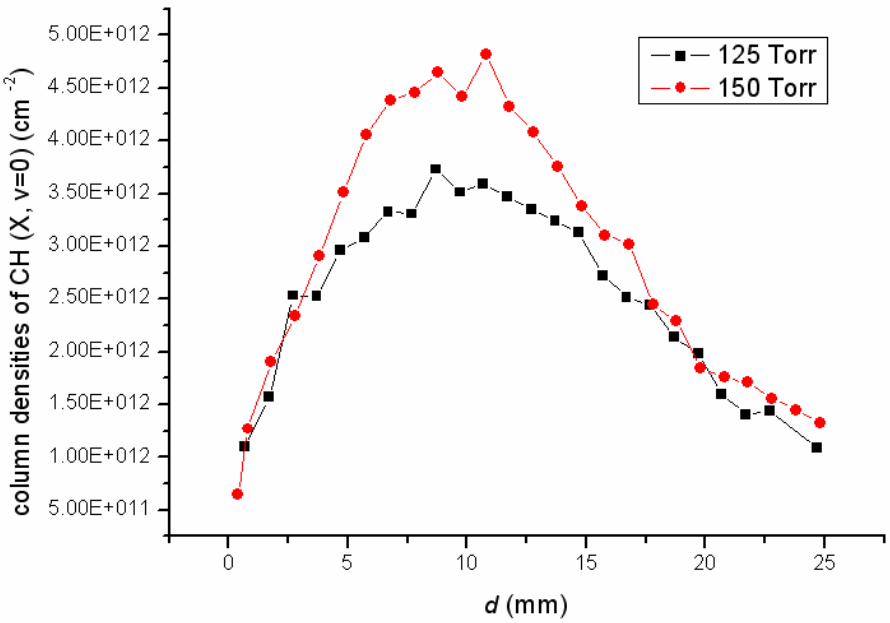

Figure 5. 18. *d* dependent profiles of CH (X, v=0) radical column densities measured at p = 125 and 150 Torr.

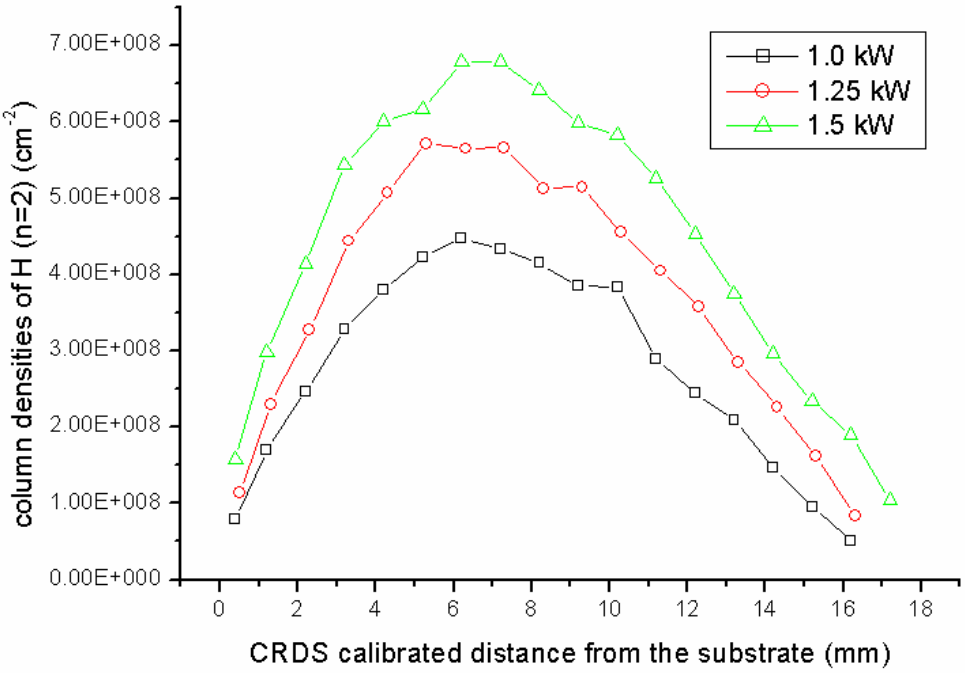

Figure 5. 19. *d* dependent profiles of H(n=2) atom column densities measured at three different input powers, *P*.

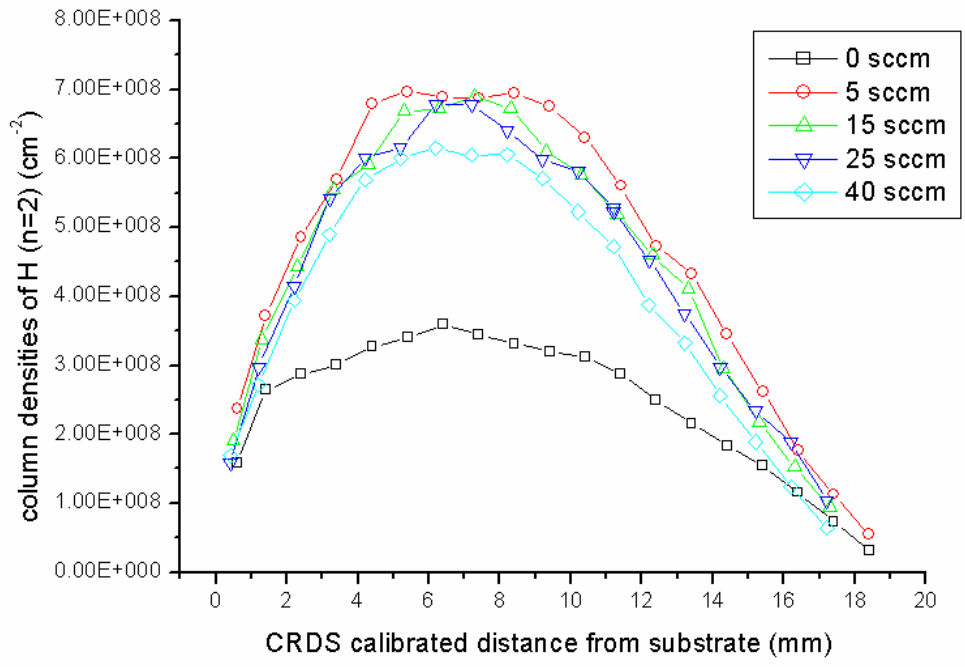

Figure 5. 20. *d* dependent profiles of H(n=2) atom column densities measured at different CH_4 flow rates

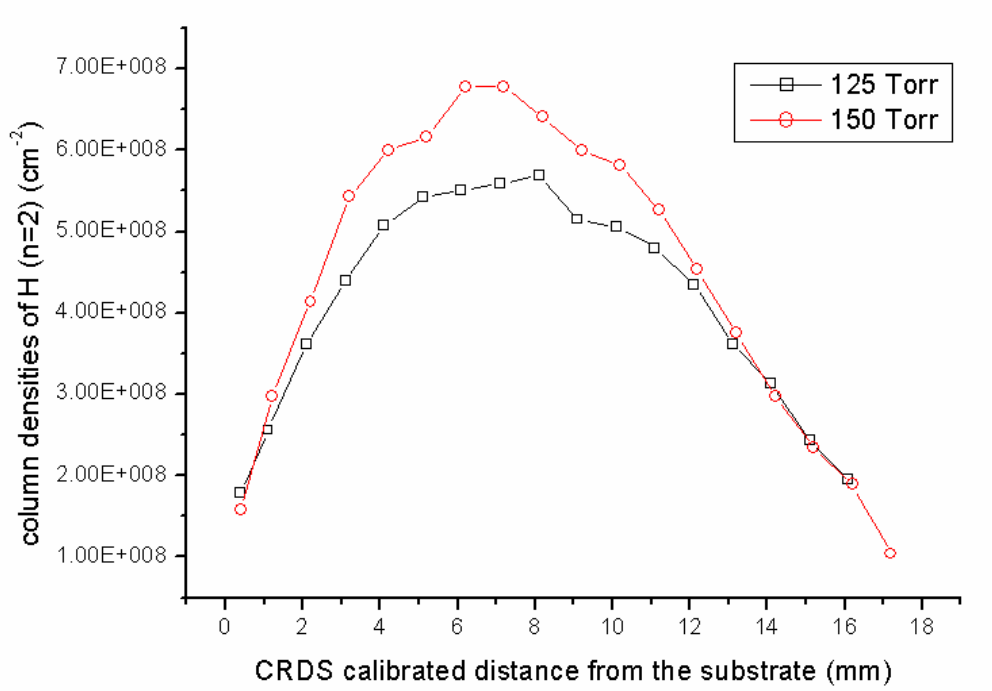

Figure 5. 21. *d* dependent profiles of H(n=2) atom column densities measured at p = 125 and 150 Torr

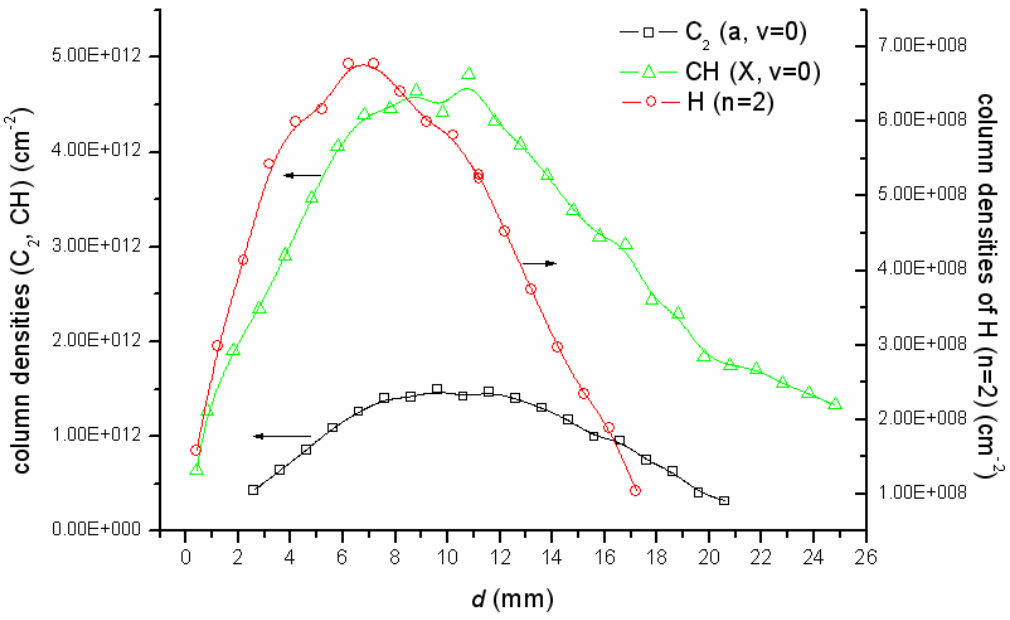

Figure 5. 22. *d* dependent profiles of C_2(a, v=0), CH(X, v=0) and H(n=2) column densities measured under standard conditions

5.3.8 Comparison between $CH_4/Ar/H_2$ and $C_2H_2/Ar/H_2$ plasma

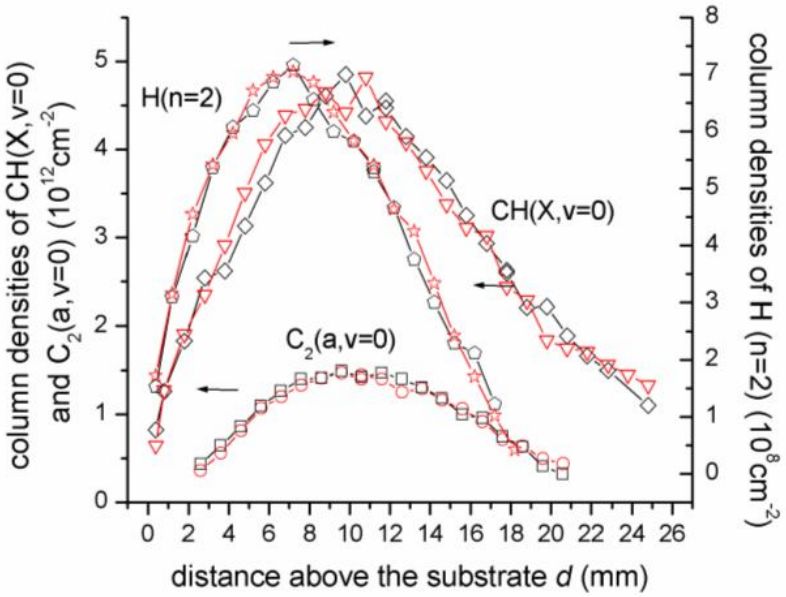

Figure 5. 23. C_2(a, v=0), CH(X, v=0) and H(n=2) column density profiles in $CH_4/Ar/H_2$ and $C_2H_2/Ar/H_2$ plasmas (black and red curves, respectively) under standard operating conditions.

The CRDS measured column density profiles of three "hot" species C_2(a, v=0), CH(X, v=0) and H(n=2) in $CH_4/Ar/H_2$ and $C_2H_2/Ar/H_2$ plasmas under 'standard' discharge conditions with the same carbon flow rate are shown in **Figure 5. 23**. As discussed in Chapter 4, due to the $CH_4 \leftrightarrow C_2H_2$ inter-conversion, no matter what kind of hydrocarbon source gas is used, in the hot region (in and around the plasma ball), the favored stable hydrocarbon is predominantly C_2H_2. Thus, the plasma chemistry is largely insensitive to the choice of hydrocarbon feedstock. The measured profiles of each species in **Figure 5. 23** are essentially identical in the two plasmas – consistent with the prediction from the reaction schemes and mechanisms described in Chapter 4.

5.3.9 H_α linewidth

As **Figure 5.5** shows, the measured H_α lineshapes are described well by a single Gaussian function. **Figure 5. 24-27** show fitted line widths w_{SG}, as a function of *d*,

for a range of discharge conditions. As these data show, the measured linewidth is fairly homogeneous throughout the plasma, and rather insensitive to changes in power, CH_4 flow rate and pressure.

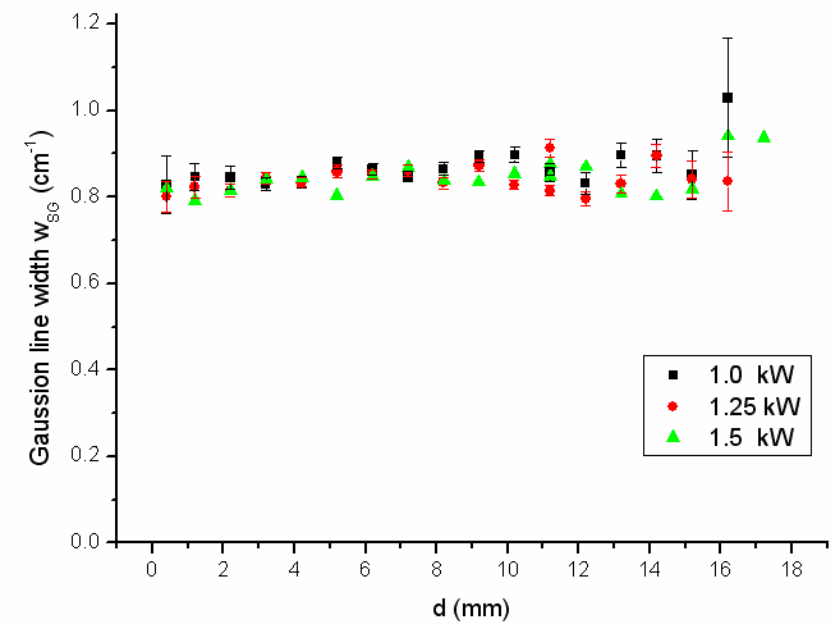

Figure 5. 24. H_α linewidths (FWHM) (fitted with a single Gaussian function) measured as a function of *d* at three different discharge powers

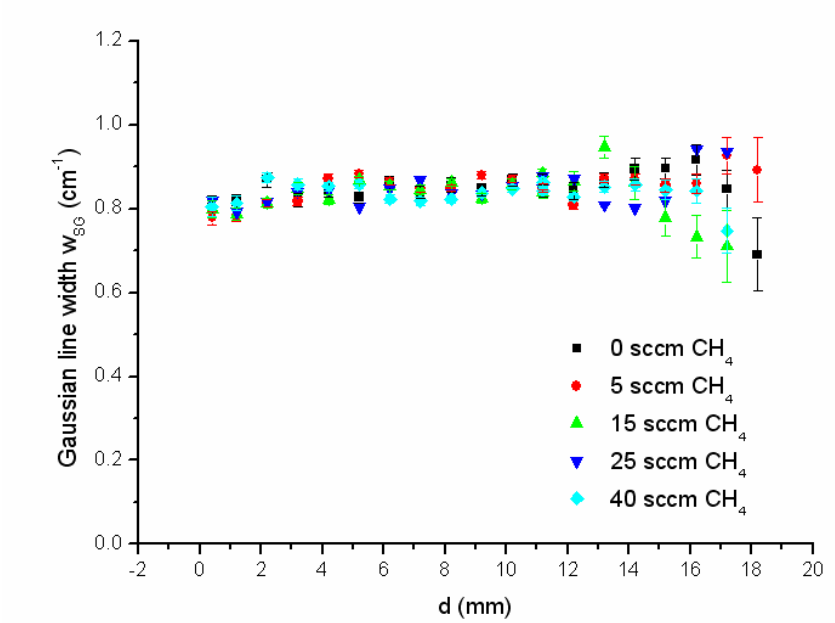

Figure 5. 25. H_α linewidths (FWHM) (fitted with a single Gaussian function) measured as a function of *d* at different CH_4 flow rates

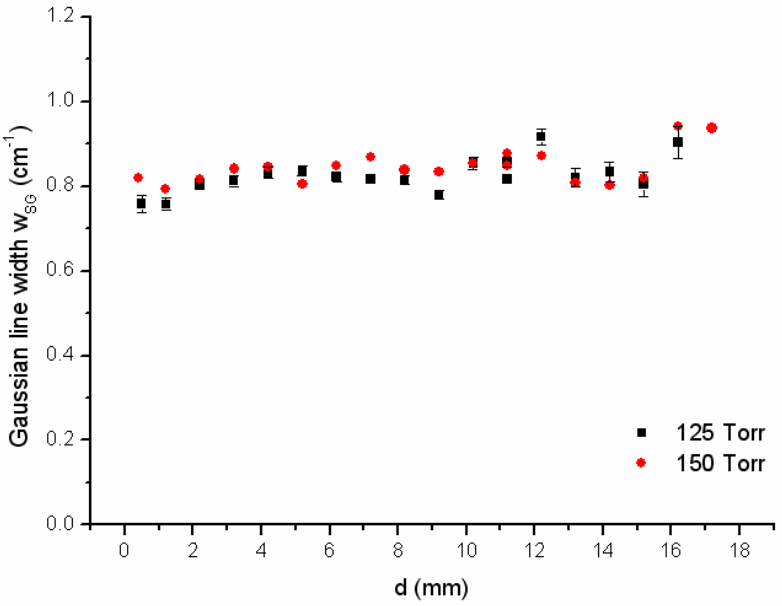

Figure 5. 26. H_α linewidths (FWHM) (fitted with a single Gaussian function) measured as a function of d at p = 125 and 150 Torr

To work out the Doppler broadening determined gas temperature, we need consider possible contributors to the measured line widths. The H_α transition actually comprises seven fine structure transitions (see **Figure 3.2**) and to extract a gas temperature from a measured lineshape it is necessary to deconvolute the contributions from these seven transitions as shown in **Figure 5. 27** – where we have assumed that each fine structure transition has the same line width and a relative intensity proportional to the product of the respective lower state population, and the relevant absorption coefficient, i.e for each transition ($j \rightarrow k$),

$$I_{jk} \propto A_{kj} \lambda_{jk}^2 g_k \text{ ,} \qquad \text{(Eq.5. 19)}$$

Here, j is the lower level and k is the upper level, I_{jk} is the absorption intensity, A_{kj} is the Einstein coefficient, λ_{jk} is wavelength, g_k is the degeneracy of the upper level. All the related coefficients are obtained from NIST Atomic Spectra Database. [16] Such analyses return a typical fine structure transition line width of ~0.75 cm^{-1}. If we attribute all of this width to Doppler broadening (the laser line width is <0.2 cm^{-1}, thus is negligible), we arrive at a gas temperature of ~4750 K – much higher than the

gas temperature estimated from the measured C_2 rotational temperature. The reason for this is still under investigation. We have checked the frequency dispersion (with an etalon), and that the line width is not sensitive to the laser pulse energy (i.e. we are not saturating the H_α transition) and/or the presence of Ar. Lang et al [17] have noted anomalously large H_α line widths in OES studies of microwave activated $CH_4/Ar/H_2$ plasmas, and suggested Stark broadening by the microwave field as a possible explanation.

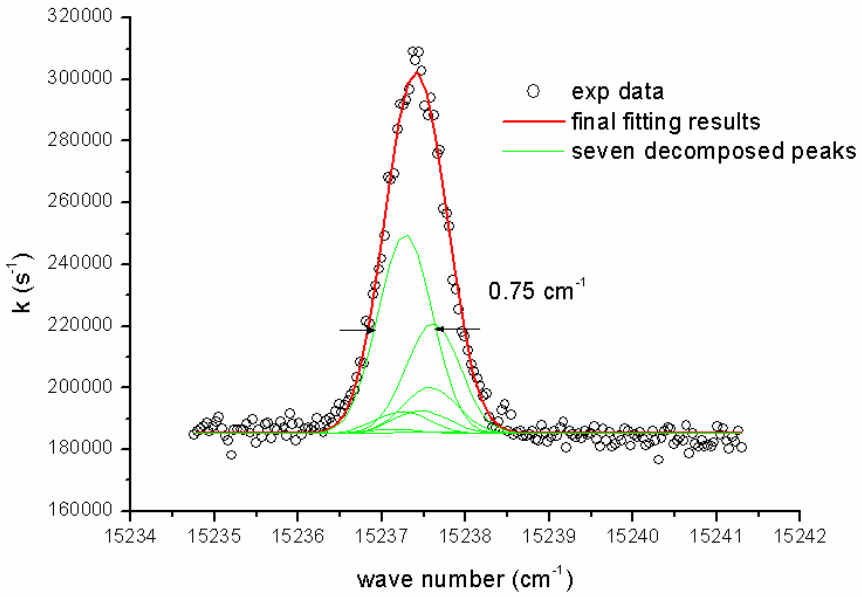

Figure 5. 27. H_α lineshape measured in 1.5 kW, 150 Torr, CH_4/H_2 plasma, along with a deconvolution into its constituent fine structure components. The CH_4 flow rate is 25 sccm and H_2 flow rate is 540 sccm. In order to exclude any broadening effect from Ar,

no Ar was not added.

5.3.10 Gas temperature behaviour

Before, when determining C_2, CH column densities from absorption spectra measured by CRDS, it was necessary to include the Pgopher coefficient, which however is temperature dependent. In previous calculations in **Subsection 5.3.3-5.38**, we have assumed that the gas temperature does not change much when varying the discharge parameters within the range of our experimental conditions.

Now, we have two methods to test the validation of this assumption. One involves using the Doppler broadening of the H_α line, the other uses the intensity ratio of the high *J* and low *J* lines in the C_2 (d-a) absorption spectra. i.e. using the rotational temperature of C_2 as a measure of the real gas temperature. For the second method, specifically, we first pick up those high *J* and low *J* lines shown in **Figure 5. 2** and calculate their total intensity ratio, i.e. $I_{(P37+P38+P39)}/ I_{(R8+R9+R10)}$. Secondly, from Pgopher, we can get a curve of the total line strength ratio of these selected high J and low J lines as a function of the temperature. As shown in **Figure 5. 28**, this curve changes sharply as temperature increases. Finally, given the measured intensity ratio, one can determine the corresponding temperature from the curve shown in **Figure 5. 28**. Such obtained gas temperatures are shown in **Figure 5. 29-32**.

In addition, though the "temperature" obtained from Doppler broadening of H_α spectral line is an overestimation (for reasons that are under investigation), in order to compare with the trend of temperature obtained from C_2, we will plot these linewidths fitted by using a single Gaussian function in **Figure 5. 29-32** as well.

The measured C_2 rotational temperature and H_α line width show very similar behaviour as varying the plasma discharge parameters (i.e power, pressure etc), see **Figure 5. 29-32**. Though, at very low pressure (e.g. 75 Torr), both C_2 rotational temperature and H_α line width indicate a lower gas temperature, (roughly ~300-400K lower than the maximum temperature for C_2), in most other cases, the C_2 rotational temperature or H_α line width show very limited changes, which confirms the previous assumption that the gas temperature is rather invariant to the different experiment conditions investigated here.

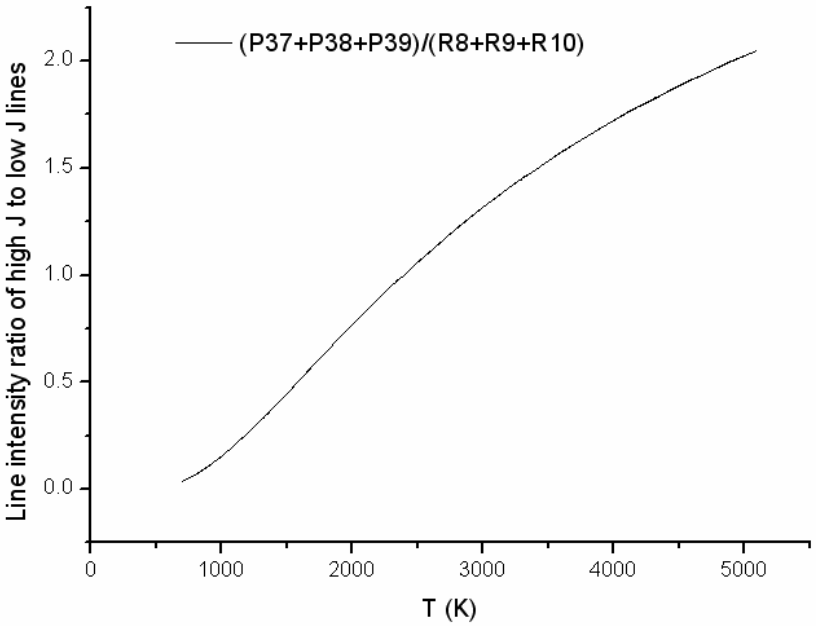

Figure 5. 28 The calculated line intensity ratio of high *J* to low *J* lines of C_2 (i.e. (P37+P38+P39) / (R8+R9+R10)) as a function of the gas temperature (calculated from Pgopher).

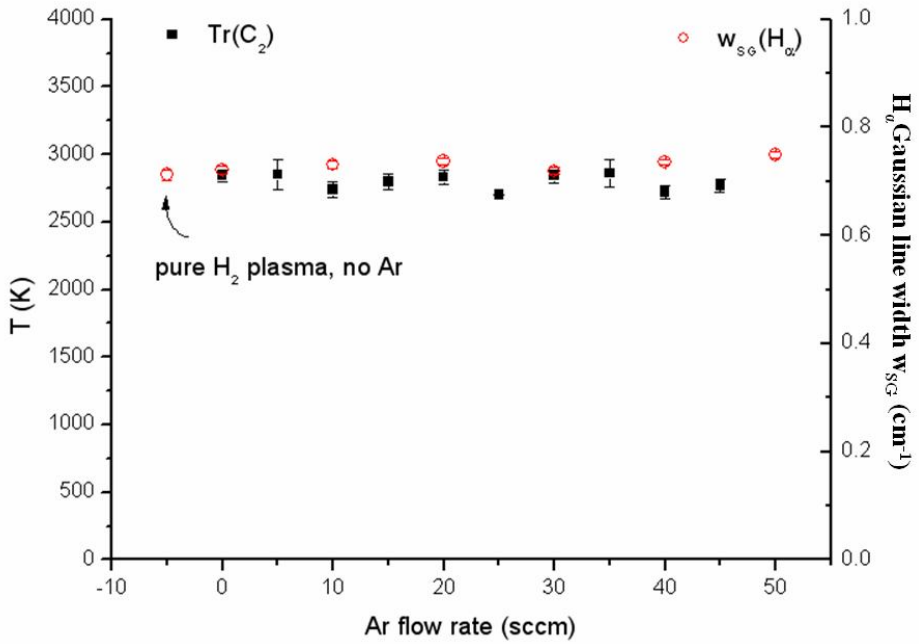

Figure 5. 29 Calculated C_2 rotational temperature and H_α linewidth (fitted with a single Gaussian function) as a function of Ar flow rate

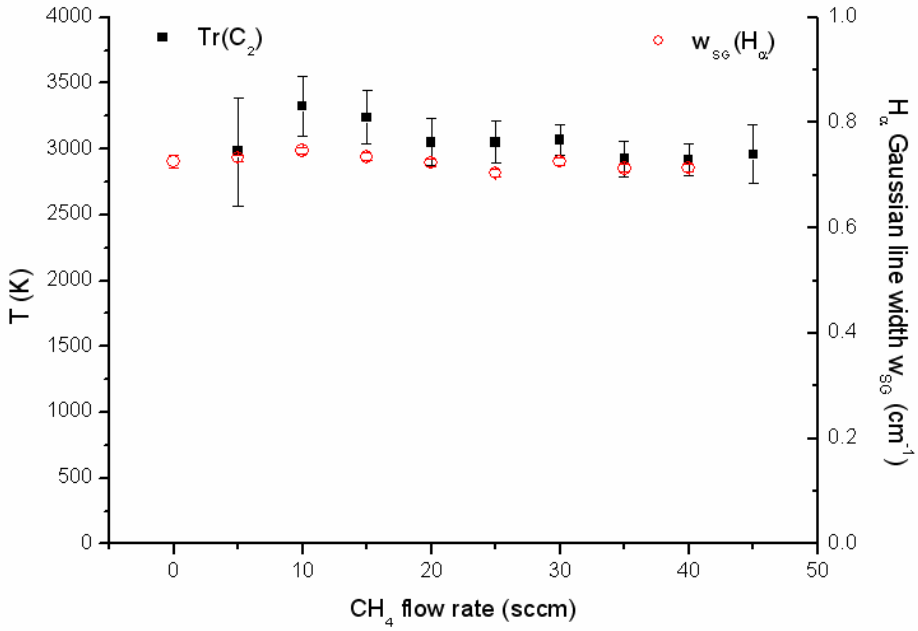

Figure 5. 30 Calculated C_2 rotational temperature and H_α linewidth (fitted with a single Gaussian function) as a function of CH_4 flow rate

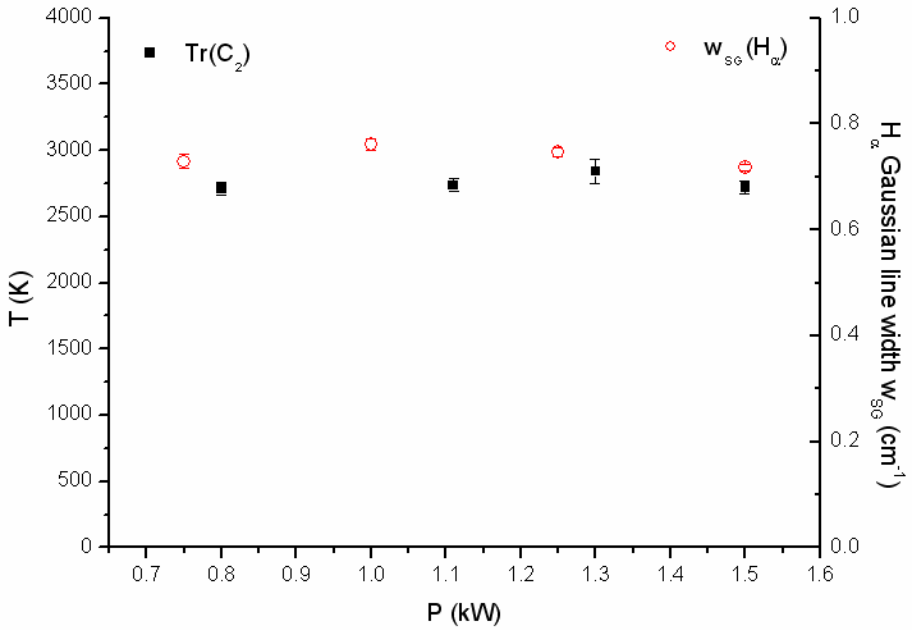

Figure 5. 31 Calculated C_2 rotational temperature and H_α linewidth (fitted with a single Gaussian function) as a function of input power

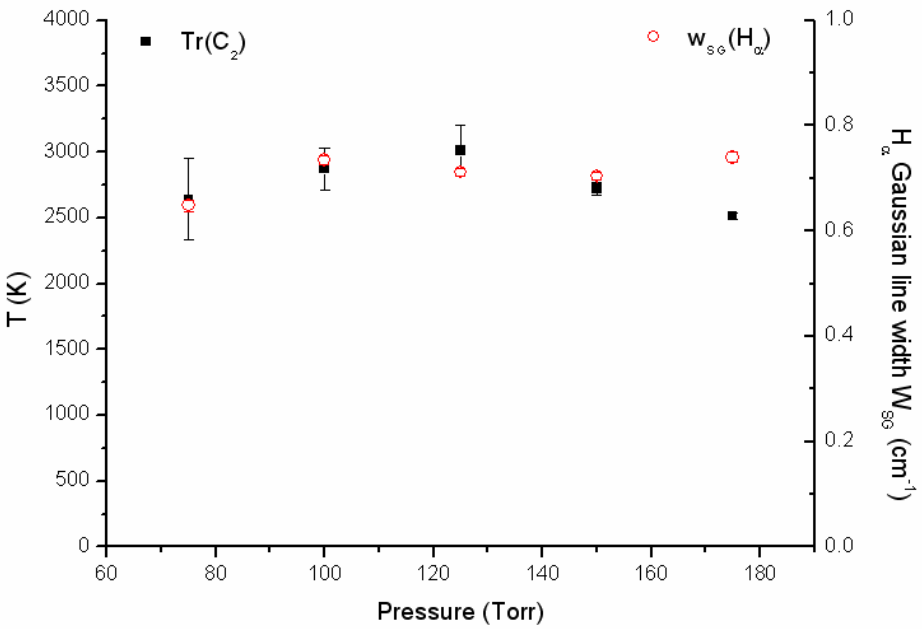

Figure 5. 32 Calculated C_2 rotational temperature and $H_\alpha$linewidth (fitted with a single Gaussian function) as a function of total pressure

5.4 Unknown absorption in $CH_4/Ar/H_2$ plasma

5.4.1. Phenomena

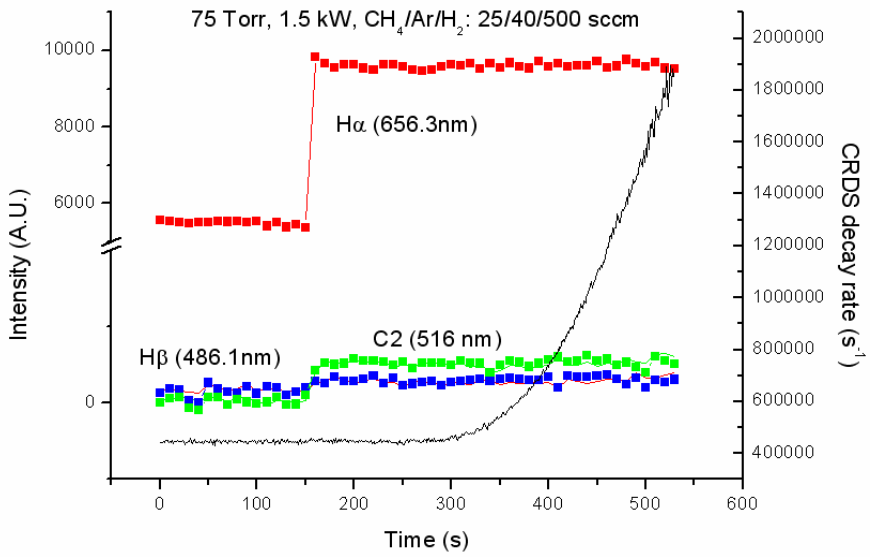

Figure 5. 33 Temporal behaviours of the ring down decay rate from CRDS (probing at λ =427 nm) and the optical emissions from H_α, H_β and C_2 in Ar/H_2 and $Ar/H_2/CH_4$ plasmas. The sudden "jump" of H_α H_β, C_2 emission indicates the time at which CH_4 is introduced.

Another interesting phenomenon observed in the experiments is that, under certain discharge conditions (e.g. low pressure, 10-15 sccm CH_4 flow rate), an as yet unidentified loss develops, which manifests itself as a continuous increase of the ring down decay rate with the time *t* since hydrocarbon is added to the plasma, as shown by the black line in **Figure 5. 33**. (Note, here, the laser wavelength was deliberately set to monitor off-resonance from any CH absorptions.)

At first sight, one might attribute this to mirror contamination. However, the original ring down rate is restored simply by switching off the plasma and evacuating the chamber. This is quite different from behaviour observed when probing the arc-jet reactor, where mirror contamination resulted in a progressive drop in ring down time which could only be restored by removing and cleaning the mirrors. Another relevant observation is that moving the laser beam so as to probe a column near the top of the plasma ball (large *d*) or very close to the substrate ($d \sim 0$), results in recovery of the original ring down rate, without any adjustment to the process conditions. This finding is also very repeatable. Thus, we exclude the effect from the mirror contamination. Given the large separation between the mirror mounts and the plasma, we rule out the possibility that thermally induced drift of the mirror alignment could be responsible for the observed deterioration of the ring down time. Further evidence in support of this conclusion comes from the fact that, when the ring down time becomes poorer, it cannot be recovered by realigning the mirrors. Thus the observation is concluded to be the result of the build-up of a plasma-induced (and as yet unknown) absorber or scatterer.

The results of more detailed investigations of the phenomenon are summarized in the following. The ring down decay rate is assumed to be proportional to the absorbance of the unknown absorber, X and, for simplicity, the argument will be developed assuming that the loss is associated with absorption rather than scattering. An increase in the ring down decay rate implies a build-up in the column density of X. To quantify this temporal behaviour, the OES is monitored at the same time.

The emission spectrum is measured every 10 seconds, over the same time period as the CRDS measurements. More details about the OES experimental setup and the typically measured spectrum can be found in Chapter 6. **Figure 5. 33** shows the background-corrected H_α H_β and C_2 (516 nm) emission intensities measured as a function of time, together with the ring down data monitoring at λ =427 nm. Time "zero" is the point at which data starts to be taken, from a pre-existing Ar/H_2 plasma. The time at which CH_4 is introduced can be easily recognized from the graph due to the "jump" in all three emissions. The reason for the increase of C_2 emission is self-evident, and reasons for the jump in the H_α and H_β emission intensities will be discussed in Chapter 6. From **Figure 5. 33**, it can be seen that absorption by X occurs after CH_4 is added - suggesting that the carrier is some carbon-containing species. As a further check, the H_α, H_β and C_2 (516 nm) emissions and the ring down decay rate at λ = 427 nm were also monitored for a much longer time period when using a pure Ar/H_2 plasma – see **Figure 5. 34**. Clearly, without CH_4 addition, the unknown absorption is not detectable.

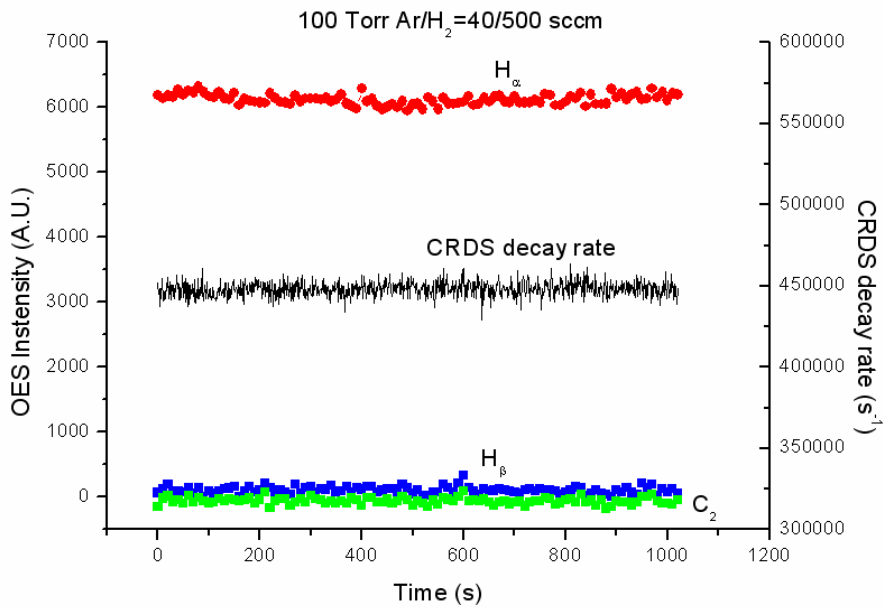

Figure 5. 34 Temporal behaviours of the optical emissions from H_α H_β, C_2 and the ring down decay rate from CRDS (probing at λ =427 nm) in Ar/H_2 plasma.

5.4.2. Spatial profile

It is not easy to determine the spatial profile of X in the reactor because the CRDS measurements cannot follow its build-up until it reaches an asymptotic value. (In all cases, the ring down rate keeps increasing and the ring down time eventually becomes too short to be fitted reliably). This time evolution of the absorption means that it cannot be profiled reliably simply by translating the probe column up and down. Nevertheless, the spatial profile does provide much information. Rather than do nothing, the following (rather rough) method was adopted to determine the spatial distribution of X. In practice, we start measuring the ring down rate at the position furthest from the substrate, d_0, and step down progressively measuring the ring down rate at each d_i for a common time interval, Δt. After reaching the position closest to the substrate, at d_n, we go back and resample at each d_i, over a similar time interval, Δt, until finally returning to the initial d_0 position. Such a procedure has been shown in **Figure 5. 35**. Thus totally, $2n+1$ ring down rates are measured at $n+1$ positions. Except for the position closest to the substrate, the ring-down decay rates have been measured twice for each position d_i, an early one at time

$$t_{early} = t_0 + i\Delta t = t_n - (n-i)\Delta t \qquad \text{(Eq.5. 20)}$$

and a later one at

$$t_{late} = t_0 + (2n-i)\Delta t = t_n + (n-i)\Delta t \qquad \text{(Eq.5. 21)}$$

Here, t_0 is the time when we measure the first ring-down rate at position d_0. t_n is the time at which the ring-down rate at position d_n is measured. If we assume that the ring down decay rate changes linearly with time with a slope A_i, (A_i can be different for different positions), then the two decay rates measured at the same position d_i can be written as

$$k_i[t_{early}] = k_i[t_n - (n-i)\Delta t] = k_i[t_n] - A_i(n-i)\Delta t \qquad \text{(Eq.5. 22)}$$

$$k_i[t_{late}] = k_i[t_n + (n-i)\Delta t] = k_i[t_n] + A_i(n-i)\Delta t \qquad \text{(Eq.5. 23)}$$

Therefore, the ringdown rate at time t_n for each position d_i can be given by averaging the two ring-down decay rates measured at the same position but different times, i.e.

$$k_i[t_n] = \frac{k_i[t_{early}] + k_i[t_{late}]}{2} \qquad \text{(Eq.5. 24)}$$

Thus the profile of the ringdown rate (i.e the column density of unknown absorber X) at time t_n can be obtained.

The assumption that the ring down decay rate changes linearly with time at a fixed position does not deviate from the truth too much. (See later in **Figure 5. 38**, the ring down decay rate increases almost linearly with time after an initial induction period, so measurements of this kind are commenced after the induction period). **Figure 5. 35** shows an illustrative set of data, measured at λ =427 nm. Data gathering for this figure started at d ~24 mm, followed the red arrow towards d = 0, then retraced its path (blue arrow) back to the starting point. Clearly, because the unknown absorber builds up with time, the ring down decay rates measured later are always larger than the earlier one. This difference in ring down decay rates is very small at the edges, however. **Figure 5. 36** shows the average decay rate determined at each position d_i. The resulting profile, which shows a hint of a central dip, suggests that the unknown absorber is closely related to the plasma ball.

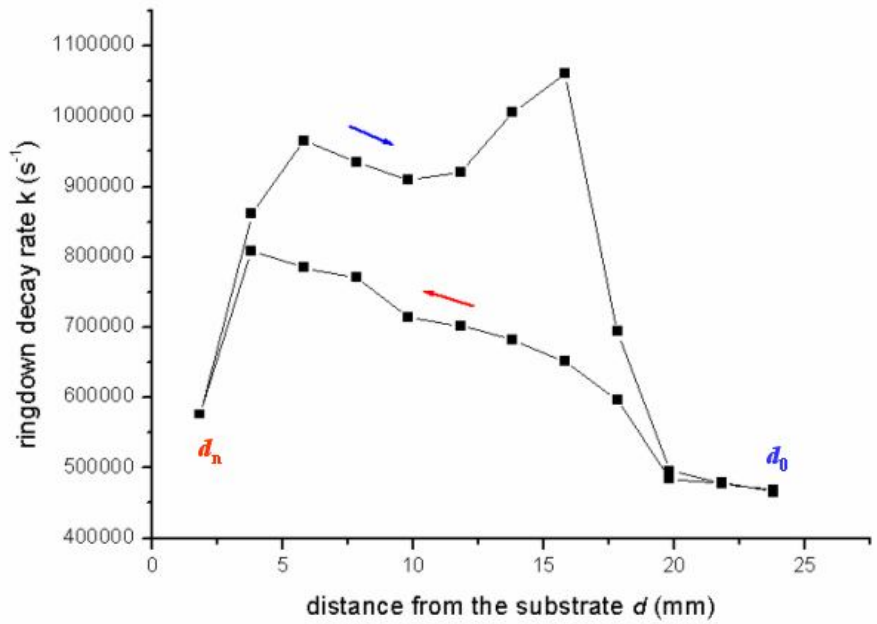

Figure 5. 35 Measured ring down decay rates at each position, *i*. Measurements started at large *d*, following the red arrow until reaching d = 0 then re-sampled at increasing *d* (blue arrow).

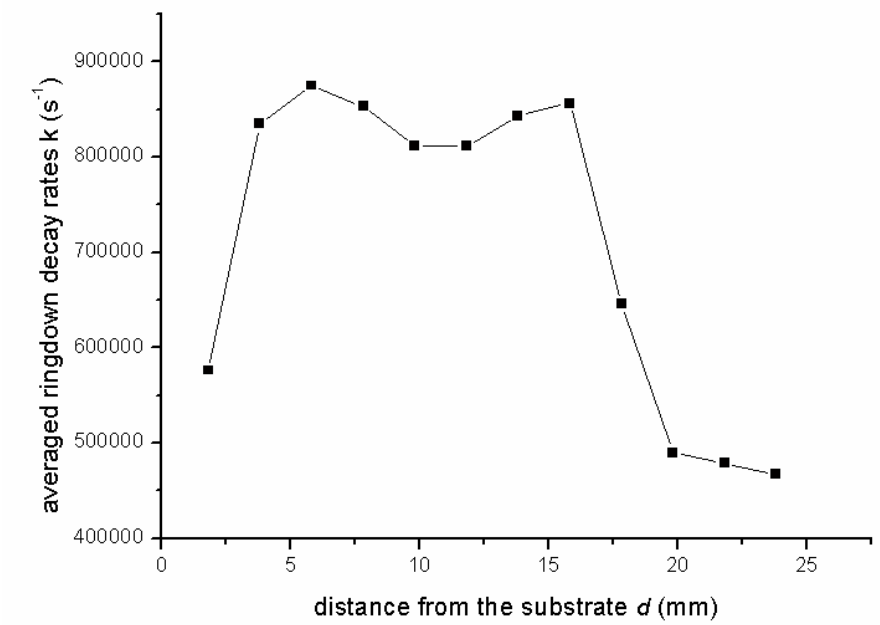

Figure 5. 36 The profile of the averaged ring down decay rates from data shown in Figure 5. 35

5.4.3. Effect of CH_4 flow rate

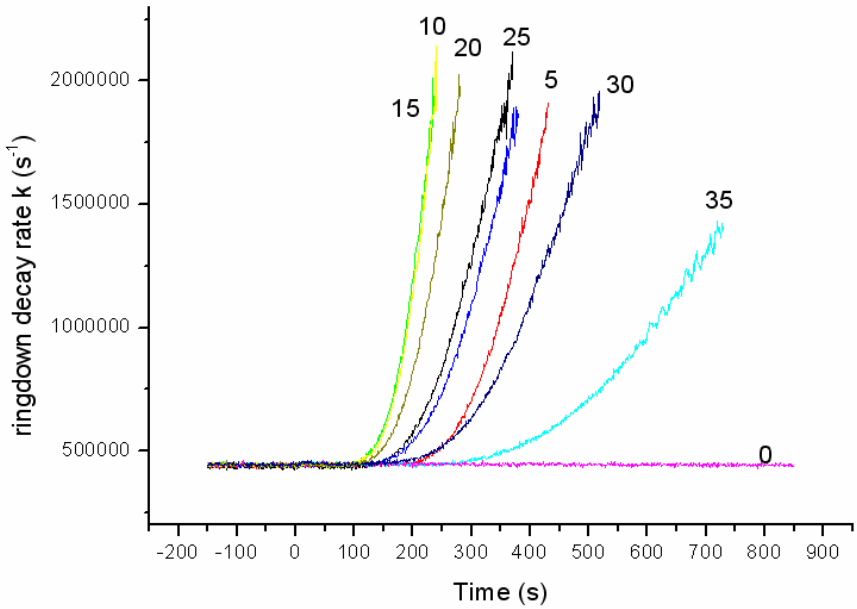

Figure 5. 37 Effect of CH_4 flow rate on temporal behaviour of the ring down decay rates measured at λ = 427 nm and p = 75 torr. Other discharge parameters are the same as the "standard conditions". Time "zero" is when the CH_4 is first introduced.

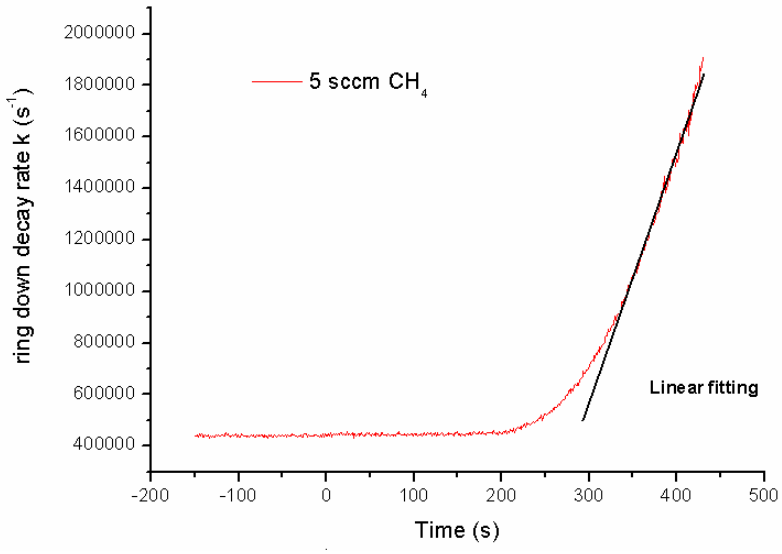

Figure 5. 38 Example of fitting the build-up speed of the unknown absorber. This ring down decay rate was measured using 5 sccm CH_4 flow rate, 75 torr and 1.5 kW microwave power, monitoring at λ =427 nm.

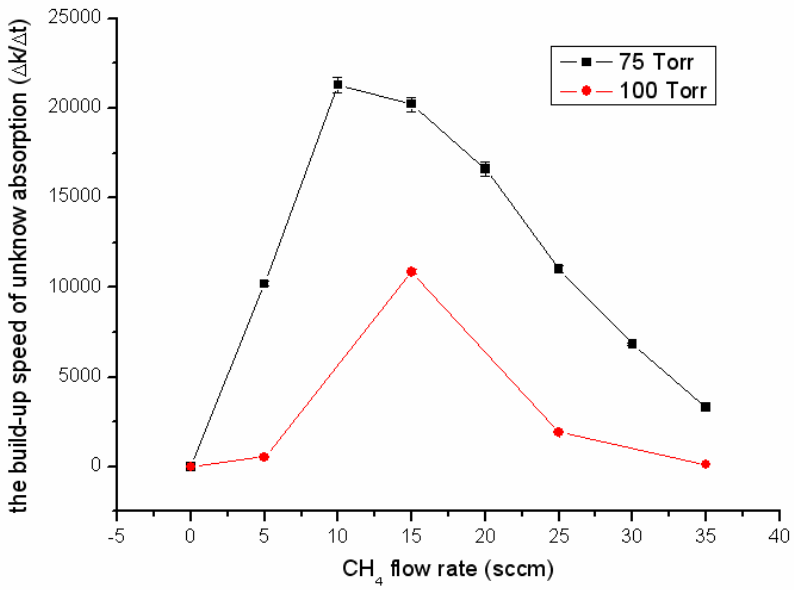

Figure 5. 39 Plot showing the variation in the speed with which the unknown absorber develops at different CH_4 flow rates

Another interesting phenomenon about the unknown absorption is that its occurrence seems very sensitive to the CH_4 flow rate. **Figure 5. 37** shows the temporal behaviour of the ring down decay rates when introducing different CH_4 flow rates to a pre-existing Ar/H_2 plasma at a total pressure, p = 75 Torr. Again, the origin of the

"*time*" axis defines the time when the CH_4 is added. As **Figure 5. 37** shows, the ring down rate remains constant when no CH_4 is added (i.e. 0 sccm CH_4 flow rate), – implying that the unknown absorber is not formed under this condition. Addition of any CH_4 yields the unknown absorption, but its build-up rate appears to be sensitive to the CH_4 flow rate ; the induction period is shortest, and the rate of change of the ring down decay rate greatest at CH_4 flow rates ~10-15 sccm. To show this trend more quantitatively, we can define a build-up rate for the unknown absorber by the method illustrated in **Figure 5. 38**. As this figure shows, the temporal behaviour of the ring down decay rate at later time is well described by a straight line. Thus we can use the slope, $R = \Delta k/\Delta t$, of this fitting line as a measure of the speed of build-up of X. The deduced speeds for different CH_4 flow rates at p = 75 torr and a probe wavelength of 427 nm are shown in **Figure 5. 39**. Clearly, the unknown absorption builds-up most rapidly when the CH_4 flow rate is ~10-15 sccm. **Figure 5. 40** shows that similar phenomena are observable at p = 100 torr. The deduced speeds for the unknown absorber under these conditions are also shown in **Figure 5. 39.** At this p, the unknown absorption builds up fastest at a CH_4 flow rate of ~15 sccm; at much higher CH_4 flow rates (e.g. 35 sccm) it builds up much more slowly.

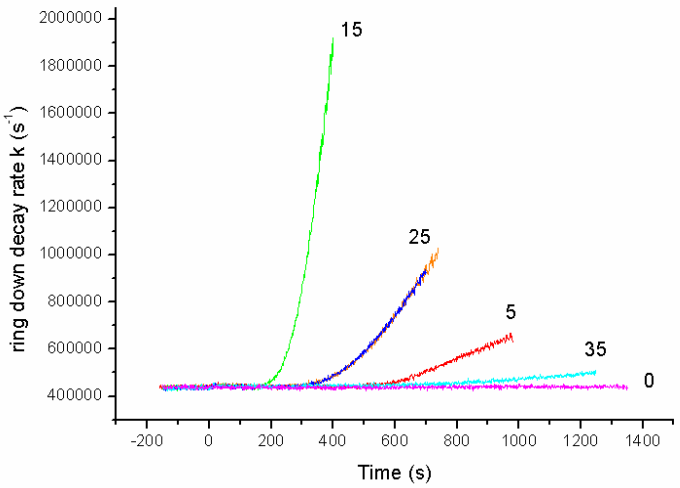

Figure 5. 40 Effect of CH_4 flow rate on temporal behaviour of the ring down decay rates measured at λ =427 nm and p = 100 torr. Other discharge parameters are as for our "standard conditions". Time "zero" is when the CH_4 is first introduced.

5.4.4. Effect of total pressure

The occurrence and build-up speed of the unknown absorber are also very sensitive to the total pressure. As shown in **Figure 5. 41**, under high pressure (e.g. p = 150 torr) it takes much longer for the ring down decay rate to change perceptibly. Conversely, at lower pressure (e.g. p = 75 or 100 torr), the absorption can build up much more quickly.

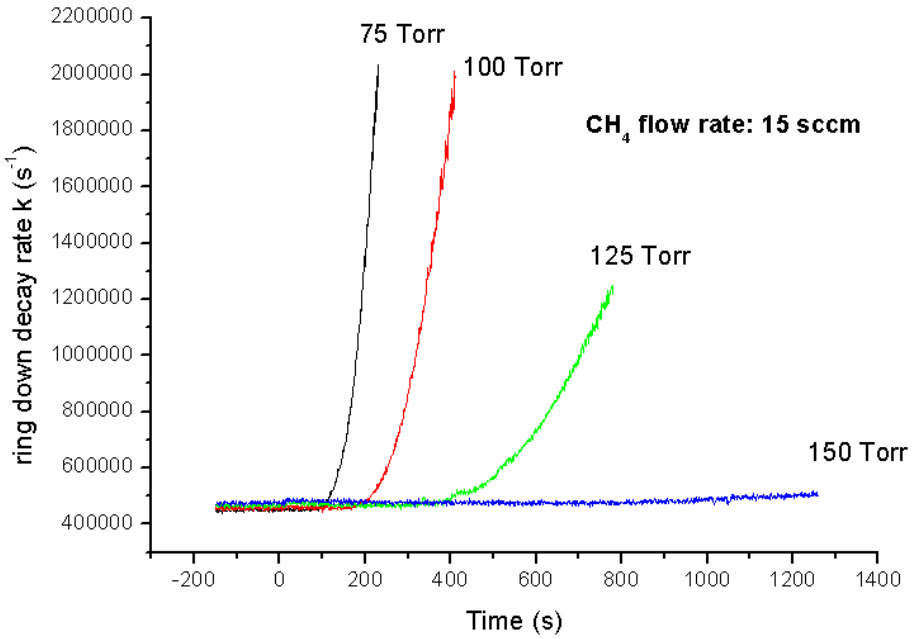

Figure 5. 41 Effect of pressure on the temporal behaviour of the ring down decay rates under 15 sccm CH_4 flow rate. Other discharge parameters are as for our "standard conditions". Time "zero" is when the CH_4 is first introduced.

5.4.5. Effect of hydrocarbon feedstock

The identity of the hydrocarbon source gas has some impact on the unknown absorption. **Figure 5. 42** shows the temporal behaviour of the ring down decay rates measured in $CH_4/Ar/H_2$ and $C_2H_2/Ar/H_2$ plasmas, at λ = 427 nm, under different carbon flow rates. At low carbon flow rates (e.g. 5 sccm) the temporal behaviours for the two hydrocarbon feedstocks are almost identical to one other. At higher carbon flow rates, however, the unknown absorption appears to grow in a bit faster when using a $C_2H_2/Ar/H_2$ plasma than with the $CH_4/Ar/H_2$ plasma. Consistent with

the QCL probing results (in Chapter 4), the parallel behaviours observed at low flow rates probably reflects the fact that, under such conditions, the $CH_4 \leftrightarrow C_2H_2$ inter-conversion is so efficient that the gas compositions in the two plasmas are essentially identical.

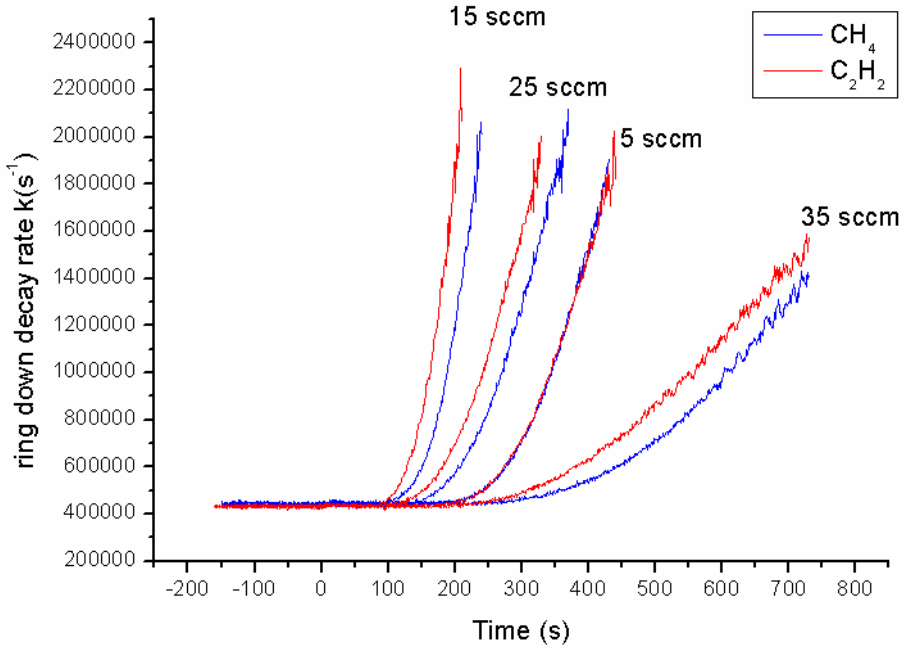

Figure 5. 42 Comparison of the temporal behaviours of the ring down decay rates in $CH_4/Ar/H_2$ and $C_2H_2/Ar/H_2$ plasmas for different carbon flow rates. Time "zero" is when the relevant hydrocarbon is first introduced.

5.4.6. Effect of wavelength

The temporal behaviour of the ring down decay rates has been monitored at several different laser wavelengths. Again, the laser wavelength is deliberately set to monitor off-resonance from any of the sharp atomic (eg H_α) or molecular (CH or C_2) absorptions. **Figure 5. 43** shows a series of measurements made under identical plasma conditions at four closely spaced wavelengths around 427 nm; no evident differences are observed, suggesting that X must have a broad and unstructured absorption (or scattering cross-section) in this wavelength range. Simply changing the excitation wavelength to 656 nm (the CRDS mirrors are also changed) while maintaining the same plasma operating conditions results in a slower build-up time, however, as shown in **Figure 5. 44**.

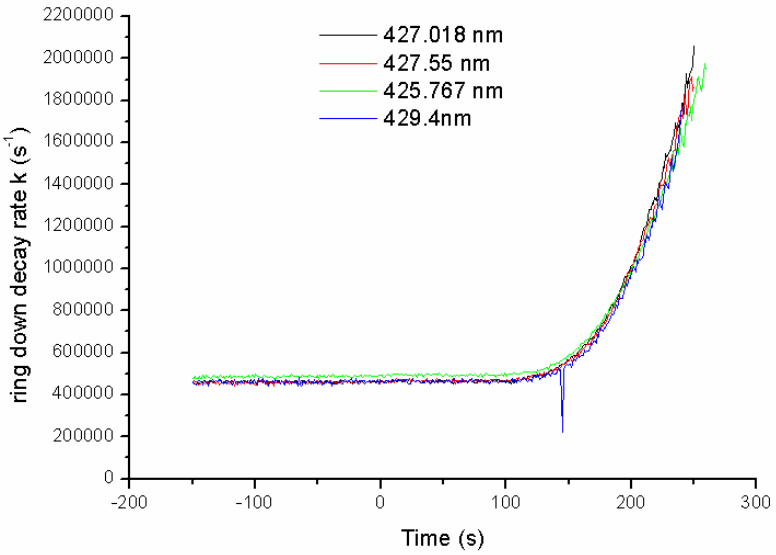

Figure 5. 43 Temporal behaviour of the ring down decay rates measured at four different wavelengths in a $CH_4/Ar/H_2$ plasma operating with 15 sccm CH_4, 510 sccm H_2 and 40 sccm Ar, 1.5 kW input power, total pressure 75 torr. Time "zero" is when the CH_4 is first introduced.

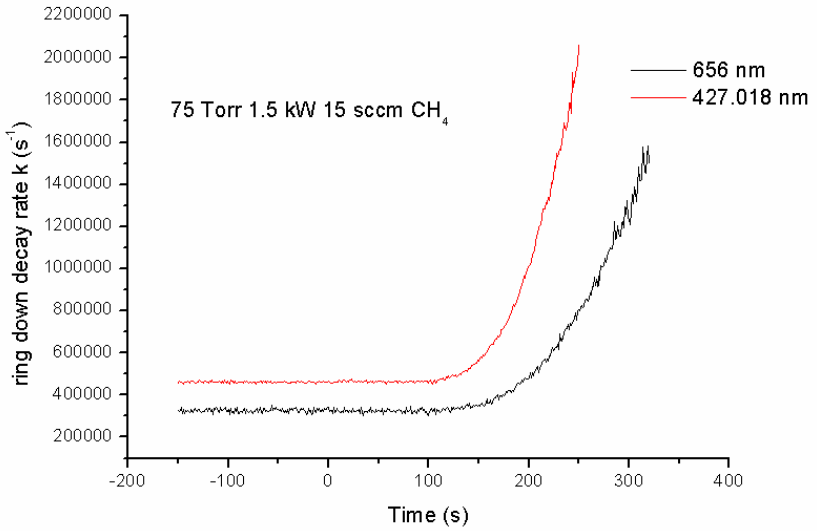

Figure 5. 44 Temporal behaviour of the ring down decay rates measured at λ = 427 nm and 656 nm in $CH_4/Ar/H_2$ plasma under the standard discharge condition. Time "zero" defines when the CH_4 is first introduced.

5.5 Summary

Cavity ring down spectroscopy has been successfully used to measure the absolute column densities of three "hot" species C_2(a, v=0), CH(X, v=0) and H(n=2), and also

their spatial profiles, as functions of discharge parameters (power, pressure etc). The essentially identical profiles of these three "hot" species in $CH_4/Ar/H_2$ and $C_2H_2/Ar/H_2$ plasmas under the same discharge conditions, with the same carbon flow rate, confirm the proposed reaction mechanisms in Chapter 4, i.e. due to the interconversion of CH_4 and C_2H_2, the hydrocarbon species around and within the plasma are mainly C_2H_2, the plasma thus is insensitive to the detailed choice of what kind of hydrocarbon feedstock. The gas temperature can also be determined from the C_2 rotational line intensity ratios and the Doppler broadening of the H_α transitions. However, "temperatures" determined from the latter show more than 1000 K higher than those determined from C_2. The reasons for this huge discrepancy are still not clear. But both approaches show that the gas temperature does not change much as a result of changing the discharge conditions.

5.6 References

[1] L. Thomas, J. L. Jauberteau, I. Jauberteau, *et al.*, *Plasma Chemistry and Plasma Processing*, **17** (1997) 193.

[2] C. J. Rennick, R. Engeln, J. A. Smith, *et al.*, *J. Appl. Phys.*, **97** (2005) 113306.

[3] C. E. Johnson, W. A. Weimer and F. M. Cerio, *J. Mater. Res.*, **7** (1992) 1427.

[4] Y.-S. Han, Y.-K. Kim and J.-Y. Lee, *Thin Solid Films*, **310** (1997) 39.

[5] C. J. Chu, M. P. D'Evelyn, R. H. Hauge, *et al.*, *J. Mater. Res.*, **5** (1990) 2405.

[6] Y. A. Mankelevich, N. V. Suetin, M. N. R. Ashfold, *et al.*, *Diamond Relat. Mater.*, **12** (2003) 383.

[7] K. Takeuchi and T. Yoshida, *J. Appl. Phys.*, **21** (1992) 2636.

[8] Pgopher spectral simulation program written by C. M. Western. *http://pgopher.chm.bris.ac.uk*.

[9] D. G. Goodwin and J. E. Butler, *Handbook of Industrial Diamonds and Diamond Films*, (Marcel Dekker, New York, 1998).

[10] A. Gicquel, M. Chenevier, Y. Breton, *et al.*, *J. Phys. III France*, **6** (1996) 1167.

[11] NIST Electron Impact Ionization Cross Section Database *http://physics.nist.gov/PhysRefData/Ionization/index.html*.

[12] G. Lombardi, K. Hassouni, G.-D. Stancu, *et al.*, *J. Appl. Phys.*, **98** (2005) 053303.

[13] G. Lombardi, K. Hassouni, G. D. Stancu, *et al.*, *Plasma Sources Sci. Technol.*, **14** (2005) 440.

[14] M. A. Lieberman and A. J. Lichtenberg, *Principles of Plasma Discharges and Materials Processing*, (John Wiley & Sons, Inc., 2005).

[15] J. B. Wills, J. A. Smith, W. E. Boxford, *et al.*, *J. Appl. Phys.*, **92** (2002) 4213.

[16] NIST Atomic spectra database *http://physics.nist.gov/PhysRefData/ASD/index.html*.

[17] T. Lang, J. Stiegler, Y. v. Kaenel, *et al.*, *Diamond Relat. Mater.*, **5** (1996) 1171.

Chapter 6 Optical emission spectroscopy diagnostics of $Ar/H_2/CH_4$ plasmas in a microwave reactor used for diamond CVD

6.1. Introduction

Optical emission spectroscopy (OES) is a non-invasive technique which enables individual monitoring of "fingerprint" optical emissions from specific species. It may be the easiest way to study the behaviour of the emitting species in the plasma. However, not all species emit and in many cases the analysis and interpretation of OES results can be ambiguous. Nonetheless, OES does provide an opportunity to have a first look at what is present in the plasma and, in some cases, careful analysis can actually yield more information than might have been expected.

When using OES (visible – UV) to study species, one must realize that these emissions are from energetic species. These species are very sensitive to the electron characteristics, i.e. electron densities and electron temperature, for the following reasons. The energy gaps corresponding to these emissions are normally much larger than these species' thermal energy. Therefore, in most cases, electron impact excitation plays the major role in "pumping" these species from the lower states to the upper states. This is especially so for atoms like H, which have very big energy gaps between their excited states and ground states. Also, in contrast to molecules and radicals, atoms do not have rotational and vibrational structures. So they can not be pumped to high excited states by "cascade pumping". Therefore, the emissions from atoms show strong dependences on the electrons. Due to such characteristics, in most cases, the results from OES carry much information about the electrons in the plasma, which is quite different from absorption spectroscopy measurements. Absorption spectroscopy measures the contribution from the lower states. If the lower states are ground states or energy levels that are not much higher than thermal

energy, thermal collisions are sufficiently energetic to populate them. As a result, absorption spectra will carry more information about the thermal chemistry rather than electron chemistry. From this point of view, OES is a more sensitive tool to investigate the electron driven chemistry than is absorption spectroscopy.

Though limited in the ability to give absolute species concentrations, some "revised" OES methods, such as actinometry, [1-7] can give the relative concentrations of species. Further careful calibration can also yield absolute values of some plasma parameters such as the degree of dissociation of a molecule. [3-5]

In the following sections, experiments describing the use of OES to investigate the behaviour of selected species, including H atoms, excited states of Ar and H_2, C_2, CH radicals are reported. Actinometry methods are also used to study the behaviour of H(n=1) atoms. The validity of actinometry methods under the present experimental conditions is discussed. Finally, the measured emission behaviours of C_2, CH and H are compared with their measured column density behaviours under different discharge conditions.

6.2. Experimental

The OES experimental set up is shown in **Figure 6. 1.** The optical fiber was firstly set up as the Optical fiber I (8), positioned at the focus of a glass lens (12). Such a system then monitors the radiation from the plasma through an aperture with diameter around 9 mm behind the chamber window. Thus the optical fibre only collects emissions from a small region around the center to bottom of the plasma ball. At the same time, spatially resolved CRDS (which has already been shown in **Figure 5.1**) measurements were performed. In addition, in order to profile the emissions of species in the plasma, the optical fiber was set up as the Optical fiber II (9) and mounted on the movable optical table (6), see **Figure 6. 1**. The bellows and CRDS mirrors in **Figure 5.1** were replaced by two diamond windows. A light-confining

device composed of two apertures and a tube was put before the optical fiber, ensuring a spatially-resolved monitoring of the emissions from the plasma with a resolution better than 2 mm. The optical system then was moved up and down by adjusting the movable bench and the emission profiles of the species then were recorded.

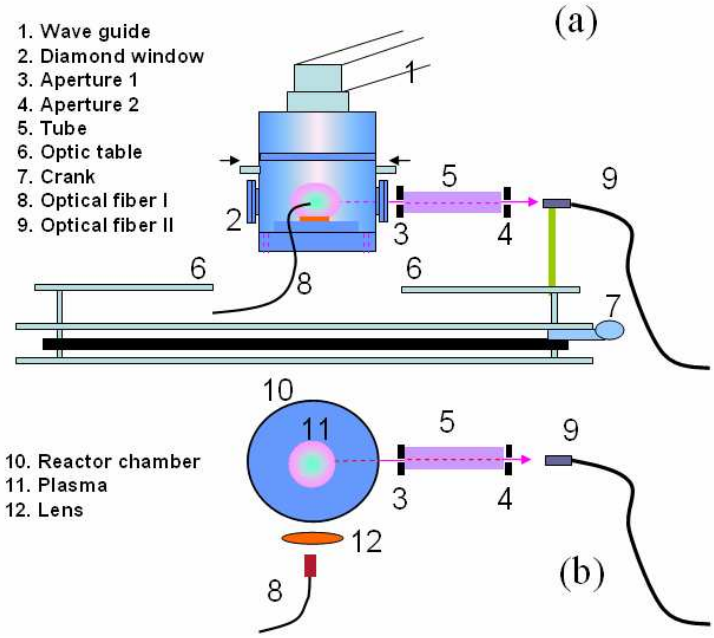

Figure 6. 1 Schematic of the OES experimental setup: (a) the front view; (b) the top view.

The collected light was sent to a monochromater equipped with a CCD detector (Oriel Instaspec IV, 600 lines mm^{-1} ruled grating). The resolution of this spectrometer is ~0.5 nm. The grating was set at two positions so as to cover two wavelength ranges: the longer wavelength range (in this chapter around 540-840nm) and shorter wavelength range (in this chapter around 380-680 nm). In order to reduce background noise, the CCD detector was cooled to 10°C. The exposure time is 100 ms and the data are averaged 2000 times for each spectrum when optical fiber was set as Optical fiber I. When the optical fiber was set as Optical fiber II in the spatially-resolved OES experiments, an extremely long exposure time 60~80 s with 3 averages is used for each spectrum. The emission lines for selected species and their corresponding transitions are summarized in Appendix C.

6.3. Results and discussion

6.3.1 The validity of actinometry method in moderate pressure Ar/H_2 and $Ar/H_2/CH_4$ plasmas

Gicquel et al have discussed about the validity of using actinometry techniques at pressures around 25 Torr. [7, 8] Though still 6 times lower than the pressure used in our experiments, their results are still quite instructive for us. Thus, a similar procedure is followed here in order to evaluate the validity of using actinometry under our experimental conditions.

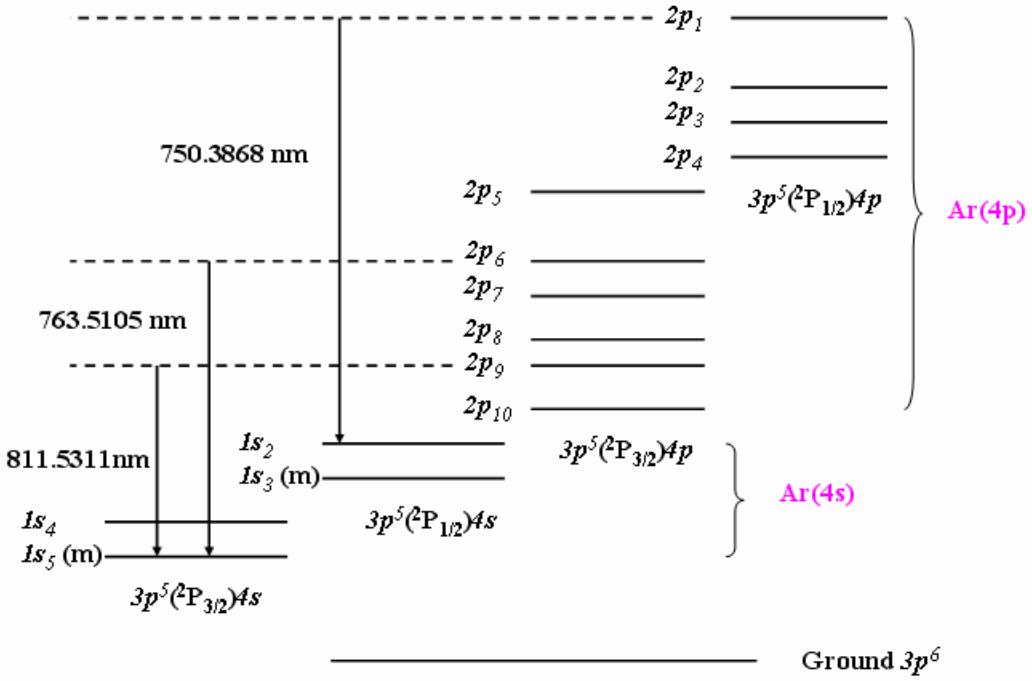

Figure 6. 2. Schematic of transitions and *4s* and *4p* energy levels of Ar

As Gicquel suggested, [8] the Ar 750.4 nm and H_α emission lines are chosen here for actinometry due to the similar thresholds and electron impact excitation cross section dependence on electron temperature of Ar ($2p_1$) and H(n=3). The Ar transitions and their corresponding energy levels are shown in **Figure 6. 2**. It can be seen that Ar has two excited states, Ar(4s) and Ar(4p), which further split into 4 (i.e.$1s_1$-$1s_4$) and 10 (i.e. $2p_1$-$2p_{10}$) energy levels, respectively. The main processes involved in the

production and consumption of the H(n=3) and Ar ($2p_1$) states are shown in **Table 6. 1** and **Table 6. 2**.

Table 6. 1 Main processes involved in the production and consumption of H (n=3)

Reaction Name	**Reactions**		**Rate constant**
Production			
Electron excitation from ground states	H(n=1)+e→H(n=3) + e	(R6.1)	$K_e^{H_\alpha}$
Dissociative excitation	H_2 + e→H(n=3) +H(n=1) + e	(R6.2)	K_{diss}
Consumption			
Radiative de-excitation	H(n=3) → H(n=2)+hv	(R6.3)	A_{32}
Radiative de-excitation	H(n=3) → H(n=1)+hv	(R6.4)	A_{31}
quenching	H(n=3)+M → H(n=1) + M*	(R6.5)	$K_Q^{H^*}$

Table 6. 2 Main processes involved in the production and consumption of the Ar ($2p_1$)

Reaction Name	**Reaction**		Rate constant
Production			
Electron excitation from ground states	Ar (3p)+e→Ar (4p) +e	(R6.6)	$K_e^{Ar^*}$
Consumption			
Radiative de-excitation	Ar(4p)→ Ar(4s)+hv	(R6.7)	A_{44}
quenching	Ar(4p)+M→Ar(3p,4s) + M*	(R6.8)	$K_Q^{Ar^*}$

Note: Ar(3p) means the ground state of Ar. Ar(4s) means states of Ar $3p^5(^2P_{3/2})4s$ and Ar $3p^5(^2P_{1/2})4s$. Ar(4p) means states of Ar $3p^5(^2P_{3/2})4p$ and Ar $3p^5(^2P_{1/2})4p$.

As suggested by Gicquel, [8]when the H atom mole fraction is higher than 1 to 5% and the electron temperature is lower than 2 eV, **R6.2** may be neglected due to its

large threshold. In comparison with Gicquel's experiment conditions (i.e. pressure around 20-50 Torr, T_e around 1-2 eV, MWPD around 9-15 Wcm^{-3}, in which the actinometry is thought to be valid), the experiment conditions used here have much higher pressure (75-150Torr) and power density (30 Wcm^{-3}). Thus, the electron temperature shall be lower and the H mole fraction shall be higher than those in Gicquel's experiments. Therefore, here, the neglect of **R6.2** is reasonable.

Now, the emission intensity of H_α can be written as

$$\begin{aligned} I_{H_\alpha} &= K(\nu_{H_\alpha})\nu_{H_\alpha}A_{32}V_{emiss}\frac{[H(n=1)]K_e^{H_\alpha}n_e}{[H]K_{QH}^{H}+[H_2]K_{QH}^{H_2}+K_R} \\ &= (K(\nu_{H_\alpha})\nu_{H_\alpha}A_{32}V_{emiss}/K_R)\frac{[H(n=1)]K_e^{H_\alpha}n_e}{[H](K_{QH}^{H}/K_R)+[H_2](K_{QH}^{H_2}/K_R)+1} \end{aligned} \qquad \text{(Eq. 6. 1)}$$

where, $K(\nu_{H_\alpha})$ is the OES response coefficient at 656 nm, ν_{H_α} is frequency corresponding to the H_α transition, V_{emiss} is the emission volume, K_{QH}^{H} and $K_{QH}^{H_2}$ are the H(n=3) quenching rates due to collision with H and H_2, respectively, and K_R is the radiation rate [8]

$$K_R = A_{32}+A_{31} = (4.36+5.39)\times10^7 s^{-1} = 9.8\times10^7 s^{-1} \qquad \text{(Eq. 6. 2)}$$

The emission of Ar can be written as

$$I_{Ar^*} = (K(\nu_{Ar^*})\nu_{Ar^*}A_{44}/K_{RAr})\frac{[Ar(3p)]K_e^{Ar^*}n_e}{[H](K_{QAr}^{H}/K_{RAr})+[H_2](K_{QAr}^{H_2}/K_{RAr})+1}. \qquad \text{(Eq. 6. 3)}$$

Consider

$$K_{RAr} = A_{44}, \qquad \text{(Eq. 6. 4)}$$

then finally, the ratio of H(n=1) and Ar(3p) can be written as

$$\frac{[H(n=1)]}{[Ar(3p)]} = F\frac{K_e^{Ar^*}}{K_e^{H_\alpha}}Q_T\frac{I_{H_\alpha}}{I_{Ar^*}}, \qquad \text{(Eq. 6. 5)}$$

where

$$F = \frac{K(\nu_{Ar^*})}{K(\nu_{H_\alpha})}\cdot\frac{\nu_{H_\alpha}}{\nu_{Ar^*}}\cdot\frac{A_{32}+A_{31}}{A_{32}} \qquad \text{(Eq. 6. 6)}$$

is a constant.

$K_e^{Ar^*}/K_e^{H_\alpha}$ as mentioned before, is only weakly dependent on T_e due to the similar threshold and electron impact excitation cross section dependence on electron temperature of Ar ($2p_1$) and H(n=3). Provided T_e does not change much as a result of the process condition changes in the experiments, $K_e^{Ar^*}/K_e^{H_\alpha}$ can also be treated as a constant. [8] Thus, only the equation

$$Q_T = \frac{[H](K_{QAr}^{H} / K_{RAr}) + [H_2](K_{QAr}^{H_2} / K_{RAr}) + 1}{[H](K_{QH}^{H} / K_{R}) + [H_2](K_{QH}^{H_2} / K_{R}) + 1} \qquad \text{(Eq. 6. 7)}$$

shall have a significant pressure and temperature dependence.

$[H_2]K_{QAr}^{H_2}$ and $[H]K_{QAr}^{H}$ can be written as

$$[H_2]K_{QAr}^{H_2} = (P/RT)\mathrm{v}_{Ar}\sigma_{Ar^*-H_2}\mathrm{x}_{H_2} \qquad \text{(Eq. 6. 8)}$$

$$[H]K_{QAr}^{H} = (P/RT)\mathrm{v}_{Ar}\sigma_{Ar^*-H}\mathrm{x}_{H} \qquad \text{(Eq. 6. 9)}$$

where v_{Ar} is the mean velocity of Ar, $\sigma_{Ar^*-H_2}$ and σ_{Ar^*-H} are the associated quenching cross sections with H_2 and H, and x_{H_2} and x_{H} are the mole fractions of H_2 and H.

Given the cross sections in Å^2, gas temperature in K and pressure in hPa (i.e. 100 Pa), Q_T can be written as[8]

$$Q_T = \frac{1 + PT^{-1/2}(0.132\sigma_{H_\alpha-H_2}\mathrm{x}_{H_2} + 0.152\sigma_{H_\alpha-H}(1\text{-}\mathrm{x}_{H_2}))}{1 + PT^{-1/2}(0.162\sigma_{Ar^*-H_2}\mathrm{x}_{H_2} + 0.226\sigma_{Ar^*-H}(1\text{-}\mathrm{x}_{H_2}))} \qquad \text{(Eq. 6. 10)}$$

Quenching of H(n=3) by Ar can be neglected because of the small amount of Ar and also the small quenching cross sections. $\sigma_{H_\alpha-H}$ is in the range 2 Å^2 [9] to 18 Å^2 [8]. σ_{Ar^*-H} is ~ 17 Å^2 [8] to 50 Å^2 [10]. $\sigma_{H_\alpha-H_2}$ is ~ 58 Å^2 [8]to 65 Å^2 [8, 11]. And $\sigma_{Ar^*-H_2}$ is ~ 42 Å^2 [8]to 58 Å^2 [8].

For the calculation, we assume the mean values of the cross sections, i.e

$\sigma_{H_\alpha-H}$ = 9Å^2, σ_{Ar^*-H} =34 Å^2, $\sigma_{H_\alpha-H_2}$ =62 Å^2, $\sigma_{Ar^*-H_2}$ =50 Å^2.

Then

$$Q_T = \frac{1 + PT^{-1/2}(8.184x_{H_2} + 1.368x_H)}{1 + PT^{-1/2}(8.1x_{H_2} + 7.684x_H)} \quad \text{(Eq. 6. 11)}$$

If H_2 dissociation degree is very small, i.e $x_{H_2} >> x_H$, this simplifies to

$$Q_T = \frac{1 + PT^{-1/2}(8.184x_{H_2})}{1 + PT^{-1/2}(8.1x_{H_2})} \quad \text{(Eq. 6. 12)}$$

For the typical condition in our experiments, P is around 100~200 hPa (i.e. 75-150 Torr), T around 2500~3200 K, then, always,

$$PT^{-1/2}(8.184x_{H_2}) >> 1 \quad \text{(Eq. 6. 13)}$$

and thus we still have

$$Q_T \approx 1. \quad \text{(Eq. 6. 14)}$$

Now the factors before the intensity ratio in **Eq. 6.5** are all constants. Therefore, the validity conditions for using actinometry are satisfied in our experiments.

6.3.2 OES studies of species behaviour versus discharge conditions

6.3.2.1. Spectra in the long wavelength range

The typical spectrum in the long wavelength range under the "standard" discharge conditions is shown in **Figure 6. 3**. The strongest emission line is from H_α. For the Ar emissions, three strong lines can be easily distinguished at 750 nm, 763 nm and 811 nm. The corresponding energy levels and transitions have already been shown in **Figure 6. 2**. It is noticed that the 750 nm ($2p_1 \rightarrow 1s_2$) transition of Ar is to a resonant state, while the 763 nm ($2p_6 \rightarrow 1s_5$) and 811 nm ($2p_9 \rightarrow 1s_5$) emissions both radiate to a metastable level.

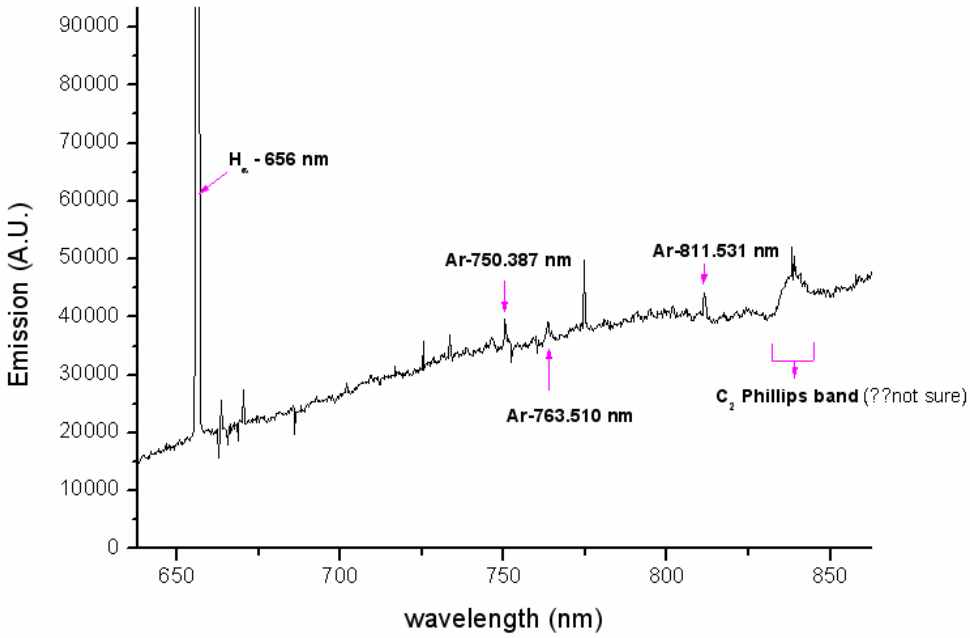

Figure 6. 3 Typical spectrum in the long wavelength range measured under "standard" conditions

The emission data shown in the following figures were taken from $CH_4/Ar/H_2$ plasmas. Such measurements have been repeated. The results seem reproducible.

In **Figure 6. 4**, the intensities of the mentioned three strong Ar emission lines, and the H_α transition are measured as a function of Ar flow rate. The measured intensities for all three Ar transitions increase almost proportionally with the amount of argon introduced. However, some authors [12] have suggested that mechanisms other than electron impact excitation of ground state Ar atoms also contribute to the population of the $2p_9$ level. In addition, in some cases, due to the long life time, the metastable states may have relatively high densities and thus self-absorption effects can not be ignored. (However, such should not be the case in our conditions. Due to the high pressure used here, the life times of these metastable state are dominated by quenching processes.) Thus, as most papers suggest, [1, 4, 13] the 750 nm emission line of Ar tends to be the best choice when using Ar as an actinometer.

As **Figure 6. 4** shows, the H_α emission is only weakly dependent on the Ar flow rate, suggesting that addition of trace amounts of Ar has little influence on the H

chemistry.

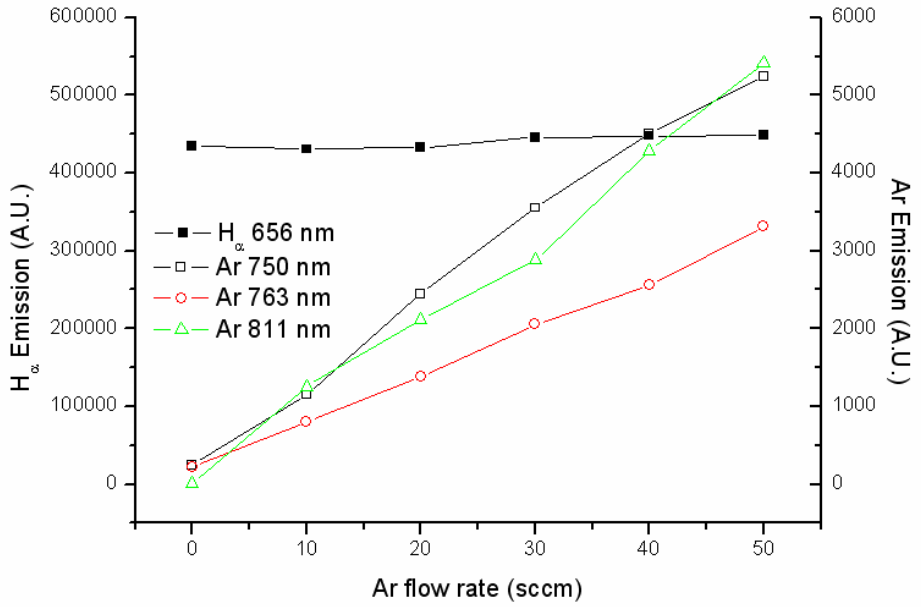

Figure 6. 4. Ar and H_α emission intensities as a function of Ar flow rate

Relative concentrations of ground state H(n=1) atoms can be determined using actinometry (see **Section 3.3.3** in Chapter 3), *i.e.* through use of the following relationship

$$[H(n=1)] \propto [Ar]\, I_{656} / I_{750} \qquad \text{(Eq. 6. 15)}$$

where the [..] represent the respective number densities and I the relative emission intensities. The relative H_2 dissociation fraction f_{Rel} can also be obtained by **Eq. 6. 16**,

$$f_D = \frac{[H(n=1)]/2}{[H_2]^0} = \frac{[H(n=1)]}{[Ar]} \frac{X_{Ar}^0}{2X_{H_2}^0} \propto \frac{I_{656}}{I_{750}} \frac{X_{Ar}^0}{2X_{H_2}^0} = f_{\text{Rel}} \qquad \text{(Eq. 6. 16)}$$

Here, $[H_2]^0$ is the assumed number density of H_2 at the same gas pressure and temperature but without dissociation. X_{Ar}^0 and $X_{H_2}^0$ are the mole fractions of Ar and H_2 in the input gas stream.

The principles and the validity of actinometry in our microwave activated Ar/H_2 and

$Ar/H_2/CH_4$ plasma have been discussed in **Section 6.3.1**. **Figure 6. 5** shows the H(n=1) relative number densities derived by ratioing the H_α emission intensity against each of the three Ar emissions. The absolute values are meaningless, because the wavelength dependent monochromater response is not calibrated, but the trend is revealing. The following explanations are based on comparisons between the H_α emission and our preferred Ar 750 nm line emission; as **Figure 6. 5** shows, trace Ar addition has little influence on the H(n=1) density, causing only a moderate increase in H(n=1) concentration. Reasons why Ar addition might enhance the H atom concentration and the degree of H_2 dissociation (**Figure 6. 6**) have been discussed in Chapter 5, e.g, through **R5.1** and **R5.2**.

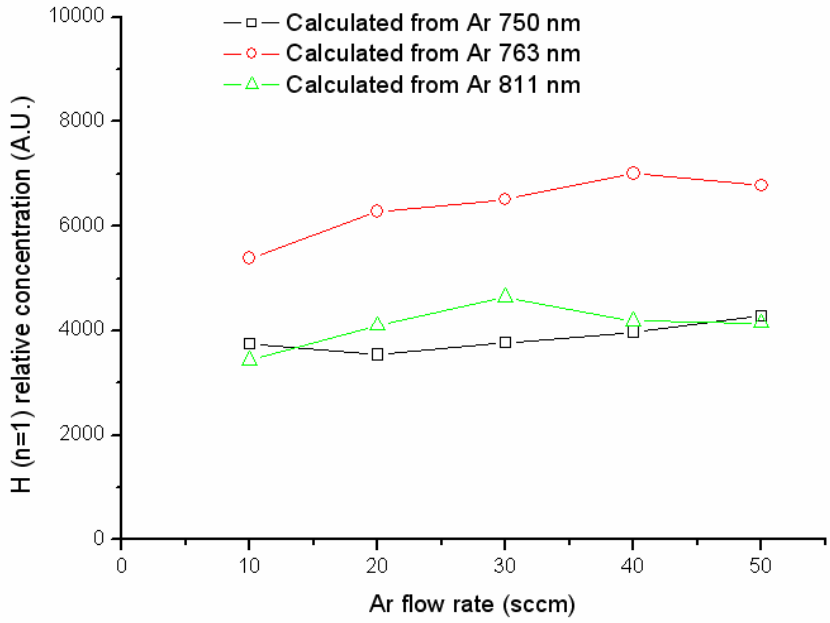

Figure 6. 5. H(n=1) relative concentrations calculated using different Ar lines as the actinometer, as a function of Ar flow rate.

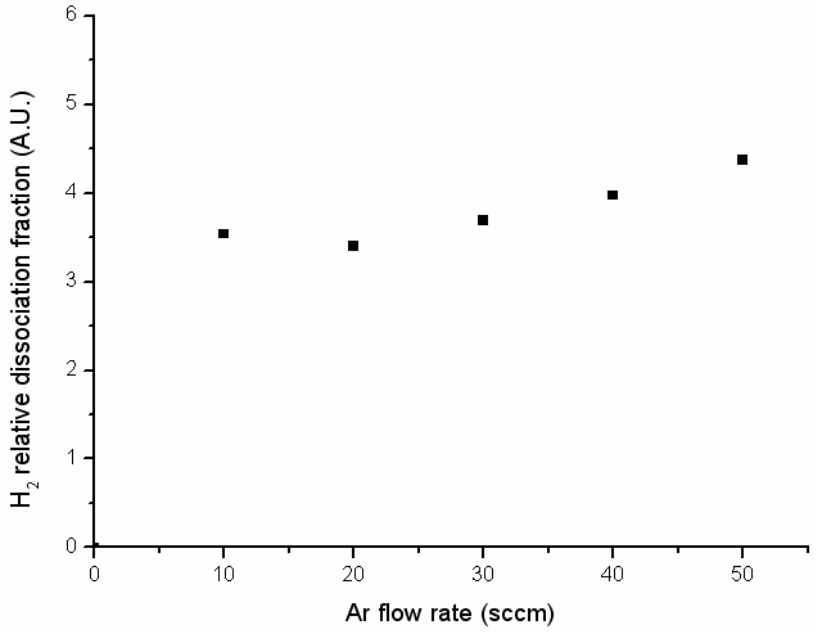

Figure 6. 6 H_2 relative dissociation fraction as a function of Ar flow rate.

Figure 6. 7 shows the variation in the measured Ar and H_α emissions with microwave power over the range 0.75–1.5 kW. The H_α emission shows a >4-fold increase whereas the Ar emissions only increase by a factor of ~2. The calculated relative concentrations of H(n=1) from the three Ar lines are shown in **Figure 6. 8**; each comparison indicates that more power into the plasma leads to a higher concentration of H(n=1) atoms. The calculated relative H_2 dissociation fraction also evidently increases with the power, see **Figure 6. 9**

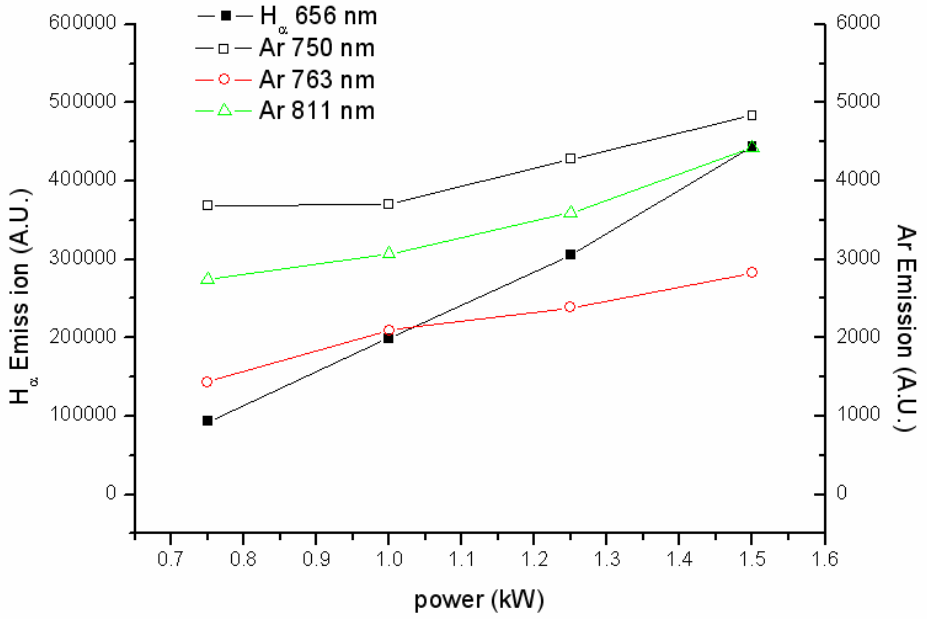

Figure 6. 7. Ar and H_α emission intensities as a function of power

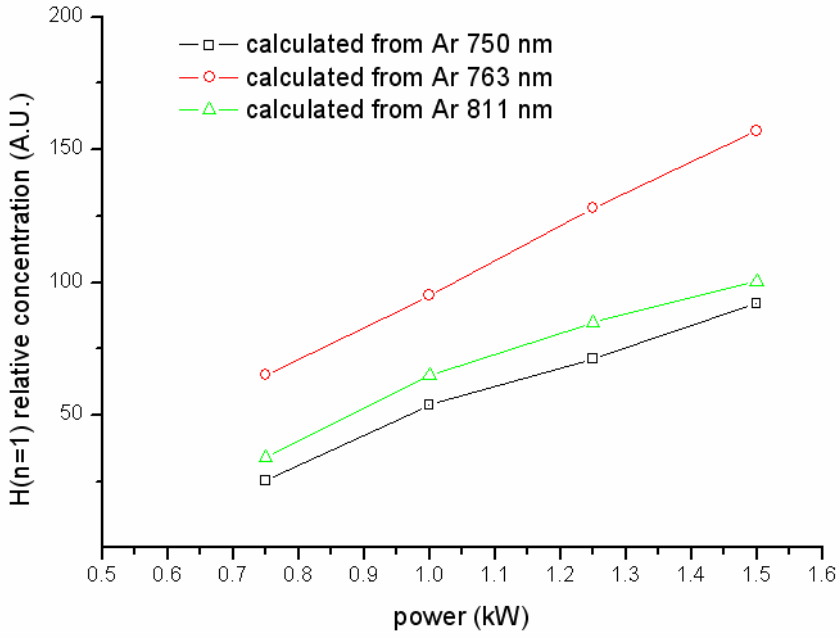

Figure 6. 8 H(n=1) relative concentrations calculated using different Ar lines as the actinometer, as a function of the input power

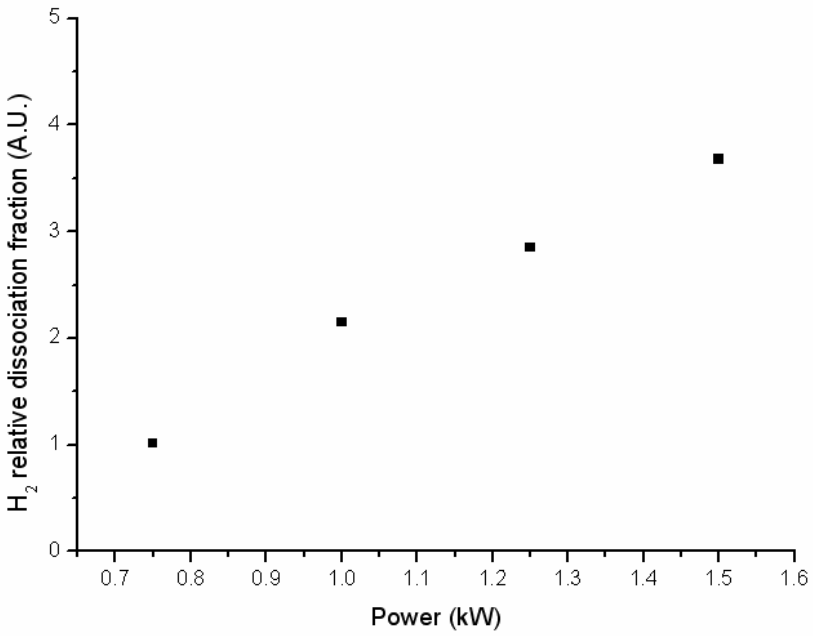

Figure 6. 9 H_2 relative dissociation fraction as a function of input power.

Figure 6. 10 shows how CH_4 addition affects both argon and H_α emissions. Note that addition of just 2.5 sccm of CH_4 (corresponding to a mole fraction <5‰) to the plasma results in a >2-fold "jump" in the measured argon and H_α emission intensities (see also **Figure 6. 11**). As **Figure 6. 12** shows, however, the relative concentration of H(n=1) atoms calculated by actinometry is rather insensitive to additions of trace amounts of CH_4. So is the relative dissociation of H_2 in **Figure 6. 13**. Indeed, if we persist with the assumption that the Ar 750 nm transition is the most reliable actinometer, **Figure 6. 12** suggests that CH_4 addition has no significant impact on the H(n=1) density. However, to make this conclusion, we also must realize that the emissions of Ar and H(n=2) only come from the glow region. Thus, such a conclusion may only be valid for this region. In the cooler region, due to the H-shift reaction with hydrocarbon molecules, we would expect some reduction in the hydrogen atom densities.

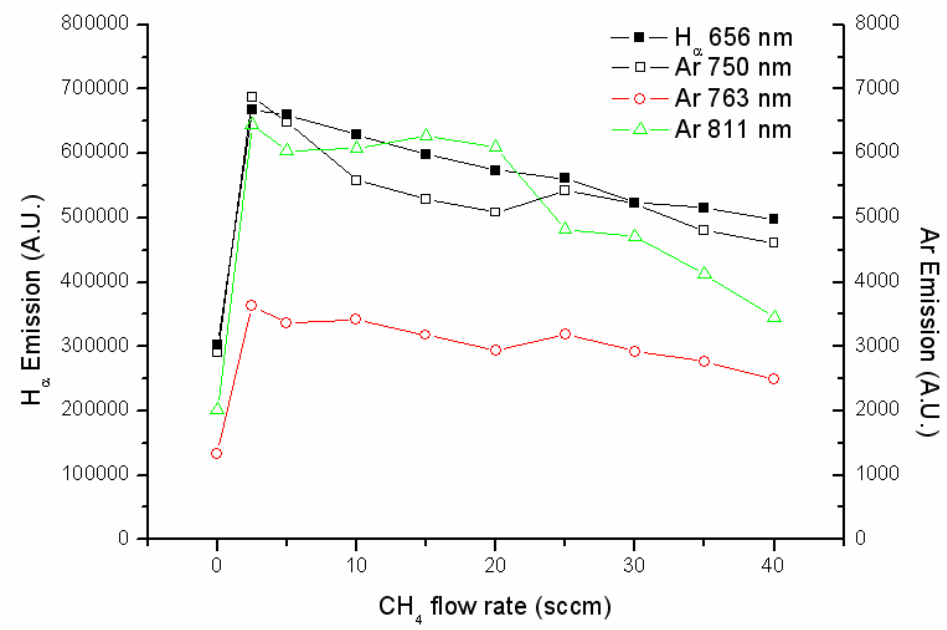

Figure 6. 10 Ar and H_α emission intensities as a function of CH_4 flow rate

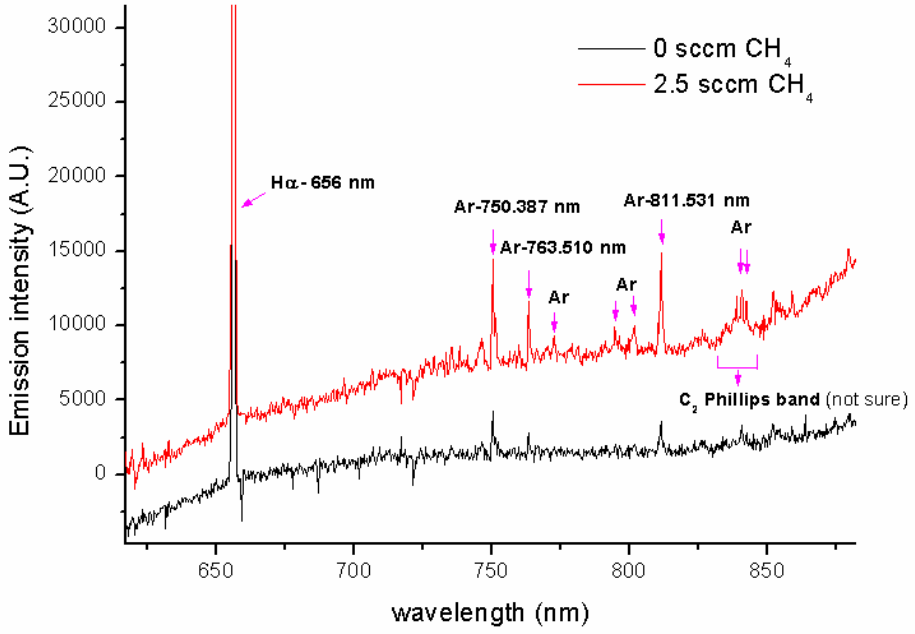

Figure 6. 11 Comparison of spectra obtained under two different conditions (0 and 2.5 sccm CH_4), with the total flow rate held constant at 565 sccm.

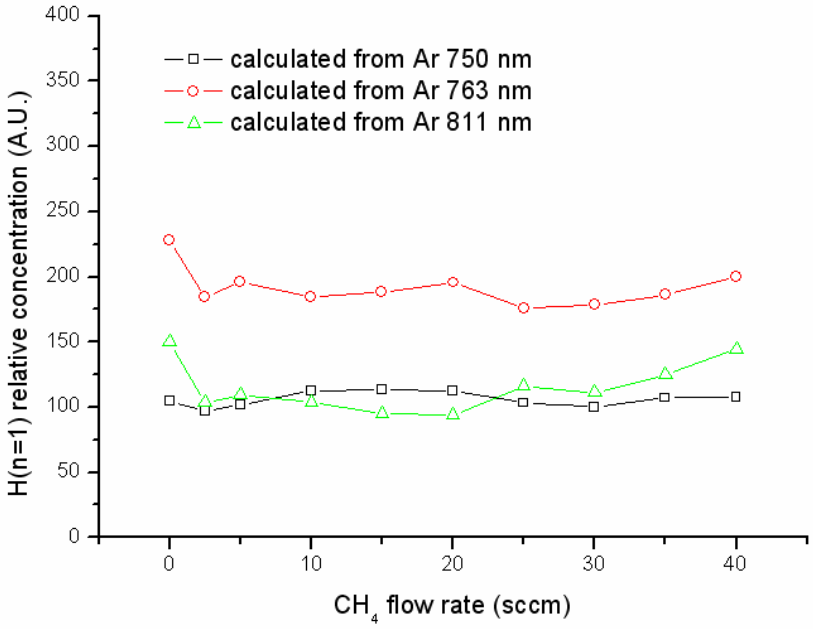

Figure 6. 12. H(n=1) relative concentrations calculated using different Ar lines as the actinometer, as a function of CH_4 flow rate

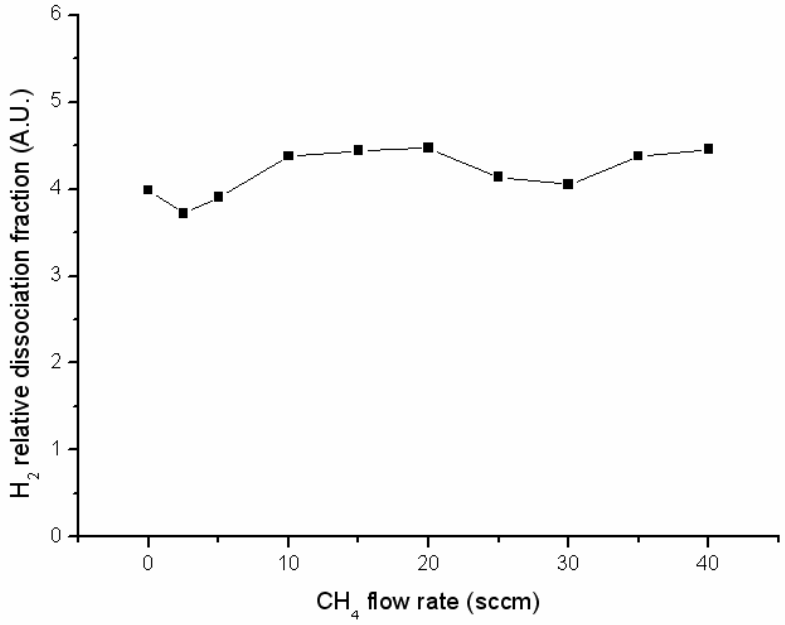

Figure 6. 13 H_2 relative dissociation fraction as a function of CH_4 flow rate.

The effects of total pressure, p, on the measured argon and H_α emission intensities are shown in **Figure 6. 14**. The Ar emissions increase markedly as the pressure is reduced. This can be attributed to an increase in T_e as the pressure drops since the reaction rate is exponentially dependent on T_e. Here we have already assumed that

electron impact excitation dominates the production of Ar*, because of the large energy gap between its ground state and excited states. The contribution from Ar metastables is assumed to be small because, at high pressure, the quenching rate is so high that the lifetime of the Ar metastable states is mainly determined by the quenching process. Thus more argon excited states (Ar*) are produced when T_e is high. This behaviour also verifies that Ar* production is dominated by electron chemistry. The H_α emission exhibits a different pressure dependence, increasing and then decreasing with increasing p. Though the measured H_α intensities do not change much as the pressure increases from 75 torr to 175 torr, the measured trend is reproducible, and thus demands an explanation. Several parameters can influence H(n=3) production rates, i.e. electron density n_e, electron temperature T_e and the H(n=1) concentration. Both n_e and H(n=1) will increase with increasing pressure – encouraging H (n=3) production – but T_e will decrease – discouraging H (n=3) production. Additionally, excited state quenching will become increasingly important at higher p. The observed pressure dependence of the H_α emission probably reflects competition between all these effects.

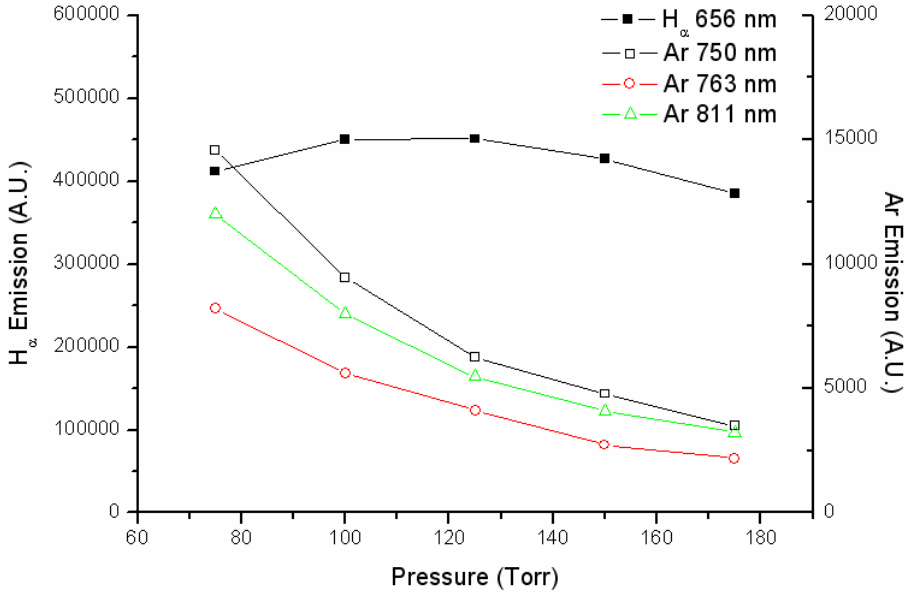

Figure 6. 14. Ar and H_α emission intensities as a function of total pressure, p

Figure 6. 15, which compares emission spectra measured at p = 75 and 150 Torr,

illustrates the pressure dependence of the Ar line intensities. Apart from the usual increase in Ar emission intensity at lower *p*, we note the broad emission at ~840 nm (which may be attributable to the C_2 Phillips system or at least related with some carbon contained radicals because it can not be seen in Ar/H_2 plasma) at higher *p*. The rising baseline is attributed to blackbody radiation from the substrate – which becomes more evident at higher pressure and/or power. Since H recombination on the surface of the substrate accounts for the major mechanism of the substrate heating, again suggesting that under high power and higher pressure conditions, more H atoms are produced.

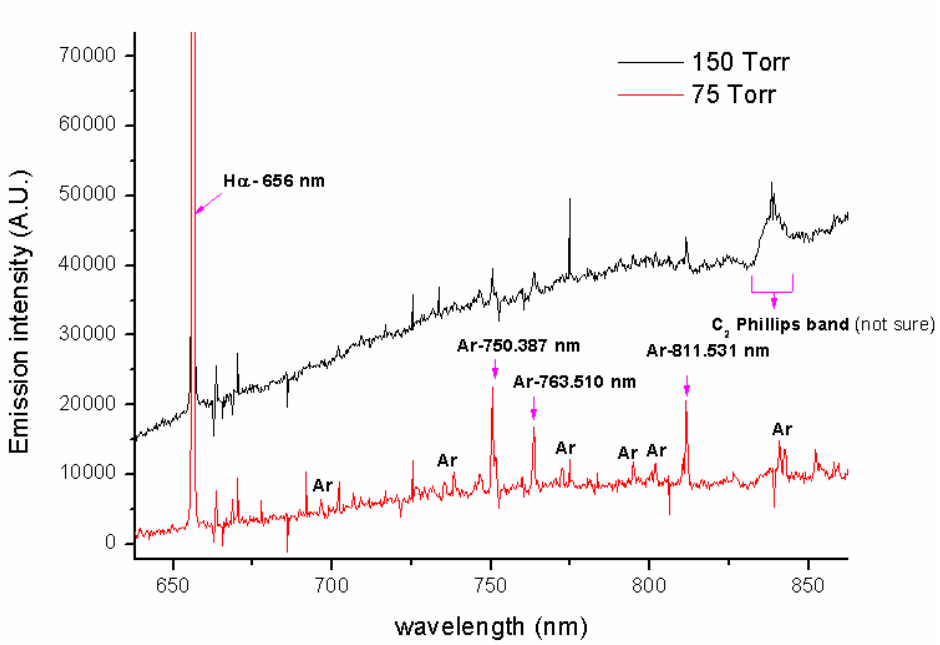

Figure 6. 15 Comparison of spectra obtained under at two different pressures, *p* = 75 and 150 torr in $Ar/H_2/CH_4$ plasma

The relative concentrations of H(n=1) atoms, calculated using different Ar lines as the actinometer, all increase with *p*, as shown in **Figure 6. 16**, in complete contrast to the observed Ar* emission intensities. This result strongly suggests thermal dissociation as the main channel for H (n=1) production. **Figure 6. 17** also shows a linear enhancement of H_2 dissociation with increasing pressure.

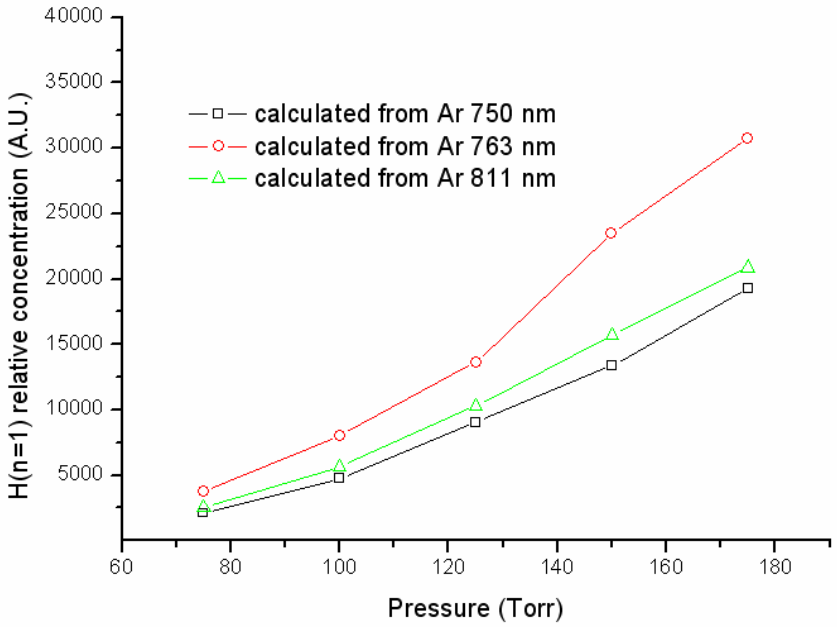

Figure 6. 16. H(n=1) relative concentrations calculated using different Ar lines as the actinometer, as a function of total pressure

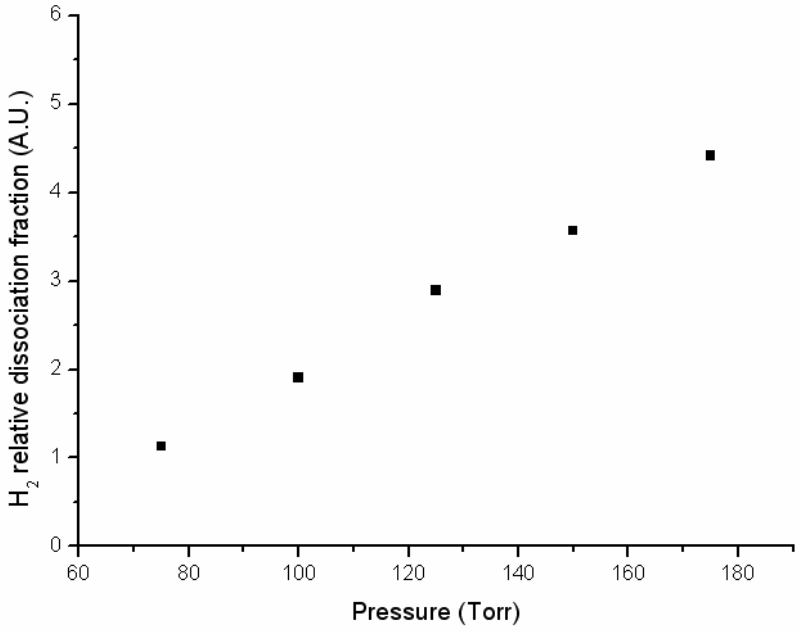

Figure 6. 17. H_2 relative dissociation fraction as a function of total pressure.

6.3.2.2. Spectra in the short wavelength range

A typical optical emission spectrum measured in the short wavelength range is shown in **Figure 6. 18**. The spectrum shows strong emissions from the H Balmer

series, and the C_2 Swan bands. We also identify weak CH ($A^2\Delta$–$X^2\Pi$) and H_2 ($3p\ ^3\Sigma_u^+$–$2s\ ^3\Sigma_g^+$) emissions. The small peaks at around 400 nm are possibly due to some sputtered products. The Ar emissions unfortunately can not be covered in this spectrum.

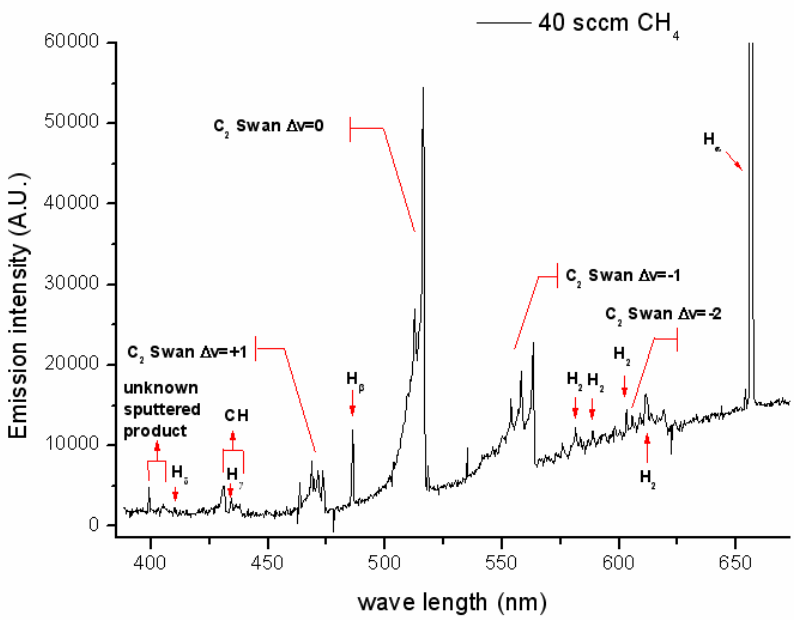

Figure 6. 18. Typical emission spectrum obtained under the condition: 1.5 kW input power, 150 torr total pressure and $Ar/H_2/CH_4$ = 40/485/40 sccm.

The measured emission intensities from the several species (H_α, H_β, H_γ, H_2, CH and C_2) are plotted in **Figure 6. 19** as a function of CH_4 flow rate. Different sub-groups of species display quite different behaviours. For example, the H_α, H_β, H_γ and H_2 emissions all show a "jump" upon adding a small amount of CH_4. Several authors [14, 15] have attributed this to enhancement of electron density; the T_e seems to change little on the basis that the H_α, H_β, H_γ intensity ratio shows little change upon CH_4 addition. The present experiments are consistent with these obervations. As **Figure 6. 20** shows, the measured H_β/H_α emission ratio is essentially independent of CH_4 flow rate. The measured H_γ/H_α ratio (**Figure 6. 20**) may show a small drop at low CH_4 flow rate, but the H_γ emission intensity is small and its associated error quite large (not least because of its overlap with the CH(A-X) emission band). The similar

behaviour of these emissions suggests that electron driven chemistry is the dominant production mechanism for H(n=3,4,5) atoms, and for electronically excited H_2* molecules. CH and C_2 show very different emission behaviours from the H_α, H_β, H_γ and H_2 emissions, consistent with thermally dominated production mechanisms; their respective behaviours show obvious differences, however. Such differences parallel those noted in the absorption measurements and, as before, we suspect these differences to be correlated with their different dependences on atomic hydrogen concentration.

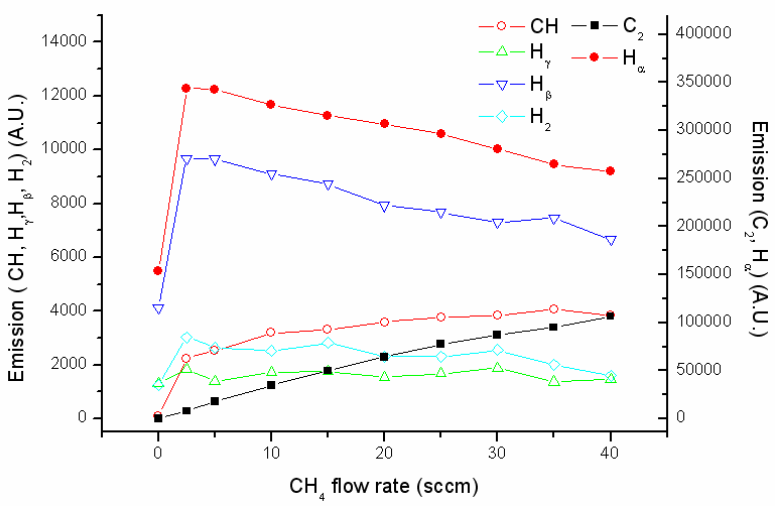

Figure 6. 19. Emission intensities of H_α, H_β, H_γ H_2, CH and C_2, as a function of CH_4 flow rate

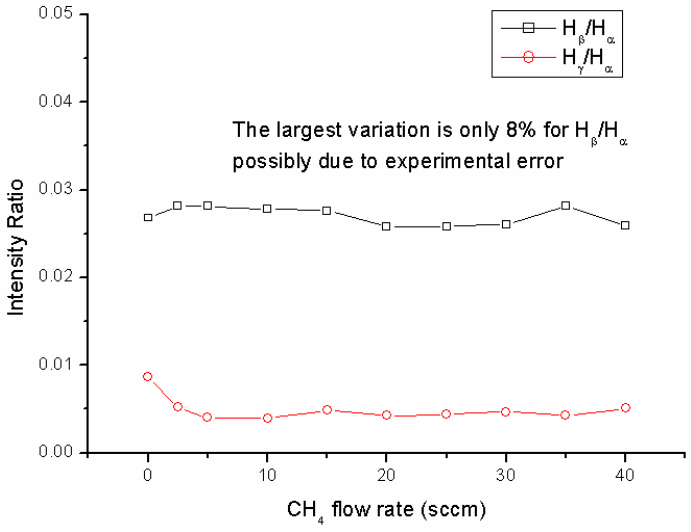

Figure 6. 20 H_β/ H_α and H_γ/H_α emission ratios, as a function of CH_4 flow rate

The emission intensities from all of the above species show some increase with

increasing microwave power (all other discharge conditions are the same as "standard" conditions), as shown in **Figure 6. 21**. The calculated H_β/ H_α and H_γ/H_α ratios (**Figure 6. 22**) are mutually consistent, showing a decreasing trend as the input power increases which may indicate that the T_e drops as power increases. Another interesting phenomenon is that the H Balmer series emissions always show a sharper increase than all other species in **Figure 6. 21**, indicating that the excited H atoms are more sensitive to the input power.

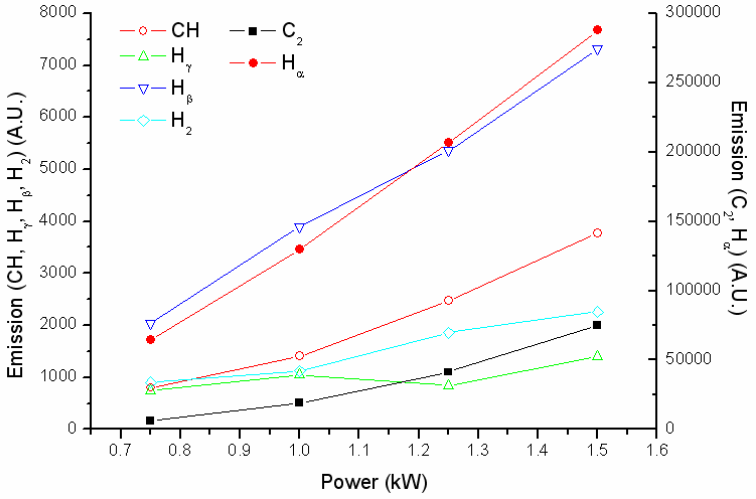

Figure 6. 21 H_α, H_β, H_γ, H_2, CH and C_2 emission intensities, as a function of input power

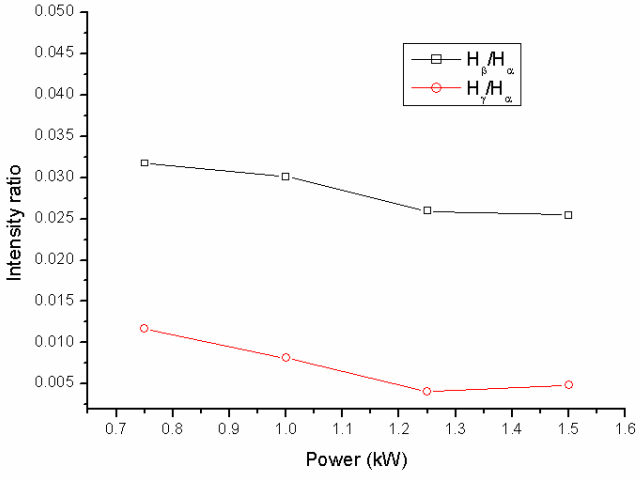

Figure 6. 22 H_β/ H_α and H_γ/H_α emission ratios, as a function of input power

The effects of increasing total pressure, *p*, on the various emissions are summarised in **Figure 6. 23**. The H_α, H_β, H_γ emissions all show similar trends, first increasing and then declining as *p* is varied from 75 to 150 torr. The H_β/ H_α and H_γ/H_α emission

intensity ratios (**Figure 6. 24**) are essentially constant however. We have previously argued (from **Figure 6. 14**) that increasing p leads to a decline in T_e. On that basis, the H_β/H_α and H_γ/H_α ratios might be expected to decline with increasing p – contrary to the apparent p independence suggested by **Figure 6. 24**. The H_2 emission shows a similar p dependence to that of Ar (in **Figure 6. 14**), further confirming that H_2* production is dominated by interactions with electrons. C_2 and CH emissions both increase with p, which is similar to the behaviour of H (n=1) determined by actinometry. In a manner, such behaviour is characteristic of species whose production is dominated by thermal chemistry.

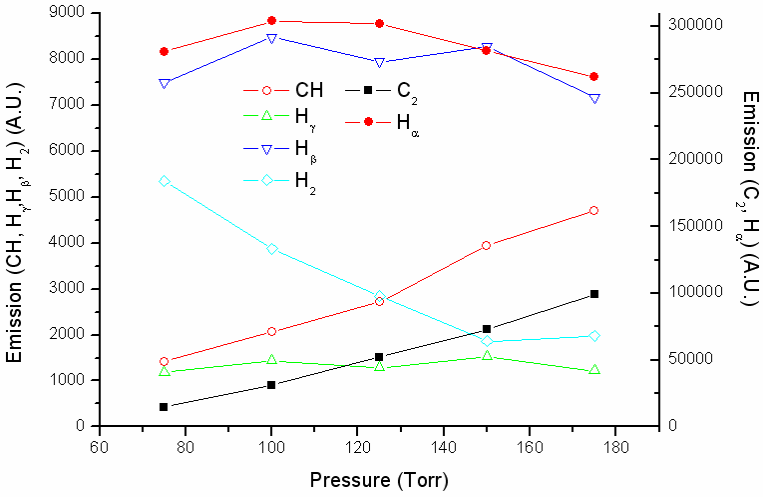

Figure 6. 23 H_α, H_β, H_γ, H_2, CH and C_2 emission intensities, as a function of total pressure

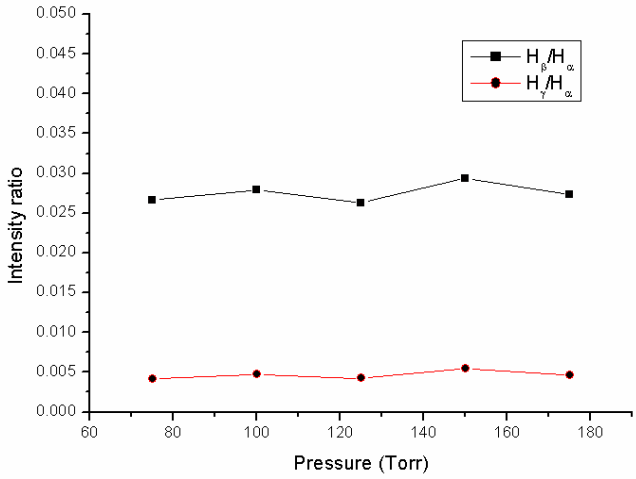

Figure 6. 24 H_β/H_α and H_γ/H_α emission ratios, as a function of total pressure

As **Figure 6. 25** shows, varying the Ar flow rate has little effect on the emission intensities from any of the monitored species. However, the increase of C_2, CH and H_α is still recognizable. The H_β/ H_α and H_γ/H_α emission ratios are also insensitive to the argon flow rate (**Figure 6. 26**).

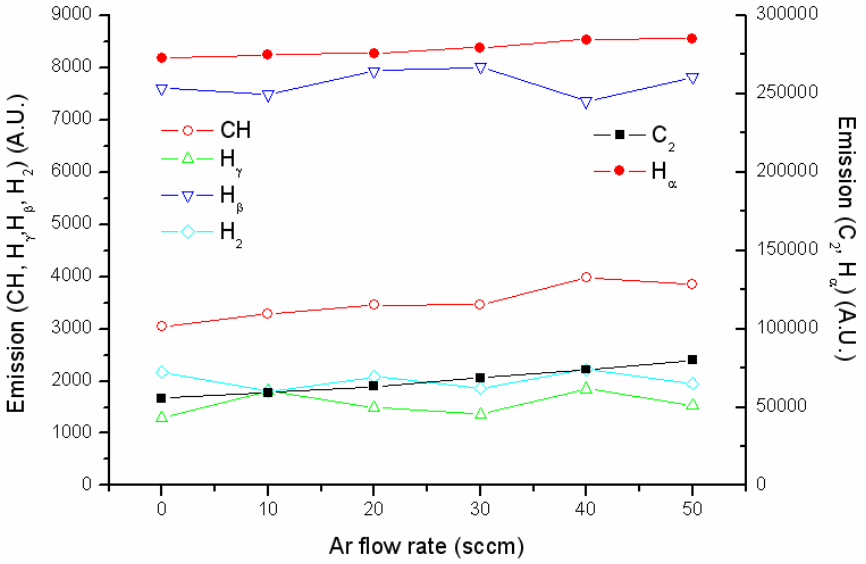

Figure 6. 25. H_α, H_β, H_γ, H_2, CH and C_2 emission intensities, as a function of Ar flow rate

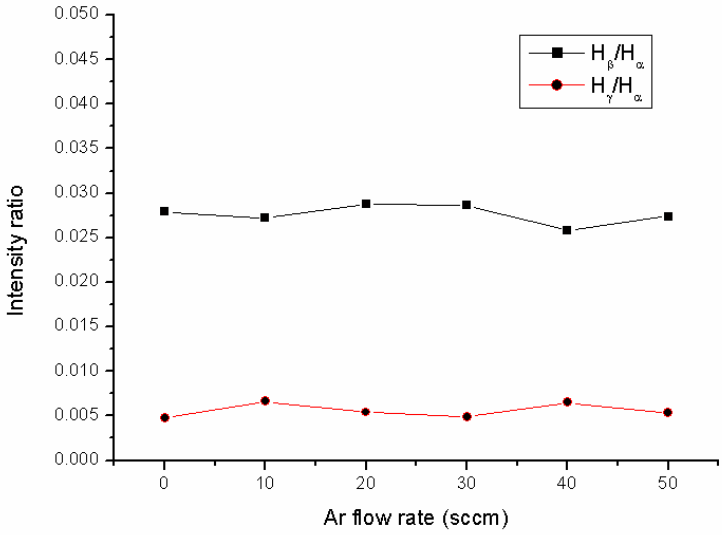

Figure 6. 26 H_β/ H_α and H_γ/H_α emission ratios, as a function of Ar flow rate

6.3.3 OES profiling of species in Ar/H_2 and $CH_4/Ar/H_2$ plasma

In order to map the emission profiles of different species in the plasma, two small

apertures with a spacing of 35 cm are put before the optical fiber. The values of geometry parameters of such a system are shown in **Figure 6. 27**. The spatial resolution thus can be calculated using primary geometry theory. For example, taking the diameter of the second aperture as 2mm, then we have

$$\frac{d}{35-d}=\frac{1}{2}\Rightarrow d\approx 11.7cm \qquad \text{(Eq. 6. 17)}$$

Thus

$$\frac{1}{x}=\frac{d}{11+d}=\frac{11.7}{22.7}\Rightarrow x\approx 1.94mm \qquad \text{(Eq. 6. 18)}$$

The resolution is around 2 mm.

Similarly, we can also calculate the spatial resolution when the second aperture is set as 1 mm. The result is about 1.63 mm. Recognizing the finite collection angle of the optical fiber, the resolution should be better than this. So it is reasonable for us to claim a resolution better than 2mm when using this OES configuration. In the experiments, the optical emission was measured every 2 mm. The price paid for the good spatial resolution is the very weak light collected by the optical fiber. Extremely long "exposure time" had to be used in the experiments to obtain sufficient signal intensities.

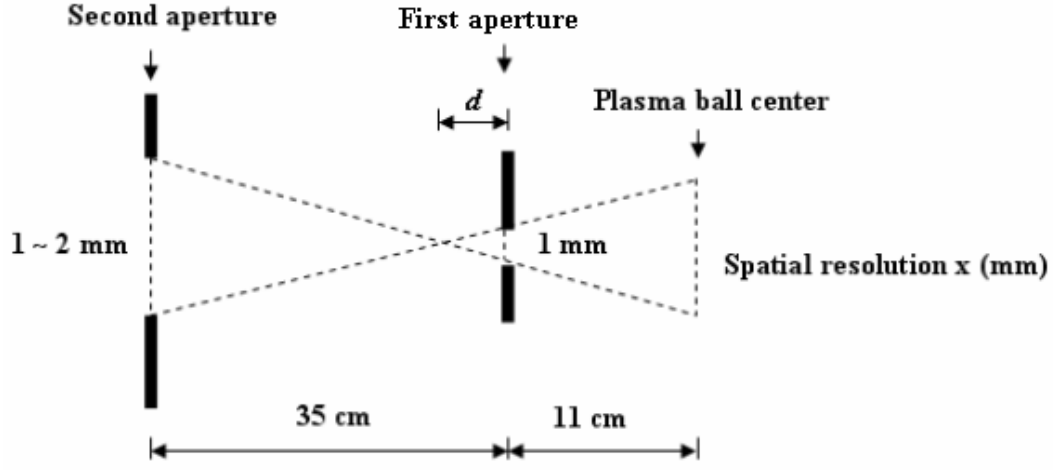

Figure 6. 27 Geometry parameters of the spatially resolved OES configuration

The measured emission profiles of H_α, H_β and Ar (750 nm) in Ar/H_2 plasma are shown in **Figure 6. 28**. The H_α and H_β emissions have a maximum at around 6~8 mm

above the substrate while the Ar 750 emissions show a peak value much closer to the substrate (around 3 mm above the substrate) than H_α and H_β emissions. The Ar 750 emission has been assumed to come mainly from the electron impact excitation of Ar (3p) (ground state) into Ar (4p), then following a spontaneous radiation from Ar(4p) to Ar(4s), see **Table 6.2**. Therefore, the profile of Ar 750 emission may be thought to provide a good approximation of the electron density profile. However, as shown in **Figure 2.1 (b)**, the electron temperature distribution has a large gradient near the substrate, which may also contribute to the measured Ar emission profiles here.

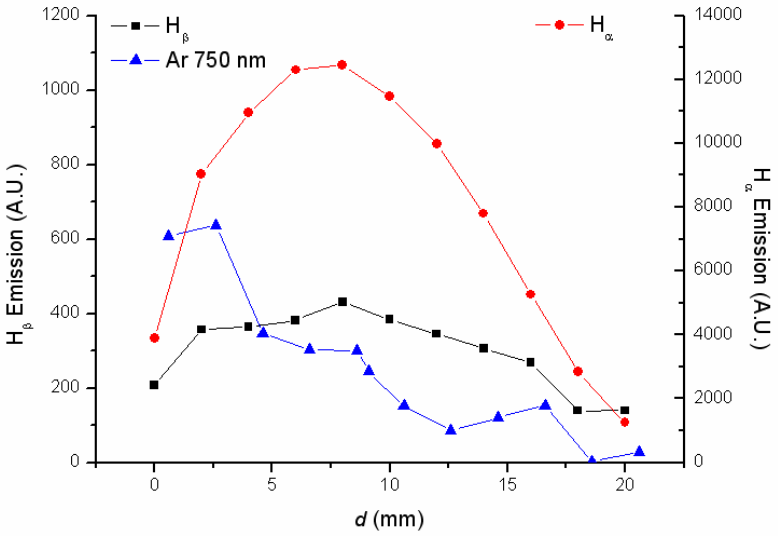

Figure 6. 28 Emission profiles of H_α, H_β and Ar (750 nm) in Ar/H_2 plasma. The flow rate of H_2 and Ar are 525 and 40 sccm, respectively. The other discharge parameters are the same as those under the "standard" condition.

Figure 6. 29 shows the measured emission profiles of CH (431 nm), H_β, Ar (750 nm), H_2 (601 nm), C_2 (516 nm), and H_α (656 nm) in $Ar/H_2/CH_4$ plasma under the standard discharge conditions. Consistent with the CRDS experimental results, the maxima of the C_2 and CH emissions occur farther from the substrate (d ~10 mm) than H_α and H_β emissions. However, the peaks of the Ar and H_2 emissions appear even closer to the substrate than those of H_α and H_β.

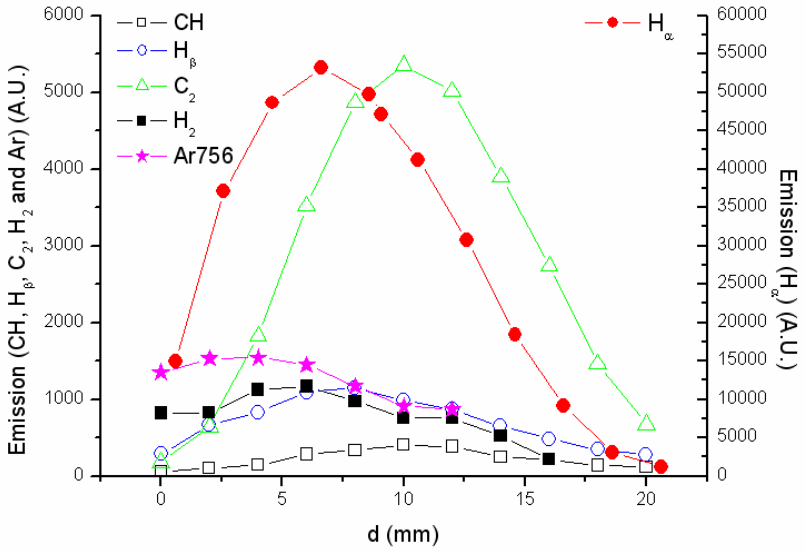

Figure 6. 29 Emission profiles of CH (431 nm), H_β, Ar (750 nm), H_2 (601 nm), C_2 (516 nm), and H_α in $Ar/H_2/CH_4$ plasma at the standard discharge conditions

In Chapter 5 when discussing the effect of a small amount of CH_4 addition, it has been suggested that the sudden switch of the dominant ions, from very light H_3^+ in Ar/H_2 plasma to the much heavier hydrocarbon ions in $CH_4/Ar/H_2$ plasma, may lead to a shrinkage of the plasma volume (i.e. the spatial distribution of electron density). The electron density distribution is not easy to measure directly in such a microwave reactor. Insertion of a Langmuir probe will change the resonant characteristics of the reactor and thus may strongly influence the plasma. The microwave interference method is non-intrusive, but it is difficult to achieve a spatial resolution better than several millimetres with this technique. OES may be another choice to give the electron information indirectly. However, the plasma volume defined by this method is also quite controversial. One may use the total illumination edge of the glow as the boundary of the plasma, or one may refer to the distribution of some specific emissions (e.g. H_α, C_2, or Ar emissions). However, to ensure that these emissions reflect the "true" electron information, their origination must be examined carefully. As discussed in **Section 6.3.2**, the C_2 and CH emissions are dominated by thermal chemistry and thus is not suitable for plasma volume definition. H_α emission has been used by Hassouni et al [16] to determine the plasma volume. However, H(n=3) generation is related to the electron impact excitation of H (n=1) and H(n=1)

production is dominated by thermal reactions. Therefore, H_α emission is influenced by both the thermal and electron chemistry. In contrast to C_2, CH and H_α, the Ar emission is dominated by the electron chemistry and hence possibly the best candidate for plasma volume determination (although any effect due to the inhomogeneous electron temperature distribution will still be included).

The measured emission profiles of Ar (750 nm) in Ar/H_2 and $Ar/H_2/CH_4$ plasmas under the same discharge conditions (power, pressure, total flow rate, etc) are shown in **Figure 6. 30** (150 Torr) and **Figure 6. 31** (100 Torr). However, these profiles look similar with and without CH_4. Especially in **Figure 6. 31**, no obvious shrinkage of the Ar emission profile can be observed upon changing from Ar/H_2 plasma to $Ar/H_2/CH_4$ plasma. In addition, a turning point (maximum) for the Ar emission profile is evident at ~3 mm from the substrate under 150 Torr. But no such turning point can be observed at 100 Torr. The reason for this observation is still under investigation.

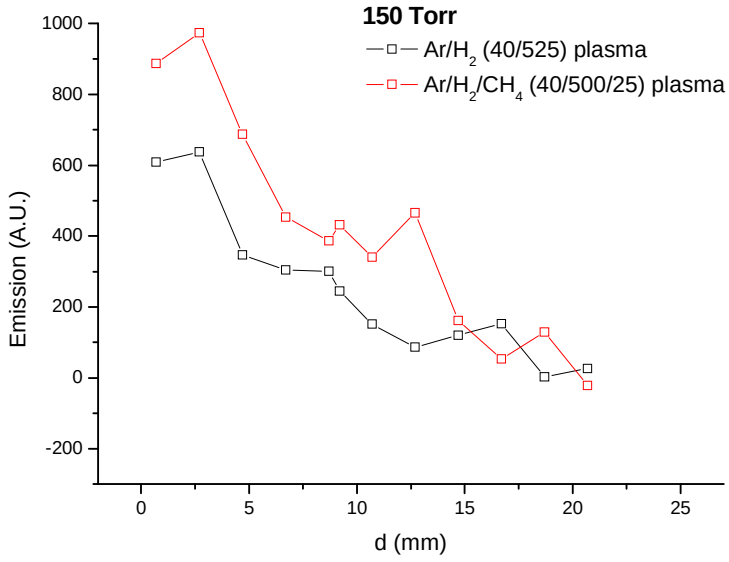

Figure 6. 30 Emission profiles of Ar (750 nm) in Ar/H_2 and $Ar/H_2/CH_4$ plasmas at 150 Torr under the same discharge conditions

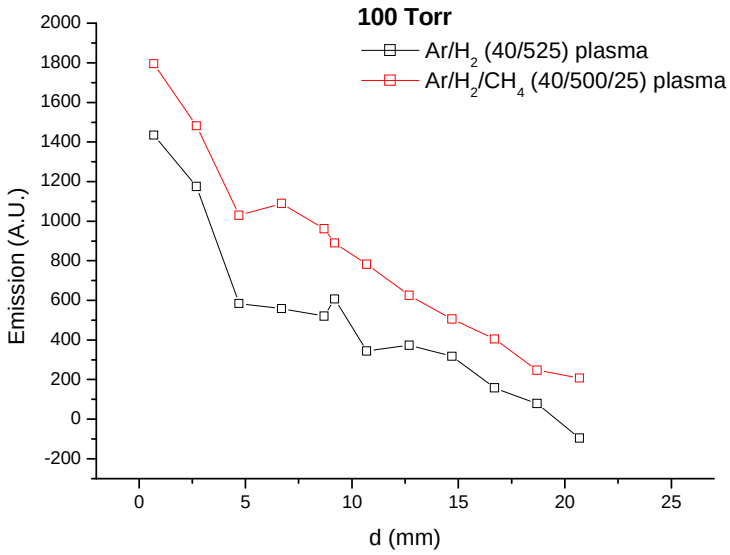

Figure 6. 31 Emission profiles of Ar (750 nm) in Ar/H_2 and $Ar/H_2/CH_4$ plasmas at 100 Torr under the same discharge conditions

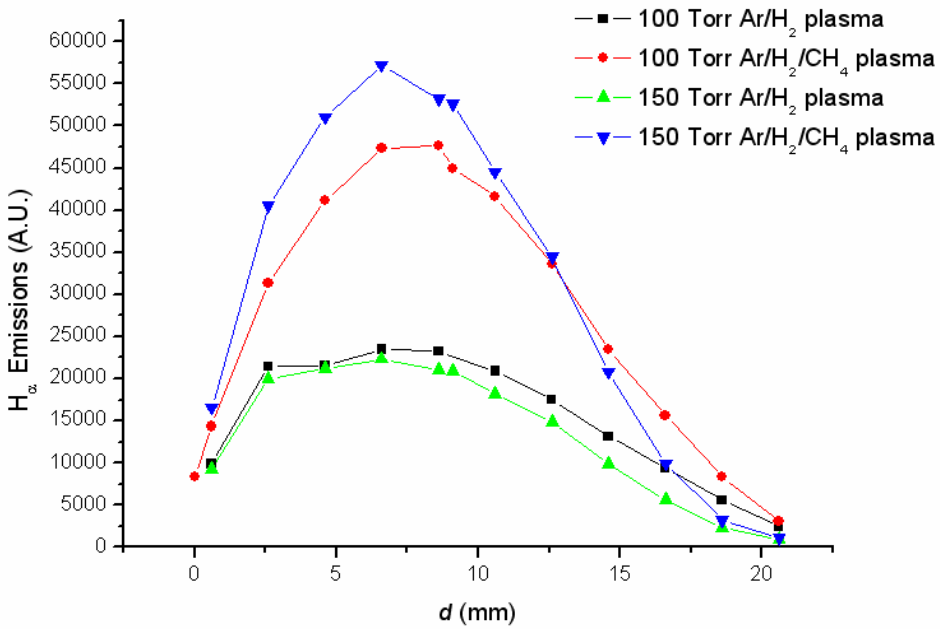

Figure 6. 32 Emission profiles of H_α in Ar/H_2 and $Ar/H_2/CH_4$ plasmas at 100 Torr and 150 Torr under the same discharge conditions

The measured profiles of H_α emission at two different pressures, 100 and 150 Torr, with and without CH_4, are shown in **Figure 6. 32**. There are two things worth noticing: Firstly, the H_α emissions show a broader profile under lower pressure (100

Torr) than under higher pressure (150 Torr), which is expected because the electron has a longer mean free path at lower pressures. Secondly, in Ar/H_2 plasma, the profile within the region 2.5-6 mm looks quite flat. However, when CH_4 is added, the profile within this region become sharper and the whole profile looks more symmetric about a y-axis drawn through the peak.

6.3.4 Comparisons of OES and CRDS measured results

OES can provide a simple and cheap way of diagnosing plasma. But it is limited in its ability to give direct information about species concentration, due to the fact that the emission intensity depends on many details about the excitation and de-excitation processes. However, in some cases, it is found that the species emissions have a linear relationship with their concentration. Such calibrated OES thus can be very useful. In an early work, Goyette et al [17] reported that the C_2 Swan band emission shows a linear relationship with the absolute C_2 concentration measured by absorption spectroscopy in an $Ar/H_2/CH_4$ microwave plasma under different experimental conditions. Here, a more detailed comparison of the OES and CRDS measured results is given.

Figure 6. 44 compare measured H_α, C_2 and CH emission intensities with CRDS column densities of H(n=2), C_2(a,v=0) and CH(X, v=0) measured under a range of discharge conditions. (All these comparison plots assume a common origin on the respective y axes, but are then scaled to emphasize the similarity of the measured trends). In most cases, the OES data (which depends on a local excited state number density) returns a similar trend to that measured by CRDS (which measures the column density of the lower energy or ground state). The disagreement in the comparison between the *p* dependent H_α emission and H (n=2) column density in **Figure 6. 36** possibly is a reflection of the different quenching rates of H(n=2) and H(n=3) atoms at higher pressure or the different regions monitored by the OES and CRDS. In addition, the C_2 and CH emissions show a sharper increase as a function

of the input power (see **Figure 6. 39** and **Figure 6. 43**), in contrast to the CRDS measured column densities. This may be because, besides the increase of the concentration of C_2 and CH ground states with power, the electron density also increases and can contribute to the enhancement of C_2 and CH emissions.

The good agreement between the OES and CRDS measurements suggests a cheaper way in the future to study the chemistry in these plasmas, though it is more or less unexpected due to the reason mentioned at the beginning of this section. The good agreement thus presumably implies local equilibrium between the lower states and the respective excited higher states as a result of very frequent collisions between electrons and heavy species and also the efficient energy transfer in these collision processes. Another thing that needs to be noticed is that all these three species (C_2, CH and H(n=2)) are "hot" species and concentrated in the plasma ball. For the "cold" stable species like C_2H_2, CH_4 and H_2, we would not expect good agreement between OES and column densities measured by CRDS.

6.3.4.1. H (n=2) atoms

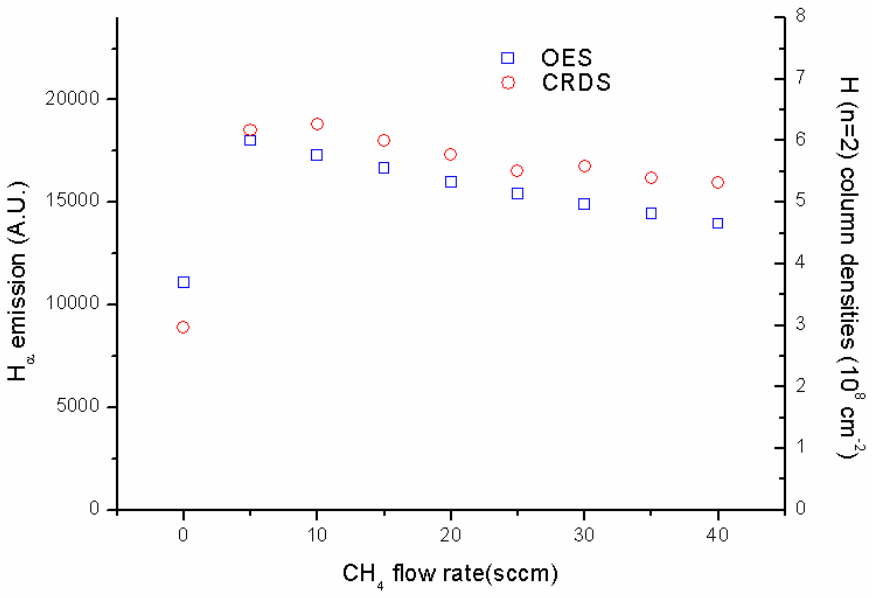

Figure 6. 33. Comparison of OES measured H_α emission and CRDS measured H (n=2) column densities at different CH_4 flow rates.

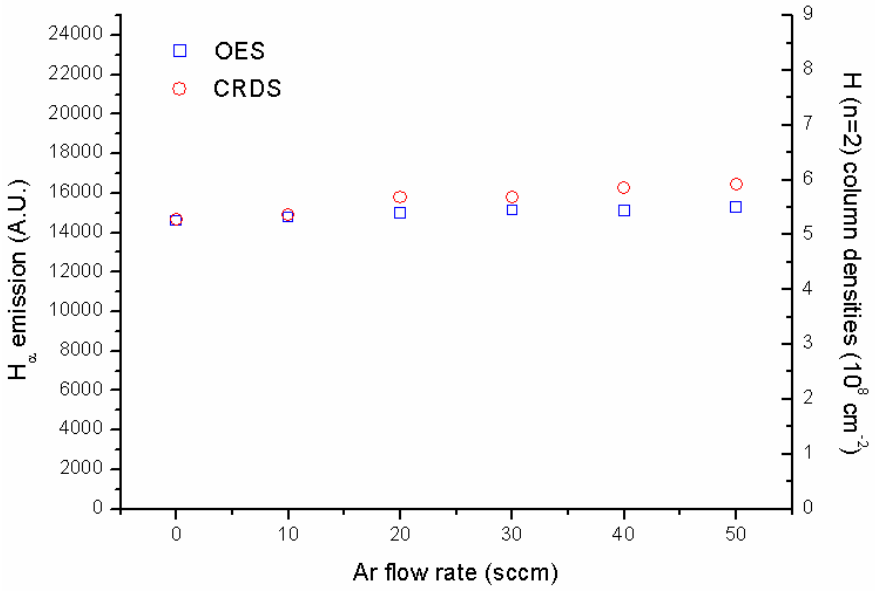

Figure 6. 34. Comparison of OES measured H_α emission and CRDS measured H (n=2) column densities under different Ar flow rates.

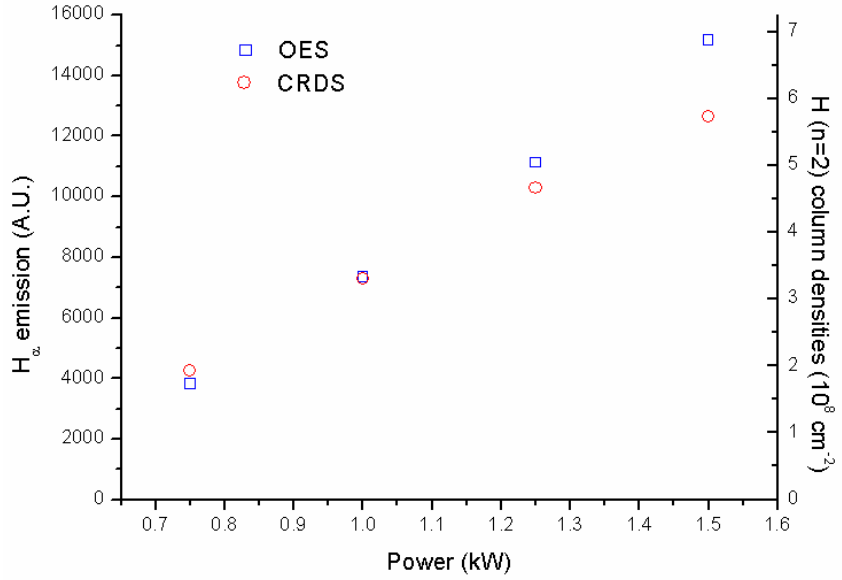

Figure 6. 35. Comparison of OES measured H_α emission and CRDS measured H (n=2) column densities under different input powers.

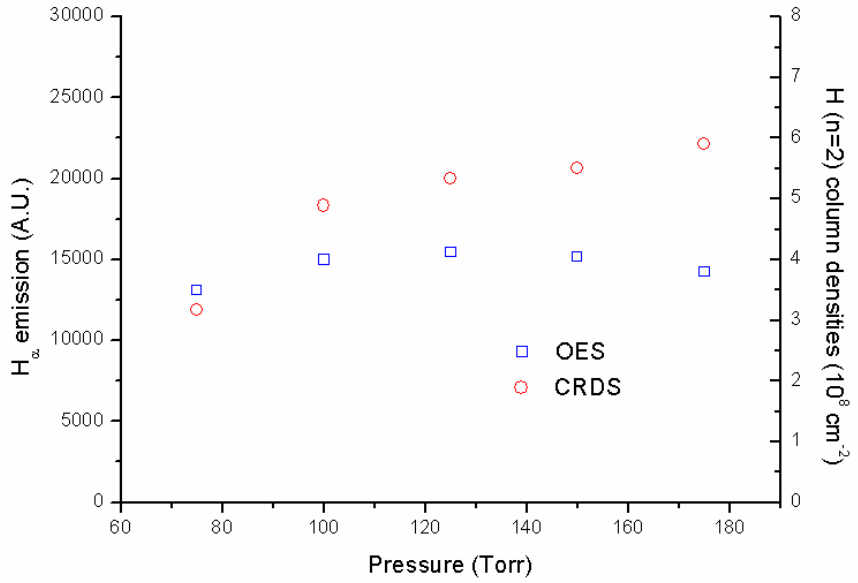

Figure 6. 36. Comparison of OES measured H_α emission and CRDS measured H (n=2) column densities under different pressures.

6.3.4.2. C_2 radical

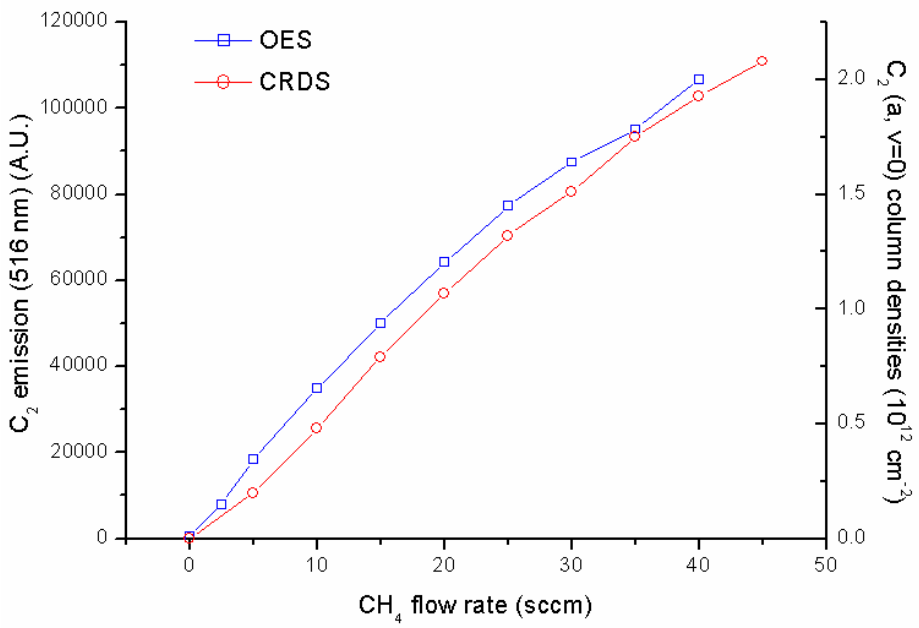

Figure 6. 37. Comparison of OES measured C_2 Swan band (516 nm) emission and CRDS measured C_2 (a,v=0) column densities under different CH_4 flow rates

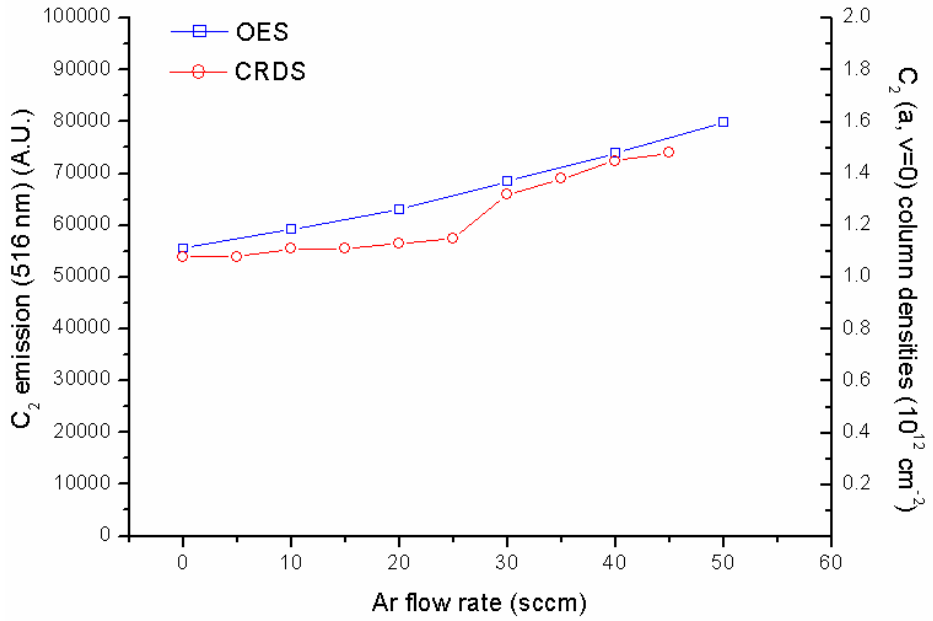

Figure 6. 38. Comparison of OES measured C_2 Swan band (516 nm) emission and CRDS measured C_2 (a,v=0) column densities under different Ar flow rates

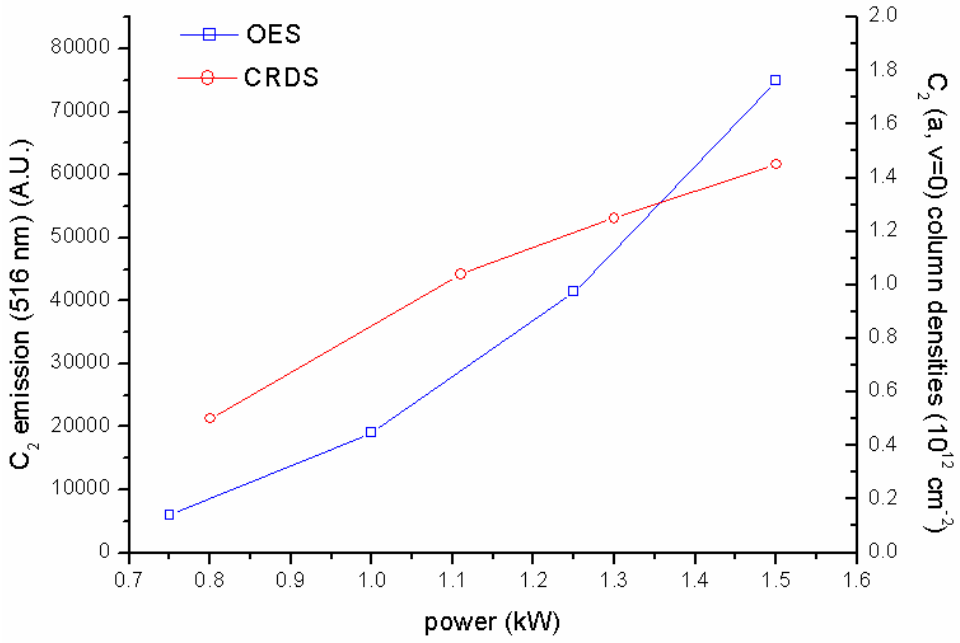

Figure 6. 39. Comparison of OES measured C_2 Swan band (516 nm) emission and CRDS measured C_2 (a,v=0) column densities under different input powers

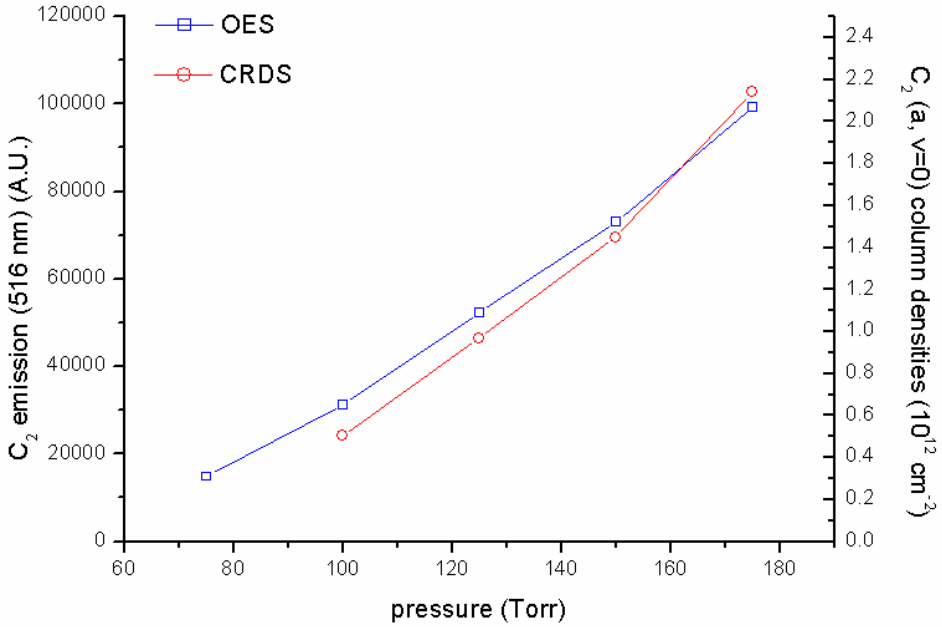

Figure 6. 40. Comparison of OES measured C_2 Swan band (516 nm) emission and CRDS measured C_2 (a,v=0) column densities under different pressures

6.3.4.3. CH radical

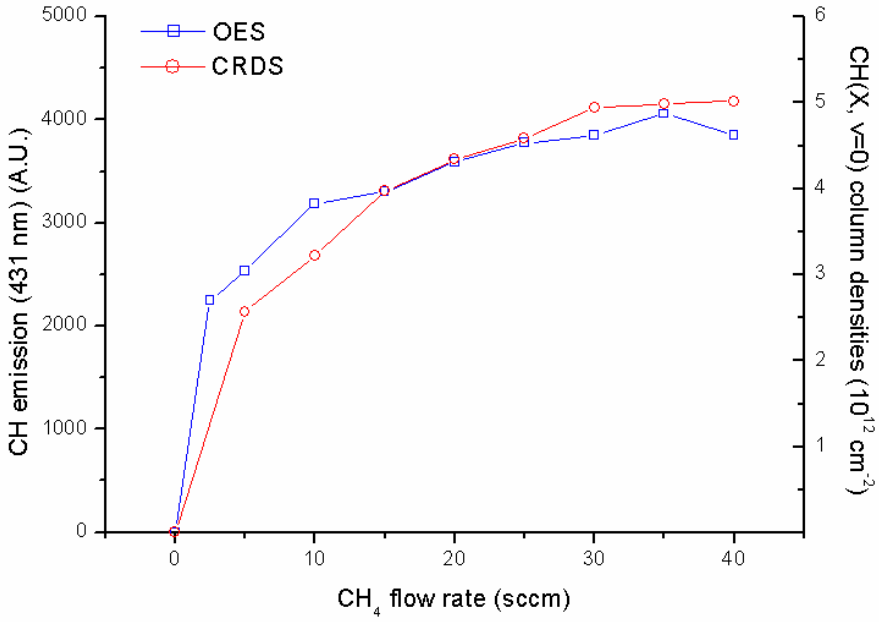

Figure 6. 41. Comparison of OES measured CH (431 nm) emission and CRDS measured CH (X,v=0) column densities under different CH_4 flow rates

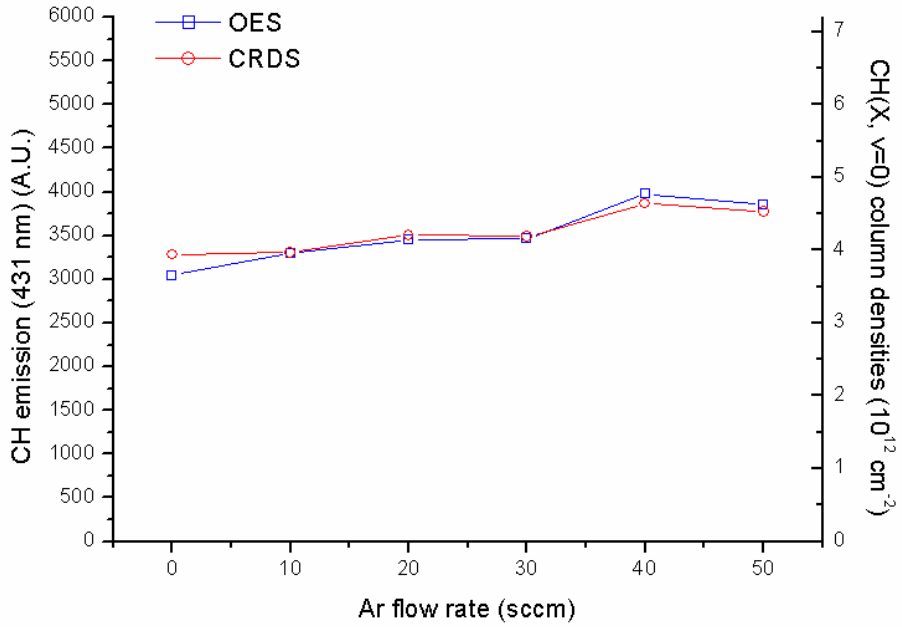

Figure 6. 42. Comparison of OES measured CH (431 nm) emission and CRDS measured CH (X,v=0) column densities under different Ar flow rates

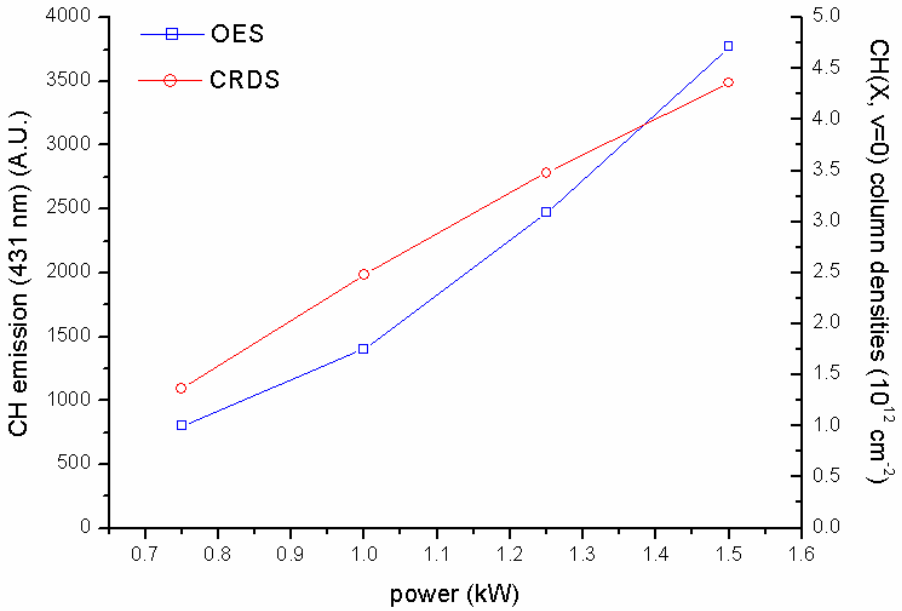

Figure 6. 43. Comparison of OES measured CH (431 nm) emission and CRDS measured CH (X,v=0) column densities under different input powers

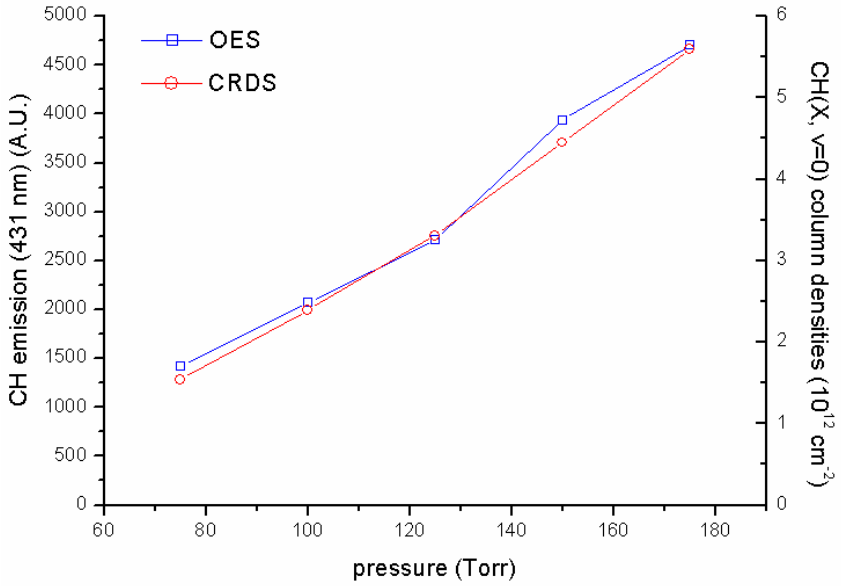

Figure 6. 44. Comparison of OES measured CH (431 nm) emission and CRDS measured CH (X,v=0) column densities under different pressures

The OES measured emission profiles of H_α, CH (431 nm) and C_2 (516 nm), compared with the CRDS measured column density profiles of H(n=2), CH(X,v=0) and C_2(a, v=0), are also shown in **Figure 6. 45** (in Ar/H_2 plasma) and **Figure 6. 46** (in $Ar/H_2/CH_4$ plasma). In order to show the comparison clearly, the OES results for H_α, CH (431 nm) and C_2 (516 nm) have each been scaled by an appropriate factor. It is noticed that, in both conditions (i.e. Ar/H_2 and $Ar/H_2/CH_4$ plasmas), the measured H_α spatial profiles in emission match the absorption profiles (i.e. the measured column density profile by CRDS) very well. At first sight, such a result is a bit surprising. However, considering that both H(n=3) (proportional to the H_α emission) and H(n=2) have very similar "origin", i.e. their generation is closely related with the electron impact excitation of the H(n=1) atoms, the good agreement between the OES and CRDS results is not unexpected. In contrast to the H_α emission profile, the emission profiles of C_2 and CH in $Ar/H_2/CH_4$ plasma in **Figure 6. 46** exhibit a significant discrepancy from the measured absorption profiles by CRDS in the region far (≥ 13 mm) away from the substrate, i.e. the emission profiles of C_2 and CH show a sharper drop than the profiles measured by CRDS there. However, the agreement between their emission profiles (by OES) and absorption profiles (by

CRDS) in the region close (<13 mm) to the substrate looks quite good. These observations can be understood by careful examination of the origin of the actually different species detected by OES and CRDS. OES, in fact, measures the excited states, i.e. C_2(d) (2.41 eV above the C_2 ground state) and CH(A) (2.88 eV above the CH ground state) while CRDS samples the lower states, i.e. C_2 (a) (only 0.09 eV above the C_2 ground state) and CH (X) (CH ground state). As discussed above, the generation of the lower states, C_2 (a) and CH (X), is dominated by thermal chemistry. The excited states, C_2(d) and CH(A) are produced mainly through the electron impact excitation of these lower states, thus they are not only related with thermal chemistry but also depend on the electron chemistry. In the region near the substrate, the electron density is high and the "electron pumping" is frequent enough to ensure a local equilibrium between the ground and excited states of heavy species. However, in the region far away from the substrate, the electron density drops very quickly. Thus the excited states will decrease fast as well. But the gas temperature there could be still high enough to sustain most of the thermal chemistry. So, the species in the lower states may still have a high concentration there. Finally, the species in the lower energy states have a wider spatial distribution than those in the highly excited states.

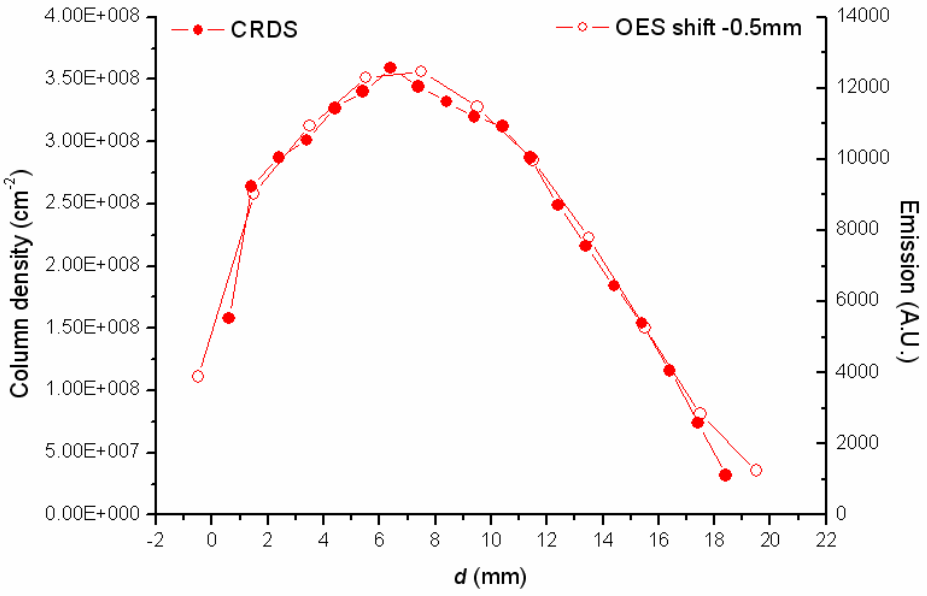

Figure 6. 45 Comparison between OES measured H_α emission profile and CRDS measured H(n=2) column densities profile in Ar/H_2 plasmas under the same discharge conditions

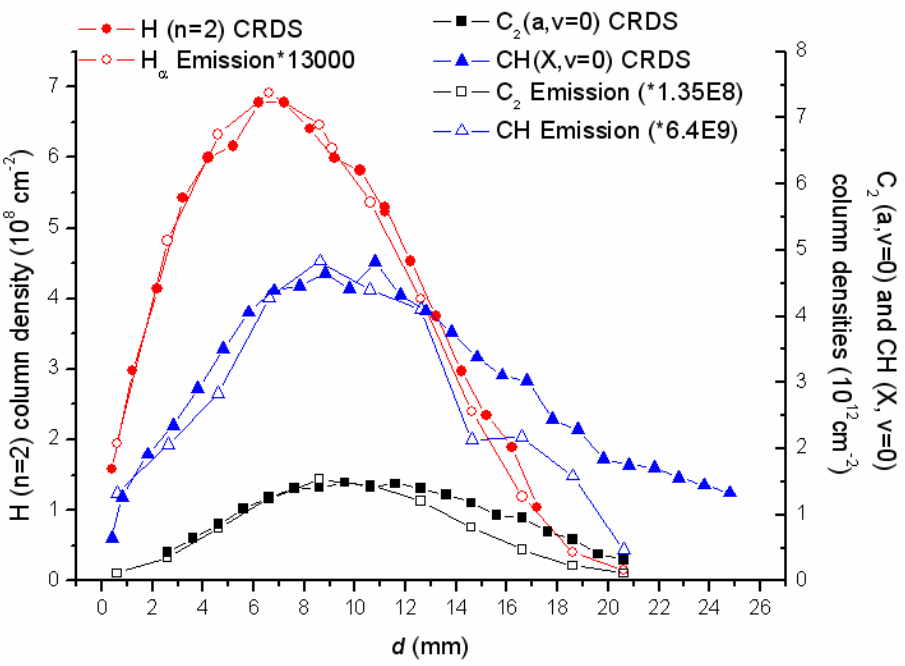

Figure 6. 46 Comparison between OES measured H_α, C_2 and CH emission profiles and CRDS measured H(n=2), C_2 and CH column density profiles in $Ar/H_2/CH_4$ plasmas under the same discharge conditions

6.4. Summary

OES has been used to investigate the behaviours of selected species in $CH_4/Ar/H_2$ plasmas. Actinometry has also been used to give information about the relative concentrations of H(n=1) and dissociation of H_2. The traced species can be classified into two groups according to the chemistry behind their generation: production of species like Ar*, H_2*, H(n=2,3) shows an electron dominated chemistry, while others like C_2, CH and H(n=1) show a thermal driven chemistry. The behaviours of these two kinds of species vary quite differently with selected discharge parameters.

The OES measured results are also compared with those obtained by CRDS. An unexpectedly good agreement is found, which suggests a cheaper method for studying these plasmas in the future.

6.5. References

[1] J. W. Coburn and M. Chen, *J. Appl. Phys.*, **51** (1980) 3134.

[2] A. Rousseau, A. Granier, G. Gousset, *et al.*, *J. Phys. D: Appl. Phys*, **27** (1994) 1412.

[3] Z.-C. Geng, Y. Xu, X.-F. Yang, *et al.*, *Plasma Sources Sci. Technol.*, **14** (2005) 76.

[4] V. S. Von. der. Gathen and H. F. Döbele, *Plasma Chemistry and Plasma Processing*,, **16** (1996) 461.

[5] M. Abdel-Rahman, V. S. Von. der. Gathen, K. T. Gans, *et al.*, *Plasma Sources Sci. Technol.*, **15** (2006) 620.

[6] A. Gicquel, K. Hassouni, S. Farhat, *et al.*, *Diamond Relat. Mater.*, **3** (1994) 581.

[7] A. Gicquel, M. Chenevier, K. Hassouni, *et al.*, *J. Appl. Phys.*, **83** (1998) 7504.

[8] D. G. Goodwin and J. E. Butler, *Handbook of Industrial Diamonds and Diamond Films*, (Marcel Dekker, New York, 1998).

[9] H. Tawara, Y. Itikawa, H. Nishimura, *et al.*, *J. Phys. Chem. Ref. Data*, **19** (1990) 617.

[10] N. Sadeghi and D. W. Setser, *Chem. Phys.*, **95** (1985) 305.

[11] J. Bitter, K. Kohse-Hoinghaus and U. Meier, *Th. Just. Chem. Phys. Lett.*, **143** (1988) 6.

[12] O. Krogh, T. Wicker and B. Chapmann, *J. Vac. Sci. Techn.*, **B4** (1986) 1292.

[13] J. P. Booth and N. Sadeghi, *J. Appl. Phys.*, **70** (1991) 611.

[14] A. Gicquel, M. Chenevier, Y. Breton, *et al.*, *J. Phys. III France*, **6** (1996) 1167.

[15] T. Lang, J. Stiegler, Y. von. Kaenel, *et al.*, *Diamond Relat. Mater.*, **5** (1996) 1171.

[16] K. Hassouni, T. A. Grotjohn and A. Gicquel, *J. Appl. Phys.*, **86** (1999) 134.

[17] A. N. Goyette, J. E. Lawler, L. W. Anderson, *et al.*, *Plasma Sources Sci. Technol.*, **7** (1998) 149.

Chapter 7 OES and CRDS diagnostics of $B_2H_6/Ar/H_2/CH_4$ plasmas

7.1. Introduction

P-type doped diamond with good conductivity can be achieved by adding boron into the diamond lattice. The frequently used boron source gas is B_2H_6. Normally it is diluted in H_2 to several percent and then used as a minor constituent in the total gas flow. A lot of work has been done with the aim to build up a relationship between the diamond film quality, doping rate and plasma parameters such as the B_2H_6 flow rate (or [B]/[C] ratio), substrate temperature, etc. [1, 2] However, the chemistry in a $B_2H_6/Ar/H_2/CH_4$ plasma is not well studied. Only a few papers can be found reporting diagnostics of such boron-containing plasmas. [3, 4] On the other hand, boron doped diamond is getting more and more attention from people, not only due to its applications in making electronic and optical devices, but also due to its newly discovered properties like superconductivity, [5, 6] and its large potential in bio-sensor applications. [7, 8] No doubt, all these applications lead to a great need to produce high quality, more versatile B-doped diamond and thus an emergent need of fully understanding the doping processes. Therefore, a detailed investigation of the chemistry in $B_2H_6/Ar/H_2/CH_4$ plasma is very timely.

The previous OES diagnostic studies done by Osiac et al [3] and Rayar et al [4] involved use of a high resolution spectrometer to measure BH emissions. Both of these works focus on measuring gas temperature from BH emission lines. In Osiac's work, they choose to measure BH emissions in $B_2H_6/Ar/H_2$ plasma in order to avoid the contamination from CH ($A^2\Delta \rightarrow X^2\Pi$) transitions. However, due to self-contamination in the P branch, only a few lines from the R branch of the BH (A–X) system were picked out to work out T_{rot}. After comparing the obtained T_{rot} with the gas temperature measured from H_2 rotational structures, a good agreement was found. But, as mentioned in Rayar et al's paper, this method encounters trouble when used in $B_2H_6/Ar/H_2/CH_4$ plasmas, where the CH ($A^2\Delta \rightarrow X^2\Pi$) transitions will totally overlap with the R branch of BH ($A^1\Pi \rightarrow X^1\Sigma^+$) transitions in the emission spectra.

Fortunately, the Q branch is not disturbed by CH emissions. Also, the convoluted shape of the Q branch can be sensitive to the rotational temperature. Thus they built up a new method which can be used to measure T_{rot} in $B_2H_6/Ar/H_2/CH_4$ plasmas based on careful measurement of the Q branch profile and then comparison with the simulated curves at various temperatures to get the best fitting.

However, there are two limits in these OES experiments. First, the direct information obtained from OES is the rotational temperature of the excited states, while the real gas temperature will be closer to the rotational temperature of the ground states. Thus a thermal equilibrium between BH (X) and BH (A) must always be assumed or checked. Secondly, the OES cannot give quantitative information about the BH concentration in the plasma. Both these problems can be solved using absorption spectroscopy. Therefore, new measurements are needed based on measuring BH (X) absorption.

Nevertheless, in view of the complexity of the B_2H_6-containing plasma, OES is still a good choice to give some first ideas of the characteristics of such plasmas. Though the absolute densities of species cannot be obtained by this method, the first impression on the behaviours of B_2H_6 plasma as a function of different discharge parameters will be achieved. Some important clues can be found to help give a better understanding of the chemistry about these boron-containing “active species”. In the following experiments, OES is thus firstly adopted and the emissions from selected species are measured as functions of different discharge parameters. After that, the more sensitive absorption spectroscopy, CRDS, is used to get the rotational temperature of BH (X), its column density and also its spatial profile.

7.2. Experimental

The experiments in this chapter involve three parts: OES (fixed position), spatially-resolved OES and CRDS. The OES experimental setup for the fixed position is shown in **Figure 7. 1**. There are small differences between this setup and the one used in the previous OES experiments (fixed position) in Chapter 6. Before, the optical system was set to monitor the plasma from the front window (made of glass thus not suitable to see emissions in the ultraviolet) and the line of sight is perpendicular to the laser beam in CRDS measurements. Now, in order to measure

the ultraviolet emission from Boron atoms (249.7 nm), the optical fiber (made of quartz) and the quartz lens were set to monitor the plasma from a side window (made of diamond) as shown in **Figure 7. 1** and the line of sight thus is parallel to the laser beam in CRDS measurement.

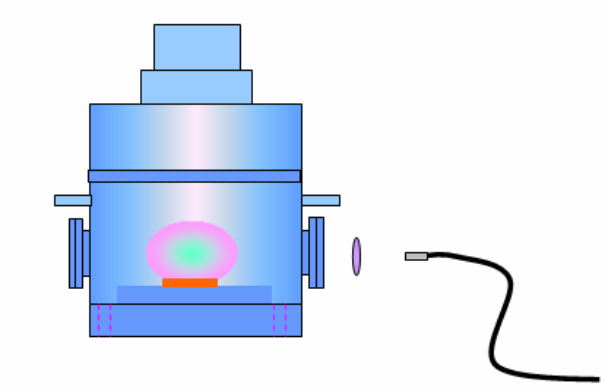

Figure 7. 1 Schematic of the OES experimental setup

The spatially resolved OES setup is the same as that used in Chapter 6, but when measuring the B emission profiles, due to the weak signal, an even longer "exposure time", 80 s, was used with 3 averages for each spectrum.

The CRDS experimental setup has already been shown in **Figure 5.1**. The mirrors and dyes used to measure BH here are the same as those used to measure CH in Chapter 5. The B_2H_6 feedstock used here is diluted to be 5% by H_2, a B_2H_6 MFC with maximum flow rate 1 sccm was used to control the flow rate of the 5% B_2H_6 in H_2 mixture.

7.3. Results and discussion

7.3.1 OES study of species behaviour as functions of different discharge parameters

7.3.1.1. Typical spectrum

The typical spectra measured by OES are shown here. In **Figure 7. 2**, the spectra were measured when the grating was set at the "middle" position. The three spectra correspond to the conditions of Ar/H_2 (40/525 sccm), $Ar/H_2/CH_4$ (40/500/25 sccm)

and $B_2H_6/Ar/H_2/CH_4$ (0.05/40/500/25 sccm) plasmas at standard pressure (150Torr) and power (1.5kW) conditions.

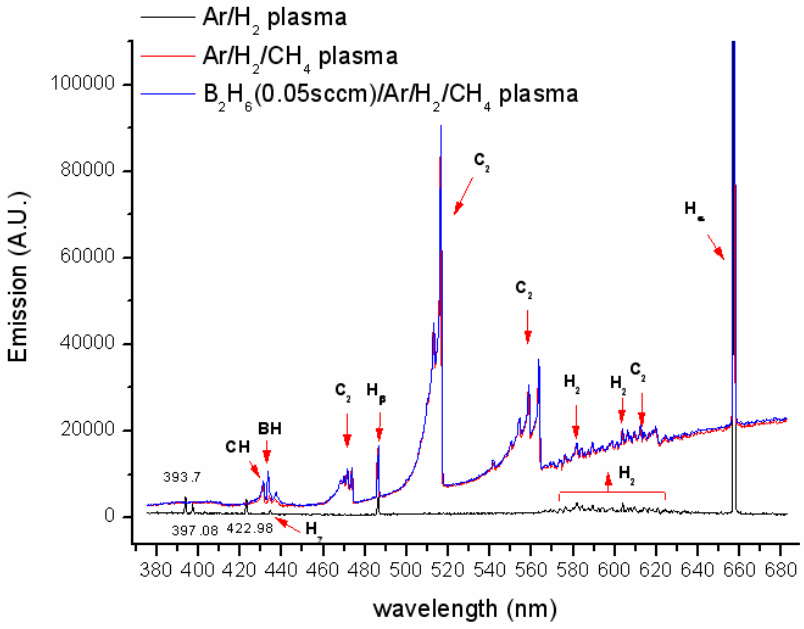

Figure 7. 2 Typical spectra at "middle" wavelength

Firstly, in the spectrum of Ar/H_2 plasma, it is worth noting that, besides the emissions from hydrogen Balmer series (H_α, H_β, H_γ) transitions and H_2 ($3p\ ^3\Sigma_u^+ \rightarrow 2s\ ^3\Sigma_g^+$) transitions, three "strange" lines at 393.7, 397.1 and 422.98 nm were also observed. They were thought to belong to some unknown sputtered or sprayed products from the substrate and would disappear as soon as the CH_4 or B_2H_6 was added.

Secondly, the spectra of $Ar/H_2/CH_4$ plasma and $B_2H_6/Ar/H_2/CH_4$ plasma look almost identical (suggesting that the B_2H_6 addition does not change the chemistry of $Ar/H_2/CH_4$ plasma much) except for a strong BH emission line at 433.2 nm from its Q branch. Since the BH spectral line is overlapped with CH and H_γ in the spectrum due to the limited resolution of the spectrometer, the baseline must be carefully removed in order to get the true BH emission intensity. The "hump" of the baseline in $Ar/H_2/CH_4$ plasma and $B_2H_6/Ar/H_2/CH_4$ plasma is due to black body radiation from the substrate as discussed in Chapter 6, suggesting that CH_4 addition can enhance heating of the substrate.

The spectra at "short" wavelength for the plasmas under the three conditions are shown in **Figure 7. 3**. It can be seen, in Ar/H_2 and $Ar/H_2/CH_4$ plasmas, no boron emission is observed, while in $B_2H_6/Ar/H_2/CH_4$ plasma, emission from boron 249.8 nm can be easily recognized.

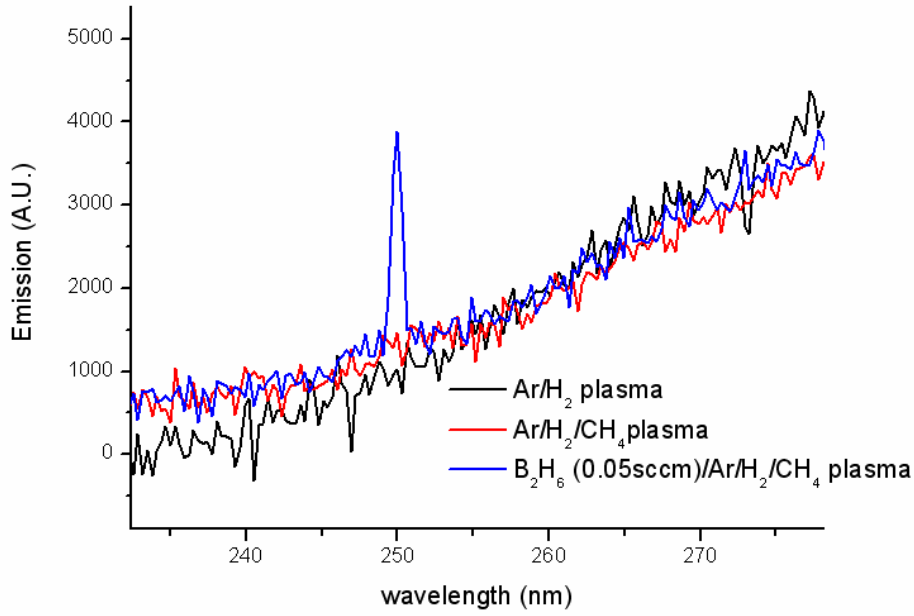

Figure 7. 3 Typical spectrum of boron emission at the "short" wavelength

7.3.1.2. Historigram

(a) Adding B_2H_6 into Ar/H_2 plasma

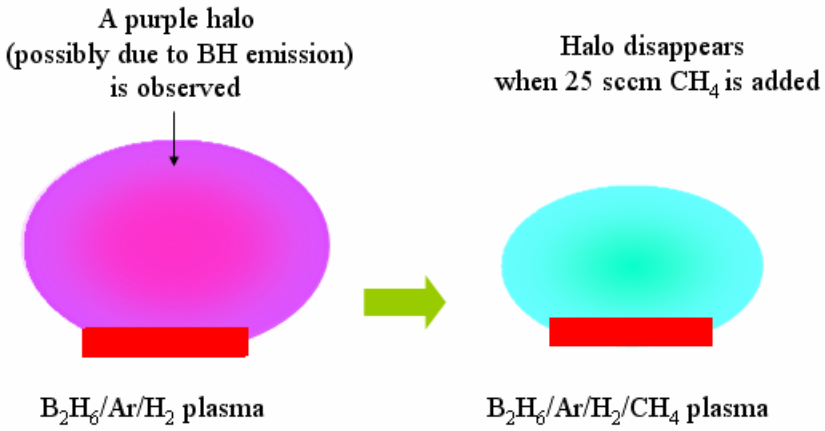

Figure 7. 4 Comparison between $B_2H_6/Ar/H_2$ plasma and $B_2H_6/Ar/H_2/CH_4$ plasma

When B_2H_6 was added into Ar/H_2 plasma, a big purple "halo" (possibly from BH emissions) can be observed around the central plasma ball, see the left picture in **Figure 7. 4**. Due to the small flow rate, it took a very long time for BH to reach equilibrium. In order to give a clearer picture of this time response, some historigrams of optical emissions from several selected species were recorded after B_2H_6 was fed in.

When the B_2H_6 is turned on, due to the long path way before entering the vacuum chamber after coming through B_2H_6 MFC, it is found that the BH signal always takes a very long time to appear. (See **Figure 7. 5**. We turn on B_2H_6 MFC at *t*=1275 *s*, however, BH emission cannot be seen until *t*=2100 *s*, around 12 minutes later after first introduction of B_2H_6 into the plasma.) Then at *t*=2880 *s*, around 28 minutes later after first introducing B_2H_6, the BH emission reaches a stable value. Such a slow time response is perhaps due to the long path that B_2H_6 has to pass before entering the chamber after crossing the MFC. So, before doing any measurements, after first introducing B_2H_6, normally, we wait more than 30 minutes for BH to build up. Later, when changing B_2H_6 flow rate, the change of BH emission can be observed immediately, with no such long response lag, see **Figure 7. 5**. Therefore, in the experiments, normally more than 5 minutes we wait for BH to reach a stable concentration after changing the B_2H_6 flow rates.

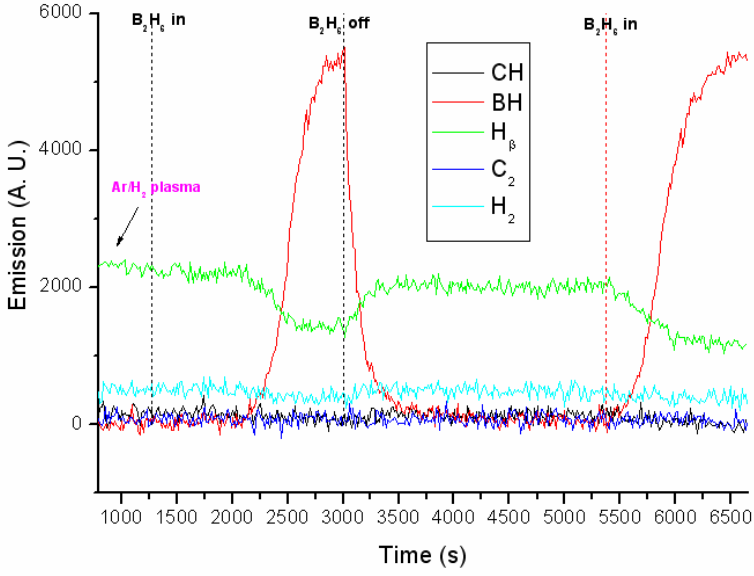

Figure 7. 5 Historigram of adding B_2H_6 into Ar/H_2 plasma

In **Figure 7. 5**, it can be noticed that, as soon as B_2H_6 begin to increase, the decrease of H_β and H_2 emission can also be observed. One explanation for this phenomenon

could be that under our conditions (high [H]), B_2H_6 perhaps dissociates into BH_3 after entering the microwave reactor. Then, the BH_3 may consume lots of H atoms by H abstraction reactions to produce BH_2, BH etc, thus reducing the density of excited H atoms as well. However, if we consider that only a tiny amount of B_2H_6 is added (the added mole fraction of B_2H_6 is 0.5*0.05/565≈44ppm while the H (n=1) mole fraction in the plasma is more than 30000 ppm estimated from Bristol-Moscow model!), this "huge" change would be surprising. Moreover, this explanation can not account for the fact that H_2 and Ar emissions (will be shown in **Subsection 7.3.1.1**) decrease as well after B_2H_6 addition. Therefore, it is more reasonable to attribute this "emission drop" to the change of the electron chemistry since the mole fraction of electrons is only about <0.3 ppm estimated from the Bristol-Moscow model (see **Figure 2.17**). In addition, B_2H_6 addition will cool the hot electrons in the plasma ball due to the lower ionization energy threshold of B_2H_6, BH_3, BH etc, through the process as follows:

$$e^- (hot) + B_xH_y \rightarrow 2\ e^- (cold) + B_xH_y^+ \quad (R7.1)$$

Therefore, though the total number of the electrons may increase after B_2H_6 addition, the number of hot electrons, which, are mainly responsible for species excitation and dominate the emissions from species like Ar*, H_2* H(n≥2), are reduced. This is the most likely reason why finally emissions from those species drop a lot when a tiny amount of B_2H_6 was added.

(b) Adding CH_4 into $Ar/H_2/B_2H_6$ plasma

When adding CH_4 into $B_2H_6/Ar/H_2$ plasma, by eye, it can be seen that the purple halo observed before soon becomes less obvious. The region around the plasma ball then looked quite transparent, see the right of **Figure 7. 4**. This phenomenon was also confirmed by the fact that we found, in $B_2H_6/Ar/H_2$ plasma, it was very easy (around 70 mins after first introducing B_2H_6 without CH_4 present) to get some polymer film (B_xH_y perhaps) deposited on the top quartz window, which finally led to poor microwave power coupling and then makes the recorded H_α, H_β emission intensities drift down with time. Some powders of this polymer produced in $B_2H_6/Ar/H_2$ plasma have already been collected. Their composition will be determined in the future. When CH_4 is present, however, no such film deposition on the top quartz window has been observed even when the $B_2H_6/Ar/H_2/CH_4$ plasma

keeps running for more than 6 hours. Such characteristics of the $B_2H_6/Ar/H_2$ plasma hinder us from thoroughly studying its behaviour. However, it is still possible to perform some quick measurements in $B_2H_6/Ar/H_2$ plasmas.

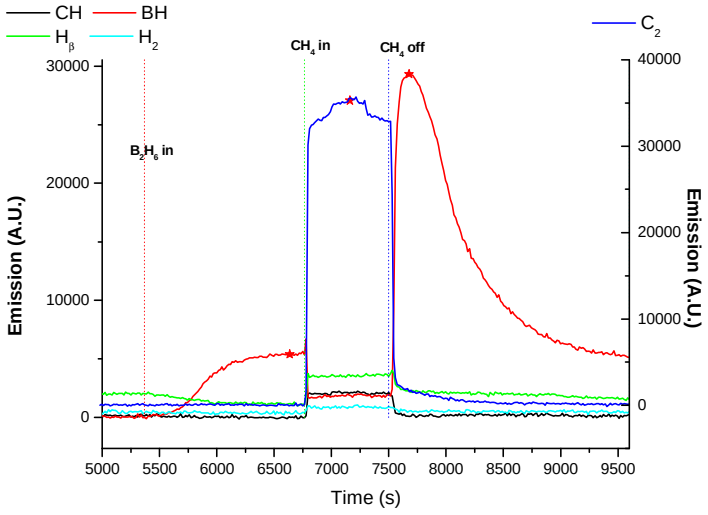

Figure 7. 6 Historigram of adding CH_4 into $B_2H_6/Ar/H_2$ plasma

The **Figure 7. 6** shows the historigram of CH_4 addition into a $B_2H_6/Ar/H_2$ plasma. It is no surprise that CH and C_2 emissions immediately become strong. Also, as we observed before (in Chapter 6), when adding CH_4 into H_2 plasma, the H Balmer series emissions increase a lot too. However, in contrast to these species, the emission from BH has an obvious decrease. One possible reason for this drop is that, when CH_4 is added, H atoms may be consumed, which will make the equilibrium of the reaction

$$BH_3 \underset{+H_2}{\overset{+H}{\rightleftharpoons}} BH_2 \underset{+H_2}{\overset{+H}{\rightleftharpoons}} BH \underset{+H_2}{\overset{+H}{\rightleftharpoons}} B \qquad \text{(R7. 2)}$$

shift towards the left.

When CH_4 is switched off, some surprising phenomenon occurs. It can be seen that CH, C_2, as well as H Balmer series and H_2 emissions immediately drop (no surprise) but BH has a sharp increase and the peak value is much higher even than that in the $B_2H_6/Ar/H_2$ plasma before! After that, it takes a very long time to reach a stable level, that is almost the same as in $B_2H_6/Ar/H_2$ plasma before. To show this phenomenon more clearly, three typical spectra picked at three different times (marked by three

"star" symbols in **Figure 7. 6**, corresponding to steady states in $B_2H_6/Ar/H_2$ plasma, in $B_2H_6/Ar/H_2/CH_4$ plasma, and a "transition" state in $B_2H_6/Ar/H_2$ plasma again when BH emission reaches the maximum after the CH_4 feedstock is suddenly switched off, are shown in **Figure 7. 7**. The dramatically enhanced emission from BH Q branch is quite remarkable.

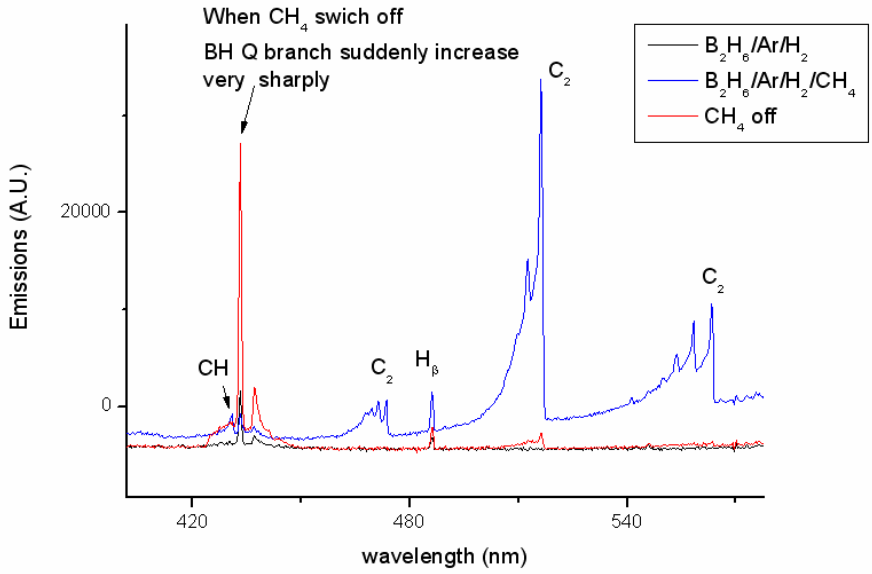

Figure 7. 7 Typical spectra picked at three different times: $B_2H_6/Ar/H_2$ plasma, $B_2H_6/Ar/H_2/CH_4$ plasma, and shortly after CH_4 is off and BH reaches its maximum.

The reason for this huge enhancement of BH emission is still under investigation. There are still two possibilities: one is that some unknown thermal chemistry makes BH densities increase a lot; the other is that BH densities may not change much, but the electron chemistry has changed a lot, which finally results in this enhancement of the BH emission. In addition, notice that, though CH_4 has already been switched off when BH reaches its maximum, some C_2 emissions still can be distinguished in the spectrum, see **Figure 7. 7**, which may imply the enhancement of BH emission has some links with the CH_4 flow rate.

7.3.1.3. B_2H_6 flow rate effect

As shown in **Figure 7. 5**, though B_2H_6 flow rate is much smaller than those of H_2, Ar and CH_4, however, if CH_4 is absent, B_2H_6 addition still can influence the Ar/H_2 plasma a lot. This shows how reactive B_2H_6 is in the plasma environment. But, when 25 sccm CH_4 is added into the plasma, B_2H_6 seems to lose its "impact" on the

plasma. This can be seen from the very small change of H_α, H_β, H_2, C_2, CH and Ar emissions in $Ar/H_2/CH_4$ plasma after even 0.05 sccm B_2H_6 is added. Only boron and BH emissions roughly have a linear dependence on the B_2H_6 flow rate. (See **Figure 7. 8 ~ Figure 7. 10**)

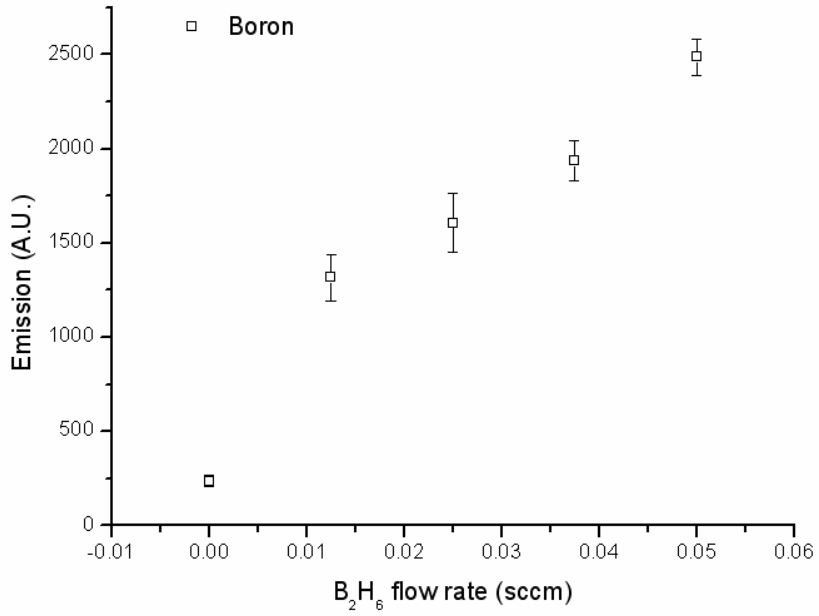

Figure 7. 8 Boron emission as a function of B_2H_6 flow rate. All other parameters are the same as used in the "standard" condition.

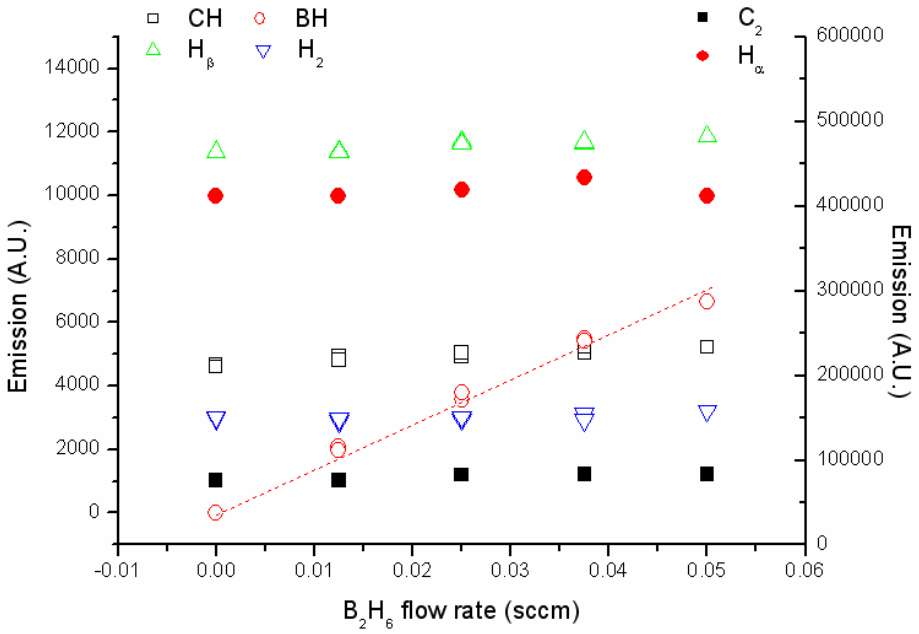

Figure 7. 9 CH, BH, H_β, H_2, C_2 and H_α emissions as functions of B_2H_6 flow rate. All other parameters are the same as used in the "standard" condition.

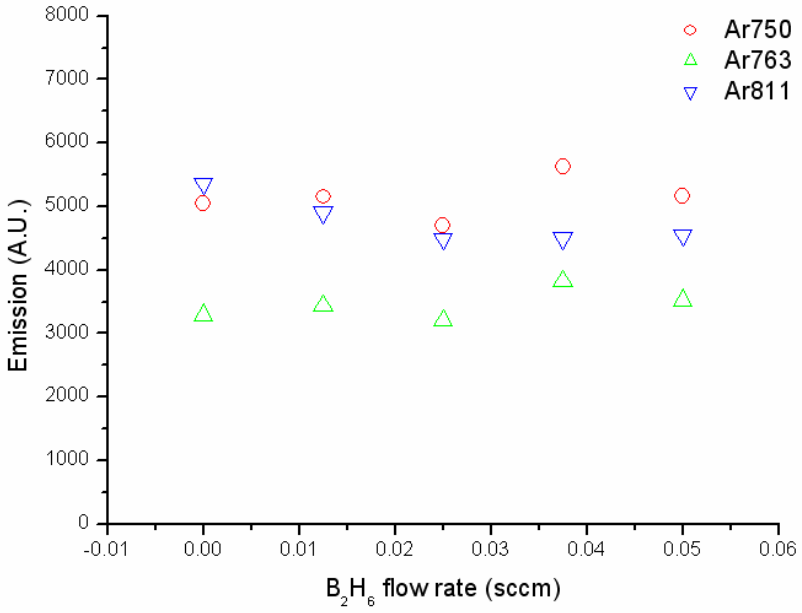

Figure 7. 10 Ar emissions as functions of B_2H_6 flow rate. All other parameters are the same as used in the "standard" condition.

7.3.1.4. CH_4 flow rate effect

The CH_4 flow rate effect on the emission of selected species is shown in **Figure 7. 11**~**Figure 7. 13**. In addition, in order to show the B_2H_6 addition effect on Ar/H_2 plasma in the same figures, the emissions from selected species in Ar/H_2 plasma are put at the "CH_4 flow rate = -5 sccm". **Figure 7. 11** shows that, when CH_4 is introduced into $B_2H_6/Ar/H_2$ (B_2H_6 flow rate is 0.025 sccm), the boron emission increases. Similar behaviour has also been observed on H Balmer series emissions, H_2 and Ar emissions (see **Figure 7. 12** and **Figure 7. 13**). The reason for such emission enhancement due to CH_4 addition has been discussed in Chapter 5. The sensitivity of boron emission on CH_4 presence or not suggests the excited boron is somehow sensitive to the electron chemistry. Further additions of CH_4 seem to have little effect on boron emission though the H Balmer and Ar emissions show a decrease after the "first jump". The latter phenomenon is the same as previously observed in $Ar/H_2/CH_4$ plasma in Chapter 6 and is thought to be an effect of T_e drop. The effect of CH_4 addition on BH emission is different from all other species described above (i.e. B*, H(n≥2), Ar*, H_2*). When a small amount of CH_4 is first introduced to $B_2H_6/Ar/H_2$ plasma, instead of the "first jump", the BH emission

shows a sharp decrease. When more CH_4 is added, it shows a much "slower" decrease. One explanation for this is that, the fed-in CH_4 possibly consumes a lot of H atoms, making the equilibrium of reaction **R7.2** shift left towards BH_3. Therefore, though n_e increases a lot as CH_4 is added, the reduction of BH has the dominant effect on the BH emission. Since here, the C_2, CH, H Balmer, H_2 and Ar emissions exhibit the same behaviour as in $Ar/H_2/CH_4$ plasma, it shows that when 25 sccm CH_4 is present in the plasma, the hydrocarbon gas will dominate the plasma characteristics.

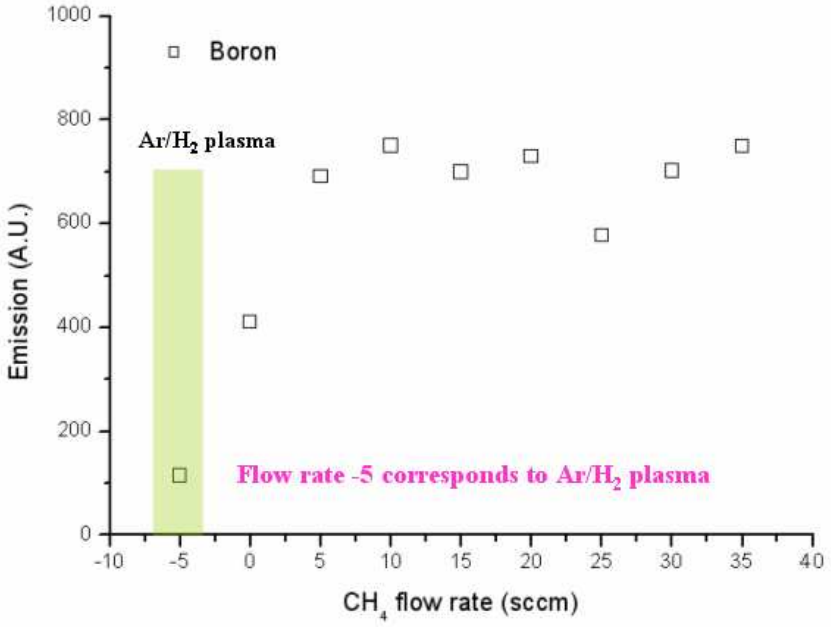

Figure 7. 11 Boron emissions as a function of CH_4 flow rate. The B_2H_6 flow rate is set at 0.025 sccm. All other parameters are the same as used in the "standard" condition.

In contrast, when a small amount of B_2H_6 was added into the Ar/H_2 plasma (CH_4 is absent), the plasma became quite different and a big purple "halo" occurred as shown in **Figure 7. 4**. In addition, in **Figure 7. 12** and **Figure 7. 13**, one can see that 0.025 sccm B_2H_6 addition cause the Ar, H_2, H Balmer emissions all to reduce a lot. This effect is exactly opposite to that observed when CH_4 is added into Ar/H_2 plasma. The reason for this, similar to that discussed before for CH_4 addition in Chapter 5, possibly is due to the change of the electron chemistry (electron temperature and/or density) when B_2H_6 is introduced. The difference, however, for B_2H_6 case, is that, the effect from T_e drop exceeds that from n_e enhancement. Therefore, a weakening,

instead of enhancement, of the emissions of species like excited Ar, H_2, H (dominated by electron chemistry) are observed.

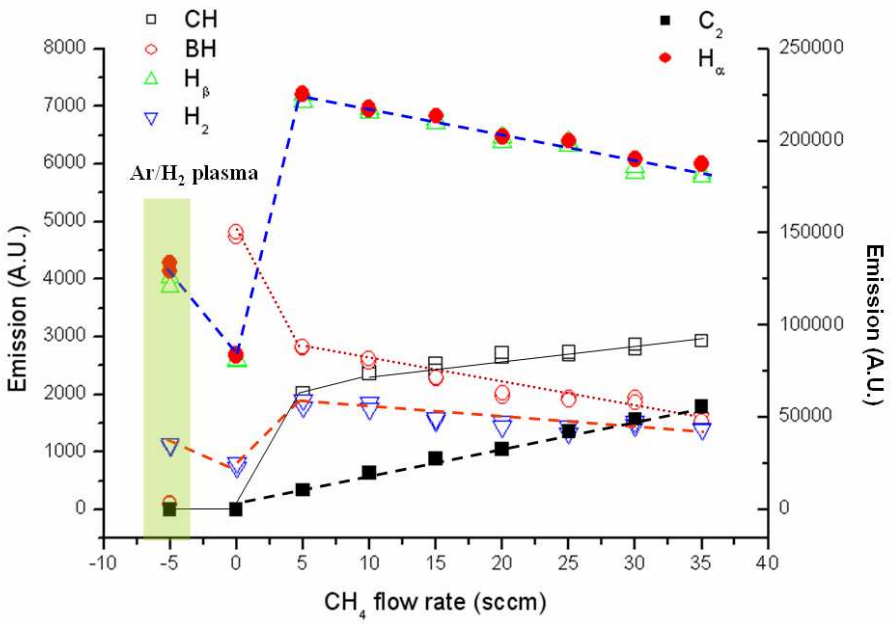

Figure 7. 12 Emissions of CH, BH, H_β, H_2, C_2 and H_α as functions of CH_4 flow rate

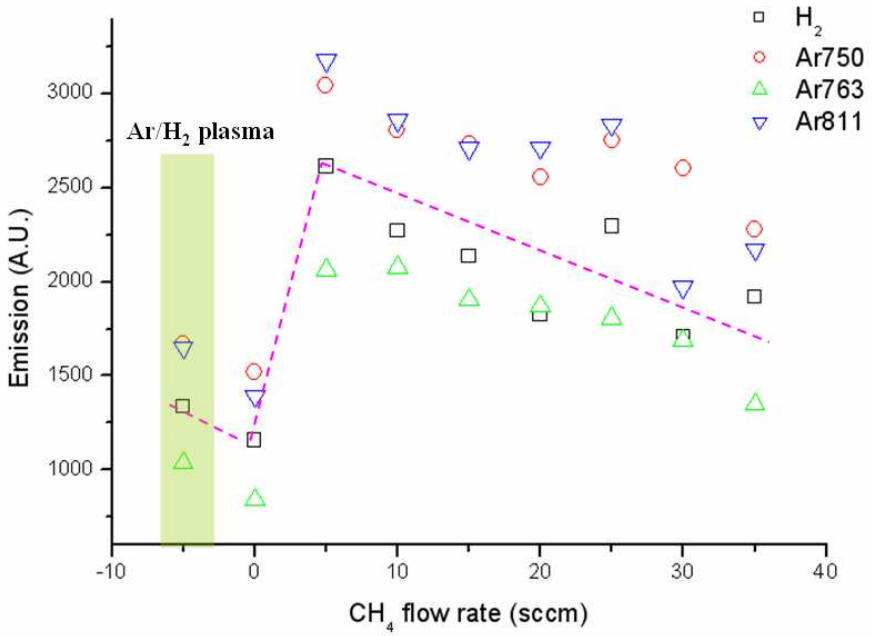

Figure 7. 13 Emissions of H_2 and Ar as functions of CH_4 flow rate

7.3.1.5. Ar flow rate effect

Under our experimental conditions, Ar flow rate has a relatively weak effect on the plasma. When Ar flow rate changes from 0 to 40 sccm, no obvious changes in boron

emission can be observed (see **Figure 7. 14**). However, **Figure 7. 15** shows that more Ar addition increases the emission from C_2, CH and H Balmer series a bit. At the same time, BH and H_2* emissions seems to drop a tiny bit. The reduction of H_2 emission may be explained by the reduction of H_2 gas input in order to compensate the increased Ar gas input and keep total flow rate constant. Of course, more Ar will make Ar emissions increase, as shown in **Figure 7. 16**. It seems that the Ar 750 nm (which always is chosen as the tracing line in actinometry) shows a better linear relationship on Ar flow rate than the Ar 763 nm and Ar 811 nm lines. All these behaviours, except those of B and BH emissions, are similar to those observed before in $Ar/H_2/CH_4$ plasma.

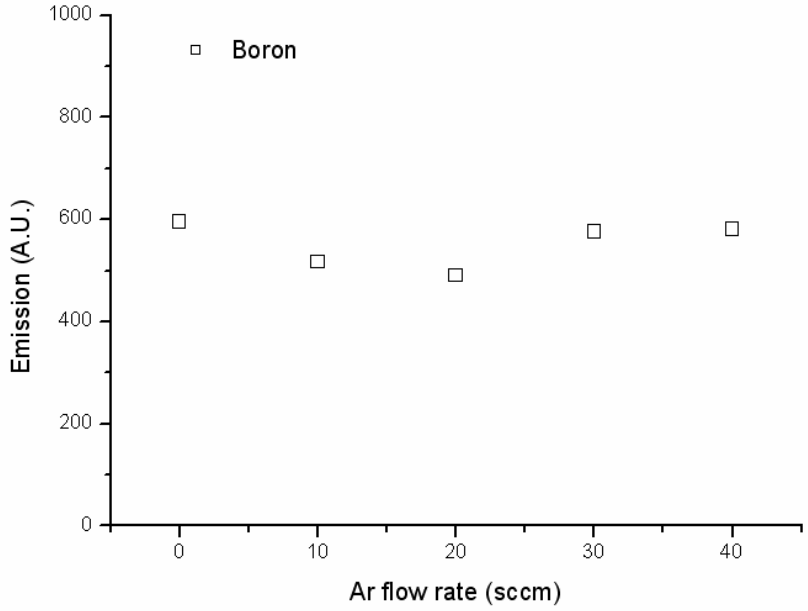

Figure 7. 14 Boron emissions as a function of Ar flow rate

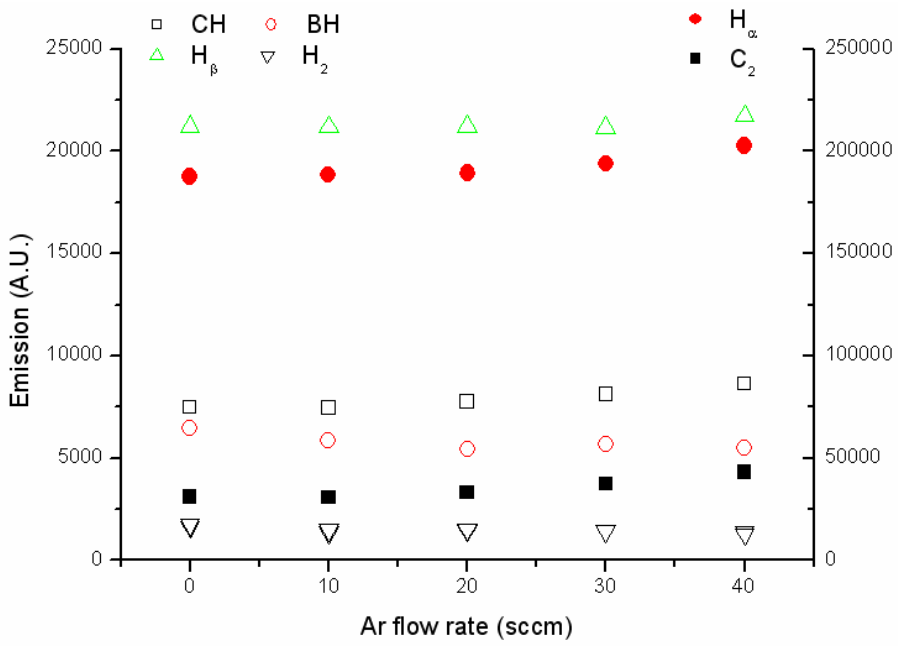

Figure 7. 15 CH, BH, H_β, H_2, H_α and C_2 emissions as functions of Ar flow rate.

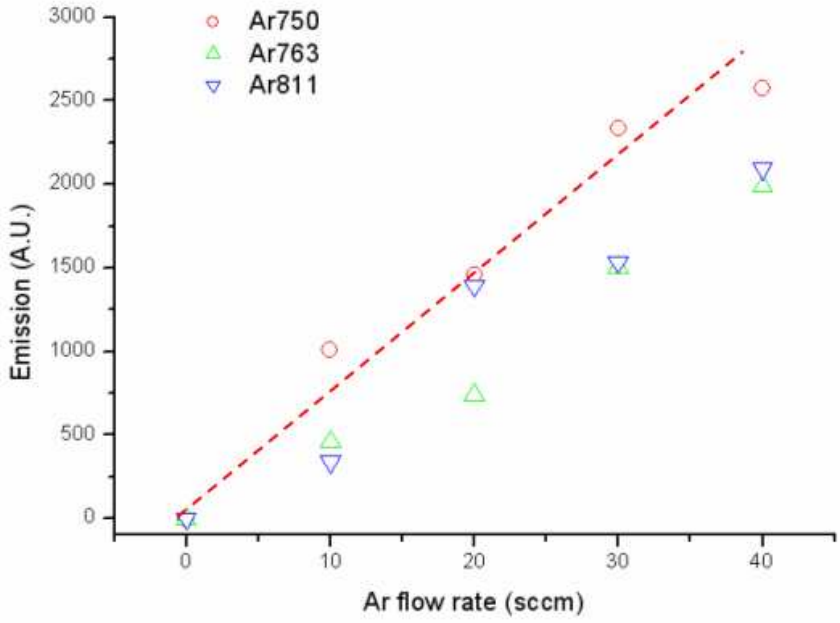

Figure 7. 16 Ar emissions as functions of Ar flow rate

7.3.1.6. Power effect

Figure 7. 17 - **Figure 7. 19** show that emissions from species (like B*, Ar*, H(n≥2), H_2*, CH*, and C_2*) increase with increasing the input power. The reason may be that, when increasing the power, both the electron density and H atom density (see

Chapter 6) will increase, which then will help generate more excited states and radicals. Therefore, such an emission enhancement for most species is somehow expected. The BH emissions shown in **Figure 7. 18** seem not very sensitive to the power, in contrast to the boron emissions in **Figure 7. 17**. This may reflect the shift of the reaction equilibrium in **R7. 2**. When the power increases, more H atoms are generated and the reaction equilibrium of **R7. 2** will be shifted towards producing more B, which may make BH densities decrease. Such a "negative" effect for BH may just be balanced by the positive effect of the enhanced electron density, rendering the BH emissions less sensitive than B to the input power. In addition, H_α and H_β emissions have almost identical trends, which may suggest the electron temperature does not change much when varying the input power.

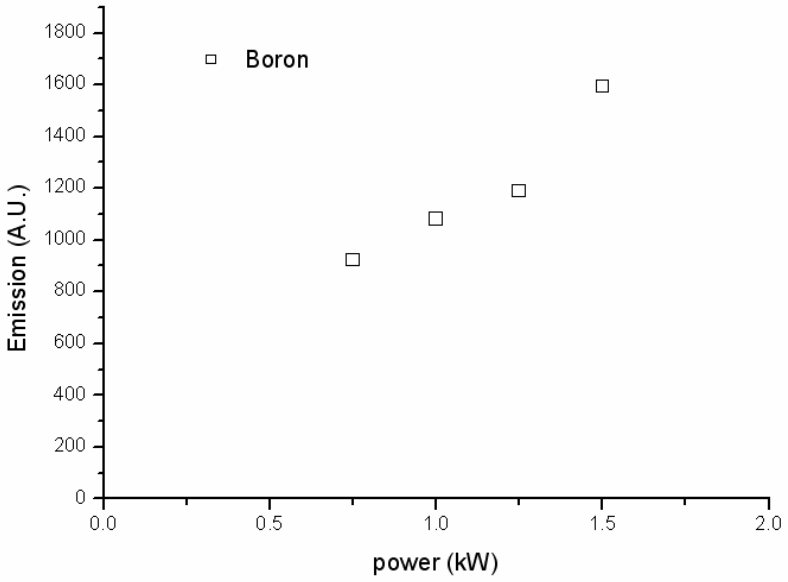

Figure 7. 17 Boron emissions as a function of input power

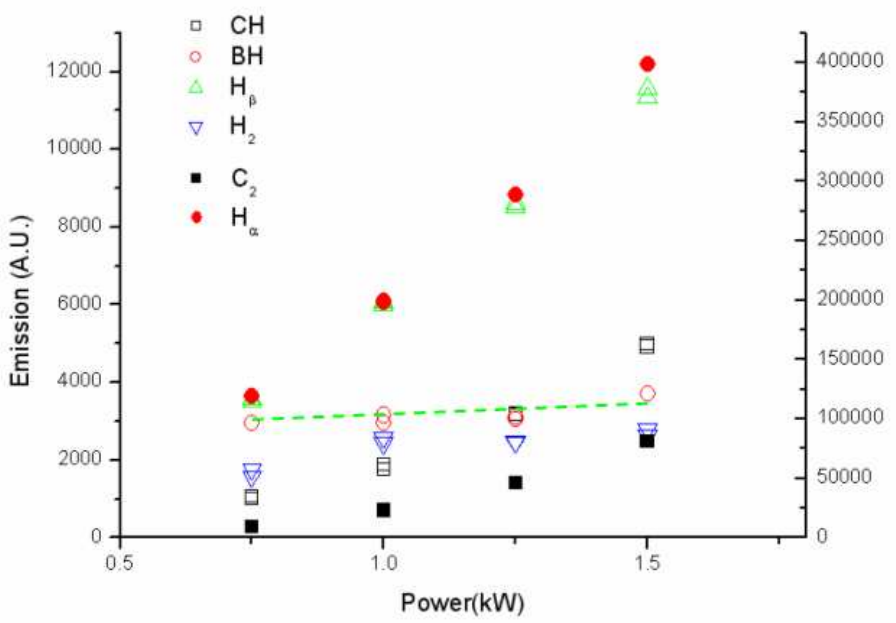

Figure 7. 18 CH, BH, H_β, H_2, C_2 and H_α emissions as functions of input power

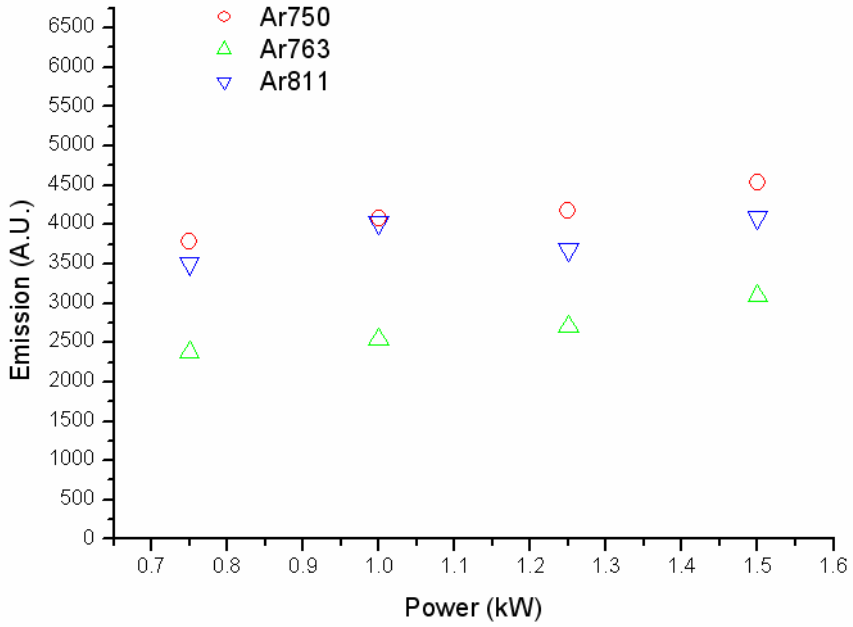

Figure 7. 19 Ar emissions as functions of input power

7.3.1.7. Pressure effect

The species discussed above exhibit different responses to changes in total pressure, see **Figure 7. 20 - Figure 7. 22**. The CH and C_2 emissions increase with pressure (**Figure 7. 21**) while the Ar emissions decrease with pressure (**Figure 7. 22**). Such

behaviours have been discussed in Chapter 6. The boron emission increases as the pressure increases then drops when the pressure becomes very high (e.g 175 Torr). However, for BH, the "turning" point is much earlier than B. It is around 100 torr. The H_α and H_β emissions do not show a "turning" point within the pressure range examined in the experiment, which is somehow different from the previous OES results shown in **Figure 6.23** but quite similar to the trend of the measured column density of H(n=2) by CRDS shown in **Figure 5.12**. This makes us suspicious that such a difference may come from the different regions monitored by the OES in these two experiments (here and in Chapter 6). The later experiment, in which the optical fiber was repositioned to monitor the plasma from the front window, verified such a point, (see in Appendix D). The emissions of B*, BH* and H Balmer series are not only influenced by the electron densities and the electron temperature, but also closely related to the details of the thermal reactions for generation of their "parent species"(e.g. B, BH and H ground states). The occurrence of those "turning" points in B, BH and H Balmer emissions may be regard as a result of the competition between the electron chemistry and the thermal chemistry. When the pressure increases, on one hand, the drop of the electron temperature (though n_e may still increase) tends to make species' emissions weaker (see Ar emissions as an example). On the other hand, the collisions between the heavy species become more frequent under a higher pressure, which favours the thermal reactions. Thus increasing pressure can help produce more "parent" species like B, BH and H ground states and hence tends to enhance species' emissions. The competition between the effects of the electron chemistry and thermal chemistry finally results in the occurrence of a turning point. However, the pressure at which this turning point occurs depends on many details of the electron chemistry and thermal chemistry of those species, is thus not easy to predict.

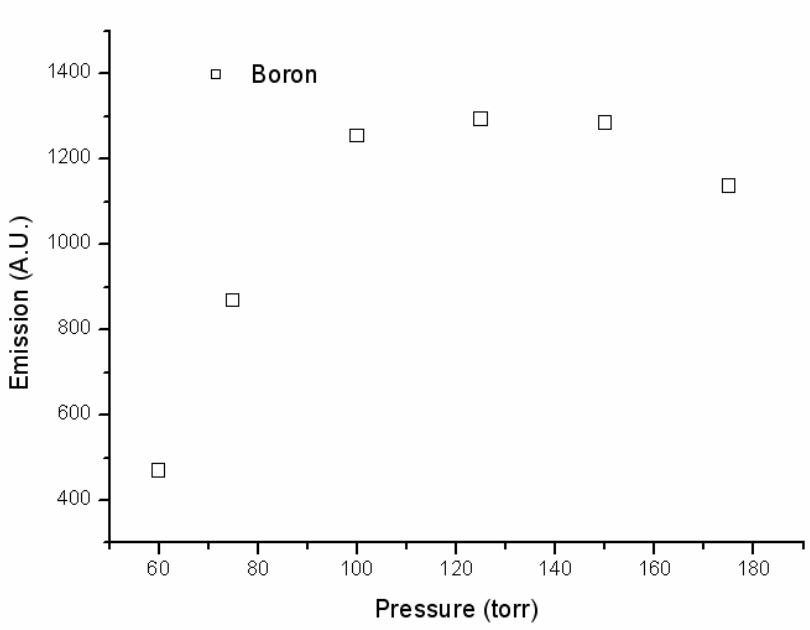

Figure 7. 20 Boron emissions as a function of pressure

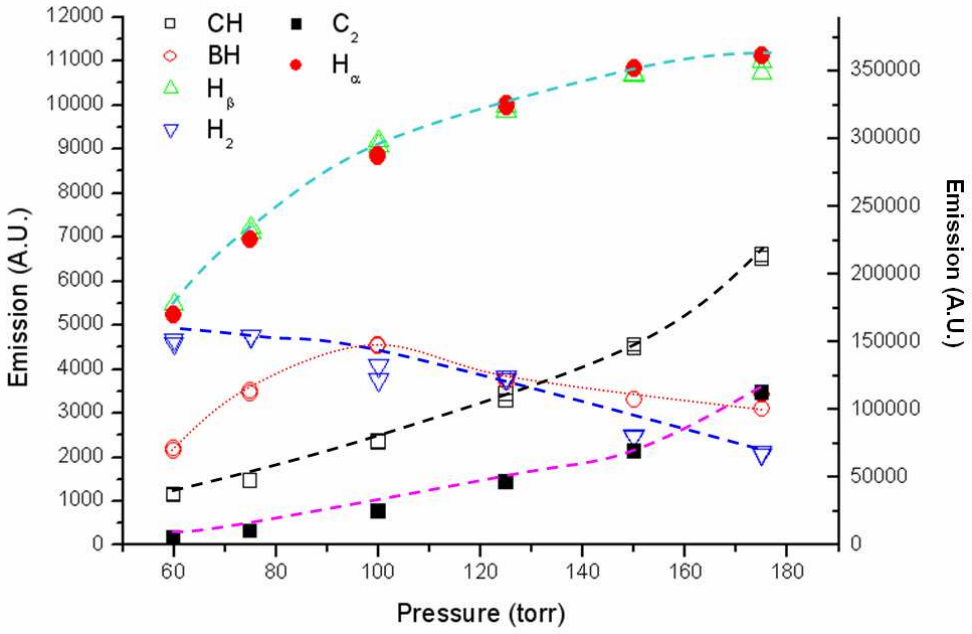

Figure 7. 21 CH, BH, H_β, H_2, C_2 and H_α emissions as functions of pressure

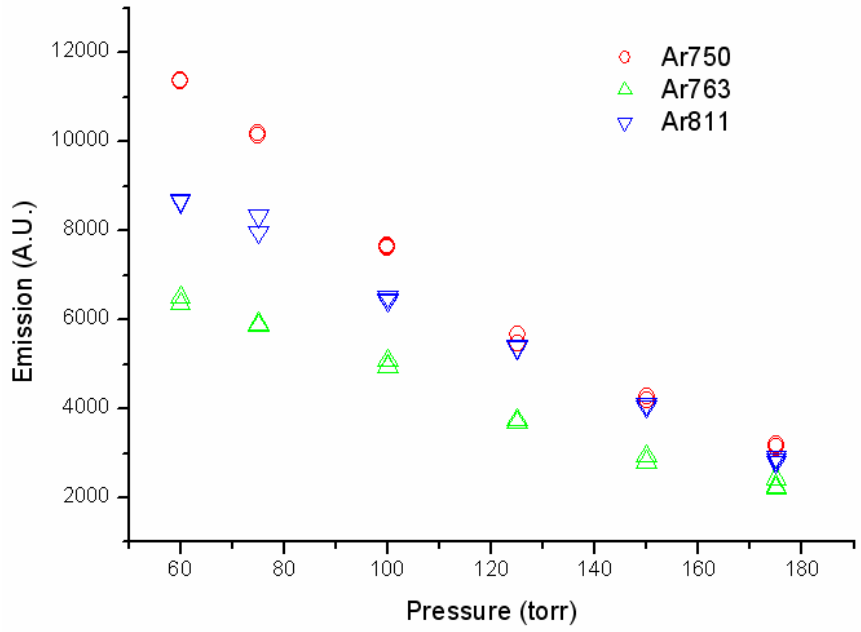

Figure 7. 22 Ar emissions as functions of pressure

7.3.1.8. Emission profiles

The spatially-resolved OES experimental setup has already been shown in **Figure 6.1** in Chapter 6. Here, the measured emission profiles of H_α, H_β, H_2, CH, C_2, BH and B in $Ar/H_2/CH_4/B_2H_6$ plasmas are shown in **Figure 7. 23 - Figure 7. 26**.

The profiles shown in **Figure 7. 23** and **Figure 7. 24** are measured in $B_2H_6/Ar/H_2/CH_4$ plasma at standard discharge conditions with B_2H_6 flow rate 0.025 sccm. It can be seen that, in **Figure 7. 23,** the measured profiles of the H_β, C_2, CH and H_2 emissions are similar to those observed in $Ar/H_2/CH_4$ plasma. However, due to the extremely long "exposure time", the measured H_α emission is saturated at intermediate *d* values. The measured BH emissions show a wider distribution than the C_2 and CH emissions, which may suggest that BH radicals are relatively more stable than C_2 and CH in cold regions. Though a bit noisy, the measured boron emission profile in **Figure 7. 24** still shows a similar peak center (at ~10mm) as the C_2 and CH emission profiles.

Figure 7. 25 and **Figure 7. 26** show the measured emission profiles of selected species also at standard discharge conditions but with a higher B_2H_6 flow rate (0.05 sccm). The higher B_2H_6 flow rate enhances the measured BH and boron emission signals and also reduces the errors in measured emission profiles. In **Figure 7. 25**,

the measured BH emissions now even exceed the CH emissions. The profiles observed under this condition are similar to those found in $B_2H_6/Ar/H_2/CH_4$ plasma when the B_2H_6 flow rate is 0.025 sccm.

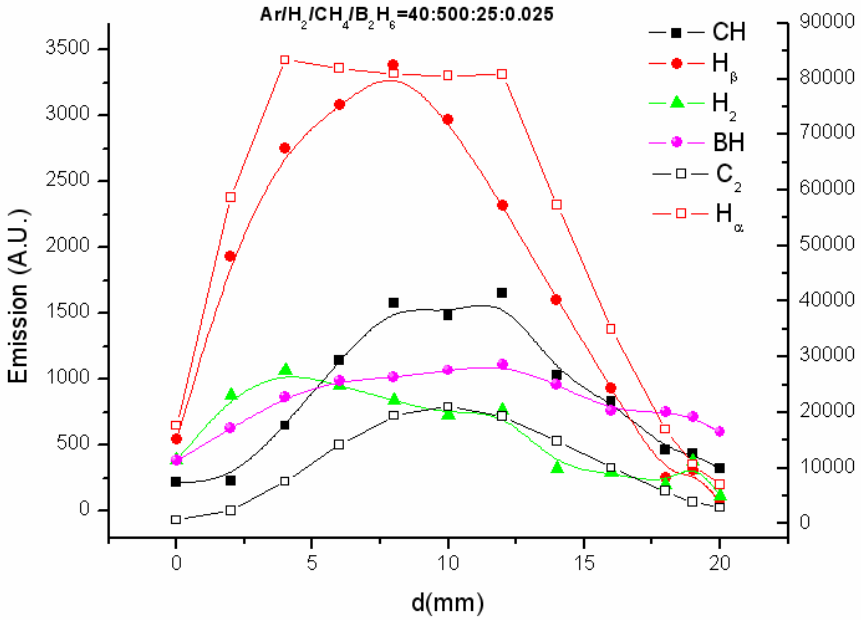

Figure 7. 23 CH, BH, H_β, H_α, H_2 and C_2 emission profiles in B_2H_6 (0.025 sccm)/$Ar/H_2/CH_4$ plasma

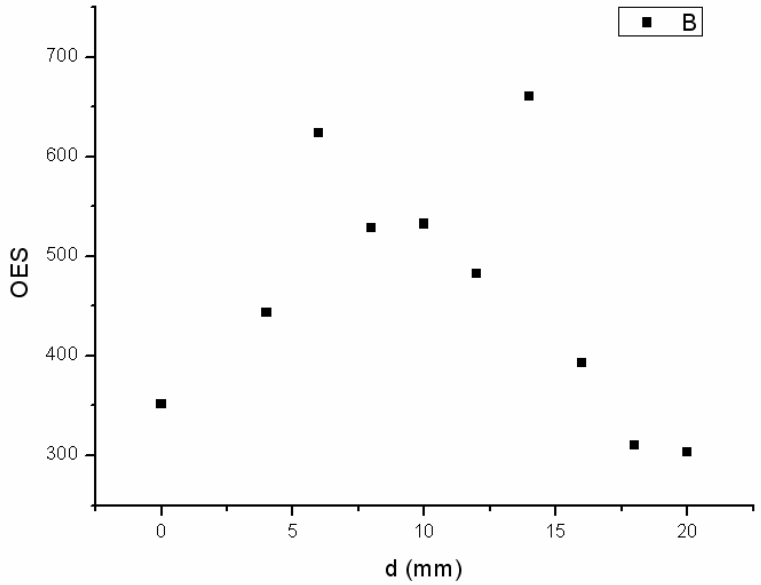

Figure 7. 24 Boron emission profile in B_2H_6 (0.025 sccm)/$Ar/H_2/CH_4$ plasma

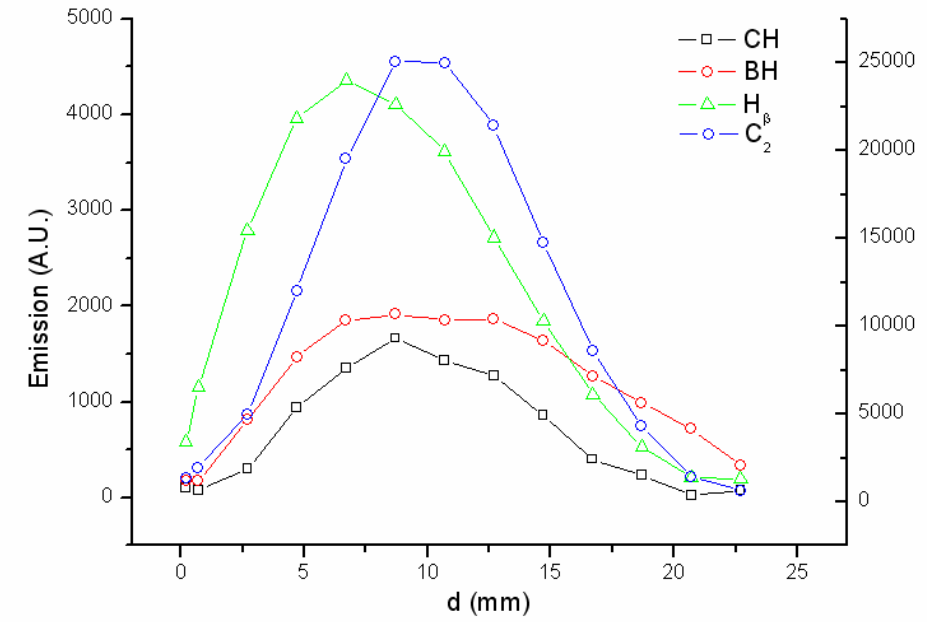

Figure 7. 25 CH, BH, H_β, C_2 emission profiles in B_2H_6 (0.05 sccm)/Ar/H_2/CH_4 plasma

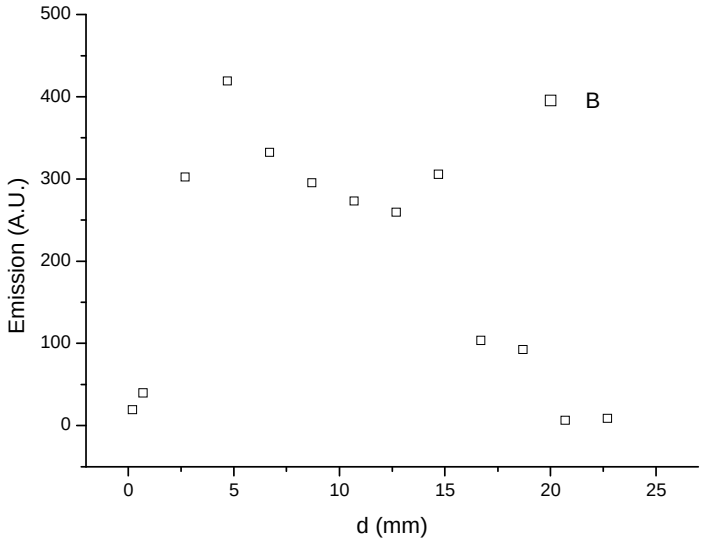

Figure 7. 26 Boron emission profile in B_2H_6 (0.05 sccm)/Ar/H_2/CH_4 plasma

7.3.2 CRDS study of $B_2H_6/Ar/H_2/CH_4$ plasma

Due to the two limits of the OES discussed at the beginning of this chapter, absorption spectroscopy can be the better choice to give more detailed information about the plasma. Similar to the studies of $Ar/H_2/CH_4$ plasma discussed in Chapter 5, the spatially resolved CRDS system (already shown in **Figure 5.1**) was also used here to measure the rotational temperature of BH, its column density and spatial profiles.

7.3.2.1. Typical absorption spectrum

As mentioned in **Section 7.3.1**, the overlap of BH ($X^1\Sigma^+ \rightarrow A^1\Pi$) and CH ($X^2\Pi \rightarrow A^2\Delta$) bands is a barrier to using BH spectral lines to get information about the $B_2H_6/Ar/H_2/CH_4$ plasma. However, by using laser spectroscopy techniques, an extremely high resolution can be achieved, and some "uncontaminated" BH lines can be identified after careful examination of the measured spectrum. Therefore, as the first step, it is necessary to pick out the "uncontaminated" BH lines. To do this, a BH absorption spectrum was firstly measured in an $Ar/H_2/B_2H_6$ plasma so as to be free of the perturbation from CH. Similarly, a CH absorption spectrum was measured in an $Ar/H_2/CH_4$ plasma, thus the influence from BH absorption can be excluded too. Then, the absorption spectrum in the $B_2H_6/Ar/H_2/CH_4$ plasma was recorded and compared with the spectra obtained before in the $Ar/H_2/B_2H_6$ and $Ar/H_2/CH_4$ plasmas. Finally, the "uncontaminated" BH lines can be identified.

The measured BH lines in B_2H_6 (0.025 sccm)/Ar/H_2 plasma under the "standard" discharge condition are shown in **Figure 7. 27**. These lines belong to the R branch of BH (A–X) (0,0) band. It is noticed that the strong ^{11}BH rotation line is always accompanied by a weak line from its isotopologue, ^{10}BH. The ratio should be about 4:1 according to the abundance of ^{11}B and ^{10}B in nature. However, due to strong absorption, the rotation lines of ^{11}BH from R(8) to R(13) are more or less saturated (though the isotope ^{10}BH lines are still fine). For these saturated rotational lines, the intensity ratios of ^{11}BH and ^{10}BH are much less than 4:1. So, in the experiments, attention must be paid to avoiding the use of saturated lines for calculation.

Part of the measured spectra in the $Ar/H_2/CH_4$ and B_2H_6 (0.025 sccm)/$Ar/H_2/CH_4$ plasmas under the "standard" discharge condition is shown in **Figure 7. 28**. It can be seen that, the BH lines can be divided into three classes: not contaminated (NC), partially contaminated by CH (1,1) hot band (PC) and totally contaminated (TC). Twelve pairs of ^{11}BH and ^{10}BH rotation lines within the range of 23287~ 23513 cm^{-1} are examined and classified by this method. The results are summarized in **Table 7.1**

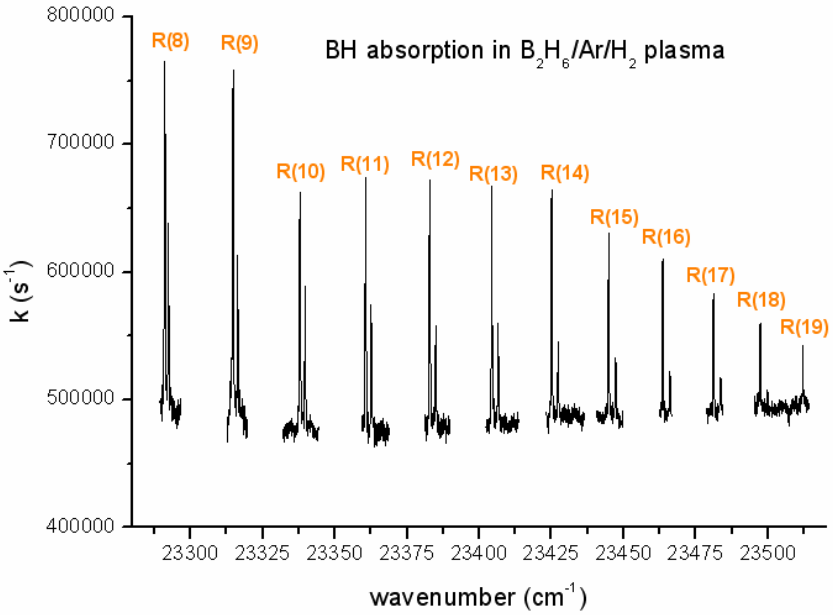

Figure 7. 27 BH rotational spectra measured by CRDS in the $B_2H_6/Ar/H_2$ plasma.

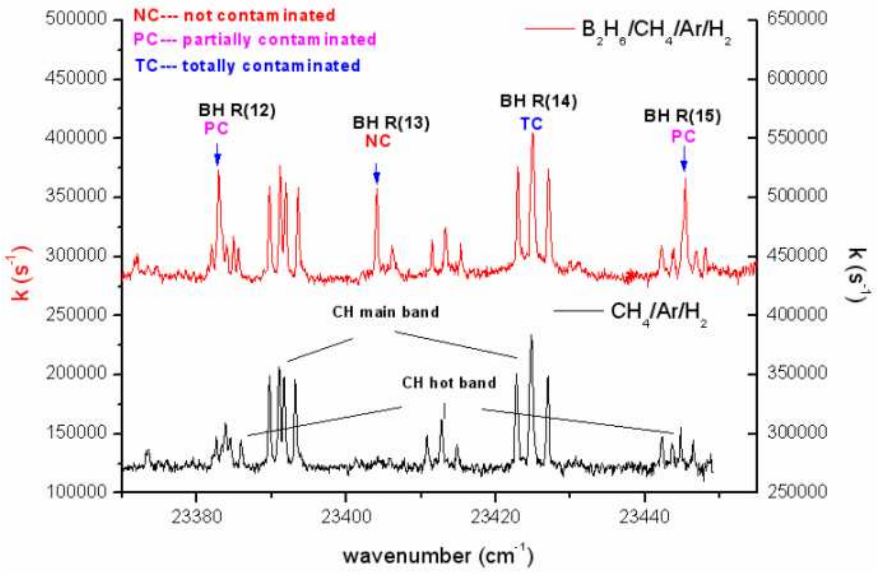

Figure 7. 28 Comparison of CRDS measured spectral in the $CH_4/Ar/H_2$ (black) and $B_2H_6/CH_4/Ar/H_2$ (red) plasmas. The BH lines (not contaminated, partially contaminated by CH (1,1) hot band and totally contaminated) are marked.

Table 7. 1 BH rotational lines and their status

Transition	Wavenumber (cm^{-1})	Status
R(8)	23291.10	**PC**
R(9)	23314.69	**NC**
R(10)	23337.91	**NC**
R(11)	23360.65	**TC**
R(12)	23382.82	**PC**
R(13)	23404.31	**NC**
R(14)	23425.02	**TC**
R(15)	23444.80	**PC**
R(16)	23463.54	**NC**
R(17)	23481.10	**NC**
R(18)	23497.31	**PC**
R(19)	23512.02	**NC**

Note: here, **NC**: not contaminated, **PC**: partially contaminated and **TC**: totally contaminated

7.3.2.2. Calculation of the rotational temperature of BH

The measured structure of the BH rotational lines can provide information about the rotational temperature of BH ground state (T_{rot}^{X}). Under high pressure, due to high collision frequency and the low excitation energy, R-T energy transfer for BH is very efficient. Thus, the rotational temperature of the BH ground state can be a good approximation of the real gas temperature.

Here, we calculate T_{rot}^{X} by following the procedure described in Rayar *et al*'s paper [4]. One thing needing caution is that, in Rayar's paper, the deduced formula are for emissions while here we need to consider absorption.

The intensity of the rovibronic absorption lines is proportional to the population in the lower level, $N_{n",\upsilon",J"}$ and the corresponding transition probability, $B_{n",\upsilon",J"}^{n',\upsilon',J'}$, which is the Einstein *B* coefficient for the transition from the lower energy level $(n",\upsilon",J")$ to the upper level (n',υ',J'), i.e.

$$I_{n",\upsilon",J"}^{n',\upsilon',J'} \propto N_{n",\upsilon",J"} \times B_{n",\upsilon",J"}^{n',\upsilon',J'} . \quad \text{(Eq.7.1)}$$

The Einstein *B* coefficient can be converted into the corresponding *A* coefficient by the relationship

$$B_{n",\upsilon",J"}^{n',\upsilon',J'} = \frac{g_{upper}}{g_{lower}} \cdot \frac{1}{8\pi hc\tilde{\nu}^3} \cdot A_{n",\upsilon",J"}^{n',\upsilon',J'} \quad \text{(Eq.7.2)}$$

Here, g_{upper} and g_{lower} are the degeneracy of upper and lower level, respectively, and $\tilde{\nu}$ is the wave number of the corresponding transition. $A_{n",\upsilon",J"}^{n',\upsilon',J'}$ is the spontaneous emission coefficient, which is determined by **Eq. 7.3**

$$A_{n",\upsilon",J"}^{n',\upsilon',J'} = \frac{64\pi^4}{3h}\tilde{\nu}^3 \frac{S_{n",\upsilon",J"}^{n',\upsilon',J'}}{2J"+1}, \quad \text{(Eq.7.3)}$$

where *J''* is the angular momentum quantum number of the lower rotational level. $S_{n",\upsilon",J"}^{n',\upsilon',J'}$ is the line strength for this transition. As discussed by Osaic *et al*, [3] the perturbations caused by interactions between electronic and nuclear degrees of freedom are very small, thus can be neglected. An adiabatic approximation can be made. A dependence of the line strengths on the rotational quantum numbers can be factorized by integration over the angular variables. Thus, the line strength can be expressed as follows:

$$S_{n",\upsilon",J"}^{n',\upsilon',J'} = \left|R_{n",\upsilon",J"}^{n',\upsilon',J'}\right|^2 H_{J',J"} \quad \text{(Eq.7.4)}$$

Here, $H_{J',J"}$ are the Hönl-London factors, and $R_{n",\upsilon",J"}^{n',\upsilon',J'}$ are the matrix elements of the dipole moment on the electronic and vibrational wave functions of the upper and lower states. Its square can be written in the form

$$\left|R_{n",\upsilon",J"}^{n',\upsilon',J'}\right|^2 = q_{\upsilon',\upsilon"}\left|R_{n"}^{n'}\right|^2 \quad \text{(Eq.7.5)}$$

Here, $q_{v'v''}$ is Franck-Condon coefficient, and $\left|R_{n''}^{n'}\right|^2$ is the electronic transition probability.

For simple cases, the Hönl-London factors only depend on the type of the electronic transition, like Σ —Σ, Π—Σ, Π—Δ, etc. Thus, for the case of BH ($X^1\Sigma^+ \rightarrow A^1\Pi$) transitions, the Hönl-London factors can be written as:

$$H_{J',J''} = \begin{cases} J' & for\ J'' = J'+1 \quad (P\ branch) \\ 2J'+1 & for\ J'' = J' \quad (Q\ branch) \\ J'+1 & for\ J'' = J'-1 \quad (R\ branch) \end{cases} \qquad \text{(Eq.7.6)}$$

In addition, according to the Boltzmann distribution, we have

$$N_{n'',v'',J''} \propto (2J''+1)\exp\left(-\frac{E_{n'',v'',J''}}{T_{rot}^X}\right) \qquad \text{(Eq.7.7)}$$

Here, $E_{n'',v'',J''}$ is the energy of the lower level relative to the lowest states (n''=0, v''=0, J''=0), T_{rot}^X is the rotational temperature of the ground states $X^1\Sigma^+$.

Combining all these equations (i.e. **Eqs.7.1~7.7**), the absorption line intensity can be written as

$$\begin{aligned} I_{n'',v'',J''}^{n',v',J'} &\propto N_{n'',v'',J''} \times \frac{g_{upper}}{g_{lower}} \cdot \frac{1}{8\pi hc\tilde{\nu}^3} \cdot A_{n'',v'',J''}^{n',v',J'} = \frac{1}{8\pi hc\tilde{\nu}^3} N_{n'',v'',J''} \times \frac{2J'+1}{2J''+1} \times A_{n'',v'',J''}^{n',v',J'} \\ &= \frac{1}{8\pi hc\tilde{\nu}^3} \times (2J''+1)\exp\left(-\frac{E_{n'',v'',J''}}{T_{rot}^X}\right) \times \frac{2J'+1}{2J''+1} \times \frac{64\pi^4}{3hc^3}\tilde{\nu}^3 \frac{S_{n'',v'',J''}^{n',v',J'}}{2J'+1} \qquad \text{(Eq.7.8)} \\ &= \frac{8\pi^3}{3h^2c^4}\exp\left(-\frac{E_{n'',v'',J''}}{T_{rot}^X}\right) S_{n'',v'',J''}^{n',v',J'} \end{aligned}$$

So,

$$-\ln\left(\frac{I_{n'',v'',J''}^{n',v',J'}}{S_{n'',v'',J''}^{n',v',J'}}\right) \propto \frac{E_{n'',v'',J''}}{T_{rot}^X} \qquad \text{(Eq.7.9)}$$

From this equation, the rotational temperature T_{rot}^{X} can be finally determined.

In our calculations, the selected absorption lines come from the same (n',v')—(n'',v'') transition, only J' and J'' are different. Since $\left|R_{n",v",J"}^{n',v',J'}\right|^2$ is only dependent on n', v' and n'', v'', according to **Eq. 7.4~7.7**, for the R branch, we have

$$S_{n",v",J"}^{n',v',J'} \propto (J'+1) \quad \text{(Eq.7.10)}$$

Thus,

$$-\ln\left(\frac{I_{n",v",J"}^{n',v',J'}}{J'+1}\right) \propto \frac{E_{n",v",J"}}{T_{rot}^{X}} \quad \text{(Eq.7.11)}$$

Plot of the measured $\ln\left(\frac{I_{n",v",J"}^{n',v',J'}}{J'+1}\right)$ in $Ar/H_2/B_2H_6$ plasma against the values of $E_{n",v",J"}$ found from Pgopher is shown in **Figure 7. 29**. In order to totally get rid of the saturation effect, the weak isotope lines from ^{10}BH instead of ^{11}BH are used, assuming it has the same $E_{n",v",J"}$ as ^{11}BH. A temperature of about 2500 K is obtained in the B_2H_6 /Ar/H_2 plasma.

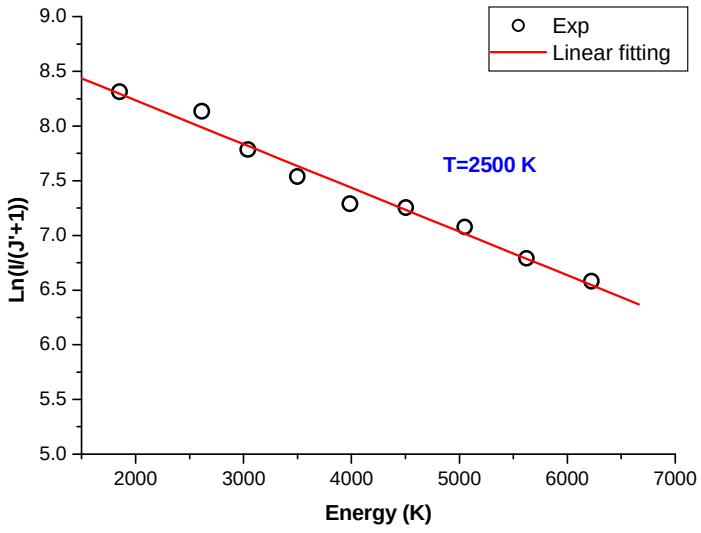

Figure 7. 29 Boltzmann plot of R branch of ^{10}BH ($X^1\Sigma^+ \rightarrow A^1\Pi$) (0,0) transitions in B_2H_6 (0.025 sccm)/Ar/H_2 plasma under the "standard" discharge condition.

When CH_4 is added into the $B_2H_6/Ar/H_2$ plasma, the BH absorption drops a lot. Thus, the saturation effect is not as serious as in $B_2H_6/Ar/H_2$ plasma. However, due to the overlapping between CH ($X^2\Pi$—$A^2\Delta$) and the BH (X—A) R branch, only the few uncontaminated BH lines in **Table 7. 1** are usable. The rotational temperature of BH determined using these absorption lines in the $B_2H_6/Ar/H_2/CH_4$ plasma is shown in **Figure 7. 30**. The temperature obtained is around 2800-3200 K, a little higher than that measured in the $B_2H_6/Ar/H_2$ plasma (~2500K). This value is very close to the rotational temperature (~3000 K) of C_2 obtained before in $Ar/H_2/CH_4$ plasma. The difference of the BH rotational temperature in the $B_2H_6/Ar/H_2$ plasma and $B_2H_6/Ar/H_2/CH_4$ plasma could be true due to the reasons as follows: Firstly, in $B_2H_6/Ar/H_2$ plasma, some BH may distribute in the cooler region (i.e. not concentrated in the plasma ball). The measured strong absorptions, which resulted in the serious saturations for some BH lines, could be a result of the much larger line strength of BH at low temperature. This is consistent with the observations of the purple halo in $B_2H_6/Ar/H_2$ plasma; Secondly, CH_4 addition seems not only to "destroy" the BH but also to "drive" them into the plasma ball. This is also consistent with the observations that, when CH_4 is added, the purple halo disappears and the region remaining around the plasma ball becomes very clear, not foggy at all.

To understand this, one needs to re-examine the chemistry of boron containing species. Here, we follow the reaction mechanism suggested in Comerford *et al*'s paper. [9] In $B_2H_6/Ar/H_2$ plasma, the reaction equilibrium **R7. 2** is established. When the CH_4 is added, as mentioned before, the reactions between hydrocarbon species and H atoms will consume lots of H atoms. In the cooler region, H atoms will be depleted quickly, shifting the reaction equilibrium in **R7. 2** towards the left. In the hot region (i.e. in and around the plasma ball), due to still relatively high H atom concentration and also the high gas temperature, the reaction equilibrium of **R7. 2** can be sustained. Though the BH concentration may also drop, the measured BH absorption now is mainly from the BH in the hot region. Thus, the measured BH rotational temperature is now much higher than that in $B_2H_6/Ar/H_2$ plasma but quite close the previously measured C_2 rotational temperature in $CH_4/Ar/H_2$ plasmas. Such

an explanation can be further tested by measuring the Doppler broadening of H_α absorption in Ar/H_2 and $B_2H_6/Ar/H_2$ plasma. If the H_α linewidths in these two plasmas are similar, it will give strong support to our discussion above. If the explanation is true, it can be seen that the H atoms play a very essential role in "tuning" the boron reaction equilibrium.

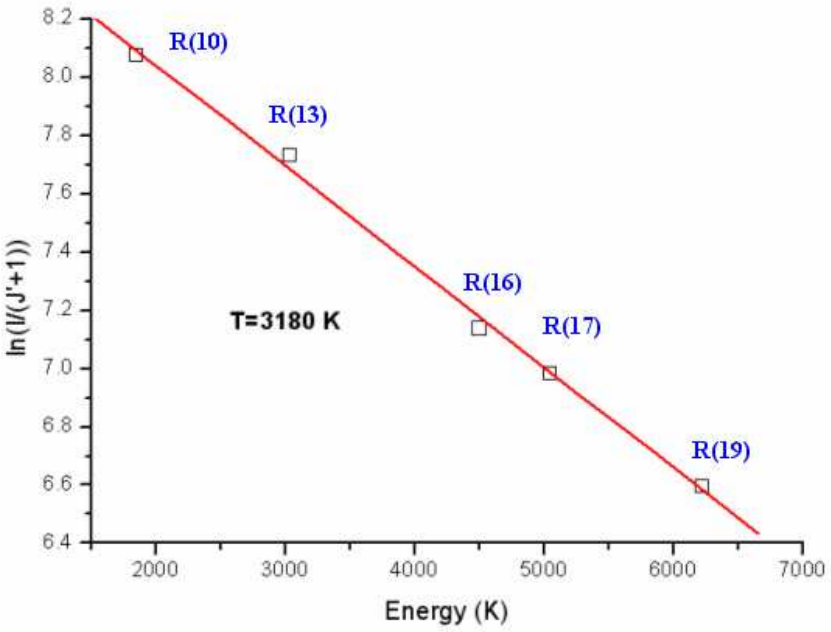

Figure 7. 30 Boltzmann plot of R branch of ^{11}BH ($X^1\Sigma^+ \rightarrow A^1\Pi$) (0,0) transitions in B_2H_6(0.025 sccm)/$Ar/H_2/CH_4$ plasma under the "standard" discharge condition.

7.3.2.3. Calculate BH column density

Similar to **Eq. 5.3** used in the calculation of the C_2 column density in Chapter 5, the column density of BH can be worked out by the following equation

$$D_{BH(X,\upsilon=0)} = [BH(X,\upsilon=0)] \cdot l_{eff} = \frac{8\pi L}{\lambda^2 A_{00} p} \frac{g_{lower}}{g_{upper}} \int \Delta k d\bar{\nu} = \frac{4\pi L}{\lambda^2 A_{00} p} A_{spec} \quad \text{(Eq.7. 12)}$$

Here, L is around 84 cm, A_{00} is ~7.86×10^6 s^{-1}. The Pgopher coefficient p is calculated to be 0.017633 for the selected BH R(10) transition after assuming T_g ~ 3000 K.

The measured BH R(10) lines used for BH column density determination are shown in **Figure 7. 31**. The reason for choosing these lines is due to their relatively better signal-noise ratio. Although suffering a saturation effect in B_2H_6(0.025 sccm)/Ar/H_2 plasma, as shown in **Figure 7. 27** and **Figure 7. 29**, the measured ^{10}BH and ^{11}BH R(10) lines in B_2H_6 (0.025 sccm)/$Ar/H_2/CH_4$ plasma under the standard discharge

condition show that saturation effects are negligible, see **Figure 7. 31**. However, in the following experiments under different discharge conditions, the measured ratio of ^{11}BH R(10) and ^{10}BH R(10) in $B_2H_6/Ar/H_2/CH_4$ plasmas is always between 3~4, which warns that some saturation effects may still be present. Thus, a further repeat of these measurements by choosing a weaker but uncontaminated BH rotational line (e.g. R(13) or R(16)) is needed. In the following sections, as some preliminary results, the column densities of ^{11}BH and ^{10}BH, calculated from the measured ^{11}BH R(10) and ^{10}BH R(10) absorption lines are given, as functions of different discharge parameters like power, pressure, CH_4 flow rate, etc. For convenience, to allow estimation of the possible influence of the saturation effects, the calculated column densities of ^{11}BH and ^{10}BH are always plotted in the same graph.

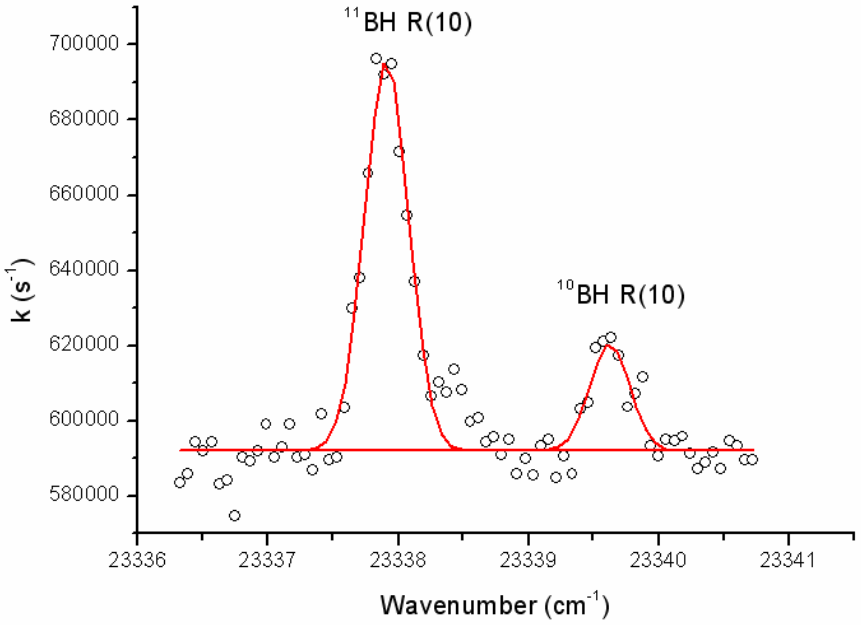

Figure 7. 31 The measured BH R(10) absorption lines in B_2H_6 (0.025 sccm)/$Ar/H_2/CH_4$ plasma under the "standard" discharge condition. The ratio of the areas covered by these two lines, i.e. ^{11}BH R(10) and ^{10}BH R(10), is ~ 4:1.

7.3.2.4. B_2H_6 flow rate effect

The measured ^{11}BH and ^{10}BH column densities (assume T_{rot} ~ 3000 K) are shown in **Figure 7. 32**. Their ratios are close to 4:1 except when the B_2H_6 flow rate is 0.05 sccm. Both of them show a nearly linear increase with B_2H_6 flow rate, which is consistent with OES results in **Figure 7. 9**. At the same time, CH column densities seem not to change much as the B_2H_6 flow rate increases (see **Figure 7. 33**), which

suggests that B_2H_6 addition has only a small effect on a pre-existent $Ar/H_2/CH_4$ plasma under the "standard" discharge condition.

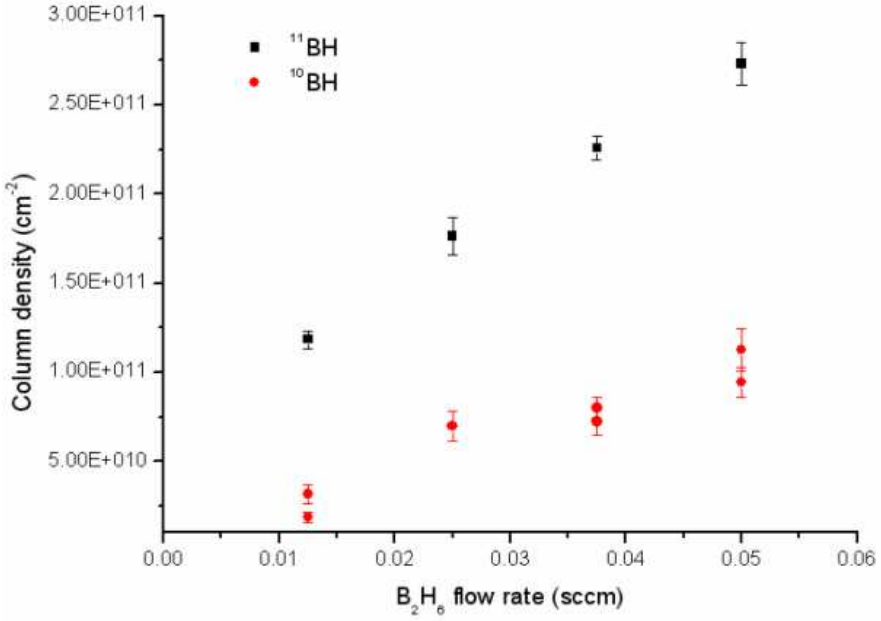

Figure 7. 32 column densities of ^{11}BH and ^{10}BH as functions of B_2H_6 flow rate

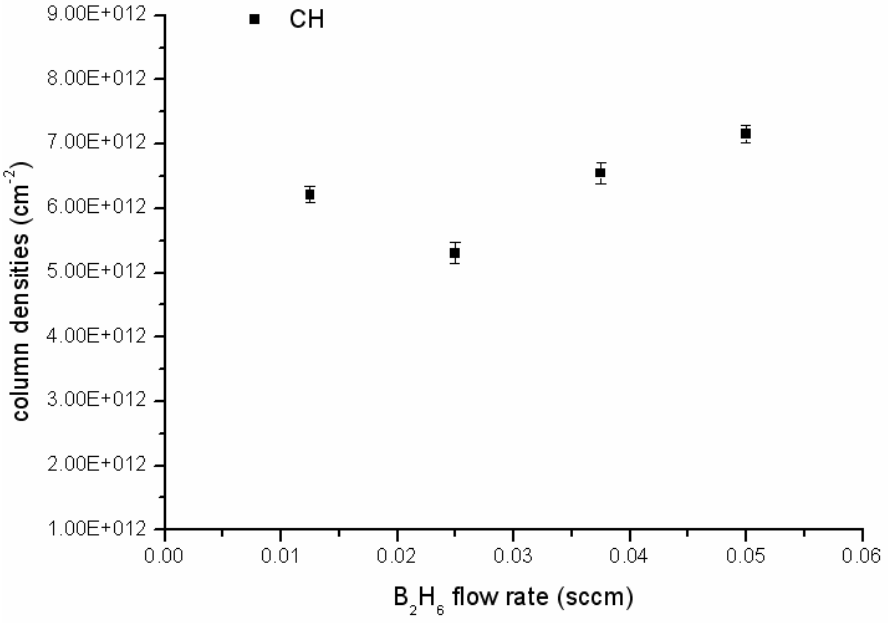

Figure 7. 33 CH column densities as a function of B_2H_6 flow rate

7.3.2.5. CH_4 flow rate effect

When a small amount of CH_4 is added into $B_2H_6/Ar/H_2$ plasma, the measured ^{11}BH and ^{10}BH column densities both first show a very sharp drop and then decrease slowly as the CH_4 flow rate increases. It is worth noticing that in the calculation of the BH column densities in $B_2H_6/Ar/H_2$ plasma (i.e. 0 sccm CH_4 condition), a different rotational temperature T_{rot} ~ 2500 K is assumed (while under other conditions T_g is still be assumed to be 3000 K). Even so, the calculated ^{11}BH column density in $B_2H_6/Ar/H_2$ plasma still underestimates the "real" value due to the saturation effect. However, absorption from the ^{10}BH has no such saturation problem and thus provides a confirmation of the trends given by the measured ^{11}BH data. The first sharp drop could be partly due to the quick decrease of BH in the cooler region when CH_4 consumes a lot of H atoms and cause the reaction **R7.2** equilibrium in that region to move to the left. The further slow decrease as more CH_4 is added, is perhaps related to some thermal reactions occurring in the plasma. The decline in BH may be due to its reaction with hydrocarbon species or to further shift in equilibrium of **R7.2** on account of the reduction of H atom density. The measured BH behaviour as a function of the CH_4 flow rate is also consistent with the OES observation. The CH behaviour is similar to the previous observation in $Ar/H_2/CH_4$ plasma and thus will not be discussed again here.

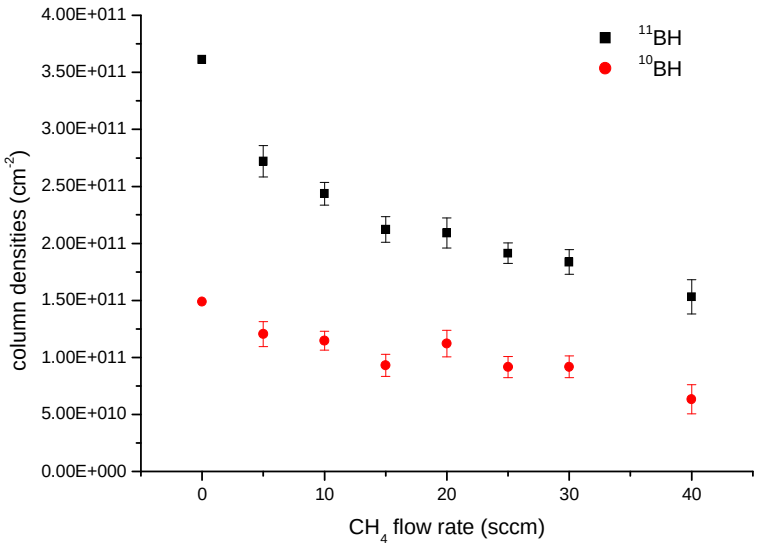

Figure 7. 34 Column densities of ^{11}BH and ^{10}BH as a function of CH_4 flow rate. For the conditions of 0 sccm CH_4, in order to convert the measured BH absorption to column densities, the T_{rot} is assume to be 2500 K. For other CH_4 flow rate conditions, T_{rot} is assumed to be 3000 K.

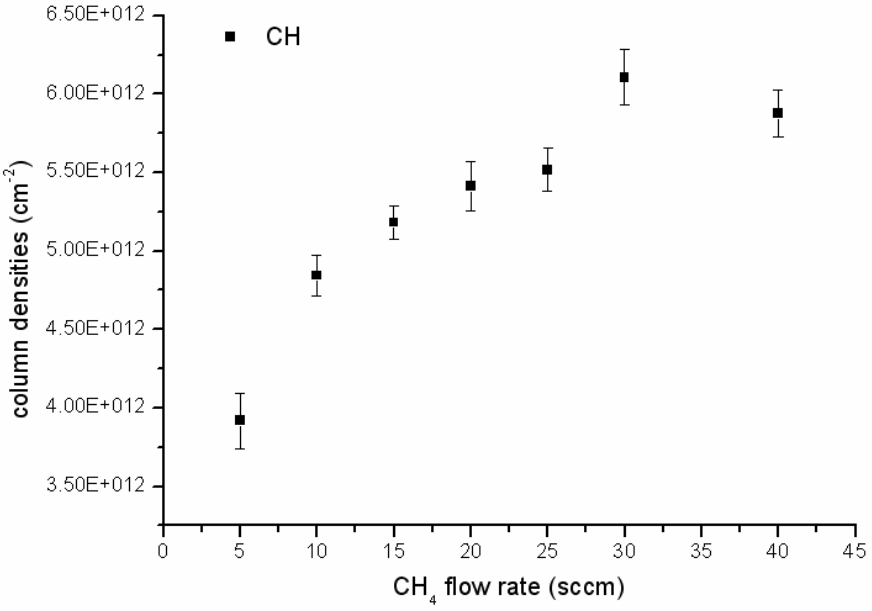

Figure 7. 35 CH column densities as a function of CH_4 flow rate

7.3.2.6. Power effect

When the input power increases, the measured column densities of ^{11}BH and ^{10}BH show a moderate decrease. The change of ^{10}BH is even less obvious (see **Figure 7. 36**). The drop of BH may come from the following fact: when more power is introduced, more H atoms are produced, which may push the equilibrium between the BH_x species (reaction **R7.2**) from BH to B. So the B atom densities shall be seen to increase as the power increases but BH densities drop. Such an explanation may also account for the sharp increase of the boron emissions in **Figure 7. 17**. The CH column densities increase as power increases, see **Figure 7. 37**. Again, this observation is consistent with the results obtained prevailing in $Ar/H_2/CH_4$ plasma before.

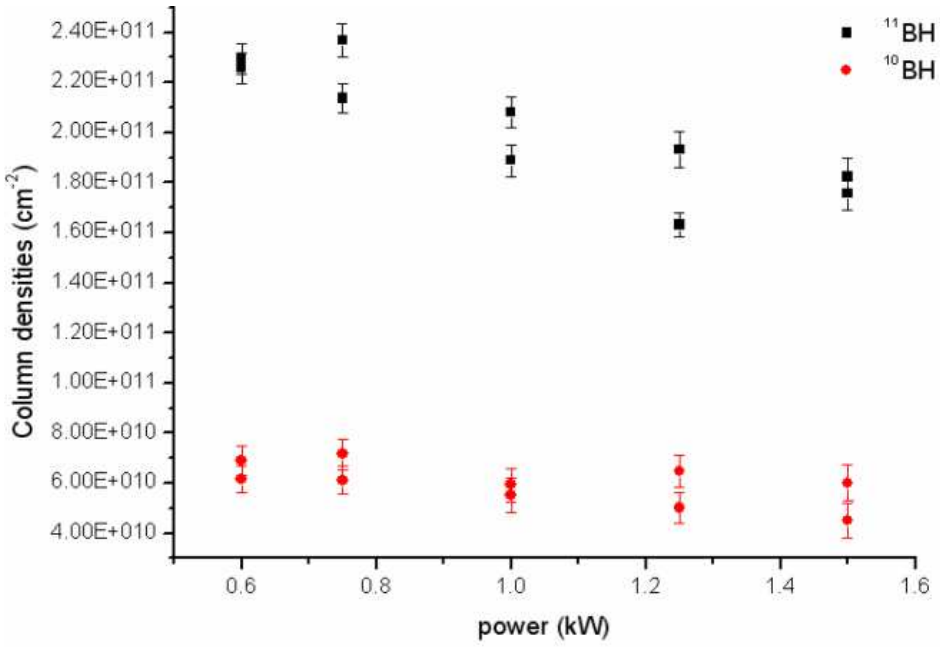

Figure 7. 36 Column densities of ^{11}BH and ^{10}BH as functions of input power

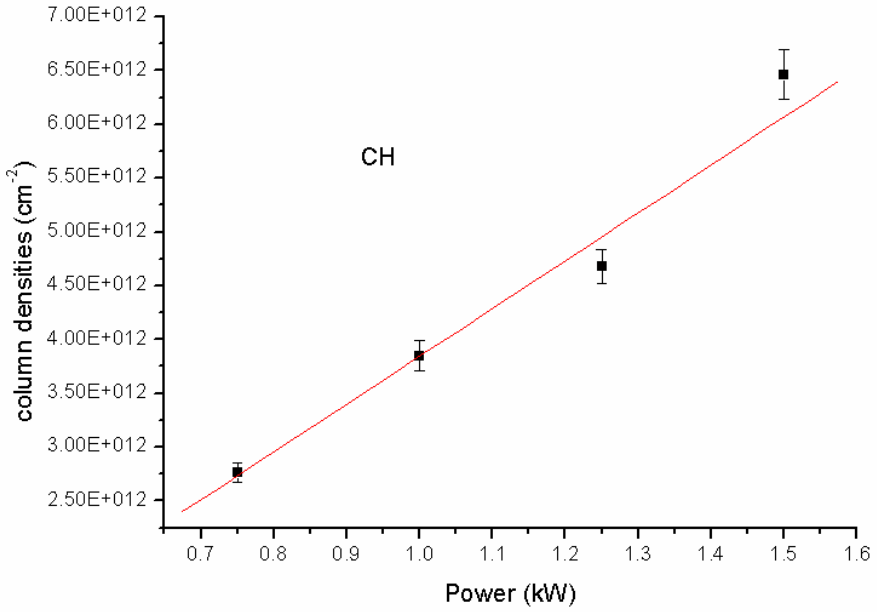

Figure 7. 37 CH column densities as a function of input power

7.3.2.7. Pressure effect

The measured column density of ^{11}BH shows a turning point at 125 Torr, see **Figure 7. 38**. However, the ^{10}BH column densities show no obvious change when the pressure varies from 75 Torr to 175 Torr. According to the previous analysis, the

BH ground states, unlike its excited states, should be dominated by thermal chemistry. Therefore, this turning point somehow looks quite suspicious, and is possibly due to the saturation effect. A further measurement performed under the same conditions but with a clearly unsaturated spectral line is required. Again, the CH column densities in **Figure 7. 39** show a similar trend as in $Ar/H_2/CH_4$ plasmas.

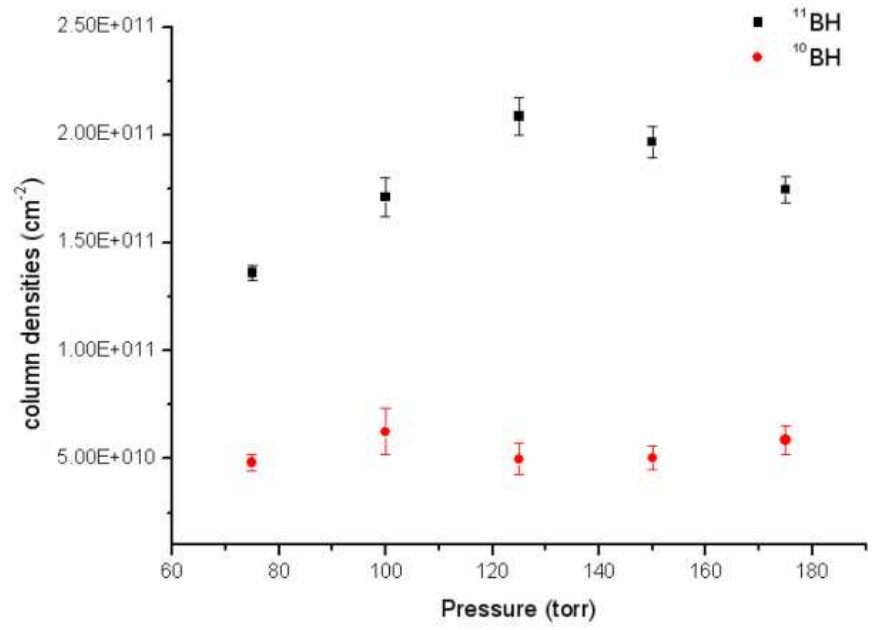

Figure 7. 38 Column densities of ^{11}BH and ^{10}BH as functions of pressure

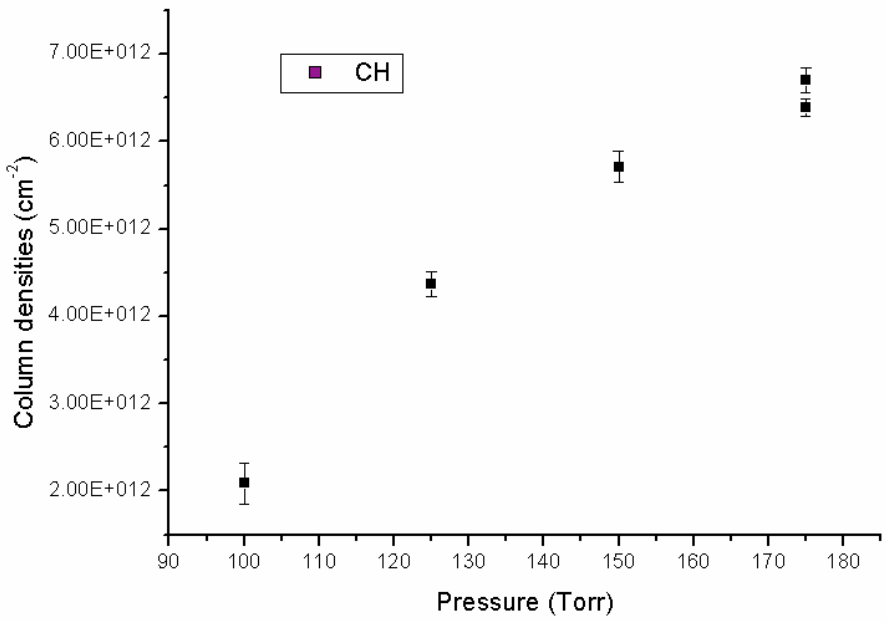

Figure 7. 39 CH column densities as a function of pressure

7.3.2.8. Ar flow rate effect

The effect from Argon flow rate has also been examined, but it is found to have minimal effect on the measured BH and CH column densities (see **Figure 7. 40** and **Figure 7. 41**).

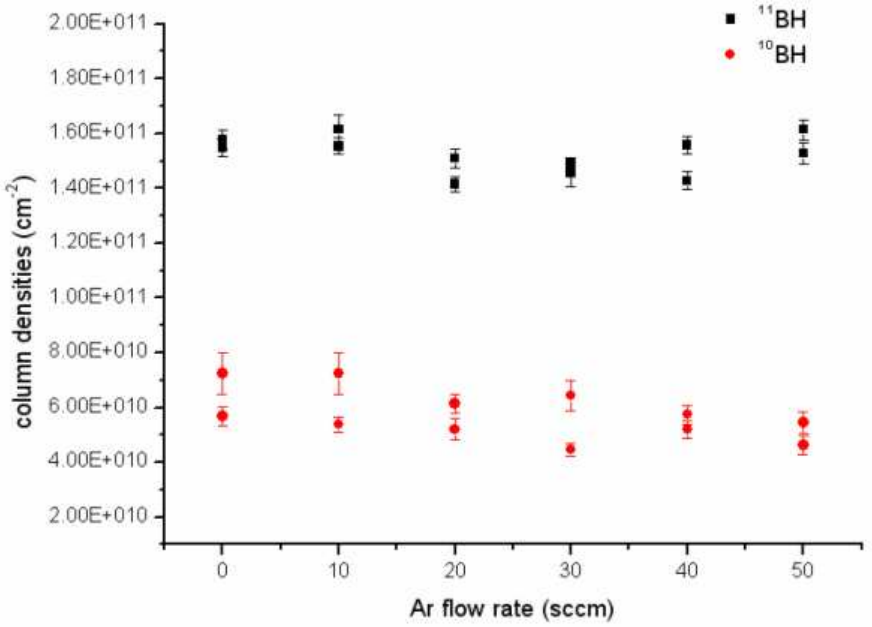

Figure 7. 40 Column densities of ^{11}BH and ^{10}BH as functions of Ar flow rate

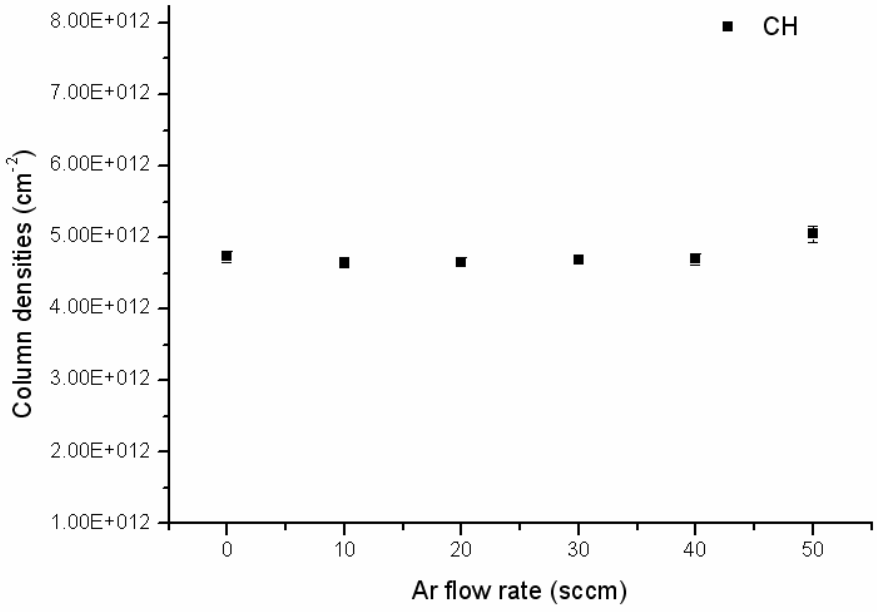

Figure 7. 41 CH column densities as a function of Ar flow rate

7.3.2.9. Profile

The measured column density profiles of ^{11}BH, ^{10}BH and CH radicals under the standard discharge conditions with B_2H_6 flow rate 0.025 sccm, are shown together in **Figure 7. 42**. It can be seen that BH has a much flatter and wider distribution than CH, which, again, confirms that, the BH radical is relatively stable in cooler regions in contrast to species like C_2, CH and H(n=2). Moreover, in **Figure 7. 43,** the CRDS measured profile of BH column densities exhibit a much wider distribution than the BH emission profile measured by OES. As discussed in Chapter 6, such a difference comes from the fact that the distribution from OES measurements is a convolution of the spatial distribution s of BH(X) and n_e.

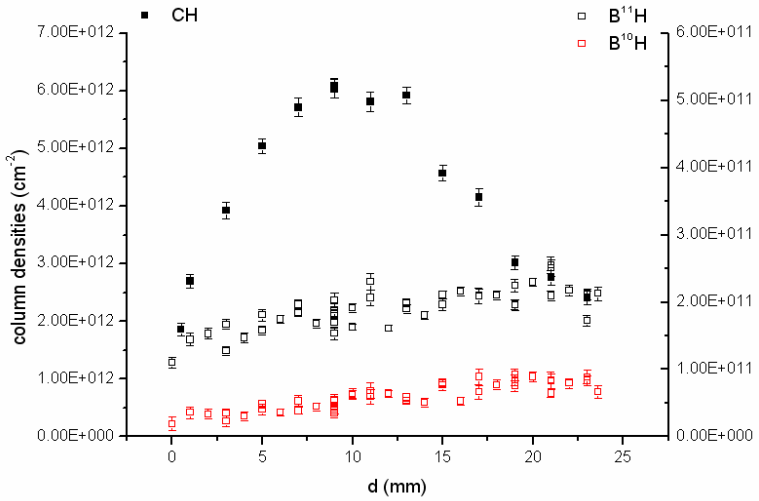

Figure 7. 42 The CRDS measured column density profiles of CH, ^{11}BH and ^{10}BH

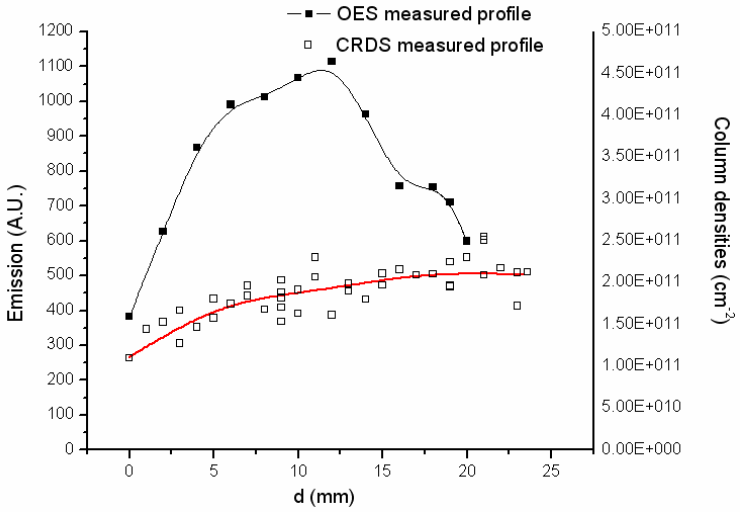

Figure 7. 43 Comparison between the OES measured BH emission profile and CRDS measured ^{11}BH column density profile

7.4. Summary

Both emission and absorption-based spectroscopic methods, with spatially-resolved abilities, have been applied to investigate the gas phase chemistry prevailing in the $B_2H_6/Ar/H_2/CH_4$ plasma used for CVD of B-doped diamond. Though the R and P branches of BH are totally mixed with CH in the OES spectra, the Q branch still can be recognized and thus can be used to monitor this species in OES. The absorption spectroscopy used here, i.e CRDS, has much higher resolution than the OES. Thus, the detailed rotational structure of BH and CH can be distinguished. Though seriously "contaminated" by the CH ($X^2\Pi$—$A^2\Delta$) (0,0) and (1,1) bands, some "uncontaminated" BH rotational lines still can be "picked out" after careful inspection of the spectra.

It is found that even very small amounts of B_2H_6 can have a significant effect on Ar/H_2 plasmas, leading to an obvious drop of H Balmer, H_2 and Ar emissions. However, when 25 sccm CH_4 is added, the B_2H_6 seems to lose its impact on the plasma. Now the plasma characteristics are dominated by the CH_4. Varying B_2H_6 flow rate can change the densities of some boron-containing species like B and BH, but it has little effect on the other species like C_2, CH and excited H atoms. The behavior of these species is still similar to that in $Ar/H_2/CH_4$ plasmas.

The hydrogen atoms seem to play an essential role in "tuning" the reaction equilibrium of boron-containing species. Due to its different thermal and chemical properties from CH and C_2, the BH species can distribute into the cooler region, which results in very strong absorptions and even lead to some of the BH lines (measured by CRDS) being saturated in $B_2H_6/Ar/H_2$ plasma. In $B_2H_6/Ar/H_2/CH_4$ plasma, the depletion of H atoms due to reaction with hydrocarbon species in the cooler region cause the BH radicals now to be mainly concentrated in the hot region. Such an adjustment of BH spatial distribution results in a sharp "jump" of the measured BH rotational temperature from $B_2H_6/Ar/H_2$ plasma to $B_2H_6/Ar/H_2/CH_4$ plasma.

Although the signal-noise ratio is the best, using CRDS to measure the strong ^{11}BH R(10) transition suffers saturation effects under some conditions. This saturation will

lead to an overestimation of the measured rotational temperature of BH in $B_2H_6/Ar/H_2$ plasma and also make the explanation of the measured BH behaviour as functions of discharge parameters in $B_2H_6/Ar/H_2/CH_4$ plasma a bit less secure. Therefore, further careful measurements of BH absorption merits attention.

7.5. References

[1] E. Gheeraert, A. Deneuville and J. Mambou, *Carbon*, **37** (1999) 107.

[2] B.-J. Lee, B.-T. Ahn and Y.-J. Baik, *Diamond Relat. Mater.*, **8** (1999) 251.

[3] M. Osiac, B. P. Lavrov and J. Ropcke, *J. Quant. Spec. Radiat. Transfer*, **74** (2002) 471.

[4] M. Rayar, P. Veis, C. Foissac, *et al.*, *J. Phys. D: Appl. Phys*, **39** (2006) 2151.

[5] Y. Takano, M. Nagao, I. Sakaguchi, *et al.*, *Appl. Phys. Lett.*, **85** (2004) 2851.

[6] V. A. Sidorov, E. A. Ekimov, S. M. Stishov, *et al.*, *Phys. Rev. B*, **71** (2005) 060502.

[7] C. E. Nebel, D. Shin, B. Rezek, *et al.*, *J. Royal Soc. Interface*, **4** (2007) 439.

[8] C. E. Nebel, B. Rezek, D. Shin, *et al.*, *J. Phys. D: Appl. Phys*, **40** (2007) 6443.

[9] D. W. Comerford, A. Cheesman, T. P. F. Carpenter, *et al.*, *J. Phys. Chem. A*, **110** (2006) 2868.

Chapter 8 Overview and Perspective

8.1. Overview

In this thesis, the chemistry occurring in both $CH_4/Ar/H_2$ and $B_2H_6/CH_4/Ar/H_2$ plasmas has been investigated using various diagnostics such as QCL diode laser absorption spectroscopy, CRDS, and OES including actinometry. In order to give a reasonably clear picture, a short summary will be made here.

When an Ar/H_2 plasma is firstly ignited, the electrons pick up energy from the microwave electromagnetic field. Then, through collision with the heavy particles, the electrons transfer their energy to the heavy particles, causing them to become excited, dissociated or ionized. Especially, through electron impact excitation, many H_2 are vibrationally excited. Such processes are very efficient. When these energetic H_2 collide with heavy species, the vibrational energy can be released and converted to the thermal energy through so-called "V-T" relaxation, thus elevating the gas temperature. Under our "standard condition", the gas temperature is around 3000 K. Such high gas temperature also drives the thermal dissociation of H_2. Therefore, under our high power density conditions, the thermal dissociation becomes the major channel for H production (instead of electron impact dissociation of H_2). Lots of H atoms are thus produced. They are not only abundant in the plasma ball but also have a relatively high concentration in the cooler regions of the reactor.

When a small amount of hydrocarbon is added, firstly, in the cool region, due to the relatively high [H] but low gas temperature, the hydrocarbon species tend to become CH_4, the most stable C1 species, by a series of H-addition reactions (or in the case of C2 species, following a C2→C1 dissociation). When such processed CH_4 diffuses into the hot plasma region, the high [H] and high gas temperatures favour the hydrocarbon species C_2H_2. The CH_4 is thus converted into C_2H_2 there by a series of

H-abstraction reactions together with a self-reaction between C1 species. The acetylene product then diffuses to the cooler regions, where the high [H] and relatively low gas temperature encourage conversion of C_2H_2 into CH_4. As more and more hydrocarbon gas is added, the H atoms in the cooler regions will be depleted and now the acetylene product can survive. However, since the favoured hydrocarbon species in the region of the plasma ball is always C_2H_2, the plasma chemistry is not sensitive to the original choice of the hydrocarbon feedstock. Actually, when using the same carbon flow rate under the same discharge conditions, the CRDS measured C_2, CH and H(n=2) profiles show that the plasmas produced from the $CH_4/Ar/H_2$ and $C_2H_2/Ar/H_2$ gas feeds are essentially the same.

Even small additions of CH_4 into Ar/H_2 plasma can result in an essential change in the charge particle chemistry because of the very low ionization degree in moderate pressure Ar/H_2 plasma. When CH_4 is added, it will firstly be converted into C_2H_2 before entering the plasma. Since C_2H_2 has a much lower ionization threshold energy than H_2, the dominant ions immediately change from H_3^+ to hydrocarbon ions such as $C_2H_2^+$ and $C_2H_3^+$. This process is somewhat like a phase transition. The electron impact ionization of hydrocarbon species will increase n_e, but will also generate lots of cold electrons and tends to lower T_e. The compromising effect of increasing n_e but lowering T_e normally leads to a reduction of those excited states in the plasma whose generation is dominated by electron impact excitation. So the emission intensities from such species tend to drop. However, notice that the new ions have a much bigger mass than H_3^+ and thus the "switch" in major ions upon CH_4 addition also causes a big change in the ambipolar field, which dominates both electron and ion losses in the plasma. Now the electrons and ions are confined by the ambipolar field more "tightly" and the plasma volume (determined by the electron density distribution) shrinks. Then the power density becomes higher and further enhances the electron density. This finally leads to generation of more excited states and enhanced emissions. Introducing more CH_4 into the plasma will not change the "major ions", and thus will not influence the ambipolar field or plasma volume much.

However, due to the low ionization threshold, more CH_4 addition will continue to increase the electron density and cool the electrons. Because of the near exponential dependence of excited state densities upon electron temperature, all the emissions will decrease.

The C_2 and CH radicals are produced by H abstraction reactions, and their emissions are more sensitive to the thermal chemistry.

The excited H atoms are mainly generated from direct electron impact excitation of H ground states and their emissions are determined by the competition of n_e, T_e and H (n=1). As the H(n=1) density is determined mainly by thermal dissociation, the emissions of excited H atoms are not only sensitive to the electron properties but also sensitive to the thermal chemistry.

The Ar* and H_2* species are mainly formed through electron impact excitation, thus their behaviour closely follows the electron properties.

Addition of a small amount of B_2H_6 into an Ar/H_2 plasma also has a significant influence on the plasma properties. However, in contrast to the case of CH_4 addition, its effect tends to reduce the densities of excited state species in the plasma. A big "purple halo" is visible on the top of the plasma ball, which indicates BH is not as "hot" as species like CH or C_2 and that its distribution extends further into the cool region. The BH in $B_2H_6/Ar/H_2$ plasma also exhibits a bit lower rotational temperature (around 2500 K). However, when CH_4 is added as well, the plasma properties is dominated by the methane. All the species (except boron-containing species like BH and B) show behaviour very similar to that observed in $CH_4/Ar/H_2$ plasma. The measured BH densities decrease with increasing CH_4 flow rate. The purple halo disappears. In addition, the measured BH rotational temperature in $B_2H_6/CH_4/Ar/H_2$ plasma is around 3000 K, consistent with the measured C_2 rotational temperature.

8.2. Perspective

Though many experimental results have been reasonably explained, there are still several phenomena that need further examination. For example, the measured H_α Doppler broadening corresponds to a temperature of 4700K, much higher than the measured C_2 rotational temperature. We have checked that such over-broadening is not an effect due to Ar, wavelength calibration or power broadening. It is suggested that Stark effect, due to average microwave field, may make some contribution. If that is true, such over-broadening should be more serious for H_β and H_γ transitions. A high resolution monochrometer can be used to measure their Doppler linewidths and thus provide further insight into this over-broadening.

For the boron chemistry study, the very low rotational temperature measured for BH in $B_2H_6/Ar/H_2$ plasma may be due to the contributions from BH radicals distributed in the cool region, while the gas temperature in the plasma still remains high. To verify this, we need to compare H_α or H_β Doppler broadening in Ar/H_2 and $B_2H_6/Ar/H_2$ plasma. In addition, measuring boron atoms as functions of different discharge parameters by CRDS will provide more valuable information about the boron chemistry.

Work of this thesis has established many of the strengths and potential limitations of OES, CRDS and QCL diagnostics as applied to diamond growing plasmas. These techniques could each be used to explore a wide range of growth environments. For example, there is still considerable uncertainty as to whether nanocrystalline (and ultra-nanocrystalline) diamond growing from plasmas containing much high C/H ratios involves similar, or different, chemistry. The gas phase diagnostic methods addressed in this thesis are ideally suited to address such questions. Similarly, in the context of microcrystalline diamond CVD, there is renewed interest in growth from CH_4/CO_2 mixtures. Again, all of the aforementioned techniques should be able to provide detailed, quantitative diagnoses of the gas phase chemistry and composition

involved in such growth and provide rigorous test of future models of the relevant gas phase chemistry. For example, to probe CH_3 and CH_2 will be important for testing on-going gas-surface chemistry modelling.

Appendix A Reactions in Bristol –Moscow Model

Table A. 1 Reactions in the model and their reacton rates at three positions along the central axis

Reactions	d=1.2cm	d=3.6cm	d=4.6 cm
H(3)->H(2)	7.97E+13	9.34E-14	2.96E-34
H(2)->H	5.84E+15	2.45E-07	2.99E-26
H(3)->H	1.81E+12	2.12E-15	6.73E-36
H2*->H2	3.75E+15	4.12E-11	6.79E-30
Ar**->Ar	3.39E+13	4.37E-13	9.60E-32
H+H+H2->H2+H2	1.35E+18	1.53E+17	3.68E+14
H2+H2->H+H+H2	2.31E+19	1.71E+15	1.75E+08
H+CH->C+H2	1.27E+19	2.36E+17	3.09E+11
C+H2->H+CH	1.27E+19	2.06E+17	4.87E+11
H+CH2(S)->CH+H2	1.15E+18	5.48E+16	1.09E+12
CH+H2->H+CH2(S)	1.16E+18	5.19E+16	5.19E+11
H+CH3->CH4	1.22E+17	2.03E+18	2.02E+17
CH4->H+CH3	2.02E+18	2.35E+16	9.22E+10
H+CH4->CH3+H2	6.17E+19	7.82E+19	2.91E+18
CH3+H2->H+CH4	6.36E+19	7.59E+19	3.03E+18
H+C2H2->C2H3	9.76E+16	1.04E+18	3.23E+17
C2H3->H+C2H2	9.81E+17	7.85E+17	3.97E+16
H+C2H3->H2+C2H2	1.55E+18	4.70E+17	2.74E+16
H2+C2H2->H+C2H3	2.64E+18	6.95E+15	1.06E+11
H+C2H4->C2H5	2.59E+13	3.29E+15	1.71E+17
C2H5->H+C2H4	3.96E+14	1.31E+16	3.66E+16
H+C2H4->C2H3+H2	3.86E+18	1.63E+18	2.40E+17
C2H3+H2->H+C2H4	4.09E+18	1.42E+18	4.94E+17
H+C2H5->H2+C2H4	5.09E+13	5.50E+14	1.37E+15
H2+C2H4->H+C2H5	5.67E+13	1.55E+12	3.04E+09
H+C2H6->C2H5+H2	2.21E+14	2.31E+16	6.63E+16
C2H5+H2->H+C2H6	4.14E+14	3.40E+15	2.25E+16
C+CH2->H+C2H	6.16E+14	3.70E+13	3.33E+06
H+C2H->C+CH2	1.05E+15	2.12E+09	6.10E-02
C+CH3->H+C2H2	3.88E+15	2.90E+15	6.99E+10
H+C2H2->C+CH3	6.65E+15	1.56E+11	4.90E+02
CH+H2->H+CH2	5.44E+19	5.74E+18	2.14E+14
H+CH2->CH+H2	5.45E+19	5.80E+18	2.09E+14
CH+CH2->H+C2H2	3.85E+14	1.55E+13	6.85E+05
H+C2H2->CH+CH2	6.53E+14	7.74E+08	1.93E-02
CH+CH3->H+C2H3	1.82E+15	9.13E+14	1.08E+10
H+C2H3->CH+CH3	1.83E+15	2.90E+12	3.10E+07

(To be continued)

(Continued)

CH+CH4->H+C2H4	2.43E+15	7.99E+15	4.50E+12
H+C2H4->CH+CH4	2.39E+15	2.81E+13	6.53E+09
CH2+H2->H+CH3	4.70E+18	6.97E+17	1.48E+14
H+CH3->CH2+H2	4.65E+18	7.41E+17	3.76E+14
CH2+CH2->H2+C2H2	8.57E+15	5.67E+14	1.00E+08
H2+C2H2->CH2+CH2	1.46E+16	2.80E+10	2.90E+00
CH2+CH2->H+H+C2H2	1.26E+15	9.19E+13	1.90E+07
CH2+CH3->H+C2H4	1.00E+16	2.87E+16	9.87E+12
H+C2H4->CH2+CH3	9.54E+15	1.03E+14	1.41E+10
CH2(S)+H2->CH3+H	2.96E+19	1.11E+19	1.06E+16
CH3+H->CH2(S)+H2	2.95E+19	1.13E+19	1.25E+16
CH2(S)+CH3->H+C2H4	3.97E+14	5.44E+14	1.08E+11
H+C2H4->CH2(S)+CH3	3.81E+14	1.87E+12	7.13E+07
CH2(S)+CH4->CH3+CH3	3.55E+14	3.18E+15	3.00E+13
CH3+CH3->CH2(S)+CH4	3.65E+14	3.13E+15	3.69E+13
CH3+CH3->C2H6	2.75E+13	2.14E+16	2.29E+16
C2H6->CH3+CH3	2.17E+14	1.97E+15	8.07E+12
CH3+CH3->H+C2H5	4.05E+15	4.55E+16	6.89E+14
H+C2H5->CH3+CH3	3.50E+15	5.48E+16	1.73E+17
C2H+H2->H+C2H2	1.07E+21	1.76E+19	2.50E+15
H+C2H2->C2H+H2	1.07E+21	1.76E+19	2.44E+15
H+H->H2	6.94E+16	3.63E+15	1.19E+13
H2->H+H	1.19E+18	4.07E+13	5.63E+06
H+CH2->CH3	8.44E+15	4.75E+15	8.23E+11
CH3->H+CH2	1.43E+17	5.66E+13	9.96E+05
H+C2H3->C2H4	1.92E+15	4.20E+15	1.32E+15
C2H4->H+C2H3	3.10E+16	5.39E+13	3.05E+08
H+C2H5->C2H6	4.82E+11	1.29E+14	4.67E+15
C2H6->H+C2H5	4.39E+12	9.83E+12	6.53E+09
CH2+CH4->CH3+CH3	9.26E+14	2.78E+15	4.46E+12
CH3+CH3->CH2+CH4	9.45E+14	2.86E+15	1.18E+13
C2H4->H2+C2H2	2.25E+17	8.03E+15	2.94E+12
H2+C2H2->C2H4	2.37E+16	9.26E+15	4.92E+13
H+C2H->C2H2	8.75E+16	3.38E+15	1.97E+11
C2H2->H+C2H	1.49E+18	3.79E+13	9.14E+04
CH2(S)+C2H6->CH3+C2H5	1.11E+09	6.63E+11	3.17E+11
CH3+C2H5->CH2(S)+C2H6	2.07E+09	9.89E+10	1.27E+11
CH3+C2H4->C2H3+CH4	1.25E+13	2.52E+14	7.16E+14
C2H3+CH4->CH3+C2H4	1.28E+13	2.27E+14	1.42E+15
CH3+C2H6->C2H5+CH4	1.58E+09	3.56E+12	6.13E+13
C2H5+CH4->CH3+C2H6	2.87E+09	5.39E+11	2.00E+13
CH2(S)->CH2	1.21E+19	4.12E+18	3.57E+15

(To be continued)

(Continued)

CH2->CH2(S)	1.22E+19	3.94E+18	1.65E+15
CH2+CH4->C2H4+H2	7.04E+15	1.32E+17	2.16E+15
C2H4+H2->CH2+CH4	6.92E+15	4.60E+14	3.21E+12
C2->C2(X)	9.51E+15	4.69E+12	2.14E+07
C2(X)->C2	8.57E+15	4.46E+12	1.39E+07
C+CH->C2+H	5.96E+14	6.27E+12	1.94E+04
C2+H->C+CH	1.14E+15	4.04E+08	1.14E-03
C+CH4->C2H3+H	2.60E+15	1.27E+16	1.46E+13
C2H3+H->C+CH4	2.70E+15	4.48E+13	2.76E+10
C+C2H->C3+H	1.10E+16	2.47E+13	3.73E+05
C3+H->C+C2H	1.11E+16	2.24E+13	5.91E+05
C+C2H2->C3H+H	3.72E+17	1.17E+17	9.74E+12
C3H+H->C+C2H2	3.72E+17	1.12E+17	1.92E+13
C+C2H2->C3+H2	3.22E+17	1.02E+17	8.43E+12
C3+H2->C+C2H2	3.26E+17	9.19E+16	1.37E+13
CH+C2->C3+H	1.48E+14	1.57E+10	2.07E+00
C3+H->CH+C2	1.33E+14	1.11E+10	1.57E+00
CH+C2(X)->C3+H	4.07E+13	5.63E+09	7.12E-01
C3+H->CH+C2(X)	4.07E+13	4.19E+09	8.35E-01
CH+C2H->C3H+H	6.98E+15	1.05E+13	7.79E+04
C3H+H->CH+C2H	6.96E+15	8.74E+12	2.36E+05
CH+C2H2->C3H2+H	5.34E+17	1.07E+17	4.11E+12
C3H2+H->CH+C2H2	5.31E+17	8.87E+16	1.27E+13
C2+CH2->C3H+H	7.35E+14	4.43E+11	1.70E+03
C3H+H->C2+CH2	6.51E+14	3.26E+11	1.60E+03
C2+CH3->C3H2+H	4.62E+15	3.47E+13	3.57E+07
C3H2+H->C2+CH3	4.13E+15	2.41E+13	1.32E+07
C2+C2H->C4+H	2.05E+15	4.63E+10	2.97E+01
C4+H->C2+C2H	1.88E+15	4.78E+10	2.90E+01
C2+C2H2->C4H+H	1.57E+17	4.69E+14	1.57E+09
C4H+H->C2+C2H2	1.42E+17	4.64E+14	1.57E+09
C2+C4H->C2H+C4	2.06E+12	5.28E+07	3.77E-02
C2H+C4->C2+C4H	1.86E+12	4.95E+07	1.15E-02
C2(X)+H2->C2H+H	9.62E+16	2.74E+14	1.43E+09
C2H+H->C2(X)+H2	9.49E+16	2.59E+14	6.69E+08
C2(X)+CH2->C3H+H	2.59E+14	2.04E+11	7.51E+02
C3H+H->C2(X)+CH2	2.55E+14	1.58E+11	1.09E+03
C2(X)+CH3->C3H2+H	1.63E+15	1.60E+13	1.58E+07
C3H2+H->C2(X)+CH3	1.62E+15	1.17E+13	8.99E+06
C2(X)+C2H->C4+H	1.45E+15	4.27E+10	2.63E+01
C4+H->C2(X)+C2H	1.47E+15	4.64E+10	3.96E+01
C2(X)+C2H2->C4H+H	1.11E+17	4.33E+14	1.39E+09

(To be continued)

(Continued)

C4H+H->C2(X)+C2H2	1.11E+17	4.50E+14	2.13E+09
C2(X)+C4H->C2H+C4	1.45E+12	4.87E+07	3.33E-02
C2H+C4->C2(X)+C4H	1.45E+12	4.80E+07	1.57E-02
C2H+C2H->C4H+H	1.24E+17	3.99E+13	1.44E+06
C4H+H->C2H+C2H	1.26E+17	4.40E+13	4.61E+06
C2H+C2H->C2H2+C2	1.24E+16	3.99E+12	1.44E+05
C2H2+C2->C2H+C2H	1.39E+16	4.45E+12	4.61E+05
C2H+C2H2->C4H2+H	3.32E+18	1.42E+17	2.65E+13
C4H2+H->C2H+C2H2	3.33E+18	1.55E+17	8.72E+13
C2H+C4H2->C4H+C2H2	8.69E+14	3.29E+13	5.08E+09
C4H+C2H2->C2H+C4H2	8.81E+14	3.32E+13	4.95E+09
C2H2+C2H2->C4H2+H2	1.14E+17	2.76E+15	4.65E+11
C4H2+H2->C2H2+C2H2	1.14E+17	3.02E+15	1.57E+12
C2+C2->C3+C	3.02E+14	4.77E+08	5.46E-03
C3+C->C2+C2	1.42E+14	5.23E+12	7.05E+04
C2(X)+C2->C3+C	6.38E+13	1.32E+08	1.45E-03
C3+C->C2(X)+C2	3.33E+13	1.52E+12	2.88E+04
C2H->C2+H	2.15E+16	5.12E+10	1.11E+00
C2+H->C2H	1.42E+15	5.09E+12	7.71E+06
C2->C+C	3.80E+11	2.69E+02	8.03E-14
C+C->C2	1.17E+10	3.24E+08	4.53E+00
C2(X)->C+C	8.05E+10	7.44E+01	2.13E-14
C+C->C2(X)	2.74E+09	9.42E+07	1.85E+00
C4+H->C4H	2.73E+13	1.49E+11	1.58E+05
C4H->C4+H	4.60E+14	1.59E+09	7.50E-02
C4H+H->C4+H2	3.56E+16	1.61E+14	1.14E+09
C4+H2->C4H+H	3.62E+16	1.68E+14	1.14E+09
C4H+H2->C4H2+H	1.72E+18	1.87E+16	1.96E+12
C4H2+H->C4H+H2	1.70E+18	1.86E+16	1.96E+12
C4H+C4H->C4+C4H2	1.50E+11	6.23E+07	2.77E+00
C4+C4H2->C4H+C4H	1.50E+11	6.47E+07	2.78E+00
C4H+H->C4H2	8.78E+14	3.86E+13	2.50E+09
C4H2->C4H+H	1.48E+16	4.30E+11	1.19E+03
C3+CH->C4+H	2.77E+13	7.46E+12	2.03E+06
C4+H->C3+CH	4.82E+13	5.49E+08	7.35E-02
C3+CH2->C4H+H	1.15E+14	1.76E+14	1.39E+09
C4H+H->C3+CH2	1.96E+14	1.23E+10	5.15E+01
C3+CH3->C4H2+H	7.22E+14	1.38E+16	2.92E+13
C4H2+H->C3+CH3	1.23E+15	8.98E+11	4.25E+05
C3H+H->C3+H2	1.51E+17	1.44E+17	1.49E+14
C3+H2->C3H+H	1.53E+17	1.37E+17	1.23E+14
C3H+H2->H+C3H2	3.05E+18	1.65E+19	4.86E+17

(To be continued)

(Continued)

H+C3H2->C3H+H2	3.04E+18	1.65E+19	4.86E+17
H+C3H->C3H2	7.45E+14	6.91E+15	6.54E+13
C3H2->H+C3H	1.27E+16	7.75E+13	3.11E+07
H+C3->C3H	3.62E+14	2.49E+15	5.34E+12
C3H->H+C3	6.09E+15	2.94E+13	3.07E+06
H2(1)+Ar->H2+Ar	1.18E+19	7.35E+05	5.38E-05
H2(1)+H->H2+H	1.16E+20	7.58E+05	9.16E-07
Ar**+e->Ar*+e	1.65E+10	6.88E-42	2.94E-79
Ar*+e->Ar**+e	1.04E+11	1.72E-40	1.35E-77
Ar*+H->H(2)+Ar	2.78E+13	3.15E-13	4.26E-33
Ar**+H->H(2)+Ar	4.42E+12	1.26E-14	9.28E-35
H2*+H->H(2)+H2	2.44E+13	5.92E-14	3.28E-34
Ar*+Ar*->Ar++Ar+e	2.53E+04	6.65E-47	1.08E-83
Ar**+Ar*->Ar++Ar+e	4.03E+03	2.66E-48	2.36E-85
Ar**+H->ArH++e	4.42E+12	1.26E-14	9.28E-35
Ar*+H->ArH++e	2.78E+13	3.15E-13	4.26E-33
H(2)+Ar->ArH++e	1.13E+13	1.85E-10	3.16E-30
H(3)+Ar->ArH++e	2.78E+11	6.86E-16	4.43E-36
H(2)+H2->H3++e	5.29E+14	3.85E-08	7.54E-27
H(3)+H2->H3++e	1.30E+13	2.64E-14	1.35E-34
Ar**+C2H2->Ar+CxHy++e	1.37E+12	4.21E-14	9.12E-33
Ar*+C2H2->Ar+CxHy++e	8.63E+12	1.05E-12	4.19E-31
Ar**+C2H->Ar+CxHy++e	1.79E+10	4.15E-18	1.73E-40
Ar*+C2H->Ar+CxHy++e	1.13E+11	1.04E-16	7.95E-39
Ar**+C->Ar+CxHy++e	9.96E+08	1.61E-18	2.80E-41
Ar*+C->Ar+CxHy++e	6.26E+09	4.01E-17	1.29E-39
Ar**+C2->Ar+CxHy++e	4.95E+08	8.02E-21	5.96E-45
Ar*+C2->Ar+CxHy++e	3.11E+09	2.01E-19	2.74E-43
Ar**+C2(X)->Ar+CxHy++e	1.05E+08	2.22E-21	1.58E-45
Ar*+C2(X)->Ar+CxHy++e	6.58E+08	5.55E-20	7.27E-44
Ar**+C3->Ar+CxHy++e	4.64E+08	1.91E-17	2.93E-38
Ar*+C3->Ar+CxHy++e	2.92E+09	4.77E-16	1.34E-36
Ar*+C3H2->Ar+CxHy++e	1.15E+10	1.55E-14	1.03E-32
Ar*+C4H2->Ar+CxHy++e	7.91E+09	8.56E-16	2.81E-34
H2*+C->H2+CxHy++e	1.65E+10	2.27E-17	2.97E-40
H2*+CH3->H2+CxHy++e	3.36E+11	2.20E-14	1.10E-33
H2*+C2H->H2+CxHy++e	2.98E+11	5.87E-17	1.84E-39
H2*+C2H2->H2+CxHy++e	2.28E+13	5.95E-13	9.67E-32
H2*+C2H4->H2+CxHy++e	6.09E+09	1.56E-15	2.86E-32
H2*+C2->H2+CxHy++e	8.22E+09	1.13E-19	6.32E-44
H2*+C2(X)->H2+CxHy++e	1.74E+09	3.14E-20	1.68E-44
H2*+C3->H2+CxHy++e	7.70E+09	2.70E-16	3.10E-37

(To be continued)

(Continued)

H2*+C3H2->H2+CxHy++e	3.05E+10	8.77E-15	2.38E-33
H2*+C4H2->H2+CxHy++e	2.09E+10	4.84E-16	6.48E-35
Ar++H2->ArH++H	2.04E+11	1.64E-15	2.73E-34
Ar++H2->H2++Ar	2.38E+10	2.05E-16	3.65E-35
Ar++C2H2->CxHy++Ar	3.29E+08	3.88E-18	4.25E-37
ArH++H2->H3++Ar	5.77E+15	2.55E-08	8.37E-27
H2++H2->H3++H	1.05E+13	7.02E-14	9.26E-33
H2++Ar->ArH++H	1.36E+11	1.10E-15	1.84E-34
H2++CH4->CxHy++H	3.10E+08	4.66E-17	5.53E-35
H2++CH3->CxHy++H	4.63E+08	1.06E-17	2.65E-37
H2++C2H2->H+CxHy+	3.14E+10	2.88E-16	2.33E-35
H2++C2H->CxHy++H	4.11E+08	2.84E-20	4.42E-43
H3++Ar->ArH++H2	5.73E+15	2.81E-08	9.14E-27
H3++C2H2->H2+CxHy+	5.81E+14	3.22E-09	5.08E-28
H3++CH4->H2+CxHy+	5.74E+12	5.21E-10	1.21E-27
H3++CH3->H2+CxHy+	8.56E+12	1.19E-10	5.78E-30
H3++C->H2+CxHy+	4.22E+11	1.23E-13	1.56E-36
H3++C2->H2+CxHy+	2.10E+11	6.13E-16	3.32E-40
H3++C2(X)->H2+CxHy+	4.44E+10	1.70E-16	8.81E-41
H3++C2H->H2+CxHy+	7.60E+12	3.17E-13	9.63E-36
H3++C3->H2+CxHy+	1.96E+11	1.46E-12	1.63E-33
H3++C3H2->H2+CxHy+	7.78E+11	4.74E-11	1.25E-29
H3++C4H2->H2+CxHy+	5.33E+11	2.62E-12	3.40E-31
Ar++CH4->Ar+CxHy+	2.69E+06	5.22E-19	8.38E-37
Ar++CH3->Ar+CxHy+	4.84E+06	1.44E-19	4.84E-39
Ar++C2->Ar+CxHy+	1.18E+05	7.39E-25	2.78E-49
Ar++C2(X)->Ar+CxHy+	2.51E+04	2.05E-25	7.37E-50
Ar++C2H->Ar+CxHy+	4.29E+06	3.83E-22	8.07E-45
Ar++C3->Ar+CxHy+	1.11E+05	1.76E-21	1.36E-42
Ar++C3H2->Ar+CxHy+	4.40E+05	5.72E-20	1.05E-38
Ar++C4H2->Ar+CxHy+	3.01E+05	3.16E-21	2.85E-40
Ar+e->e+Ar*	6.44E+13	9.72E-13	2.03E-31
Ar+e->e+Ar**	4.41E+13	6.64E-13	1.39E-31
Ar*+e->e+Ar	6.52E+08	1.08E-42	8.50E-80
Ar**+e->e+Ar	8.65E+07	3.61E-44	1.54E-81
H(2)+e->H(3)+e	1.22E+12	1.31E-36	2.82E-74
H(3)+e->H(2)+e	1.37E+10	5.20E-43	3.22E-82
ArH++e->Ar+H(3)	2.96E+09	1.93E-40	6.97E-78
H+e->H(2)+e	6.25E+15	1.19E-11	4.42E-32
H(2)+e->H+e	3.10E+12	4.21E-36	1.00E-73
H+e->H(3)+e	9.36E+13	1.39E-13	4.66E-34
H2+e->H2(1)+e	1.28E+20	6.73E-06	2.05E-24

(To be continued)

(Continued)

H2(1)+e->H2+e	1.09E+17	1.21E-22	1.02E-51
H2+e->H+H+e	8.67E+16	1.32E-09	2.39E-28
H2(1)+e->H+H+e	4.36E+13	1.32E-26	6.37E-56
H2+e->H2*+e	2.62E+15	3.25E-11	5.37E-30
H2(1)+e->H2*+e	1.32E+12	3.23E-28	1.43E-57
H2+e->H+H+e	4.01E+15	4.97E-11	8.20E-30
H2+e->H+H+e	7.60E+15	9.42E-11	1.55E-29
H2+e->H2*+e	7.92E+14	9.81E-12	1.62E-30
H2+e->H2*+e	2.99E+14	3.71E-12	6.12E-31
H2+e->H2*+e	6.41E+12	7.94E-14	1.31E-32
H2+e->H2*+e	8.12E+13	1.01E-12	1.66E-31
CH4+e->CH3+H+e	1.34E+13	5.98E-12	1.09E-29
C2H2+e->C2H+H+e	3.95E+15	1.07E-10	1.33E-29
C2H+e->C2+H+e	5.16E+13	1.06E-14	2.52E-37
Ar+e->Ar++e+e	2.28E+11	2.04E-15	3.42E-34
Ar*+e->Ar++e+e	1.98E+08	1.95E-43	1.23E-80
Ar**+e->Ar++e+e	3.15E+07	7.80E-45	2.68E-82
H2*+e->H2++e+e	5.23E+08	1.10E-43	2.84E-81
H+e->H3++e+e	1.37E+13	1.66E-14	5.15E-35
H2+e->H2++e+e	1.07E+13	7.86E-14	1.04E-32
H2(1)+e->H2++e+e	5.34E+09	8.30E-31	3.03E-60
C2H2+e->CxHy++e+e	9.70E+13	1.69E-12	1.74E-31
CH4+e->CxHy++e+e	5.06E+10	1.18E-14	1.62E-32
CH3+e->CxHy++e+e	3.45E+12	1.81E-13	6.18E-33
CH2+e->CxHy++e+e	2.59E+11	1.10E-15	1.39E-37
CH+e->CxHy++e+e	4.83E+10	3.58E-17	1.57E-40
C+e->CxHy++e+e	3.29E+10	3.62E-17	3.23E-40
C2H+e->CxHy++e+e	1.27E+12	2.01E-16	4.28E-39
C2+e->CxHy++e+e	3.51E+10	3.88E-19	1.48E-43
C2(X)+e->CxHy++e+e	7.42E+09	1.07E-19	3.91E-44
C2H6+e->CxHy++e+e	1.02E+06	2.34E-17	1.93E-33
C2H4+e->CxHy++e+e	5.34E+10	1.09E-14	1.37E-31
C3+e->CxHy++e+e	3.58E+10	1.01E-15	7.89E-37
ArH++e->Ar+H(2)	1.15E+11	1.04E-38	4.29E-76
ArH++e->Ar+H(3)	3.85E+10	2.97E-39	1.15E-76
H2++e->H(2)+H	2.63E+07	3.58E-45	5.93E-83
H3++e->H2+H(2)	3.61E+12	2.97E-37	9.57E-75
CxHy++e->C2H+H	6.91E+14	3.78E-38	3.52E-75

Appendix B Spectral constants for Pgopher simulation

Table B. 1 Spectral constant for C_2 ($a^3\Pi_u$, v''=0)→ ($d^3\Pi_g$ v'=0) simulation

Constant	Lower state ($a^3\Pi_u$,, v''=0)	Upper state ($d^3\Pi_g$, v'=0)
Origin	0	19378.46456
B	1.624075	1.7456043
A	-15.2696	-14.0005
LambdaSS	-0.1476	0.031
o	0.675355	0.6094784
p	0.002402	0.0039452
q	-0.000497	-0.0007636
D	6.479E-6	6.855E-6
H	7.85E-12	0
AD	0.000276	0.000542
oD	-8.22908E-6	1.202E-8
pD	1.1996E-7	-2.404E-8
qD	-1.288E-8	1.202E-8

Table B. 2 Spectral constant for CH ($X^2\Pi$, v''=0)→ ($A^2\Delta$, v'=0) simulation

Constant	Lower state ($X^2\Pi$, v''=0)	Upper state ($A^2\Delta$, v'=0)
Origin	0	23173.45853
B	14.192406	14.579083
A	28.146724	-1.10088
Gamma	-0.02565	0.04217
p	0.03351	6.6E-7
q	0.0386724	-2.89E-8
D	0.00146183	0.00156604
H	1.1668E-7	9.761E-8
L	1.459E-11	2.666E-11
gammaD	8.56E-6	-9.25E-6

Table B. 3 Spectral constant for BH ($X^1\Sigma^+$, v''=0)→ ($A^1\Pi$, v'=0) simulation

Constant	Lower state ($X^1\Sigma^+$, v''=0)	Upper state ($A^1\Pi$, v'=0)
Origin	0	23073.9708
B	11.815745	11.906298
q	0	0.037364
D	0.00122305	0.00143853
H	9.86E-8	5E-8
L	-4.5E-12	-6.88E-12
q_D	0	-1.6846E-5

Appendix C OES and CRDS measured transitions

Table C. 1 OES traced species

Species Name	Spectral line	Upper level	Lower level
B*	249.68 nm	$^2S_{1/2}$---4.98 eV	$^2P_{1/2}$----0 (ground state)
	249.77 nm		$^2P_{3/2}$----1.989E-2 eV
CH*	431.4 nm	$A^2\Delta$---2.88 eV	$X^2\Pi$----0 (ground state)
BH*	433.2 nm	$A^1\Pi$---2.87 eV	$X^1\Sigma$----0 (ground state)
H(n=4) --H_β	486.1 nm	H(n=4)---12.75 eV	H(n=2)---10.2 eV
C_2	516.5 nm	$d^3\ \Pi_g$---- 2.41 eV	$a^3\ \Pi_u$---0.09 eV
H_2*	602.1 nm	$3p^3\Sigma_u^+$---13.28 eV	$2s\ \Sigma_g^+$---11.84 eV
H (n=3)--H_α	656.3 nm	H(n=3)---12.1 eV	H(n=2)---10.2 eV
Ar*	750.4 nm	$3s^23p^5(^2P°_{1/2})4p$ –13.52	$3s^23p^5(^2P°_{1/2})4s$---11.86 eV
	763.5 nm	eV	$3s^23p^5(^2P°_{3/2})4s$ --11.58 eV
	811.5 nm	$3s^23p^5(^2P°_{3/2})4p$ –13.21	$3s^23p^5(^2P°_{3/2})4s$-- 11.58 eV
		eV	
		$3s^23p^5(^2P°_{3/2})4p$ -13.11	
		eV	

Table C. 2 CRDS traced species

Species Name	Spectral line	Upper level	Lower level
B (to be done)	249.68 nm	$^2S_{1/2}$---4.98 eV	$^2P_{1/2}$----0 eV (ground state)
	249.77 nm		$^2P_{3/2}$----1.989E-2 eV
CH $X^2\Pi$	431.4 nm	$A^2\Delta$---2.88 eV	$X^2\Pi$----0 eV (ground state)
BH $X^1\Sigma$	433.2 nm	$A^1\Pi$---2.87 eV	$X^1\Sigma$----0 (ground state)
C_2 $a^3\ \Pi_u$	516.5 nm	$d^3\ \Pi_g$---- 2.41 eV	$a^3\ \Pi_u$---0.09 eV
H (n=2)--Hα	656.3 nm	H(n=3)---12.1 eV	H(n=2)---10.2 eV

Appendix D OES results in $B_2H_6/Ar/H_2/CH_4$ plasma (from front window)

D.1. B_2H_6 flow rate effect

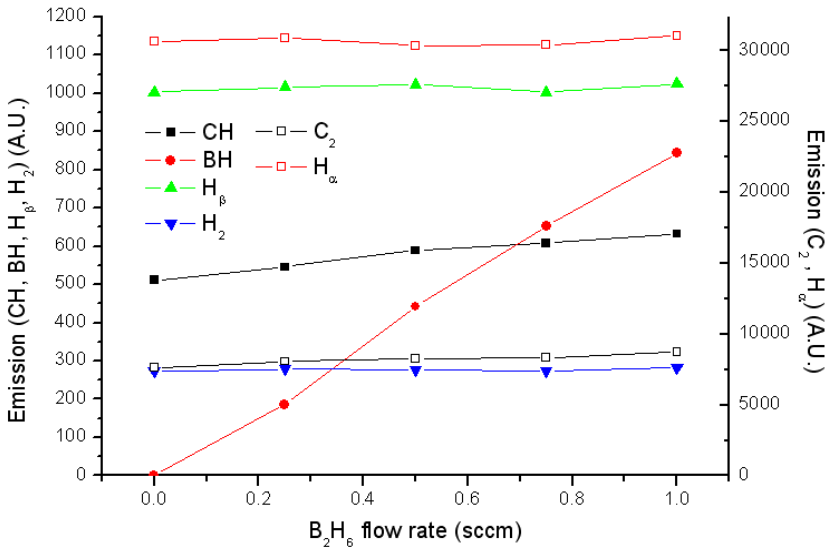

Figure D. 1 CH, BH, H_β, H_2, C_2 and H_α emissions as functions of B_2H_6 flow rate, other parameters are the same as the standard discharge condition

D.2. CH_4 flow rate effect

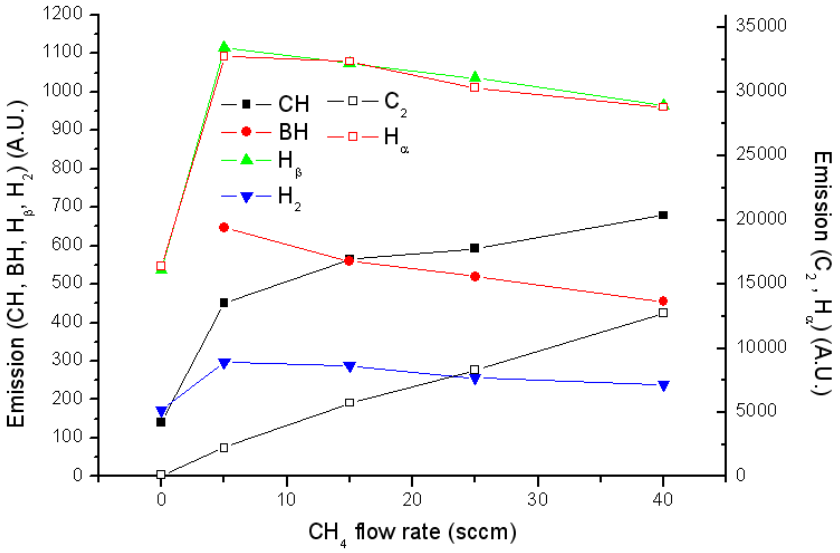

Figure D. 2 CH, BH, H_β, H_2, C_2 and H_α emissions as functions of CH_4 flow rate, other parameters are the same as the standard discharge condition

D.3. Ar flow rate effect

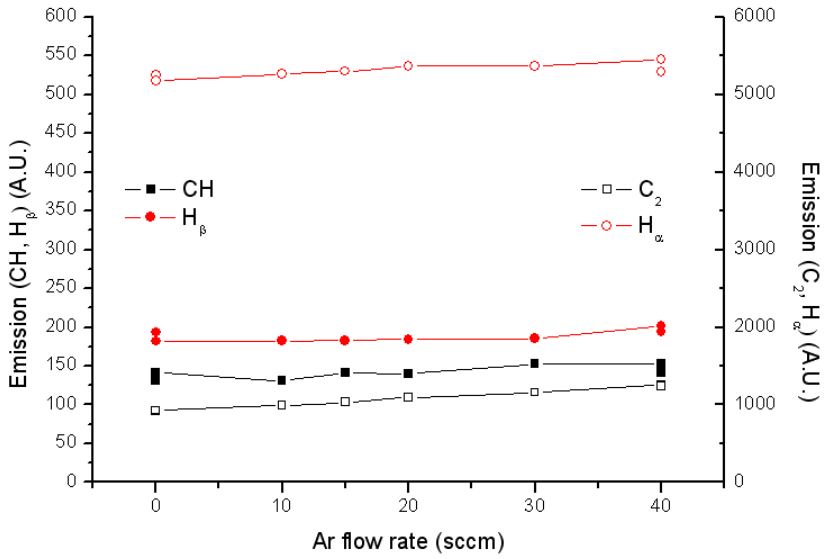

Figure D. 3 CH, H_β, C_2 and H_α emissions as functions of Ar flow rate, other parameters are the same as the standard discharge condition. BH and H_2 are too noisy to be recognized from the spectra

D.4. Power effect

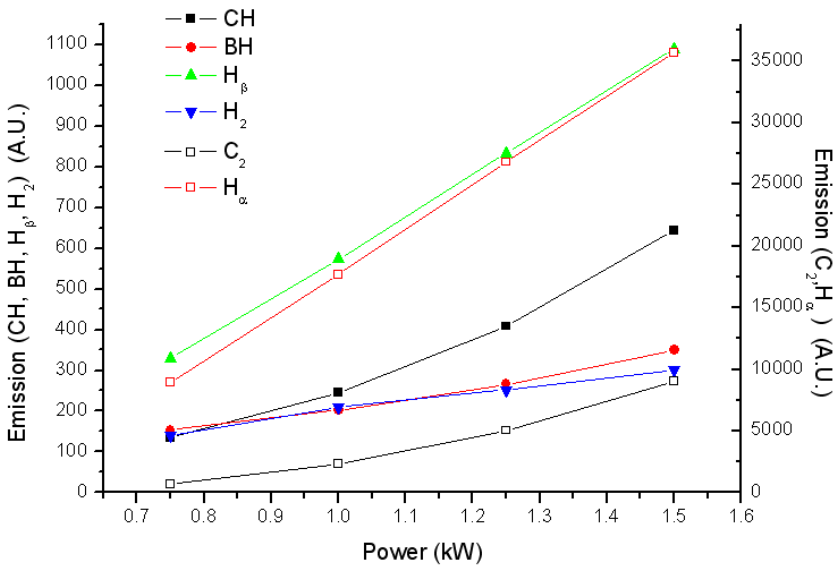

Figure D. 4 CH, BH, H_β, H_2, C_2 and H_α emissions as functions of input power, other parameters are the same as the standard discharge condition

D.5. Pressure effect

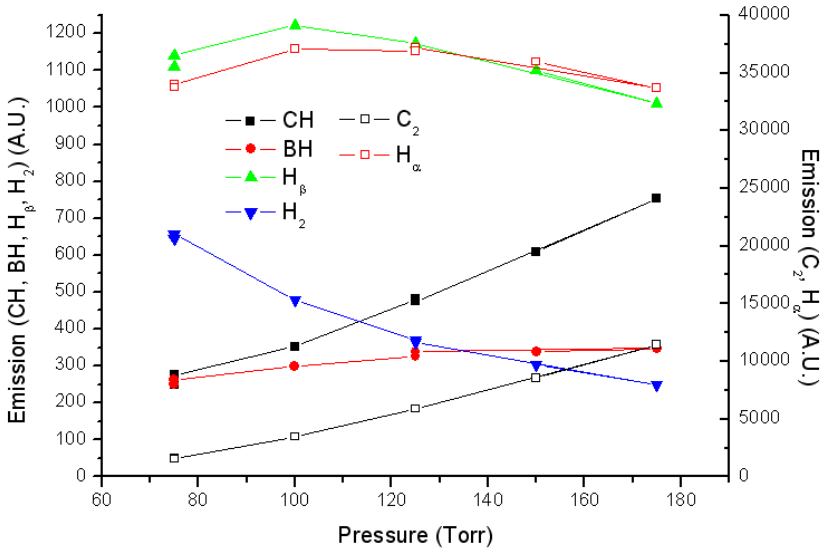

Figure D. 5 CH, BH, H_β, H_2, C_2 and H_α emissions as functions of total pressure, other parameters are the same as the standard discharge condition

Publication List

(1) "Spatial profiling of H(n=2) atom number densities in a DC arc jet reactor", C.J. Rennick, J. Ma, M.N.R. Ashfold, A.J. Orr-Ewing and Yu.A. Mankelevich, *Plasma Sources Sci. Tech.* **15** (2006) 432-440.

(2) "Measurement and modelling of $Ar/H_2/CH_4$ arc jet discharge CVD reactors I: intercomparison of derived spatial variations of H atom, C_2 and CH radical densities", C.J. Rennick, J. Ma, J.J. Henney, J.B. Wills, M.N.R. Ashfold, A.J. Orr-Ewing and Yu.A. Mankelevich, *J. Appl. Phys.* **102** (2007) 063309.